# Femtosecond Spectroscopy of Coherent Phenomena in Quantum Materials

A dissertation by

Fahad Mahmood

B.S. Physics, Engineering - Aero/Astro
Stanford University, 2010

Submitted to the Department of Physics
in partial fulfillment of the requirements for the degree of

Doctor of Philosophy in Physics

at the

Massachusetts Institute of Technology

June 2016



Author .....
Department of Physics
May 17th, 2016

Certified by .....
Nuh Gedik
Associate Professor of Physics
Thesis Supervisor

Accepted by .....
Nergis Mavalvala
Associate Department Head for Education

# Femtosecond Spectroscopy of Coherent Phenomena in Quantum Materials

by

Fahad Mahmood

Submitted to the Department of Physics
on May 17th, 2016, in partial fulfillment of the
requirements for the degree of
Doctor of Philosophy

## Abstract

Quantum materials are solids that cannot be described by the single-particle band models of conventional condensed matter physics. Rather strong inter-particle interactions and coupling between various degrees of freedom (charge, spin, orbital and lattice) lead to emergent phases such as high-temperature superconductivity, spin and charge density wave ordering and topologically protected 2D Dirac fermions.

In the time-resolved experiments in this work, an initial laser 'pump' pulse drives the sample out-of-equilibrium by manipulating the electronic band structure, generating quasi-particles and/or exciting specific collective modes. The resulting dynamic changes are then tracked as a function of time by using two different spectroscopic tools: transient reflectivity and time and angle resolved photoemission (Tr-ARPES).

One approach is to perturb the system gently (low pump intensity) to preserve the underlying order. Transient reflectivity experiments are done in this weak perturbation regime to study the following phenomena: (1) Collective excitations (amplitude and phase mode) of the fluctuating charge density wave order in the cuprate superconductor $La_{2-x}Sr_xCuO_4$; (2) Decay dynamics of valley polarized excitons in the monolayer transition metal dichalcogenide $MoSe_2$; and (3) a confinement-deconfinement transition of single-particle excitations in the spin-orbit assisted Mott insulator $Na_2IrO_3$.

In the opposite regime (strong perturbation), it is possible to drive electronic materials into non-equilibrium phases with fundamentally different properties than in equilibrium. This work uses mid-IR pump pulses to directly couple photons to an electronic system to create hybrid electron-photon states. In this case, the oscillating electric field of the pump causes Dirac fermions to experience a time-periodic potential to generate Floquet-Bloch states which repeat in both energy and momentum. These and other similar photo-induced states are observed and characterized using Tr-ARPES on the topological insulators $Bi_2Se_3$ and $Bi_2Te_3$.

Thesis Supervisor: Nuh Gedik
Title: Associate Professor of Physics

# Femtosecond Spectroscopy of Coherent Phenomena in Quantum Materials

Fahad Mahmood

Gedik Lab, MIT

# Contents

# List of Figures

# Acknowledgements

A batsman's success in cricket is often described as a feat of individual determination and skill, perseverance and patience, controlled aggression, adaptability and calculated risk. After all, it is one batsman trying to hit and maneuver a ball of varying speed, swing and bounce through a packed field again and again for hours or even days. Lost in all such accolades are the people behind-the-scenes supporting you one step at a time: the batting partner who was able to keep the scoreboard ticking while you settled in, the batsmen before who discovered that it was a slow wicket, the teammate who whispered 'watch-out for the first eight overs' right before you went in, the captain who gave you the freedom to take time and play according to your own style, the coaches who worked with you day and night to expand your timing and repertoire of shots and of course the spectators in the stands cheering your every shot and bucking you up when you miss.

My PhD has been quite like this: excellent and rewarding partnerships, novel techniques started by others that I could improve and build upon, guidance from some of the very best experimental physicists, an innovative advisor who let me explore and develop different interests, and family and friends who believed in me and carried me through each setback.

I first thank my advisor Prof. Nuh Gedik whose vision and passion for new approaches in experimental physics has made all this work possible. He is always looking to innovate and approach problems in a unique way, a trait from which I have learned tremendously. His mantra of 'What's next?' has kept me thinking and searching for different interpretations, ideas and possibilities which has ultimately made me a better scientist. He allowed me the flexibility and gave me the guidance to pursue my drastically varying interests. Most importantly, he has been extremely personable and approachable on a day-to-day basis throughout my six years at MIT.

In the Gedik lab, I have been extremely fortunate to learn from and work with some of the brightest minds in condensed matter physics and time-resolved spectroscopy. Foremost, Darius Torchinsky (now professor at Temple) who transferred part of his physics brain to me. He is the best experimentalist I know; most of my knowledge about optics, laser and time-resolved techniques is credited to him. He was my partner-in-crime for our adventures of K.F.C. during my early years at MIT. He is a brilliant scientist and his 'vision' of the

amplitudon while recovering from surgery led to the first part of this work. I am also grateful to David Hsieh (now professor at Caltech) who mentored me during my first few months at MIT. His advice on 'designing experiments in context to the materials being studied' has proven to be invaluable. He has a wonderful skill to elevate data into a coherent interpretation and I am lucky to have learned that from him right at the beginning of my PhD.

I've also had the privilege to work closely with my officemate Zhanybek Alpishev on a number of different projects. I admire his vast knowledge and his ability to break down complex topics into the simplistic terms possible. It's truly been an enriching experience to bounce ideas around with him. More importantly, his pearls of wisdom such as 'good physics is what takes a human to do, not a monkey', his history-of-physics stories and his constructive criticism has kept me honest, inquisitive and thoughtful about the experiments in my PhD. Its also been rewarding to interact and work with Inna Vishik, who is a living, breathing encyclopedia on cuprate superconductors. I am also indebted to Yihua Wang (now professor at Fudan) who initially set up the Tr-ARPES setup in the lab and pioneered the Floquet-Bloch experiments which motivated part of my research.

I've also forged meaningful friendships with members of the lab. In particular, Dan Pilon, who engaged with me in many squash duels over the past few years. These were a healthy way for me to navigate through many research setbacks and I thank him for 'letting me win' at least one out of every ten games. Alex Frenzel, whose attention to detail and devotion to 'doing good science' is infectious and galvanizing. Changmin Lee, whose 'anthropological' insights into graduate school and academia gave me much needed perspective and introspection. He has patiently been a sounding-board for my vague scientific ideas countless times, and I thank him for that.

Other past and present members of the Gedik group have been quite engaging and inspiring. I appreciate and respect the big-picture optimism of James McIver, the dogged work ethic and tenacity of Timm Rohwer and Edbert Sie, the perseverance and dedication of Ozge Ozel and the experimental prowess of Byron Freelon. It's also been a pleasure to work with newcomers Emre Ergecen and Alfred Zong who are both extremely bright and energetic. The future of the Gedik lab is in good hands!

The projects in the second half of my PhD were made possible by Ching-Kit (Chris) Chang in theoretical physics at MIT. It has been a pleasure to collaborate with him on the Floquet-Bloch experiments. He is brilliant at relating theory to a particular experiment. He has been extremely helpful in advancing my understanding of periodically driven systems and topological states of matter and I thank him for that.

I am also grateful to a number of physics faculty at MIT, in particular Prof. Pablo Jarillo-Herrero and Prof. Raymond Ashoori for their advice and entrusting me with the

condensed matter journal club at MIT. Prof. Patrick Lee, Prof. Joe Checkelsky and Prof. Liang Fu were very gracious to meet with me a number of times for illuminating discussions. In addition, I thank Monica Wolf, our group's administrative assistant, who maintains a joyful and humorous attitude despite somehow managing to keep track of finances and other details of nearly eight different experiment labs. She was especially supportive to me during some very difficult times in my PhD. It's also been illuminating to share scientific and non-scientific conversations with Ferhat Katmis, Ahmet Demir, Valla Fatemi, Dillon Gardner and many others in Building 13. I also want to acknowledge Palmgren Pal (Paul) from VG Scienta for teaching me the technical details of the ARTOF system and troubleshooting it with me many times.

My PhD would certainly not have been possible without a number of mentors in my undergraduate education at Stanford. My adviser, Prof. Hari Manoharan, inspired in me a wonderment and appreciation of cutting-edge experimental techniques in physics. Prof. Katherine Moler gave me a solid foundation in quantum mechanics which has proved indispensable. Rick Pam taught me much of the basics of experimental design, cryogenics and data acquisition. Chaya Nanavati and my fellow TA-in-crime Ahmed Ismail taught me how to synthesize and communicate my knowledge at the very basic level during teaching and presenting. Special thanks to all of them.

The middle period of my PhD was uplifted due to the MIT cricket club which allowed me an escape from countless experimental setbacks. I thank all of my teammates, present and former, for all our cricketing exploits on the field. They entrusted me with the captaincy and that proved to be invaluable in teaching me how to balance a multitude of factors in decision making: the importance of which during Tr-ARPES experiments cannot be overstated. In particular, I am grateful to Koustuban Ravi, Priyank Kumar and Usman Naseer for our countless culinary adventures and enlightening discussions after matches.

The lessons my friends taught me are why I even got to graduate school at MIT in the first place. I am thankful to have shared life with Aadel, Bhatti, Waqas, Hajra, Taimur, Sundus, Asmara, Asfandyar and many others.

I thank my sister Sana who pushed me to learn outside my comfort zone and taught me a deep sense of skepticism, and my niece Zoya who learned how to sit-up straight, crawl, walk, talk, sing, swim, write, multiply and divide all while I only learned to cool things down and shoot lasers at them! It's been a joy seeing them regularly throughout my graduate school.

My parents-in-law, the ever-so 'wise' and 'genius', Lou and Peggy, have been a constant source of encouragement, humor and fun. Their ability to somehow work more than 12 hours each day and remain exceedingly jovial and funny has been very inspiring. Lou's sage advice on 'getting off the train only if you can get back on or if you know another train is coming'

has served me well. Peggy's sweetness, calmness and warmth has been especially comforting during difficult times. Not to mention the foolproof quiche, meatloaf and crabcakes!

I also thank my father for inculcating in me a healthy dose of discipline and work-ethic. My mother fostered in me a love of reading and knowledge and taught me the importance of considering different possibilities and points-of-view. She gave me independence at a very young age to allow me to develop my own interests. Despite her illness, she encouraged and pushed me to pursue being a physicist at the best universities possible, even if they were 11,000 miles away from her. Her resilience and strength have been key inspirational guides throughout my education. She wanted to see me graduate from 'the great' MIT ever since our family learned about it nearly 22 years ago. She came close to that within a year. I'll always cherish her unconditional love.

Finally, my PhD would not have been possible without the love, support and encouragement of my wife, Maggie. She has been by my side through each and every step; comforting me during qualifying exams, picking me up from lab after dreaded all-nighters and reassuring me through the writing of this thesis. More importantly, she has always found a way to make me laugh. I am grateful for all of our traveling, hiking and cooking adventures together. She even learned how to make the best *rotis* in the Western hemisphere. She is a brilliant and creative teacher and extremely kindhearted and compassionate. I am in awe of how she manages to balance everything she does. I am so thankful she got placed in Roble and that we found each other.

*to my mother, Shama*

لب پہ آتی ہے دُعا بن کے تمنّا میری
زندگی شمع کی صورت ہو خدایا میری

*my wish is put into words as a prayer*

*may my life be like the candle light (shama)*

--- Iqbal, *A child's poem*

*I think a good case can be made that science has now moved from an Age of Reductionism to an Age of Emergence, a time when the search for ultimate causes of things shifts from the behavior of parts to the behavior of the collective.*

— Robert Laughlin *A Different Universe: Reinventing Physics from the Bottom Down*

# 1 Introduction

## Contents



In this chapter we introduce the term 'quantum materials' as applied to contemporary condensed matter physics while explicitly focusing on unifying features of different materials studied in this work. We then address why time-resolved studies with a laser excitation and femto-second resolution are ideally suited to study excitations in quantum materials. We will also describe the overall organization of this thesis and list the collaborations involved in the various experiments.

## 1.1 Quantum materials

'Quantum materials' is an umbrella term used to provide a common link between a variety of problems in condensed matter physics. At face value, this term appears quite broad and catchy. Indeed, all materials exist due to quantum mechanics at the fundamental

level. Nevertheless, this term is increasingly being used (e.g. [1, 2]) over the last few years to characterize solids with 'emergent' unconventional properties such as high-temperature superconductivity and topologically protected phases. One way to define this term is to include materials that can't even be understood qualitatively without invoking quantum mechanics [3]. This excludes simple metals since they can be understood reasonably well by using the Drude model which is purely based on classical statistical mechanics of an ideal gas.

Of course, even when quantum mechanics is introduced as is done in the well-known Landau's Fermi-liquid theory [4], the description of a metal can be reduced to a system of non-interacting quasi-particles which are well modeled by the Drude model. In Landau's theory, the state of strongly interacting fermions (e.g. electrons interacting through Coulomb forces between them) can either be reduced to a gas of non-interacting electrons or a state with spontaneously broken symmetry (e.g. ferromagnet) if the interactions are sufficiently strong. This concept of symmetry breaking remained the key framework to characterize different materials before the 1980s. Symmetry breaking referred to the idea that an ordered phase has lower symmetry than its unordered part, for example a ferromagnetic phases breaks time-reversal symmetry as well as the rotational symmetry of spin space. To characterize materials, physicists would devise scattering probes (e.g. X-ray diffraction) and look for discrete peaks as evidence that some symmetry was being broken.

Two crucial developments led to a change in this paradigm. First, the discovery of topological order in the integer [5] and fractional [6, 7] quantum hall phases which do not break any symmetries. They were instead characterized by the topology of their electron wave-function. Second, the discovery of high-temperature superconductors (HTS) [8] reflected a breakdown of Landau's Fermi-liquid theory since their normal state metallic properties deviated from Landau's famous $T^2$ behavior of electrical resistivity. Moreover, HTS materials displayed a host of different electronic, structural and magnetic phases with similar energy scales. These phases were termed 'emergent' because they cannot be accounted for by using a reductionist approach i.e. properties of individual electrons. Rather we must also include

strong electron correlations and interactions. Other examples of these so-called strongly correlated electron systems include Mott insulators [9] and heavy fermion materials [10].

The increased focus on emergent phases in strongly correlated systems coincided with the characterization of graphene [11] and the discovery of topological insulators (TIs) [12–14] which have topologically protected metallic surface states without strong interactions. In both graphene and the surface of 3D TIs, electrons behave as massless 2D Dirac fermions. Recent studies have also identified monolayer transition metal dichalcogenides (TMDs) as useful playgrounds to study emergent phenomena such as the valley hall effect [15]. These emergent properties in TIs and monolayer TMDs are due to strong coupling between spin and orbital degrees of freedom.

Thus, the term 'quantum materials' has been applied to include both strongly correlated materials as well as materials with topological order and low dimensionality. The thread tying these together is the presence of strong coupling between the charge, lattice, spin and/or orbital degrees of freedom which leads to collective behavior whose properties are fundamentally different from that of the constituent particles.

A useful way to understand the 'quantum materials' discussed in this thesis is to consider interaction strength between electrons and other degrees of freedom together with the strength of spin-orbit coupling (SOC). This is illustrated in fig. 1.1. The interaction strength is usually denoted as the ratio of the on-site Coulomb repulsion $U$ to the hopping amplitude $t$ between nearest neighbor sites. SOC is the coupling between the orbital angular momentum ($\mathbf{L}$) and spin angular momentum ($\mathbf{S}$) of an electron i.e $\lambda \mathbf{L} \cdot \mathbf{S}$. Conventional materials such as metals lie in the bottom left corner of fig. 1.1 with both weak interaction strength $U/t \rightarrow 0$ and weak SOC.

Strongly correlated materials, as described above, are one extreme in fig. 1.1 in which strong $U/t$ plays a crucial role in determining the electronic structure but SOC is negligible. Prototypical examples are $3d$ transition metal oxides in which the small spatial extent and narrow bandwidth of the $3d$-orbitals leads to a large $U/t$. Cuprate compounds are examples of these oxides in which strong inter-particle interactions lead to a number of

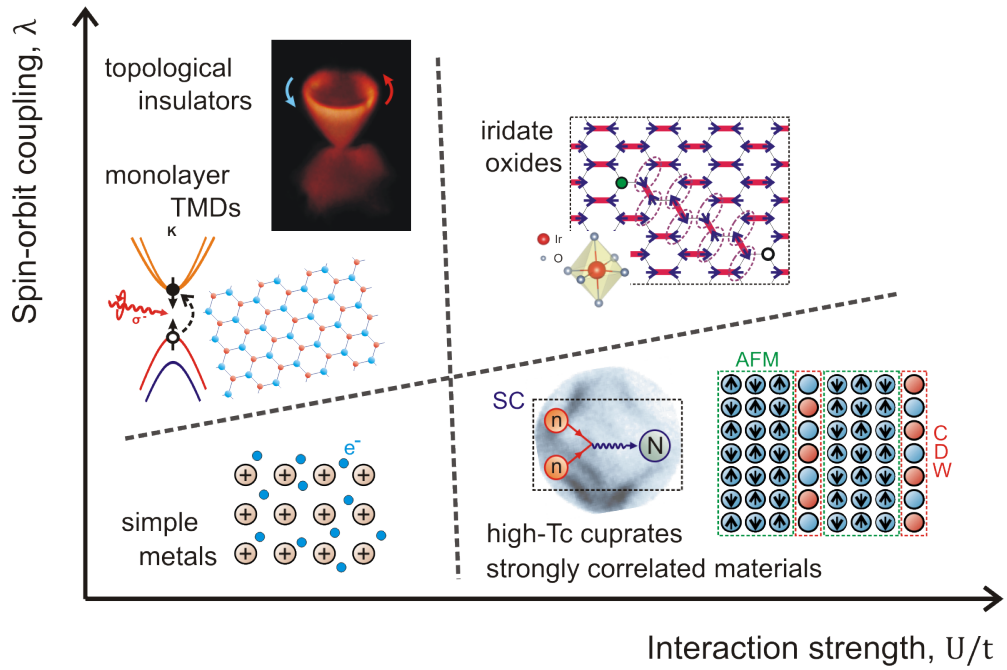


**Figure 1.1:** Classification of materials based on interaction strength between different degrees of freedom and spin-orbit coupling. The materials illustrated are the ones studied in this work.

competing/co-existing emergent quantum phases such as high-temperature superconductivity and spin and/or charge density wave ordering [16]. Cuprate superconductors will be studied in chapter 3.

In the other extreme are materials with strong SOC but negligible $U/t$. Examples of these include TIs in which strong SOC inverts the usual ordering of conduction and valence bands to generate robust metallic surface states with Dirac fermions. These Dirac fermions and their manipulation will be studied in chapter 8. Another category of materials in regime are semi-conducting monolayer TMDs in which strong SOC splits the valence band by 100s of meV allowing the spin to be controlled optically. Moreover, broken inversion symmetry in these 2D materials locks the valley index of an electron to its spin which allows manipulation of the valley index as well. These materials will be studied in chapter 4.

The presence of both strong SOC and strong $U/t$ (right corner in fig. 1.1) has largely been unexplored so far. There is significant interest in this regime to search for topological order in the presence of interactions (e.g. [17]). Examples include $5d$ iridate-oxides whose

electronic structure is affected by both SOC and $U/t$. This can lead to strongly frustrated magnetic phases which will be studied in chapter 5.

In this work we study different properties of these aforementioned 'quantum materials' as listed below:

1. Collective modes of their broken symmetry electronic phases. For example, the amplitude and phase mode of charge density wave order in cuprates (ch. 3).
2. Robustness of a particular degree of freedom such as the valley index of excitons in monolayer TMDs (ch. 4).
3. Behavior of fractional excitations in the presence of frustrated order. For example, a confinement-deconfinement transition in an iridate oxide (ch. 5).
4. Coherent manipulation of Dirac electronic states using periodic driving as is the case in the generation of Floquet-Bloch states in a topological insulator (ch. 8).

As will be discussed in the next section, femtosecond time resolved spectroscopies give us the ability to understand such properties at the fundamental time scale of electronic and atomic motion.

## 1.2 Time-resolved spectroscopy

To understand the emergent phases in quantum materials, it is important to disentangle the coupled interactions between the charge, spin, lattice and orbital degrees of freedom. As shown in fig. 1.2 electron-electron (e-e) interactions and electron-phonon (e-ph) interactions occur in the tens of fs to tens of ps time scales. Emergent phases can also have short-lived collective modes and can temporally fluctuate and compete with each other (e.g. see ch. 3) over very short times scales ($\sim$ ps). Similarly, these quantum materials exhibit a delicate balance between different electronic phases making them susceptible to manipulation using intense short-duration light pulses as will be discussed below. Such short pulses also allow probing coherently coupled electron-photon states before the states scatter due

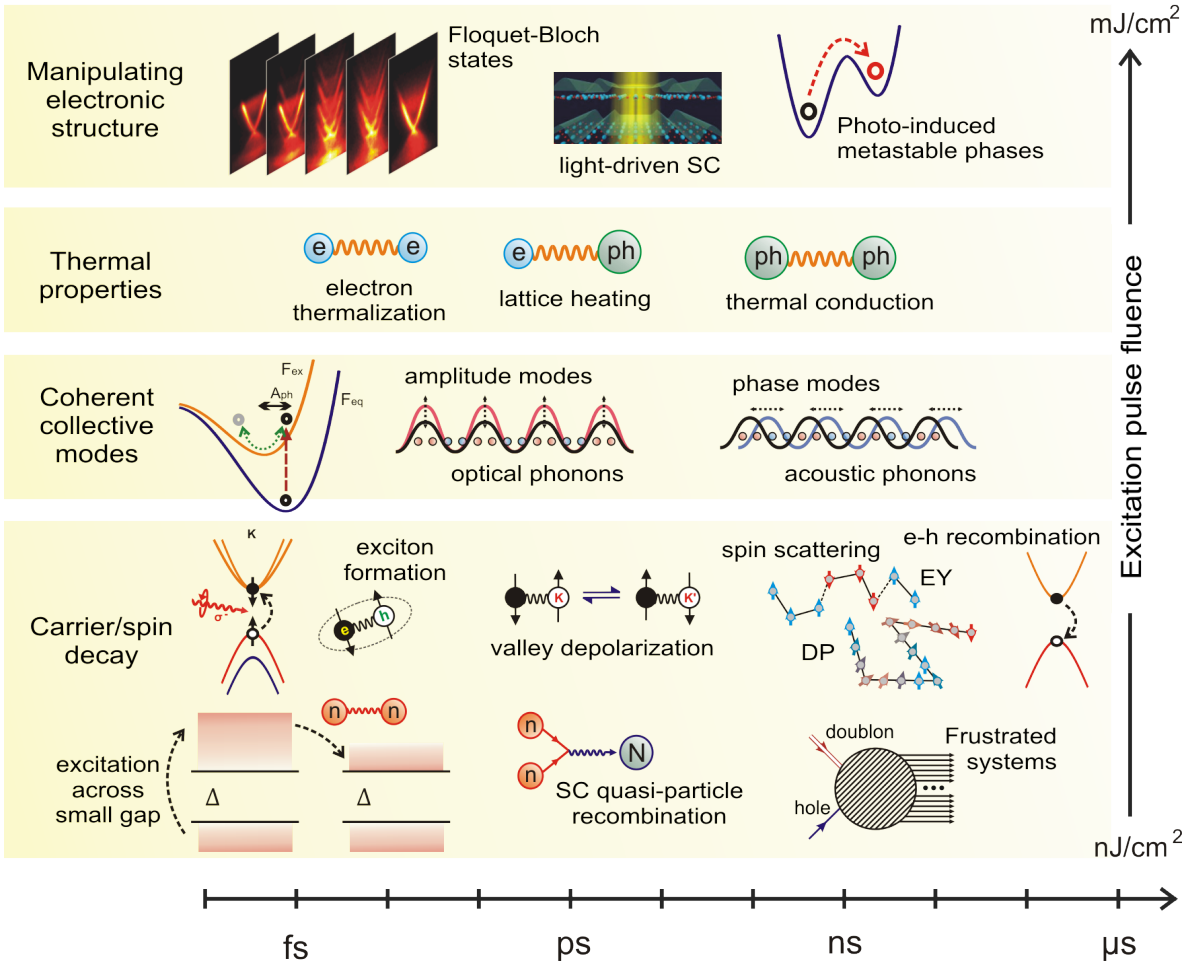


**Figure 1.2:** Time-scales of different electronic, lattice & spin processes as discussed in this work. Image on light-induced SC is from the A. Cavalleri group website.

to e-e or e-ph interactions. Thus, the study of such phenomena requires experimental tools that can access such short time scales.

To achieve this, time-resolved spectroscopies on quantum materials with femtosecond ($> 10\,\text{fs}$) resolution are increasingly being utilized [1]. All such spectroscopies are based on a pump-probe scheme whereby a laser pulse ('pump') with a short temporal duration ($< 1\,\text{ps}$) perturbs the material to create a non-equilibrium electron distribution and/or generate other excitations such as phonons or excitons. The frequency and polarization of the pump pulse can be tailored to selectively couple to particular degrees of freedom. For example, circularly polarized pulses will only couple to a particular spin in some semi-conductors.

Similarly, pulses with a frequency in the THz spectrum can directly excite a particular phonon mode. In this way, such excitations disentangle the coupled system and cause a change in the observable properties of the system which can the be measured using a time-delayed 'probe' pulse. Such properties can include the reflection/transmission spectrum, the optical conductivity, the crystal structure or the band-structure of the electronic system. By tracking the dynamic change in such properties as a function of the delay time between the pump and probe pulses, we can obtain important clues into different types of interactions in the system.

Here it is important to distinguish between weak and strong perturbation depending on the intensity of the pump pulse (fig. 1.2) . In time-resolved experiments, one approach is to perturb the system gently (low pump fluence) to preserve the underlying order. Here the pump fluence (a measure of the pulse energy over the area excited) is typically kept $\lesssim 10\,\mu J/cm^2$. Ordered phases in quantum materials often result in opening up of small energy gaps in the electronic structure. In this weak perturbation regime, electrons are excited above the gap without it closing fully. Similarly, the low fluence prevents a large change in the material temperature which ensures that the changes measured are due to the photo-excitation rather than just a simple increase in temperature. Examples of experiments in this regime include the measurement of quasi-particle recombination [18–20] and diffusion [21] in high-Tc cuprates. Low pump fluences can also be used to excite coherent collective modes of the order parameter (e.g. amplitude modes of the CDW order parameter [22]). The low pump fluences often result in extremely small changes in measurable quantities. For example, the change in reflectivity is typically around one part in a million ($10^{-6}$). This necessitates the use of pulse trains with a high repetition rate ($N$) for better signal-to-noise (S/R $\propto \sqrt{N}$). Chapters 2−5 discuss time-resolved experiments in this weak perturbation regime.

In the opposite strong perturbation regime, the goal is to manipulate the electronic structure or the order parameter itself by using an intense pump pulse. Here the pump fluence is typically $\gtrsim 500\,\mu J/cm^2$. As discussed before, quantum materials have a complex phase diagram often with competing phases. An intense laser pulse can be used to alter the free-energy landscape to allow one phase to dominate over another in ways which would be

not be possible using equilibrium methods (e.g. chemical doping, temperature). Prominent examples are possible light-induced superconductivity in high-Tc cuprates [23, 24] where intense mid-IR or THz pulses are used to excite particular coherent vibrational modes which are believed to weaken charge ordering in cuprates in favor of superconducting order. Another example, which will be explored in chapter 8, is to use an intense pump to directly couple photons to electrons to fundamentally alter the electronic band structure. As will be seen in ch. 8, the change in the band structure (e.g. opening up of gaps) directly scales with the pump electric field which necessitates the use of high $> 500\,\mu J/cm^2$ pump fluences.

We now briefly discuss the two different types of probes used in the time-resolved experiments in this work. For the weak perturbation regime, the IR reflectivity/transmission (ch. 2) of a material is monitored in response to an optical pump pulse. However, IR reflectivity is insensitive to the momentum of excitations as it averages over all momentum space. To resolve the energy and momentum distribution of electronic excitations we use photoemission (ch. 6) as the probe. This gives snapshots of the transient band-structure of a solid as a function of the delay time between the pump and the probe. Photoemission experiments are mostly performed in the strong perturbation regime.

## 1.3 Organization of thesis & collaborations

This thesis is primarily divided into two parts. The first part (ch. 2 to ch. 5) discusses time-resolved reflectivity experiments. Chapter 2 introduces the techniques used for time-resolved reflectivity: optical pump-probe (OPP) and transient grating (TG) spectroscopy with an emphasis on the physical principles. We also discuss the technical details as they were implemented in the course of this work. This thesis will focus on three particular applications of these techniques as follows.

Chapter 3 applies OPP and TG to high-Tc cuprates to resolve the dynamics of collective modes of the charge-density-wave phase and study its interaction with the superconducting phase. Chapter 4 applies a variation of TG (spin-TG) to study the decay dynamics of spin

and valley polarized excitations in a monolayer TMD. Lastly, chapter 5 utilizes another aspect of TG spectroscopy (optical phase separation) to selectively study single-particle excitations and Hubbard excitons in an iridate oxide. In each of these three chapters, detailed descriptions of the materials studied are provided.

The second part of the thesis (ch. 6 to ch. 8) discusses photoemission experiments. Chapter 6 introduces the techniques of Time and Angle Resolved Photoemission (Tr-ARPES) with an emphasis on the physical principles, capabilities and limitations. A few specific examples of Tr-ARPES experiments are also presented to illustrate is applications. Chapter 7 describes the technical details of Tr-ARPES and its implementation in the Gedik lab.

Chapter 8 uses Tr-ARPES to illustrate the coherent optical manipulation of a quantum material. Here mid-IR pump photons hybridize with Dirac fermions on the surface states of a topological insulator to form Floquet-Bloch states. This chapter gives a detailed description of topological insulators and the generation and characterization of these hybrid states.

The results presented in this thesis were performed under the supervision of my adviser Nuh Gedik, as part of collaborative research efforts which are described below.

The work on cuprates (ch. 3) was done in conjunction with Darius Torchinsky (now at Temple university). Anthony T. Bollinger and Ivan Bozovic at the Brookhaven National Lab grew and characterized the samples with mutual inductance measurements. The results are published in Nature Materials [25].

The results on monolayer TMD $MoSe_2$ (ch. 4) were interpreted with assistance from Zhanybek Alpichshev (MIT). Yi-Hsien Lee (now at National Tsing Hua university) and Jing Kong (MIT) grew and characterized the samples.

The experiments on $Na_2IrO_3$ (ch. 5) were primarily led by Zhanybek Alpichshev (MIT). Gang Cao (University of Kentucky) grew and characterized the samples. The results are published in Physical Review Letters [26].

The first part of photoemission experiments in chapter 8 are a continuation of work started by Yihua Wang (now at Fudan university) [27]. The second part was done in close collaboration with Ching-Kit Chan (MIT) who developed the theoretical methods and the

numerical simulations. Patrick Lee (MIT) and Zhanybek Alpichshev (MIT) provided crucial inputs about interpreting the data. The samples were synthesized by Dillon Gardner and Young Lee (MIT). Some of the results in ch. 8 are published in Nature Physics [28].

*A passerby noticed Nasruddin curiously inspecting the ground under a street lamp.*
*"Mullah," he said, "What are you doing?"*
*"I'm looking for a ring I dropped," Nasruddin replied.*
*"Oh," the man said as he also began searching. After a few minutes he asks Nasruddin, "Are you sure you dropped it here?"*
*"Not at all, I actually dropped it in my bedroom"*
*"Your bedroom?!" the passerby exclaimed. "Then why are you looking for it out here"*
*"Because," Nasruddin replied, "the light is so much better out here!"*

— "Tales of Mullah Nasruddin" - Persian folklore

# 2

# Time-resolved optical spectroscopy

## Contents



This chapter describes the techniques of optical pump-probe (OPP) and transient grating (TG) spectroscopy and their implementation in the Gedik lab. In general, optical pump-probe involves perturbing a material with a short pulse ('pump') light in the optical spectrum and then tracking the resulting change in the material's reflectivity by using a time-delayed 'probe' pulse. We will first describe how this dynamic change in the reflectivity can be used to learn about different excitations in a material. Examples of optical phonons in

$Bi_2Se_3$ and phase transitions in the superconductor Bi-2212 are described to illustrate the usefulness of this technique.

Transient grating spectroscopy is similar to optical pump-probe but the material is excited with two pump pulses that interfere on the material surface to generate a sinusoidal excitation pattern. The decay of this spatially varying excitation can then be tracked by monitoring the intensity of a probe beam that is diffracted from this transiently generated grating. We will discuss four different applications of this technique and how it is implemented using heterodyne detection.

The last section of this chapter describes the experimental setup for both these time-resolved techniques as they are implemented in the Gedik lab with an emphasis on the physical principles behind the workings of each component.

## 2.1 Optical pump-probe spectroscopy

Optical pump-probe spectroscopy (OPP) is a widely applicable technique used to understand the non-equilibrium dynamics of a quantum material after it is photo-excited. It does this by measuring the transient change in the reflectivity of a sample ($\Delta R(t)$) after it is perturbed with an ultra-short light pulse in the optical spectrum. The perturbing optical pulse is usually called the 'pump' while the pulse that monitors $\Delta R(t)$ is called the 'probe'. $\Delta R(t)$ is obtained as a function of time $t$ by changing the optical path length (the delay time) between the pump and probe pulses.

Optical pump-probe can either be single color (both pump and probe have the same frequency) or two-color (different frequency). Similarly, the technique can be used to monitor the change in the broadband reflectivity of a sample by varying the frequency of the probe or by using a 'white-light' probe beam. In this work, we use single-color pump-probe spectroscopy with both the pump and probe beams set to an energy of $\sim 1.55\,\text{eV}$ (fig. 2.1a). The precise energy can be tuned to within $\pm 60\,\text{meV}$. Each pump and probe pulse has a duration of $\sim 60 - 100\,\text{fs}$ which sets the time-resolution in our experiments. This particular

setup is optimized for measuring extremely small changes in the reflectivity ($\sim 10^{-5}$) in response to weak excitation. For that the pump fluences are usually kept below $5\,\mu J/cm^2$. Full details of the setup can be found below in sec. 2.3.

OPP measures the transient change in the reflectivity which can be directly related to the optical conductivity as follows. The complex reflectivity $\tilde{r}$ can be written in terms of the dielectric function $\epsilon$ using the Fresnel equations (for normal incidence):

$$\tilde{r} = \frac{1-\sqrt{\epsilon}}{1+\sqrt{\epsilon}} \tag{2.1}$$

Small changes in $\tilde{r}$ ($\delta\tilde{r}$) can be related to small changes in $\epsilon$ ($\delta\epsilon$) as:

$$\delta\tilde{r} = \frac{\partial\tilde{r}}{\partial\epsilon}\delta\epsilon = \frac{-1}{\sqrt{\epsilon}(1+\sqrt{\epsilon})^2}\delta\epsilon \tag{2.2}$$

$\delta\epsilon$ can then further be related to small changes in the optical conductivity $\sigma(\omega)$ at 1.5 eV as:

$$\epsilon(\omega) = 1 + \frac{4\pi i\sigma(\omega)}{\omega}$$
$$\delta\sigma = -\frac{i\omega}{4\pi}\delta\epsilon \tag{2.3}$$

Simple OPP only measures changes in the magnitude of $\tilde{r}$ and as such cannot be used to reconstruct the complex change in the optical conductivity. This limitation can be overcome using heterodyne detection in transient grating spectroscopy which will be discussed in detail in sec. 2.2.

We will now discuss different ways to interpret data obtained by OPP. For this it's important to consider how the pump pulse perturbs the sample. In general an optical pump pulse directly couples to the electrons in the sample to initially generate single-particle excitations far above the Fermi level in a metallic sample or across the electronic gap in case of a semi-conductor or insulator. These excitations quickly thermalize amongst each other within tens of fs. Since this is within the time resolution of our setup, this electron-electron thermalization will not be discussed further in this work. What happens after this thermalization depends on the particular system being studied. Below are four examples of optical pump-induced phenomena that we have encountered and the systems in which they typically occur:

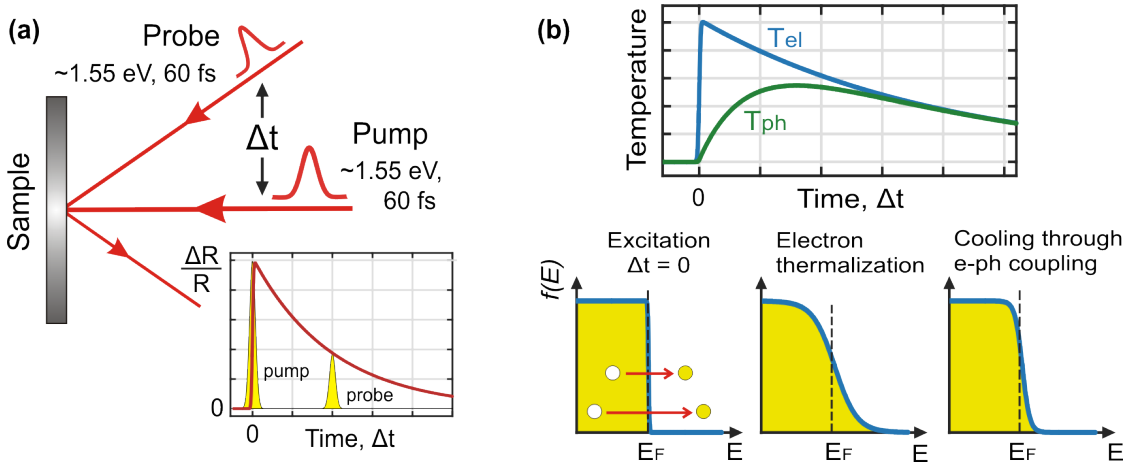


**Figure 2.1:** Optical pump-probe: electronic & lattice teperature relaxation **(a)** Schematic of the OPP setup. The 1.55 eV, 60 fs pump pulse excites the sample and the resulting dynamics of the photo-excitations are monitored by measuring the transmission or reflection of a time-delayed probe pulse. The data is usually presented as the fractional change in the reflectivity ($\Delta R/R$) as a function of the delay time $\Delta t$ between the pump and the probe. **(b)** Illustration of electronic and lattice temperature relaxation in a metal after excitation with an optical pulse. Bottom panel shows the energy distribution of electrons at various time delays.

1. **Electronic & lattice temperature relaxation:** This usually occurs in metals and is the most commonly encountered scenario. Depending on the electronic heat capacity and the pump fluence, the pump pulse can raise the electronic temperature ($T_{el}$) from tens to hundreds of Kelvin. The electronic system then transfers some of its excess energy to the lattice through electron-phonon coupling to raise the temperature of the lattice $T_{lat}$ (fig. 2.1b). $T_{el}$ and $T_{lat}$ then equilibrate amongst each other within a few tens of ps after which the overall relaxation depends on the rate at which heat leaves the area being probed (determined by thermal conductivity etc.). The overall dynamics are usually described by the well known 'two-temperature model' [29]. It is important to note that in the OPP experiments described in this work the pump fluences are deliberately kept low enough so as to minimize the initial change in the electronic temperature.

2. **Single-particle excitations & exciton relaxation dynamics:** This refers to the pump pulse exciting charged particles across a large gap such as in a semi-conductor.

This leads to electron-hole (e-h) pairs which can also form excitons. The initial temperature of this transient state depends on whether the excitations are generated resonantly or not (fig. 2.1c). The resulting dynamics then probe both the radiative and non-radiative recombination of e-h pairs and excitons. Various polarizations of the pump can be used to selectively excite carriers or excitons with a particular spin, as will be seen in chap. 4. Similarly, in strongly correlated materials such as Mott insulators, the pump pulse can produce doubly occupied sites (doublons) and holes which can bind to form Hubbard-type excitons. The resulting dynamics can probe both the generation of these excitons and their subsequent recombination. This situation will be discussed in chap. 5.

3. **Quasi-particle recombination dynamics:** This involves the generation of quasi-particles in materials with a small gap at the Fermi-level such as in a superconductor. In that case, the pump pulse breaks apart Cooper pairs to generate energetic quasiparticles far above the Fermi-level. These quasi-particles quickly relax to the top of the gap and then recombine across the gap by emitting a binding boson (e.g. a phonon in BCS superconductors). The overall dynamics are well understood by the Rothwarf-Taylor model [30] which takes into account the population of both the quasi-particles and the binding bosons. This model is described in Appendix A. It is important to note here that even though the probe energy of 1.5 eV is much greater than the energy scale in the system (e.g. superconducting gap $\sim$ a few meV), OPP is able to detect small changes in the reflectivity at 1.5 eV due to an overall redistribution of spectral weight in the optical conductivity. This is demonstrated below in sec. 2.1.2.

4. **Collective modes of the electronic & lattice degrees of freedom:** OPP can give a direct measurement of collective modes (phonons, amplitude modes of electronic order parameters etc.) in the time domain. These are generated via the DECP (Displacive Excitation of Coherent Phonons) mechanism [31] and manifest as oscillations in the reflectivity transients. DECP is described in detail in sec. 2.1.1 below. In this thesis,

this particular case will be applied to identifying the amplitudon mode in the CDW order in cuprates (chap. 3).

### 2.1.1 Example: optical phonons in $Bi_2Se_3$

This section describes a prototypical example of a pump-probe trace taken on $Bi_2Se_3$ which is characterized as a topological insulator with an insulating bulk but conducting surface states. Here will not discuss the 'topological' aspect of $Bi_2Se_3$ since the pump and probe energy (1.55 eV) is much larger than the bulk band-gap (300 meV). As such, the pump pulse does not directly couple to the topologically protected surface states and the system response at 1.55 eV is dominated by the bulk. Chapter 8 discusses the time and momentum resolved manipulation and spectroscopy of these topological surface states. For now, we treat $Bi_2Se_3$ as a trivial n-doped semi-conductor in which the optical pulse generates a non-equilibrium charge distribution via interband transitions in the bulk.

Figure 2.2 shows the fractional change ($\Delta R/R$) in the transient reflectivity of single crystals of $Bi_2Se_3$ following photo-excitation with a 1.55 eV pump pulse. Following the fast initial dip, the reflectivity undergoes a slow recovery that can be described by an exponential with a time constant of 2.3 ps. This is attributed to the cooling of photoexcited carriers through electron-phonon scattering (two-temperature model). The focus here is the fast oscillatory component that is superimposed on the decay. A Fast Fourier Transform (FFT) of the data (inset fig. 2.2) reveals the frequency to be 2.16 THz which matches precisely with the frequency of the $A_{1g}$ longitudinal optical phonon in $Bi_2Se_3$ [32, 33]. Due to the large OPP response ($\sim 10^{-4}$) of $Bi_2Se_3$, these crystals are regularly used in the Gedik lab for the initial alignment of the OPP setup. Moreover, the frequency of the sharply resolved $A_{1g}$ oscillation allows us to verify the time calibration of our setup as explained below in sec. 2.3.

To understand how the $A_{1g}$ mode is coherently excited using OPP, we invoke the DECP mechanism [31] in which modes with $A_1$ symmetry are typically observed. These are modes which do not lower the symmetry of the lattice. The optical pulse generates a non-equilibrium electronic distribution which in turn will change the equilibrium nuclear coordinates by a

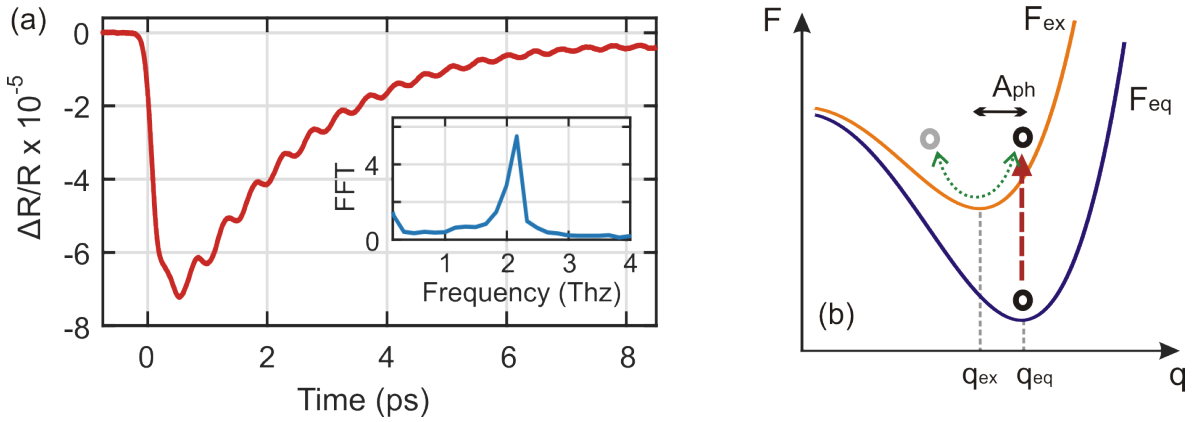


**Figure 2.2:** OPP response of $Bi_2Se_3$ and the DECP mechanism. **(a)** Fractional change in reflectivity $\Delta R/R$ with time $t$ for single-crystals of $Bi_2Se_3$. Inset: Fast Fourier Transform (FFT) of the background subtracted $\Delta R/R$ to highlight the oscillatory component due to a coherent phonon. The background is assumed to be a sum of exponentials. **(b)** Representation of the displacive excitation mechanism (DECP) which generates the coherent phonon. The free energy of the system changes from $F_{eq}$ to $F_{ex}$ due to the laser excitation.

displacement of $A_1$ symmetry. We can refer to Landau theory [31] to see how this initial change launches coherent oscillations. Here the free energy per unit cell of the system can be written as a function of the nuclear coordinate $q$ as:

$$F = -aq^2 + bq^4 + ... \tag{2.4}$$

where $a$ and $b$ are positive numbers. The pump pulse then produces photoexcited carriers with a concentration of $n$ carriers per unit cell. Due to the transfer of $n$ carriers across a gap, the free energy gets modified by a positive term $c_1 n$. Moreover, the due to strong coupling of the electronic system to the lattice, a term dependent on both $n$ and $q$ can be added to the system. Since $A_1$ symmetry is preserved, $F(q) = F(-q)$ and so this term can be written as $c_2 nq^2$ where $c_2$ can be positive or negative. The free energy per unit cell for this excited system is then given by:

$$F = -aq^2 + bq^4 + c_1 n + c_2 nq^2 + ... \tag{2.5}$$

Both the original and modified $F$ as a function of $q$ are plotted in fig. 2.2 along with the equilibrium value of $q = q_{eq}$ in each case given at the minimum of $F$. As can be seen, the

pump pulse causes an impulsive shift in the the local minimum of the system. In response, coherent atomic motion is induced about this new minimum in the excited state with the phonon amplitude $A_{ph}$ maximum at the arrival of the pump pulse ($t = 0$). This produces characteristic $\cos(\omega t)$ oscillations in the reflectivity transients.

### 2.1.2 Example: tracking phase transitions in Bi-2212

This section demonstrates that OPP is sensitive to various phase transitions in a high temperature cuprate superconductor. The phase diagram of cuprates is discussed in detail in sec. 3.1. Here we focus on slightly underdoped Bi-2212 ($Bi_2Sr_2CaCuO_{8+x}$) ($T_c = 85\,\mathrm{K}$) which shows both the superconducting (SC) and the pseudogap (PG) phase. These phases have energy gaps to the order of few tens of meV. Thus, it is not clear whether single-color OPP with a pump and probe energy of 1.55 eV, orders of magnitude greater than the SC and PG energy gaps, can be used to study these phases.

To explore this we performed simultaneous OPP and electrical resistance ($r(T)$) measurements on single crystals of Bi-2212. Resistance is measured using a four-point probe technique on a custom home built device as described in fig. 2.3(a). This device is mounted in an optical cryostat which allows a measurement of the reflectivity transients and resistances at different temperatures from 40 K to room temperature. Figure 2.3(b) shows the fractional change in reflectivity ($\Delta R/R$) with time due to a pump with fluence $2\,\mu\mathrm{J/cm^2}$. Three characteristic temperatures are shown. At 200 K, the signal is to the order of $10^{-5}$ and approaches a constant value after 4 ps. This signal slows down considerably and increases in magnitude by nearly a factor of 10 upon cooling to 160 K which is below the superconducting transition temperature. In an intermediate temperature ($T = 120\,\mathrm{K}$), the signal is initially negative and crosses-over to a positive value within 1 ps.

To understand this behavior further, we determine the maximum and minimum values of $\Delta R/R$ at each temperature and plot them in fig. 2.3c and fig. 2.3d respectively. These are compared with the resistance curved acquires simultaneously $r(T)$ (fig. 2.3e). As can be seen, three distinct temperature regions can be identified. Below 85 K, the resistance drops

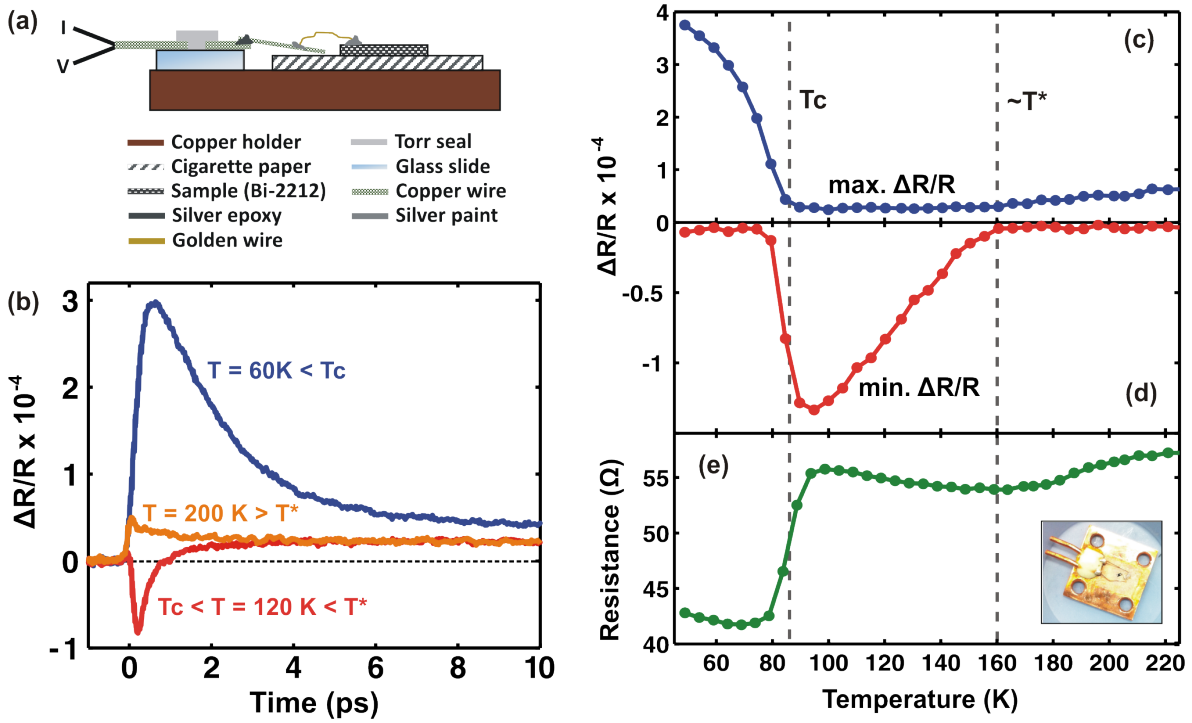


**Figure 2.3:** Simultaneous measurement of electrical resistance & transient refelectivity of Bi-2212. **(a)** Schematic of the four-point probe device constructed to measure the resistance. A picture of the device is shown in the inset of (e). The device shows considerable contact resistance but we are able to identify the superconducting transition. **(b)** $\Delta R/R$ with time for single crystal underdoped Bi-2212 ($T_c = 85\,\mathrm{K}$) at three characteristic temperatures. **(c)** Maximum and **(d)** minimum value of $\Delta R/R$ with temperature. **(e)** Electrical resistance of the device in (a) with temperature. The superconducting ($T_c$) and pseudogap ($T^*$) transition temperatures are indicated.

sharply, the sample is superconducting and the OPP signal is large and positive. Between 85 K and 160 K, the OPP signal is negative while the resistance shows a slight cusp at 160 K. Beyond 160 K, the signal again switches sign. Based on previous ARPES and tunneling experiments [34], we associate this temperature as the PG transition temperature ($T^*$). It is clear that reflectivity transients change sharply at both $T_c$ and $T^*$ indicating that the response represents the dynamics of quasi-particles excited across the SC gap and across the PG.

There has been considerable prior work (e.g. [35, 36]) using OPP on Bi-2212 and related cuprates especially in the superconducting regime. At low excitation densities, such as the ones used in our work, the signal in the SC region displays pump-fluence (excitation density) dependent decay rates due to the bimolecular nature of quasi-particle recombination as

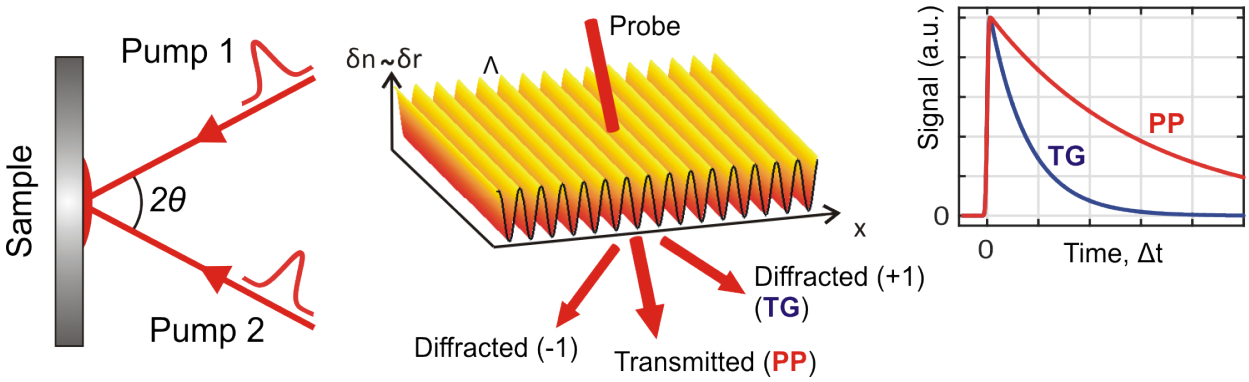


**Figure 2.4:** Transient grating spectroscopy: interference pattern & diffraction. Two pump beams with the same intensity and an angle $2\theta$ between them interfere on the sample surface to generate a sinusoidal excitation pattern of wavelength $\Lambda$ as indicated in the middle diagram. This causes the change in the reflectivity ($\delta r$) to be modulated spatially. An incident probe beam is both transmitted and diffracted from this transient grating. The signal measured with the transmitted beam is the same as the OPP response and is called PP in this work. The diffracted signal encodes information about the decay of the grating and is called TG. The right panel shows an illustration of the change in the transmitted and diffracted beams with time that is typically expected in such measurements.

described by Rothwarf-Taylor equations [18, 19, 30]. This particular explanation for the OPP signal has been corroborated by recent Tr-ARPES measurements on Bi-2212 [20].

## 2.2 Transient grating spectroscopy

In transient grating spectroscopy (TGS) tw o coherent co-polarized pump beams, each with a wavelength $\lambda$, impinge on the sample surface at an angle $2\theta$ between them (fig. 2.4). The net electric field at the sample is given by:

$$\vec{E} \propto e^{ikx\sin\theta}\hat{e_1} + e^{-ikx\sin\theta}\hat{e_2} \tag{2.6}$$

where $\hat{e_{1,2}}$ are the polarization vectors of the incident pump beams, $k = 2\pi/\lambda$ is the wavevector with $\lambda$ the pump beam wavelength and $x$ denotes the position along the sample surface. For co-polarized pump beams i.e. $\hat{e_1} \parallel \hat{e_2}$, the net intensity $I = |\vec{E}|^2$ can be written as:

$$I \propto \cos^2(kx\sin\theta) \propto 1 + \cos(2kx\sin\theta) \tag{2.7}$$

Thus, we get an intensity interference pattern of wavelength $\Lambda = \lambda/(2\sin(\theta))$ which in turn produces a sinusoidal varying transient photo-excitation density across the sample surface. If these photo-excitations effect the refractive index of the sample, then the varying excitation density acts as a transient diffraction grating. A time-delayed probe beam that is incident on the sample will not only be transmitted/reflected but also be diffracted from this transient grating (fig. 2.4). The change in intensity of the transmitted/reflected probe beam encodes information about the time decay of the average excitation while the diffracted beam encodes information of the excitation at the grating wave-vector $q = 2\pi/\Lambda$. TGS has been applied to a a number of systems to study exciton and thermal diffusion as well as propagation of ultrasound [37]. Below are four possible ways relevant to this work in which the dynamics of the diffracted beam can be used to study pump-induced excitations in materials:

1. **Quasi-particle & e-h diffusion:** This can occur in clean semiconductors and superconductors. As discussed above, an optical pump pulse can generate single-particle excitations in various systems (e-h pairs in semiconductors and quasi-particles in superconductors). While simple OPP tracks the dynamic recombination of these excitations, in the TGS case the decay of the diffracted beam intensity not only depends on recombination but also on the diffusion of excitations from regions of high intensity to regions of low intensity. On the other hand, the transmitted/reflected beam in the TGS case simply tracks the changes in the mean value of the grating which only depends on the overall recombination of quasi-particles. Thus, in this case, the decay rate of the intensity of the diffracted beam ($\Gamma_D$) will be greater than the decay rate of the transmitted beam intensity ($\Gamma_R$) (fig. 2.4). $\Gamma_D$ is simply given by $\Gamma_D = \Gamma_R + Dq^2$ where $D$ is the diffusion constant and $q$ is the grating wave-vector. In this way TGS can be used to measure the diffusion constant of excitations as has been done for quasi-particles in a cuprate superconductor [21] and for e-h pairs in various semiconducting quantum wells [38].

2. **Collective modes at the grating wave-vector *q*:** This refers to the excitation of collective modes in the system with a non-zero wave-vector. Unlike OPP which generically creates excitations with $q = 0$, TGS can excite acoustic-type modes at the wave-vector $q$ of the grating. Examples include acoustic phonons in thin metallic films [39] and the phase-mode of the CDW state in cuprates as will be discussed in detail in sec. 3.3.2.

3. **Optical phase separation & complex change in conductivity:** As mentioned above (sec. 2.1), simple OPP cannot be used to learn about the complex change in reflectivity. This information becomes relevant in experiments in which the system response in reflectivity is due to different types of excitations (e.g. single-particles, excitons, phonons etc.). By using a heterodyne detection scheme, TGS allows us to overcome this limitation and gain information about the phase of these different excitations in the complex plane of the reflectivity. This "optical phase separation" is discussed in detail in sec. 2.2.2 and applied to understand the confinement-deconfinement transition of single-particle excitations in $Na_2IrO_3$ (chap. 5).

4. **Diffusion & decay of spin polarized excitations** This is studied in spin-grating experiments which is variation of the usual TGS technique described above. In this case two *cross*-polarized pump beams interfere on the sample to generate a spatially modulated circularly polarized intensity across the excitation spot. In spin-split systems with the correct optical selection rules, this generates a spatially modulated spin density referred here as the spin-grating. The probe beam that is diffracted from this spin-grating encodes information about both the decay and spatial diffusion of spin-polarized excitations. This technique is discussed in detail in sec. 2.2.3 and applied to understand the dynamics of spin-polarized excitations in monolayer $MoSe_2$ (chap. 4).

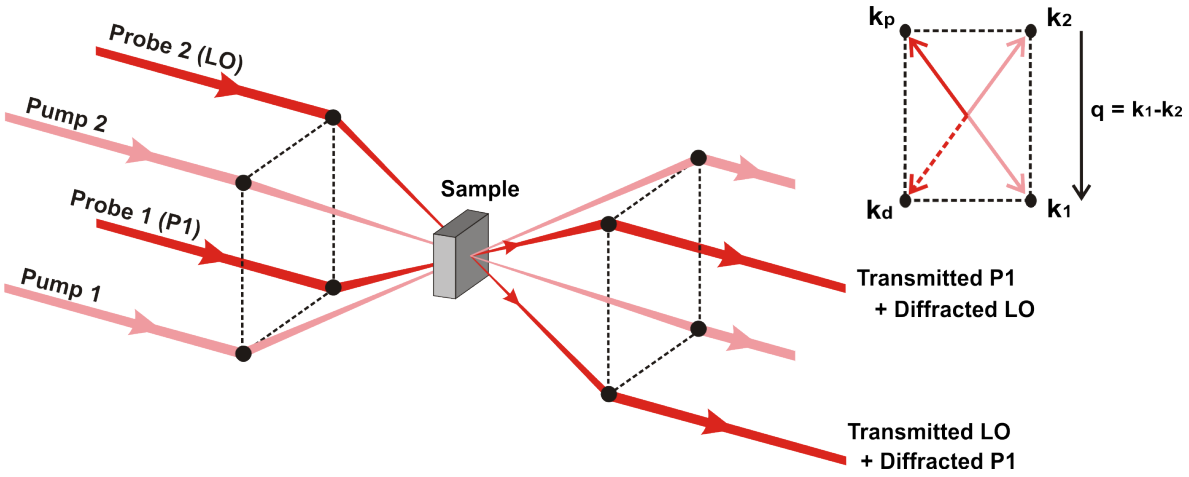


**Figure 2.5:** Box-car geometry & heterodyne detection. The two pump and two probe beams are arranged along the corner of a rectangle and then focused onto the sample. $\mathbf{k_{1,2}}$ are the in-plane wave-vector of the pump while $\mathbf{k_p}$ and $\mathbf{k_d}$ are the wave-vectors of the incident and diffracted probe respectively.

### 2.2.1 Box-car geometry & heterodyne detection

TGS relies on accurately measuring the intensity of the diffracted beam as a function of the delay time between the pump and probe. This is challenging since the diffracted intensity is typically orders of magnitude weaker than the reflected beam. To overcome this we need to 1) find the direction in which the probe beam diffracts, 2) set-up the experiment so as to maximize the intensity of the diffracted beam and 3) develop a sensitive detection scheme to measure small intensities. As described below, the first two are done by using a box-car geometry and the third is achieved by using heterodyne detection.

The box-car geometry is illustrated in fig. 2.5. Here the three degenerate beams (pump 1, pump 2 and probe) are arranged parallel to each other such that they each pass through a different corner of a rectangle in a plane perpendicular to their path. A lens aligned to this rectangle is then used to focus the three beams onto the sample. The in-plane momentum (parallel to the sample surface) of each of these three incident beams corresponds to each corner of the rectangle ($k_1$, $k_2$ and $k_p$) (fig. 2.5b). The grating wavevector is simply $q = k_1 - k_2$. By conservation of in-plane momentum and noting that the three incident beams are degenerate, it's apparent that one order of the diffracted beam with wavevector

$k_d$ will emerge at the fourth corner of the rectangle as $k_d = k_1 - k_2 + k_p$ (Bragg condition). Thus, by arranging the three incident beams in this box-car geometry, we get a convenient way to determine, beforehand, the outbound path of the diffracted beam. Moreover, in the box-car geometry the phase-matching condition ($\Delta k = k_1 - k_2 + k_p - k_d = 0$) is automatically fulfilled which assures that the diffracted beam has maximal intensity [40].

To detect the diffracted beam accurately we rely on heterodyne detection in which the weak diffracted beam is mixed with a strong beam known as the local oscillator (LO). The detected intensity is given by:

$$I \propto |E_{LO}|^2 + |E_d|^2 + 2Re(E_{LO}E_d^*) \tag{2.8}$$

where $E_{LO}$ and $E_d$ are the electric field of the LO and the diffracted beam respectively. The last term ($2Re(E_{LO}E_d^*)$ is the "heterodyne" term which refers to the mixing between the two beams. Since the diffracted beam originates from a small change in the refractive index ($\Delta n$) of the material, its obvious that the heterodyne term is first order in $\Delta n$ while the homodyne term ($|E_d|^2$) is second order in $\Delta n$. As seen in sec. 2.1.1, $\Delta n \sim 10^{-4} - 10^{-5}$. Therefore, detecting the heterodyne term is 4-5 times more accurate than detecting the homodyne term. In fact, the current sensitivity of our setup is $\sim 10^{-7}$ making it impossible to detect the small homodyne term.

The box-car geometry of the setup provides a natural way of implementing heterodyne detection. Here the LO beam is also made parallel to the three other beams but is incident along the fourth corner of the box-car rectangle (fig. 2.5). In this way, one order of the diffracted probe beam is guaranteed to be collinear with the transmitted/reflected LO beam. Similarly, the diffracted LO beam is now collinear with the transmitted/reflected probe beam. Either one of these can be detected to measure the heterodyne signal. We discuss below how the diffracted signal is extracted from the measured overall signal.

We consider the reflected LO beam mixing with the diffracted probe beam. The pump beams change the reflectivity coefficient by $\delta\tilde{r}$ for spatially uniform excitation. The LO beam interacts with the sample so that the electric field of the reflected LO beam is given

by $E_{LO}(\tilde{r}_0 + \delta\tilde{r})$ where $\tilde{r}_0$ is the equilibrium reflection coefficient and $E_{LO}$ is the electric field of the incident LO beam before interacting with the sample. Similarly, the electric field of the diffracted beam can be written as $E_p\eta$ where $\eta$ is defined as the diffraction coefficient. Both $\delta\tilde{r}$ and $\eta$ are time-dependent quantities that depend on the pump-excitation. The detected intensity is then given by:

$$I \propto |E_{LO}(\tilde{r}_0 + \delta\tilde{r}) + E_p\eta|^2 \tag{2.9}$$

In our case the LO and the probe beam are interchangeable within a phase factor i.e. $|E_{LO}| = |E_p|$. The detected intensity can be simplified by only keeping terms that are first order in $\delta\tilde{r}$ and $\eta$:

$$I \propto |E_{LO}\tilde{r}_0|^2 + |E_{LO}|^2|\tilde{r}_0|[|\delta\tilde{r}|\cos(\phi) + |\eta|\cos(\phi - \psi)] \tag{2.10}$$

where $\phi$ is the phase of $\delta\tilde{r}$ relative to $\tilde{r}_0$ and $\psi$ is the phase of $E_p$ relative to $E_{LO}$ i.e. the phase between the LO and probe beams. In eq. (2.10) the first term is just the reflected LO beam in equilibrium. We can get rid of this contribution to the detected beam by using standard lock-in techniques (sec. 2.3). To separate out the terms in $\delta\tilde{r}$ and $\eta$, we can detect $I$ at various values of the phase $\psi$ and then solve for $\delta\tilde{r}$ and $\eta$. This process is outlined in detail in sec. 2.3.4.

We note here that $\delta\tilde{r}$ is the system response corresponding to the $q = 0$ uniform excitation i.e. the same response as the one obtained with OPP (sec. 2.1). On the other hand $\eta$ gives the response at the finite $q$ grating wave-vector i.e. the response due to the transient grating. As a result we refer to $\delta r$ as PP and $\eta$ as TG in this work (fig. 2.4).

### 2.2.2 Optical phase separation

The pump-probe response $\delta\tilde{r}$ is a complex quantity that has phase $\phi$ relative to the equilibrium reflectivity $\tilde{r}_0$. Simple OPP detects the quantity $|E_{probe}(\delta\tilde{r})|^2$ which destroys any information about $\phi$. This limitation is easily overcome in heterodyne detection in TGS as eq. (2.10) allows us to determine $\phi$ in addition to $\delta\tilde{r}$ and $\eta$. Along with a knowledge of the real and

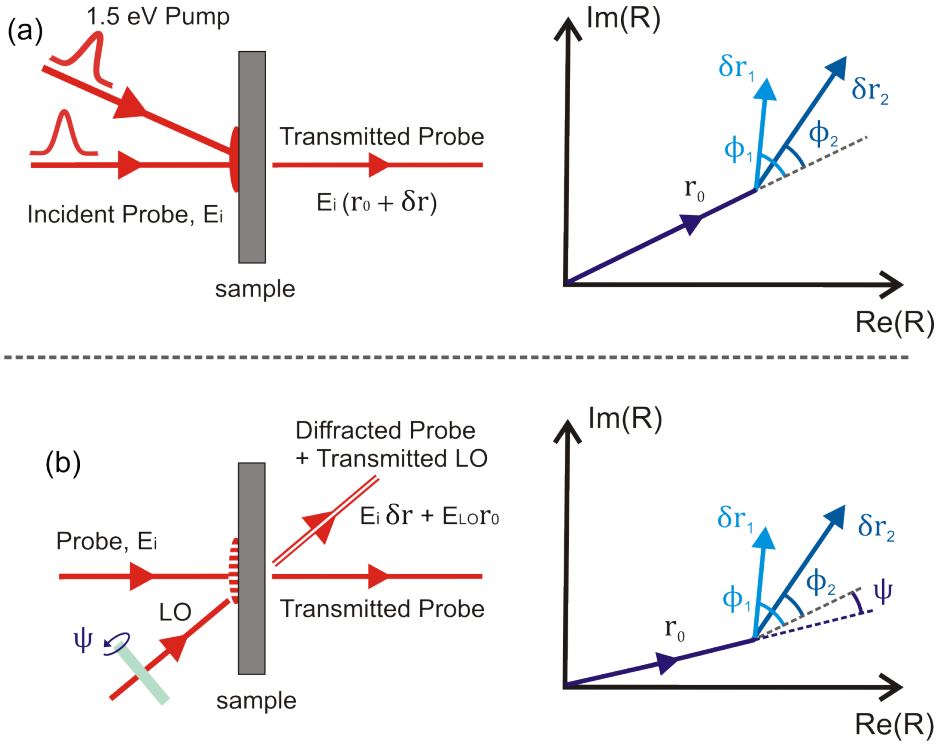


**Figure 2.6:** **(a)** Standard optical pump-probe measurement. The phasor diagram illustrates the complex transmission or reflection coefficient. The pump-induced responses $\delta\tilde{r}_1$ and $\delta\tilde{r}_2$ are both projected on to static reflectivity $\tilde{r}_0$. **(b)** Heterodyne transient grating measurement. The probe beam then diffracts from this grating into a direction determined by the grating wavevector. The diffracted beam mixes with a transmitted local oscillator (LO) beam, the phase $\psi$ of which can be controlled by a rotatable cover slip. In the phasor diagram $\delta\tilde{r}_1$ and $\delta\tilde{r}_2$ are again both projected on to $\tilde{r}_0$ but the phase $\psi$ can now be controlled systematically to suppress or enhance one component relative to the other.

imaginary parts of the equilibrium dielectric function $\epsilon$, we can use $\phi$ to reconstruct the complex change in the optical conductivity using eq. (2.2) and eq. 2.3.

More importantly, heterodyne detection in TGS allows us to separate out the response of different types of excitations using their optical phase. Examples can include coexisting single-particle excitations and bound excitons in a gapped system or excitations of different coexisting orders (e.g. charge-density wave order and superconductivity). Suppose we have two different excitations with complex response $\delta\tilde{r}_1$ and $\delta\tilde{r}_2$ and phase $\phi_1$ and $\phi_2$ relative to the equilibrium reflectivity $\tilde{r}_0$. In general these responses will have different time dependence.

In this case, the signal measured by standard OPP is just a sum over the different components:

$$I_{homodyne} = |\delta\tilde{r_1}| \cos\phi_1 + |\delta\tilde{r_2}| \cos\phi_2 \tag{2.11}$$

This can be understood by considering the phasor diagram for the case of these two components contributing to the pump-induced change (fig. 2.6a). $\tilde{r}_0$ is the equilibrium reflectivity. $\delta\tilde{r_1}$ and $\delta\tilde{r_2}$ are the pump induced responses. As shown in fig. 2.6a, in a standard OPP measurement, the phasors $\delta\tilde{r_1}$ and $\delta\tilde{r_2}$ are projected onto $\tilde{r}_0$ and there is no way to isolate the behavior of each component.

This limitation can be overcome with heterodyne detection in our transient grating setup which measures the response at both $q = 0$ and at the finite wave-vector $q$ of the grating as described by eq. (2.10). In the absence of spatial diffusion and $q$-dependent collective modes, the finite $q$ response $\eta$ is the same as the $q = 0$ response $\delta\tilde{r}$. Taking this into account and considering two different excitations with different responses as discussed above, the measured signal in a TG experiment can be written as (from eq. (2.10)):

$$I_{heterodyne} = |\delta\tilde{r_1}| \cos(\phi_1 - \psi) + |\delta\tilde{r_2}| \cos(\phi_2 - \psi) \tag{2.12}$$

where $\psi$ is the phase of the probe with respect to the LO as noted earlier. Note that first two terms in eq. (2.10) are gotten rid off by using lock-in techniques as described in sec. 2.3.4. This intensity is now similar to the measured signal in standard OPP (eq. (2.11)) except for the additional phase $\psi$ due to heterodyne detection. This phase can easily be controlled by a rotatable coverslip along the path of the LO beam. Figure 2.6b shows the phasor diagram for this case. Again the two phasors $\delta\tilde{r_1}$ and $\delta\tilde{r_2}$ are projected onto $\tilde{r}_0$ but this time by controlling $\psi$ we can enhance or suppress the contribution on component relative to the other. In particular, by tuning $\phi_1 - \psi$ to $\frac{\pi}{2}$, the first component can be completely eliminated.

In a standard OPP measurement, the pump-induced change is mixed with a large transmitted or reflected probe beam and there is now way to distinguish the change caused by different types of excitations. However, in a TG measurement, the diffracted beam comes out in a background free direction and is then mixed with the LO while the phase between them

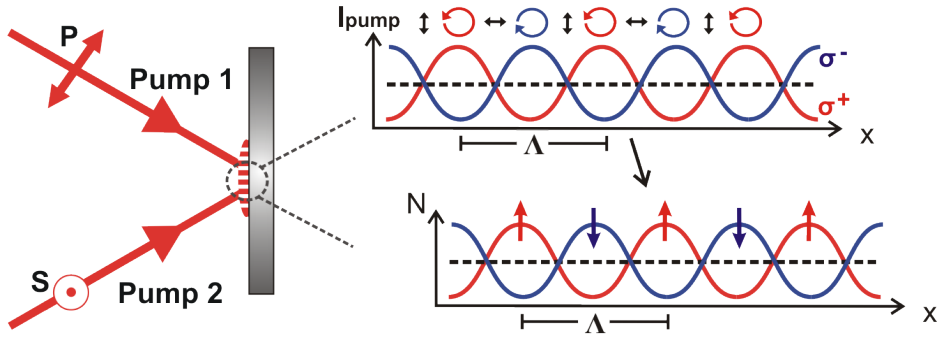


**Figure 2.7:** Spin transient grating: generation & excitation pattern. Two linearly cross-polarized pump beams interfere on the sample surface to generate a spatially varying circularly polarized intensity with wavelength Λ. Opposite helicities (right and left polarized) vary out-of-phase with each other on the sample (top-right). This can lead to a spatially varying density of spin polarized excitations in the sample (bottom-right)

can independently be controlled. This allows suppressing the response due to one excitation relative to the response due to another type of excitation. This method is applied to separate out the response due to single-particle excitations and Hubbard excitons in $Na_2IrO_3$ in chap. 5.

### 2.2.3 Spin transient grating

This is a variation of the standard TGS technique discussed earlier. In TGS two linearly *co*-polarized pump-pulses interfere on the sample such that the overall intensity varies sinusoidally along the surface as seen in eq. (2.7). In contrast, in spin transient grating (spin-TG) two linearly *cross*-polarized pump-pulses impinge on the sample. In this case $\hat{e_1} \perp \hat{e_2}$ in eq. (2.6) and so the net intensity is independent of $x$ and spatially uniform. However, the electric field polarization is modulated spatially across the excitation spot. To see this it is useful to work in the circularly polarized basis, that is:

$$\begin{aligned} \hat{e_R} &= \frac{1}{\sqrt{2}}(\hat{e_1} - i\hat{e_2}) \\ \hat{e_L} &= \frac{1}{\sqrt{2}}(\hat{e_1} + i\hat{e_2}) \end{aligned} \tag{2.13}$$

where $\hat{e_R}$ and $\hat{e_L}$ denote right and left circular polarizations respectively.In this basis the net electric field in eq. (2.6) is:

$$\vec{E} \propto \cos(kx\sin\theta - \pi/4)\hat{e_R} + i\sin(kx\sin\theta - \pi/4)\hat{e_L} \tag{2.14}$$

Thus, the intensity can be written as:

$$I \propto I_R cos^2(kx \sin\theta - \pi/4) + I_L sin^2(kx \sin\theta - \pi/4) \tag{2.15}$$

where $I_R$ and $I_L$ are the intensities for right and left circular polarization respectively. Thus, we get an intensity grating for each helicity but with a phase difference of 90° between them i.e. the two gratings are spatially separated by a quarter-wavelength. This leads to alternating regions of right and left circularly polarized pump light across the sample as shown in fig. 2.7. This excitation pattern can lead to a spin grating being generated at the sample. It is known that a particular photon helicity can directly couple to a particular carrier spin in spin-orbit split semi-conductors as is the case in GaAs and monolayer TMDs (chap. 4). Therefore, the alternating right and left helicities generated above leads to alternating regions of 'up' and 'down' spins excited at the sample surface. While the total excitation denstiy is uniform with $x$, the density for opposite spins varies sinusoidally across $x$ (fig. 2.7). This way of understanding spin grating as separate intensity gratings for opposite helicities is referred to as the 'grating decomposition method' [41].

How does a linearly polarized probe beam interact with this spin grating? Since 'up' and 'down' spins are spatially separated, there is a difference in the refractive index for right and left polarized light i.e. the sample has a transient circular birefringence. Suppose that the probe beam is linearly polarized along $\hat{e_1}$. This linear polarization can be written as a superposition of right and left circular polarizations i.e. $\hat{e_1} = \frac{1}{\sqrt{2}}(\hat{e_R} + \hat{e_L})$. When this beam interacts with the spin grating, the 'right' and 'left' parts diffract such that they are phase shifted by 90°. This phase shift corresponds to a 90° rotation of the light polarization. Thus, a vertically polarized probe beam becomes horizontally polarized after diffracting from the spin grating (fig. 2.8a).

To realize spin transient grating we again rely on heterodyne detection in a box-car geometry (fig. 2.8). In this case the polarization of one of the pump beams and that of the local oscillator (LO) is rotated by 90° (sec. 2.3). Thus the polarization of the diffracted probe

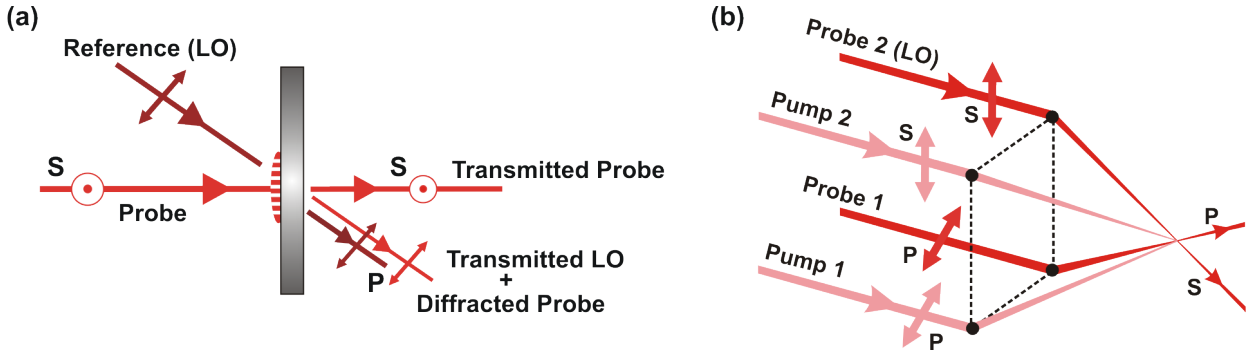


**Figure 2.8:** **(a)** The out-of-plane (S) polarized probe beam diffracts such that its polarization is rotated to be in-plane (P). The diffracted beam is mixed with a P-polarized local oscillator (LO) for heterodyne detection. **(b)** Box-car geometry for spin grating measurements.

beam is the same as the polarization of the transmitted/reflected LO beam. This mixes the two and allows for a convenient way to detect the diffracted signal from the spin grating.

## 2.3 Experimental setup

This part gives a broad overview of the experimental setup and the beam path. Specific details about each component are discussed in the subsections below.

The complete setup for the OPP and TG experiments is shown in fig. 2.9. The laser is a Newport Tsunami oscillator that outputs vertically polarized pulses centered at $\sim 1.55\,\text{eV}$ (800 nm) at a repetition rate of 80 MHz. The duration of each pulse is about $\sim 60 - 100\,\text{fs}$ and the average power at the output is $\sim 2.2\,\text{W}$. This corresponds to a pulse energy of $\sim 27.5\,\text{nJ}$. The laser output then passes through a half-wave plate ($\lambda/2$) to rotate the polarization to horizontal. The beam then goes through a Conoptics pulse-picker that reduces the repetition rate to 1.6 MHz. This is done to avoid cumulative heating of the samples under study. The beam then goes through a prism pair (GVD compensator) that pre-compresses each pulse temporally to account for the dispersion in the setup optics. The beam is then collimated using a lens pair. A 90:10 beam splitter (BS) is used to split the beam into the pump and probe paths respectively.

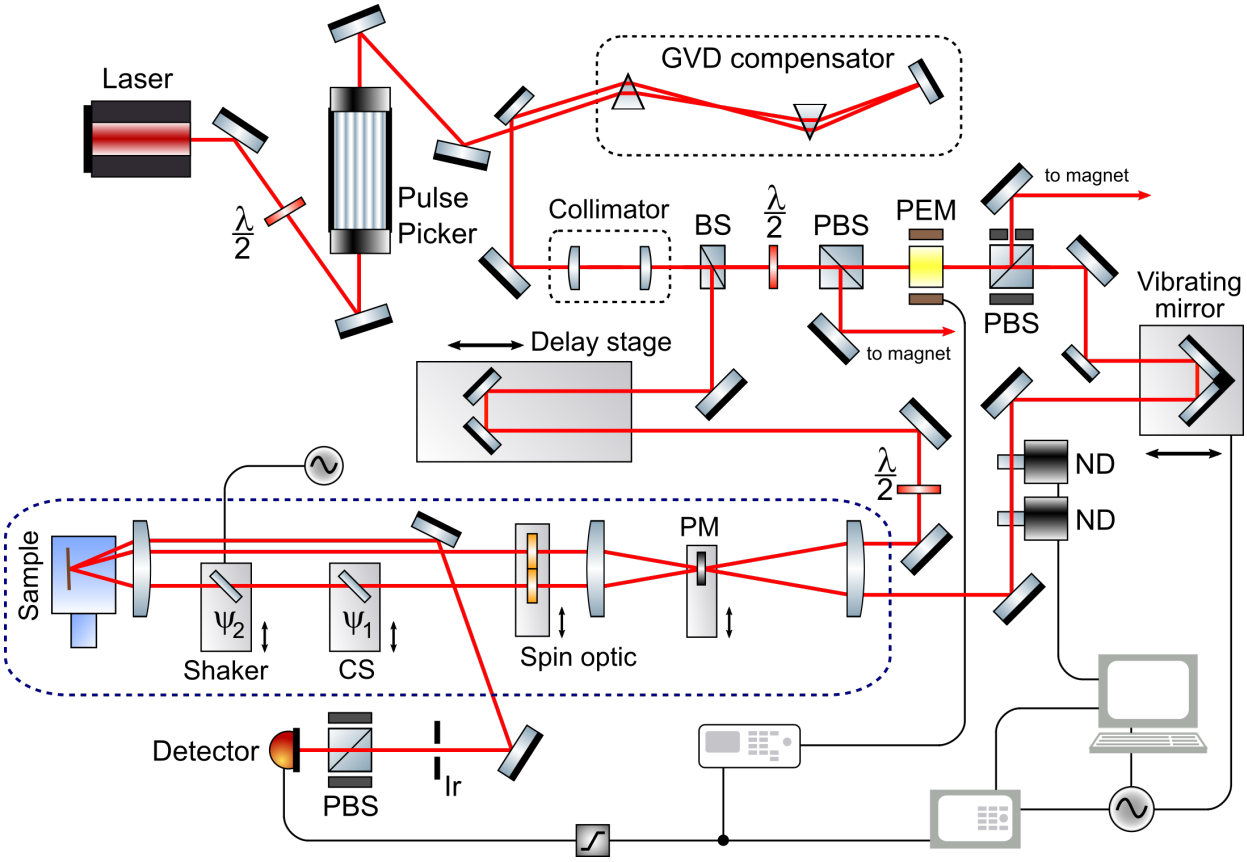


**Figure 2.9:** Experimental setup for OPP & TG showing the complete beam path from the laser to the sample and the detector. A few key electronic connections are also indicated. See text for a detailed description of the beam path and the indivindual components. A few abbreviations are as follows: $\lambda/2$: half-wave plate, BS: beam splitter, PBS: polarizing beam splitter, PEM: photo-elastic modulator, ND: neutral-density filter, PM: phase mask, CS: cover-slip, Ir: Iris. Drawings of individual optical components are adapted from [42].

The pump part goes through a Hinds instrument photo-elastic modulator (PEM-90) which modulates the polarization of beam such that it goes between vertical, right circular polarized, horizontal and left circular polarized at a rate of 50 kHz. This modulated beam then passes through a polarizer and so the intensity of the light oscillates between maximum and zero at a rate of 100 kHz. Thus, the PEM combined with a polarizer acts as a chopper the modulates the intensity of the beam at a very high frequency of 100 kHz which greatly limits the $1/f$ noise. The PEM controller gives a reference signal 100 kHz which can be used in standard lock-in detection while measuring the pump induced change in the reflectivityy.

Here we note that the polarizer is actually a polarizing beam splitter (PBS) such that it gives two outputs, vertical and horizontal polarized, each of which has its intensity modulated at 100 kHz. One part is used for measurements discussed in this thesis while the other part is sent to a similar OPP and TG setup with the capability of performing these measurements in an optical magnetic cryostat with fields upto 7 T.

After the chopping stage, the pump beam goes through a vibrating delay line (A.P.E. scanDelay 50) that is simply an oscillating mirror that can change the time delay between the pump and probe beams to upto 50 ps at a frequency of upto 20 Hz. This time-delay and frequency can be adjusted through the A.P.E. controller and computer interface. The controller also provides a sinusoidal signal that tracks the motion of the oscillating mirror. This signal is used as an oscilloscope trigger for fast acquisition of the pump-probe signal. Note that this way of acquiring data is much faster than using a stepper motor to change the time delay between the pump and probe. This greatly helps with the overall signal-to-noise in the measurements. We have also used another delay line (Clark-MXR) that can have an amplitude upto 100 ps. After the delay line, the pump beam goes through a pair of neutral density filters which are placed on computer controlled wheels (Thorlabs FW102C) that allow adjustment of the pump fluence.

The probe part of the beam goes through an optical delay stage (Newport) that is driven by a stepper motor. It consists of a two mirrors that can be moved so as to adjust the time-delay between the pump and the probe to more than 1 ns. This stage is used to adjust the probe pulse path such that the pump pulse overlaps with it in time within the 50 ps range of the A.P.E. delay line. One this 'time-zero' is found, the probe stage is not adjusted further during a measurement unless we measure OPP signals beyond 50 ps. The polarization of the probe beam is then rotated by 90° such that is perpendicular to the pump beam polarization. In this way, we limit the pump beam from leaking into the detector (pump-scatter). The probe beam is then made parallel to the pump and both beams are focused onto the sample for OPP experiments or onto a diffractive phase mask (PM) for TG measurements. The specifics of the TG setup components are discussed below in sec. 2.3.2.

The spot size of the pump and probe at the sample is typically $60 - 70\,\mu m$. To ensure spatial overlap between the pump and the probe on the sample, a $50\,\mu m$ pinhole is used beforehand and the beams are passed through it at the focus of the lens. The reflected probe is picked off by a D-mirror and sent into a Si photodiode detector (Thorlabs PDA-36A). We use an iris and polarizer in front of the detector to limit any scattered pump from reaching the detector. This is possible since the pump and probe are cross-polarized. Nevertheless, some pump scatter can reach the detector and appear as a background in the acquired OPP/TG signal. The rougher the sample surface, the worse the pump-scatter. To limit pump-scatter we use freshly cleaved flat surfaces or MBE/CVD grown thin films.

### 2.3.1 Laser system & optical components

This section details the working principles of the oscillator laser and other optical components common to the OPP and TG setup.

**Oscillator:** An oscillator laser system generates short pulses with duration $< 100\,fs$ using 'modelocking' which refers to a fixed phase relationship between the allowed longitudinal modes of the oscillator cavity (fig. 2.10). In general, light trapped between two mirrors in an optical cavity forms standing waves or modes whose frequency separation is determined by the length of the cavity. These standing modes are the only ones allowed in the cavity since all other modes interfere destructively. In addition, the gain medium in the cavity amplifies only certain modes determined by its frequency bandwidth. In a simple cavity, these modes oscillate independently i.e. the phase between different modes is not fixed resulting in a constant intensity in time i.e. Continuous wave (CW) operation. Instead if we 'lock' the relative phases of the longitudinal modes, then the modes will all constructively interfere with each other at a given time producing an intense pulse of light circulating within the cavity. The more the number of modes involved, the sharper i.e. shorter the pulse. Since a gain medium with a larger bandwidth allows more longitudinal modes, the wider the bandwidth of the laser, the shorter the pulse. This explains why Ti:Sapphire (titanium doped sapphire) is typically used for ultra-short pulses as its bandwidth can exceed $100\,THz$

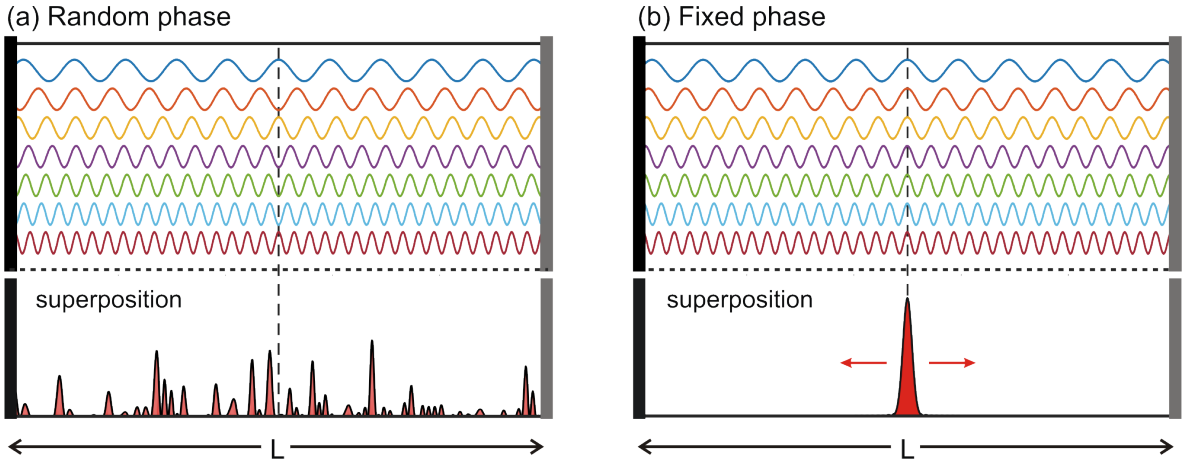


**Figure 2.10:** Longitudinal cavity modes in an oscillator for **(a)** Random phase between the modes and **(b)** fixed phase. Bottom panel shows the intensity profile of the superposition of these modes at a given. For random phases, the resulting superposition averages out with time leading to a constant osillator output (CW operation). For a fixed phase, the superposition results in a sharp and short pulse (mode-locked).

to produce pulses as short as 10 fs. The repetition rate of the oscillator is determined by the round-trip time of the pulse in the cavity and is 80 MHz for our system. Here it is important to note that modelocking in an oscillator can easily be disturbed by thermal changes in the cavity since that can cause the phase of the longitudinal modes to vary rapidly. To ensure modelocking, oscillators use different mechanisms; the simplest of which is to rely on the self-focusing of laser beam within the Ti:sapphire crystal. Here, the refractive index is a function of the intensity. The higher peak intensity of mode-locked pulses improves the self-focusing of the beam better into the crystal which further increases the optical gain allowing the oscillator to favor mode-locking over CW operation

**Pulse-picker:** The pulse-picker consists of an electro-optic modulator (EOM) and a polarizer. The EOM modulates the polarization of an incoming pulse while the polarizer transmits or blocks it. The EOM consists of a long nonlinear crystal whose refractive index along a certain axis changes when a high voltage pulse is applied to it. The resulting birefringence rotates the polarization of the incoming light pulse. Consider $F_p$ light pulses in a pulse train of repetition rate 80 MHz. The duration of the voltage applied to the EOM

can be adjusted such that it leaves the polarization of only 1 out of every $F_p$ light pulses unchanged. In this way, the polarizer after the EOM blocks $F_p - 1$ of the laser pulses while allowing 1 pulse to go through. Thus, the repetition rate after the pulse-picker is reduced to $80/F_p$ MHz. The factor $F_p$ is typically set to 50 in our experiments. This reduction in repetition rate helps to avoid cumulative heating of the sample. The magnitude of the voltage pulse and its timing relative to the optical pulse train is adjusted such as to maximize the ratio of the output pulse with respect to the blocked pulses. Ratios as high as 400 can be achieved for optimum operation of the pulse picker.

**GVD compensator:** An ultra-short pulse quickly spreads in time as it travels through air and various optics. Due to its short pulse duration in time the pulse has a broad bandwidth in frequency. A pulse of FWHM duration of 60 fs with center wavelength 800 nm has a FWHM bandwidth of $\sim 16$ nm. This follows from the uncertainty principle (sec. 7.1.1). Since most mediums, including air are dispersive i.e. the velocity of light is a function of its wavelength, the finite bandwidth of the pulse results in different frequency components of the pulse propagating with different velocities in air and in the optics. This is known as group-velocity dispersion (GVD) and it broadens the time duration of the pulse which worsens the time resolution. GVD is illustrated in fig. 2.11.

The refractive index of most materials decreases with increasing wavelength and so the 'red' part of the pulse leads the 'blue'part. GVD can be compensated for by using a prism-pair which compresses the pulses temporally. Each pulse is aligned at the minimum deviation-angle positions. In this way, different frequency components in the pulse acquire different path lengths. As shown, in fig. 2.11 the 'red' part of the pulse travels through a greater optical path length due its greater distance of propagation in the second prism. In this way, the 'red' part ends up lagging the 'blue' part after the prism pair. Ideally these components should then overlap in time when they pass through dispersive optics resulting in the shortest pulse duration. This compensation can be adjusted by controlling the distance between the two prisms as well as the distance the beam travels in the second prism. In our case, the second prism is mounted on a micrometer translation stage to control the amount

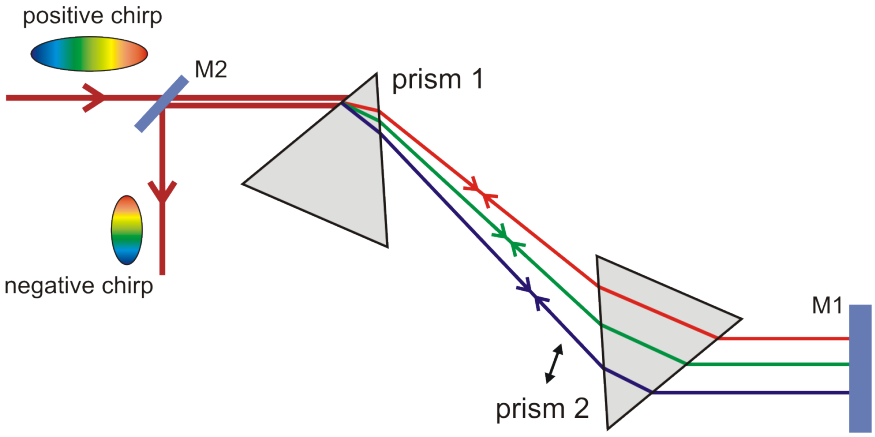


**Figure 2.11:** A positive chirped pulse ('red' part leads 'blue' part) goes through a pair of prisms. Mirror M1 reflects the beam back through the prims. M1 is slightly angled so that we can pick-off the outgoing beam by mirror M2. Since the 'red' part goes through a greater optical path length, it ends up lagging the 'blue' part i.e. the output is negatively chirp. The amount of chirp can be adjusted by moving prism 2 in and out of the beam path.

of glass the beam goes through. The distance between the prisms is set to compensate for the expected broadening in the optics. This was calculated using a commercially available software (http://www.lab2.de/) that simulates the pulse broadening.

**Photo-elastic modulator (PEM)** The PEM modulates the polarization of th pump beam at a fixed frequency. It is is based on the photoelastic effect. Here a transparent material develops birefringence when stress is applied to it. A light wave passing through a birefringent crystal experiences different refractive indices along different crystal directions. Different polarization components of the light wave thus develop a phase retardation between them. The birefringence is directly proportional to the applied stress. In the PEM, stress is applied to the transparent crystal using a piezoelectric transducer which modulates the stress along a certain axis at a frequency of 50 kHz and thus modulates the birefringence (phase retardation) at the same frequency. The PEM axis is mounted at a 45° angle with respect to the horizontal polarization of the pump. In this way the pump beam experiences a phase retardation between $\pm\lambda/2$ at a rate of 50 kHz as it goes through the PEM. When the retardation is $|\lambda/2|$, the PEM acts as a half-wave plate and the polarization of the pump gets rotated by 90°. When it is $|\lambda/4|$, the PEM gives a circularly polarized beam. A horizontally

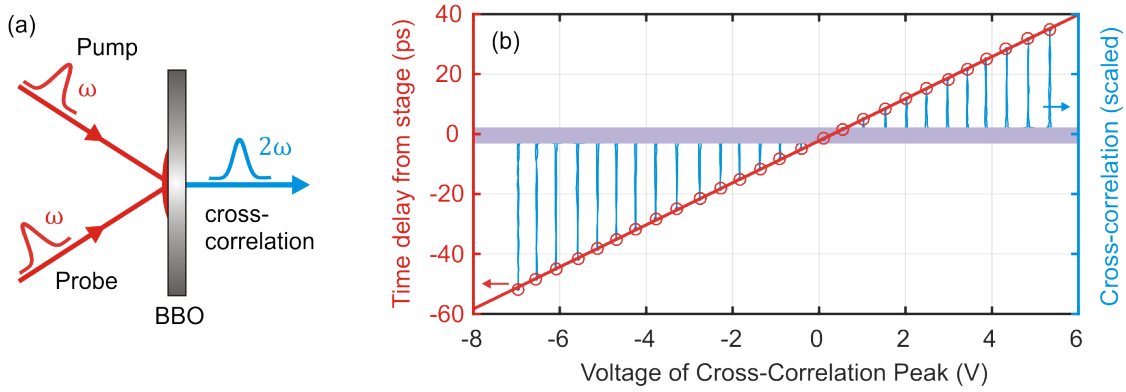


**Figure 2.12:** Calibration of the A.P.E oscillating delay line. **(a)** The pump and probe pulse, both at frequency $\omega$, are made to spatially and temporally overlap in a BBO crystal to generate their cross-correlated pulse at $2\omega$, the profile of which is measured by a fast detector. **(b)** The position of the $2\omega$ pulse relative to the voltage signal is tracked as function of the time delay between the pump and probe which is adjusted using a stepper motor stage. The slope of the red line gives the calibration factor used to convert the A.P.E. voltage signal to a real time axis.

aligned polarizer placed after the PEM changes this polarization modulation to intensity modulation e.g. when the PEM retardation is 0, all the intensity goes through; when it is $|\lambda/4|$, half the intensity goes through; when it is $|\lambda/2|$, the laser beam is blocked. Note here that the intensity modulation frequency is twice that of the retardation frequency. In this way the PEM/polarizer combination acts as an optical chopper with a frequency of 100 kHz.

**A.P.E. delay line calibration** As noted above, the A.P.E. delay line controller provides a sinusoidal voltage signal that tracks the motion of the oscillating pump mirror i.e. it directly corresponds to the time delay between the pump and the probe beams. This voltage signal can be used as the time (x-axis) in the reflectivity transients (e.g. in fig. 2.2) if the voltage axis is converted to a real time axis. This is done by cross-correlating a pump and probe pulse and then scanning the probe path using the stepper motor stage. Cross-correlation is achieved by sum-frequency generation SFG (sec. 7.1.2) in a BBO non-linear crystal. This combines a pump pulse at frequency $\omega$ and the probe pulse also at $\omega$ to give a pulse at $2\omega$ (3.1 eV) if the pump and probe both spatially and temporally overlap in the BBO crystal (fig. 2.12a). A photodetector is used to measure the $2\omega$ signal on the oscilloscope with

respect to the voltage signal from the A.P.E. delay line. Changing the probe path length with the stepper motor then changes the position of the $2\omega$ pulse along the voltage signal as illustrated in fig. 2.12b. In this way we can measure the voltage change that corresponds to a particular change in the time-delay. This calibration factor is obtained by a linear fit to different data points. The calibration is checked by ensuring that the frequency of the $A_{1g}$ optical phonon mode measured in reflectivity transients of $Bi_2Se_3$ is 2.16 THz as outlined in sec. 2.1.1. It should also be noted that the temporal profile of the $2\omega$ pulse is a measure of the time-resolution of the OPP setup.

### 2.3.2 Transient grating setup components

For both the TG and spin-TG experiments the pump and probe beams are focused onto a diffractive phase mask (PM) rather than the sample (fig. 2.9). The PM is a transmission grating which splits pump and probe into two beams each. These are then collimated to achieve the box-car geometry (fig. 2.5 and fig. 2.13 ). Thin glass cover slips are placed in the probe beams to control the optical phase $\psi$ between them in eq. (2.10). One coverslip is mounted on a fast modulating rotator (shaker) to isolate TG component in the signal (see below). The four beams are then focused onto a sample in 2:1 imaging i.e. the focal length of the last lens is half that of the collimating lens before. In this way, the grating imaged by the pump beams has period half that of the grating on the phase mask. To align TG, all four beams are passed through a 50 µm pinhole. For spin-TG, a special 'spin-optic' is placed into the path of the beams from the PM. This rotates the polarization one of the pump and probe beams by 90°. We note here that both the TG specific components described above are mounted on translation stages so that they can be removed from the beam path without disturbing the alignment. In this way, both OPP and TG/spin-TG experiments can be performed with the same setup. Below we discuss details of each of the TG specific components.

**Phase mask (PM):** The PM consists of different surface gratings etched in fused silica. Both the pump and probe beams diffract of this etched grating. Each grating is optimized

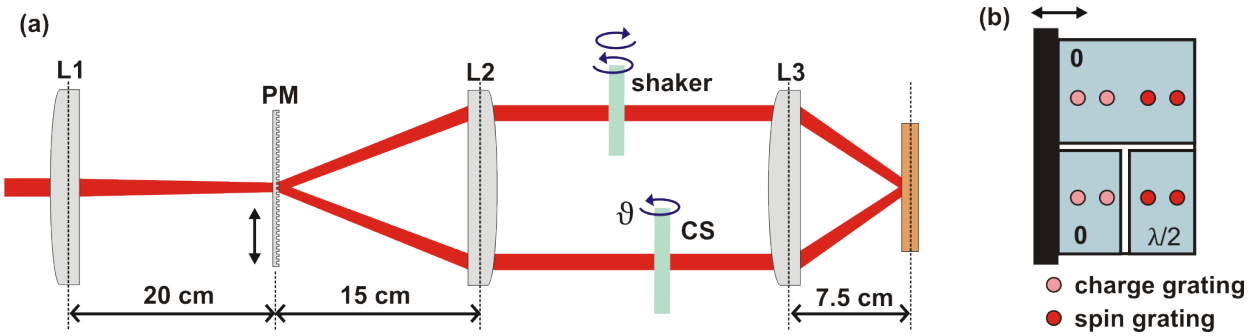


**Figure 2.13:** Transient grating specific components. **(a)** Side-view of the probe beam path from the first focusing lens to the sample. Lens L1 focuses the beam onto a diffractive phase mask (PM) which splits the beam into ±1 diffracted order. L2 collimates the beams and L3 focuses them onto the sample. CS is a thin glass cover-slip that can rotated with angle $\varphi$ along an axis parallel to this plane. The PM can be moved vertically for different grating spacings. The pump beam follows a similar beam path as this but without the CS and the shaker. **(b)** Spin-optic used for spin grating measurements. The number in each section indicates the phase retardation induced on a beam. For spin grating, the bottom two beams (one pump, one probe) have their polarization rotated by 90°. The spin-optic is mounted on a translation stage to switch between charge and spin grating.

at the 800 nm and blazed so as to maximize the intensity of the ±1 diffracted orders. This ensures that the incident beam in mostly split into two beams. The PM consists of about 20 different gratings each in a square shape (2.5 mm × 2.5 mm) with grating spacings ranging from 2 µm to 20 µm. This gives us a grating period from 1 µm to 10 µm at the sample. The smallest grating spacing that can be achieved is limited by the aperture of the 2" focusing lens and is currently 1.75 µm. The use of the PM is quite advantageous since it tilts the wavefront of the incident beam which preserves the temporal resolution as well as the pump fluence for different grating spacings. The phase mask is mounted on two translation stages, one of which allows us to change grating spacing without adjusting the alignment. The second allows fine positioning of the PM along the beam propagation axis to ensure that the grating is placed precisely at the focus (spatial overlap) of the pump and probe beams. A useful way to optimize the TG signal is to adjust this position of the PM.

**Cover slip & shaker:** As noted in eq. (2.10), the intensity in heterodyne detection depends on the phase angle $\psi$ between the local oscillator and the probe beam. $\psi$ is controlled by placing a thin microscope glass cover slips in the path of the probe beams diffracted

from the PM (fig. 2.9a). These cover slips are placed at roughly 45° from the direction of the probe beam. One of the coverslips is placed on a rotation stage with a stepper motor to adjust its angle with respect to the other. In this way, $\psi$ can be adjusted without a significant change in the beam path of the two probe beams. We find that typically a cover slip rotation of 1° corresponds to a full phase rotation of 360° (sec. 2.3.4.

One way to separate the $\delta\tilde{r}$ (PP) and $\eta$ (TG) terms in eq. (2.10) is to take values at different values of $\psi$. However, a faster way to just isolate the TG terms is to use phase-modulation. This consists of mounting one of the glass cover slips on a torsional oscillator (Camtech) which rotates the cover slip by a small amount at frequency of $\sim 2\,\mathrm{kHz}$. This causes the phase $\psi$ and thus the third term in eq. (2.10) to be modulated sinusoidally at a frequency of 2 kHz. Note that the second and third terms in eq. (2.10) are already modulated at a rate of 100 kHz which is the intensity modulation of the pump. One lock-in amplifier synchronized to 100 kHz is used to isolate these two terms. In addition, the output of this lock-in is then fed into another lock-in synchronized to 2 kHz to only get the TG term. This oscillating cover slip is called the 'shaker' in our lab.

**Spin-optic:** The spin-optic is custom-made by Altechna and consists of three separate glass pieces (fig. 2.9b). Each of them has the same thickness and they are all mounted parallel to each other. One of them is essentially a half-wave plate and rotates the polarization by 90° while the other two leave the polarization unchanged. In this way, the polarization of one of the pump and one of the probe beams is rotated to realize the spin-TG heterodyne detection illustrated in fig. 2.8 while ensuring that all the four beams remain temporally overlapped and the phase matching condition between them is fulfilled. The spin-optic can be moved in and out to go between charge transient grating or spin transient grating.

### 2.3.3 Sample mounting & cryogenic components

The samples under study are mounted in an optical cryostat (Oxford Microstat HE) to perform measurements in temperatures down to 4.2 K. This is a continuous flow cold finger cryostat that has a very small working distance of $\sim 1\,\mathrm{cm}$. This permits a large angle of

incidence for the pump and probe beam as required by TG experiments. The cryostat is pumped out using a turbo pumping system (Agilent TPS compact) so that the sample under study is kept in vacuum at a pressure better than $5 \times 10^{-5}$ Torr. The cryostat can reach base temperature of 4.2 K within 30 mins of cooling starting from room temperature. The optimum helium consumption rate is better than 0.5 L/h of liquid helium. To measure the temperature in the cryostat, two silicon diodes are used. One (diode A) is mounted right at the end of the liquid helium transfer line however this point is about an inch away from the sample mount which is typically at a slightly higher temperature. To accurately measure the sample temperature, a second diode (B) is mounted right next to the sample. The temperature is controlled using a heater mounted next to diode A. Standard PID feedback techniques are used to control the current in the heater to set a given temperature.

The sample is mounted onto a copper plate using silver epoxy (Epo-Tek H20E) which provides excellent thermal and electrical conductivity. For thin-film samples with transparent substrates as studied in this work, it is essential to mount the sample over a $\sim$ 5 mm hole in the copper plate. This allows the strong pump beam to go through the cryostat rather than being diffusively reflected from the copper plate and contributing to pump-scatter in the measurements.

The entire cryostat is placed on a home-built mount that allows rotation along the pitch and yaw axis. This is quite useful; since the sample surface might not be uniform, the reflected probe might be in an arbitrary direction rather than going through the pick-off mirror. Adjusting the pitch and yaw allows us to control the path of the reflected probe beam. This mount is placed onto three translation stages that allow positioning of the sample along all three axes. Adjusting the z-axis (i.e. axis along the direction of beam propagation) is essential in fine positioning the sample at the spatial overlap of the pump and probe beams. Adjusting the x- and y-axis allows us to find a flat and shiny part of the sample with minimum pump scatter.

### 2.3.4 Data acquisition

To acquire OPP data, the output of the photodetector in fig. 2.9 is passed through a low-pass filter (KIWA electronics) to limit high-frequency noise. It is then sent to a lock-in amplifier (Stanford Research Systems SR830) which is synchronized to a 100 kHz reference signal from the PEM controller. The time constant of the lock-in is set to 30 µs for good signal-to-noise while maintaining a time resolution of $< 100$ fs. The output of the lock-in is measured using an oscilloscope (Lecroy) that is triggered off the A.P.E delay line. As discussed above, the calibrated signal from the A.P.E is the time axis while the lock-in output is the pump modulated change in reflectivity ($\Delta R$). We also record the DC output of the photodetector on the oscilloscope as a measure of the static reflectivity ($R$). In this way $\Delta R/R$ is acquired as a function of time.

The acquisition of the TG data can be separated into what we refer to in our lab as the '3-point' or the '2-point/shaker' scheme. As the name suggests, the 3-point scheme refers to solving for the variables $\delta\tilde{r}$, $\eta$ and $\phi$ in eq. (2.10) using 3 different values of $\psi$ which is controlled using a thin cover slip as discussed above. The challenge is determining how the physical cover slip angle $\vartheta$ is related to optical phase $\psi$. This is overcome by utilizing the symmetry between the probe and local oscillator (LO) as illustrated in fig. 2.5. The probe and the LO are interchangeable within a phase factor. As such we now refer to them as probe 1 (P1) and probe 2 (P2). The reflected P1 heterodynes with the diffracted P2 and following eq. (2.10) the measured intensity of this mixing can be written as:

$$I_{P1} \propto |\delta\tilde{r}|\cos(\phi) + |\eta|\cos(\phi - \psi) \tag{2.16}$$

Similarly, the reflected P2 heterodynes with the diffracted P1 and the measured intensity of this mixing is similar to that above except that the sign of $\psi$ is flipped since we are now measuring the opposite diffracted order i.e.

$$I_{P2} \propto |\delta\tilde{r}|\cos(\phi) + |\eta|\cos(\phi + \psi) \tag{2.17}$$

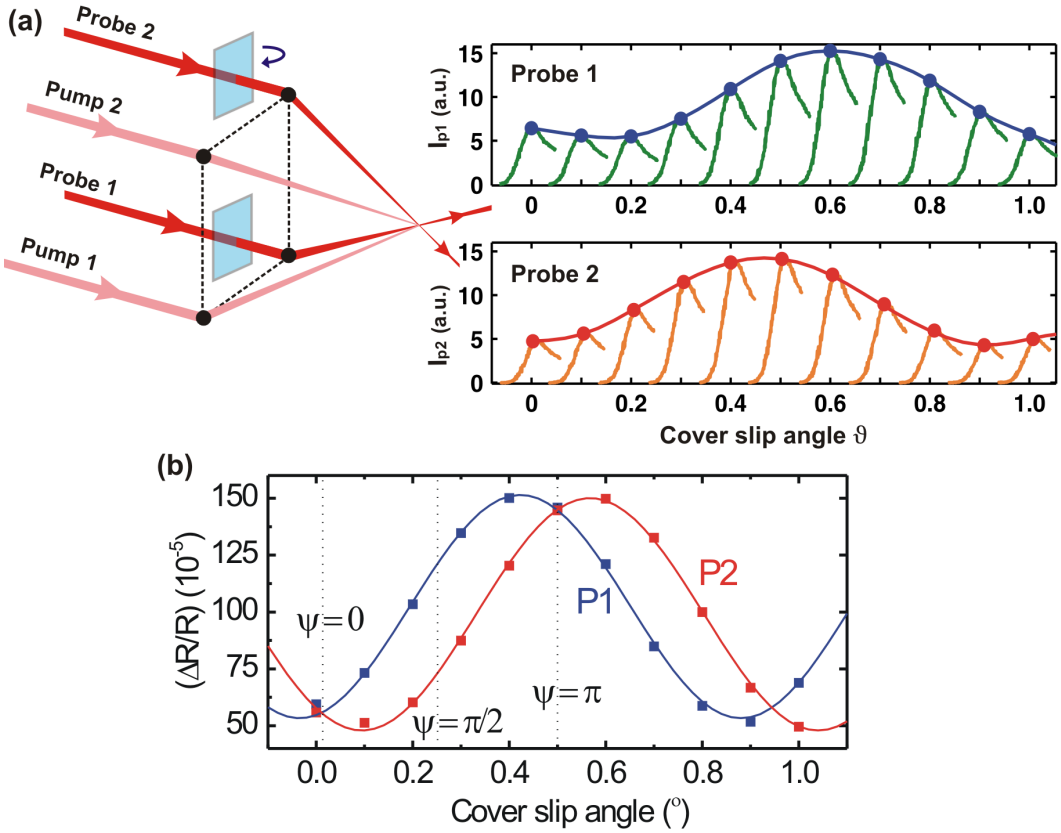


**Figure 2.14:** Calibration of the phase in TG experiments. **(a)** The cover slip is rotated in steps of 1° and reflectivity transients are recorded at each value of the angle for each probe arm (top-right). **(b)** The initial maximum value is plotted with the cover slip angle and fitted to sinusoidal curves. From the intersection points between the two curves we obtain the cover slip angles corresponding to $\psi = 0$, $\psi = \pi/2$ and $\psi = \pi$.

To calibrate the phase $\psi$, we obtain time-resolved traces at various values of the cover slip angle $\vartheta$ for each probe arm as shown in fig. 2.14a. We then plot the initial peak value of the traces in each arm with $\vartheta$ (fig. 2.14b). The values of $\vartheta$ where the curves from each arm intersect correspond to $\psi = 0$ and $\psi = \pi$ while the value between them gives $\psi = \pi/2$. Performing measurements at these 3 values of $\vartheta$ gives us the following

signals from which we can solve for $\delta\tilde{r}$, $\eta$ and $\phi$:

$$\begin{aligned} I_0 &\propto |\delta\tilde{r}|\cos(\phi) + |\eta|\cos(\phi) \\ I_{\frac{\pi}{2}} &\propto |\delta\tilde{r}|\cos(\phi) + |\eta|\sin(\phi) \\ I_{\pi} &\propto |\delta\tilde{r}|\cos(\phi) - |\eta|\cos(\phi) \end{aligned} \tag{2.18}$$

The procedure used to calibrate $\psi$ is only dependent upon alignment and not upon the properties of the sample. Thus, the calibration is typically carried out once per data run. In the 3-point scheme, only one lock-in is used with the signal being modulated by the PEM at 100 kHz. One main advantage of the 3-point scheme is that it allows a simultaneous measurement of both the $\delta\tilde{r}$ (PP) and $\eta$ (TG) part of the response within one set of measurements.

In contrast, the '2-point/shaker' scheme only acquires the $\eta$ (TG) part of the response. This scheme uses the shaker to modulate $\psi$ so as to get rid of the first term in eq. (2.16) and in eq. (2.17). In this case, we only need data at two angles of the cover slip corresponding to $\psi = 0$ and $\psi = \pi/2$ to solve for $\eta$ and $\phi$. In this case, the output of the photodetector goes through two lock-in amplifiers. The first is set to 100 kHz and a time constant of 10 µs to allow the signal modulated at 2 kHz to pass through the output. The second lock-in is set to 2 kHz and a time constant of 30 µs. While the shaker allows faster acquisition of the TG data, the data is slightly nosier then that in the 3-point scheme due to mechanical instabilities in the motion of the torsional oscillator. Nonetheless, the shaker is is extremely useful in optimizing the TG signal and in optical phase separation experiments discussed earlier.

*And so these men of Indostan*
*Disputed loud and long,*

*Each in his own opinion*
*Exceeding stiff and strong,*

*Though each was partly in the right,*
*And all were in the wrong!*

— John Godfrey Saxe,
*The Blind Men & the Elephant*

# 3

# Fluctuating charge density waves in cuprates

## Contents



Cuprate materials hosting high-temperature superconductivity (HTS) also exhibit various forms of charge and/or spin ordering whose significance is not fully understood. To date, static charge-density waves (CDWs) have been detected by diffraction probes only at special doping or in an applied external field. However, dynamic CDWs may also be present more broadly and their detection, characterization and relationship with HTS remain open problems. In this chapter we present a new method, based on ultrafast pump-probe and

transient grating spectroscopy, to detect the collective modes (amplitudon and phason) of the fluctuating CDW in a $La_{1.9}Sr_{0.1}CuO_4$ thin film. Following uniform photoexcitation by an ultrashort laser pulse, we observe highly damped oscillations in the transient reflectivity of a time-delayed probe pulse (pump–probe (OPP) spectroscopy). The frequency of these oscillations as well as the temperature and excitation density dependence of their amplitude indicates that they arise from the amplitudon of the CDW. When we perturb the system with a spatially varying sinusoidal excitation density (transient grating (TG) spectroscopy), we observe an additional slow response that we ascribe to the phason. Using theoretical predictions for the temperature evolution of the phason damping rate we obtain an estimate of the CDW fluctuation lifetime ($\tau_F$). In contrast, in an optimally doped $La_{1.84}Sr_{0.16}CuO_4$ film ($T_c = 38.5\,\mathrm{K}$), we detect no signatures of fluctuating CDWs at any temperature which suggest a competition between the superconducting and the CDW order parameters. Similarly, an analysis of the magnitude of the detected amplitudon in terms of Ginzburg-Landau theory further supports the competition scenario.

## 3.1 Cuprate superconductors

In 1986, superconductivity in copper-oxide compounds was discovered by J. Bednorz and K. M*ü*ller when they cooled down $LaBaCuO_4$ and found that it superconducts below 30 K [8]. It was soon realized that the superconducting phase in these compounds is highly unconventional in that it differs from the Bardeen, Cooper and Schreiffer (BCS) theory of superconductivity. For example, it is known that unlike BCS superconductors, the order parameter in cuprate superconductors is not simple *s*-wave. Moreover, it is still not clear if the pairing mechanism between Cooper pairs is derived from electron-phonon interaction. Several cuprate superconducting compounds have now been discovered with superconducting transition temperatures ($T_c$) even higher than the boiling temperatures of liquid nitrogen (77K). Cuprates are ideal examples of quantum materials; not only do

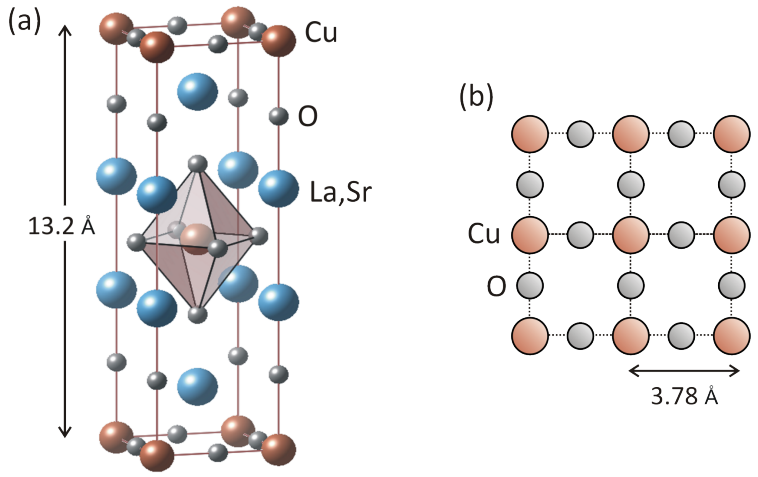


**Figure 3.1:** Crystal structure of $La_{2-x}Sr_xCuO_4$ **(a)** Three dimensional structural arrangement with one tetragonal unit cell being represented. Drawn using [43] **(b)** $CuO_2$ plane with copper atoms in orange and oxygen atoms in grey.

they host the macroscopic quantum phenomena of superconductivity but they also exhibit a delicate balance between various other electronic and magnetic phases.

Figure 3.1 shows the crystal structure of the cuprate $La_{2-x}Sr_xCuO_4$ which is the main focus of this chapter. $La_{2-x}Sr_xCuO_4$, like other cuprates, is a layered material whose elementary units are $CuO_2$ planes separated by layers containing La atoms, a few of which are replaced by Sr atoms to introduce dopant holes into the $CuO_2$ planes. Superconductivity as well as other types of electronic/magnetic ordering originate within this $CuO_2$ plane. In general, cuprate properties can vary significantly depending on the charge carrier concentration in this plane.

For example, as the hole doping is varied, various forms of charge and/or spin ordering emerge, as shown in the phase diagram in fig. 3.2. At zero doping ($p = 0$), the 'parent' compound is an anti-ferromagnetic (AFM) insulator due to strong Coulomb repulsion between adjacent Cu sites. As the doping is increased, long-range AFM ordering is suppressed but at very low temperatures there is evidence for a spin-glass or spin density wave phase for dopings upto p = 0.06. As the doping is increased, superconductivity (SC) sets in within a dome shaped region. The maximum of this dome, corresponding to the highest superconducting temperature, occurs at $p \sim 0.16$. This doping is called optimal doping while the regions

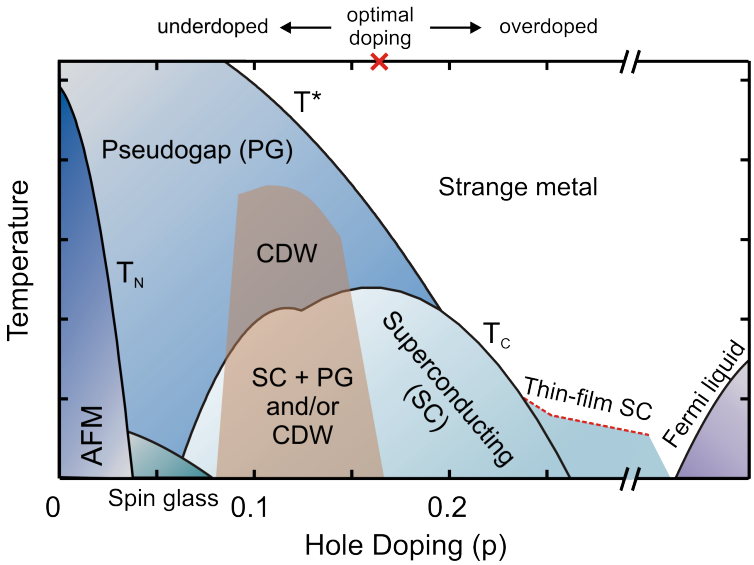


**Figure 3.2:** Typical phase diagram of hole doped cuprates. AFM refers to anti-ferromagnetism while CDW is the charge density wave phase which will be the main focus of this work. $T_c$, $T^*$, and $T_N$ mark the temperatures at which superconductivity, the pseudogap and AFM onset respectively. Red dashed line refers to the SC transition in MBE grown thin film cuprates which show a SC phase persisting far into the overdoped regime. Figure adapted from [45]

for $p < 0.16$ and $p > 0.16$ are known as underdoped and overdoped respectively. For very high hole dopings, SC is completely suppressed and Fermi liquid (FL) resistivity ($\rho \propto T^2$) is observed [16]. In between the SC and FL phases is the so-called strange metal regime for which the resistivity $\rho \propto T$ for exceedingly high temperatures. It is important to note here that for MBE grown thin-film $La_{2-x}Sr_xCuO_4$ superconductors, which are the main subject of this chapter, the superconductivity dome persists quite far into the overdoped region [44].

Above the SC transition temperature $T_c$, the cuprate phase diagram features two phases that are believed to be the key to understanding high-temperature SC in cuprates: the pseudogap (PG) phase and charge density wave ordering (CDW) The PG phase onsets at a temperature $T^*$ and was first seen in NMR experiments [46]. There is substantial debate on whether the PG is a distinct quantum phase or a precursor to the SC phase with preformed Cooper pairs. The transition to the PG is usually seen as a decrease in the electronic component of the specific heat [47]. As shown in sec. 2.1.2, optical pump-probe is able to distinguish between the SC and PG phases quite accurately. Further discussion

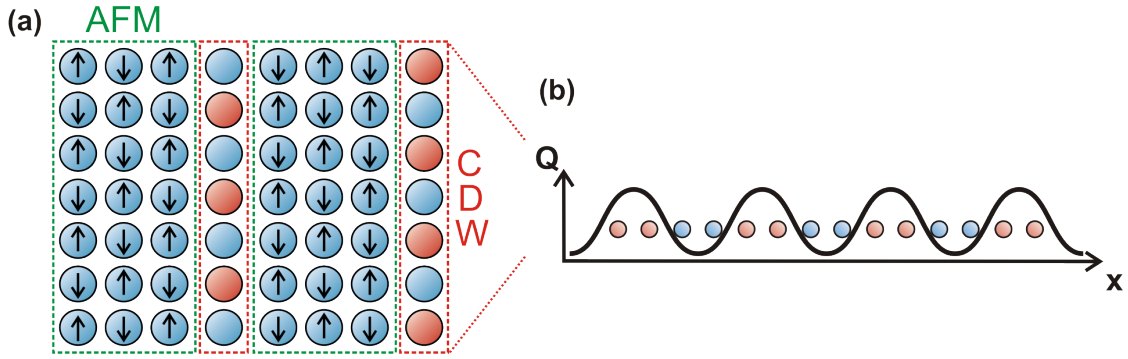


**Figure 3.3:** **(a)** Visualization of magnetic and charge order in the $CuO_2$ plane of cuprates. Only the Cu sites are shown. Alternating anti-ferromagnetic regions (green rectangles) are separated by 1D charge density wave regions (red rectangles) **(b)** Charge density profile across the 1D chain of Cu atoms separating the AFM regions in **(a)**

on the PG phase is beyond the scope of this thesis. Instead, the focus will be on the CDW phase which occurs in a narrow region on the underdoped side of the phase diagram and is believe to co-exist with both the SC and the PG phase.

### 3.1.1 Charge ordering in cuprates

As pointed above, among the rich structural, magnetic, and electronic phases of the cuprates, there exist various forms of modulated charge order [48–53]. A particularly well-studied example is found in underdoped $La_{2-x}(Sr,Ba)_xCuO_4$ where a fraction of the carriers forms a charge density wave (CDW) phase [54] coexistent with magnetic density-wave ordering in a configuration sometimes referred to as 'stripes' [55, 56]. One way to visualize this 'stripe order' in $La_{2-x}(Ba)_xCuO_4$ at $x = \frac{1}{8}$ is to consider alternating AFM and CDW order on the Cu sites in the $CuO_2$ planes as shown in fig. 3.3a. In general the CDW is a broken symmetry electronic phase in which translational symmetry is broken due to a sinusoidal spatial variation in the charge density along 1D chains of Cu sites (fig. 3.3b). It is important to note that the charge order in $La_{2-x}(Ba)_xCuO_4$ is static which means that the correlation length and time for the order parameter diverge to infinity at the transition. At the special doping of $x = \frac{1}{8}$ this CDW order completely eliminates superconductivity [57] indicating that static CDW order competes with superconductivity.

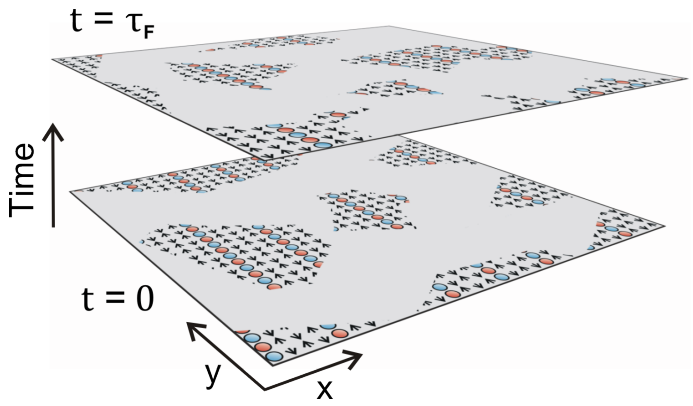


**Figure 3.4:** Schematic illustrating the dynamics of the fluctuating CDW order. The spatial organization of the CDW order changes within the fluctuation lifetime $\tau_F$

.

In contrast to this static order, in most cuprates including $La_{2-x}(Sr)_xCuO_4$ (LSCO), the CDW order parameter is thought to be fluctuating. This implies that a particular configuration of the CDW order dynamically changes within a characteristic lifetime as represented schematically in fig. 3.4. Here the order has some finite correlation length and correlation time ($\tau_F$). Due to this dynamical nature, the impact of the density wave in LSCO is mitigated [44], causing only a slight depression in $T_c$ in the vicinity of $x = \frac{1}{8}$.

This fluctuating characteristic has been a central issue in the debate surrounding the role of CDWs in the cuprates [58], in particular, whether they favour—or even enable—HTS, or compete with it. In the competition scenario, the stability of the fluctuating CDW should decrease with higher values of Tc because both the CDW and the superconducting order would compete for charge carriers. Another open question in the field is a determination of the lifetime associated with this fluctuating order i.e. how long a particular configuration of the order remains stable.

To study fluctuating order, researchers have relied on quasi-static probes of local order [58] in a configuration where the density wave has been stabilized either by an external magnetic field [59] or by adding specific dopants, for example, Nd [55, 60] or Eu [61]. These requirements have only recently been surmounted by the use of resonant inelastic X-ray scattering [52, 62, 63] and high-energy X-ray diffraction [53], although these techniques

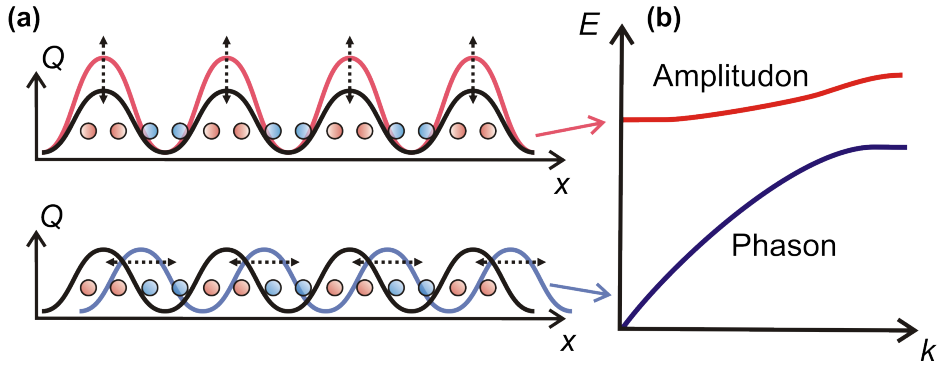


**Figure 3.5:** **(a)** The CDW gives rise to two collective excitations: the amplitude mode (amplitudon), which represents an overall oscillation of the CDW amplitude, and the phase mode (phason), which is due to a sliding of the CDW along the modulation direction **(b)** The amplitudon exhibits optical dispersion whereas the acoustic phason dispersion is gapless owing to the incommensurability of the density wave with respect to the lattice.

have yet to provide dynamical information about the CDW from which the critical behavior of $\tau_F$ may be elucidated.

### 3.1.2 Collective excitations of the CDW phase

In contrast to the above techniques, ultrafast methods provide a new opportunity to probe dynamics of charge orders directly without the need for stabilizing fields or impurities [64]. Among the various degrees of freedom that may be probed are the collective modes of the CDW, as depicted in fig. 3.5. Here, absorption of an ultrafast laser pulse generates single-particle excitations of the CDW and hot carriers [65]. These may be manipulated to either coherently drive the amplitude mode (amplitudon) or the phase mode (phason) of the CDW phase. The amplitudon is the coherent oscillation of the charge density's magnitude and has a dispersion similar to that of an optical phonon and is gapped [66]. On the other hand, the phason, which is the collective sliding of the modulated charge, is gapless for incommensurate CDWs and has a dispersion similar to that of an acoustic phonon [66]. A key point to note here is that for a fluctuating CDW order, each of these excitations cannot live longer than underlying CDW configuration so the lifetime of these excitations could be based on the CDW fluctuation lifetime.

In the cuprates, the amplitudon and phason of the CDW have so far been probed using Raman scattering in LSCO single crystals [67, 68] where their broad frequency-domain features did not allow a reliable extraction of their lifetimes. In contrast, a time-domain approach, similar to studies in conventional CDW systems [65, 69–72] would allow an accurate characterization of these highly damped modes, and thus provide information on the dynamical nature of the CDW and yield its fluctuation time.

In this work, ultrafast techniques are used to generate the collective modes of the CDW phase in an underdoped LSCO thin film. The amplitudon is generated by uniform illumination of the sample using optical pump-probe as detailed in sec. 2.1. Whereas the phason may be driven by a sinusoidally modulated excitation density - a transient grating - created by the interference of two temporally and spatially coincident beams. The principles behind the transient grating technique can be found in sec. 2.2.

## 3.2 Experimental methods

This section describes the sample and the ultra-fast optical setups used for this work.

### 3.2.1 LSCO: sample synthesis and characterization

The $La_{2-x}Sr_xCuO_4$ thin films used in this work were grown and initially characterized by Anthony T. Bollinger and Ivan Bozovic at the Brookhaven National Laboratory. Three dopings were studied: $x = 0.1$ and $x = 0.16$. The films were synthesized using atomic-layer-by-layer molecular beam epitaxy (ALL MBE) [73–76] on single-crystal $LaSrAlO_4$ substrates which were polished to epitaxial smoothness with the (001) axis perpendicular to the surface. The thickness of each LSCO film was set to 50 nm. More detail on the sample growth process and verification can be found in the supplementary information of [25].

To determine the superconducting transition temperature ($T_c$) for each film, mutual inductance measurements [77] were done in the transmission geometry i.e. the cuprate thin-film was situated between the drive and pick-up coils. The data was acquired at frequency of $\nu = 10\,\text{kHz}$. The drive coil current excitation was $I_{dr} = 5\,\mu\text{A}$; given the geometry of the

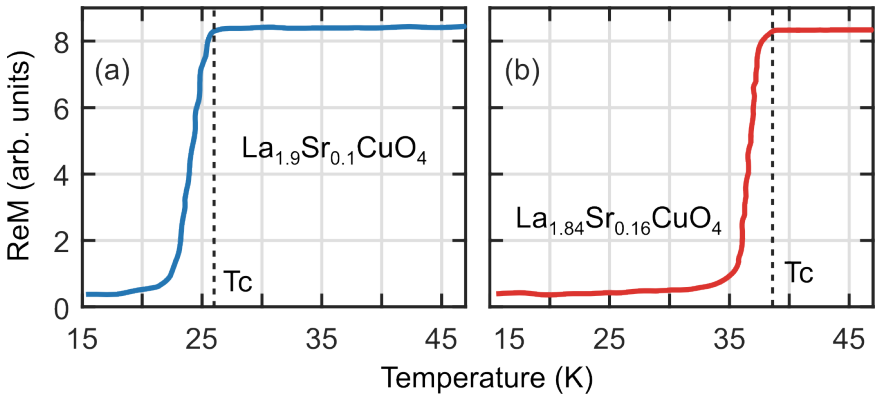


**Figure 3.6:** **(a)** The real (reactive) part of the mutual inductance in the underdoped MBE grown $La_{1.9}Sr_{0.1}CuO_4$ thin film showing diamagnetic screening below $T_c \approx 26\,\mathrm{K}$. **(b)** Same measurement for optimally doped MBE grown $La_{1.84}Sr_{0.16}CuO_4$ showing a $T_c \approx 38.5\,\mathrm{K}$

coil assembly, this corresponds to a screening current density in the film of $j_f \sim 10^3\,\mathrm{A/cm^2}$. The data for these measurements is displayed in fig. 3.6. This indicates a $T_c \approx 26\,\mathrm{K}$ in $La_{1.9}Sr_{0.1}CuO_4$ and a $T_c \approx 38.5\,\mathrm{K}$ in $La_{1.84}Sr_{0.16}CuO_4$.

### 3.2.2 Optical setup details

Full experimental details on the optical pump-probe and transient grating setups are given in chap. 2. For completeness, a few specific points are highlighted as follows. Experiments were performed with a Ti: sapphire oscillator lasing at the center wavelength of 60 nm ($\hbar\omega = 1.55\,\mathrm{eV}$) producing pulses 60 fs in duration. The repetition rate of the laser was reduced to 1.6 MHz with an extracavity pulse picker to avoid cumulative heating effects on the sample. Two separate experimental geometries were used. In the pump-probe (PP) geometry, the sample was excited by a spatially Gaussian pump pulse of 60 µm FWHM. The sample response was then recorded through measurement of the normalized change in the reflectivity, $\Delta R(t)/R$, of a separate probe pulse as a function of delay time $t$ between the pump and the probe. In the transient grating (TG) geometry, the intersection of two equal-intensity, temporally coincident copies of the excitation pulse at an angle $\theta$ produces a sinusoidal modulation of the excitation profile with spacing $\Lambda = \lambda/(2\sin(\theta/2))$, where $\lambda$ is the laser wavelength. Signal was recorded using a beam that both diffracted off the induced grating

and reflected specularly from the excited region. The contribution due to the sinusoidal excitation was separated from the transients to yield the TG response [41].

## 3.3 Time-resolved signatures of the CDW phase

Figure 3.7a shows pump-probe(PP) data for an underdoped ($x = 0.1$) LSCO thin-film at various temperatures. For $T < T_c$, there is a short $\approx 1\,\mathrm{ps}$ 'spike' which is identical to the response for $T > T_c$ and was not observed to change in dynamics up to 300 K. This is interpreted as arising from uncondensed electrons and will refer to it below as the 'normal' component. This fast electronic response is followed at short times by highly damped oscillations which are superposed upon the slow response due to quasiparticle recombination; this slow response has been studied extensively [78, 79] and will not be discussed further in this chapter. Refer to appendix A for more details on the dynamics of this quasi-particle recombination. The observed oscillations are isolated by subtracting the slow response (fig. 3.7a inset). As the temperature is increased across $T_c$, the oscillations persist with decreasing strength up to $\approx 100\,\mathrm{K}$, above which they cannot be discerned from the noise.

In order to study the CDW dynamics without the presence of the superconducting state, data is shown in the PP and transient grating (TG) geometry at 45 K (i.e. $T > T_c$) (fig. 3.7b). Here, the presence of the normal response is observed as described above and an additional component which provides a TG response that decays more slowly than that measured in the PP geometry. This additional response disappears when the temperature is raised to 100 K (fig. 3.7b inset). In contrast with the data of fig. 3.7a and 3.7b, there are no oscillations in an optimally doped $La_{1.84}Sr_{0.16}CuO_4$ ($T_c = 38.5\,\mathrm{K}$) sample at any temperature, as seen in fig. 3.7c for 5 K and 50 K. In addition, this sample produced a TG response which was identical to the PP response above $T_c$, as shown in fig. 3.7d.

### 3.3.1 Identifying the amplitudon

This subsection establishes that the oscillatory response of fig. 3.7a originates from the amplitudon. Adapting an approach similar to Demsar et al. [65], the data in fig. 3.7a

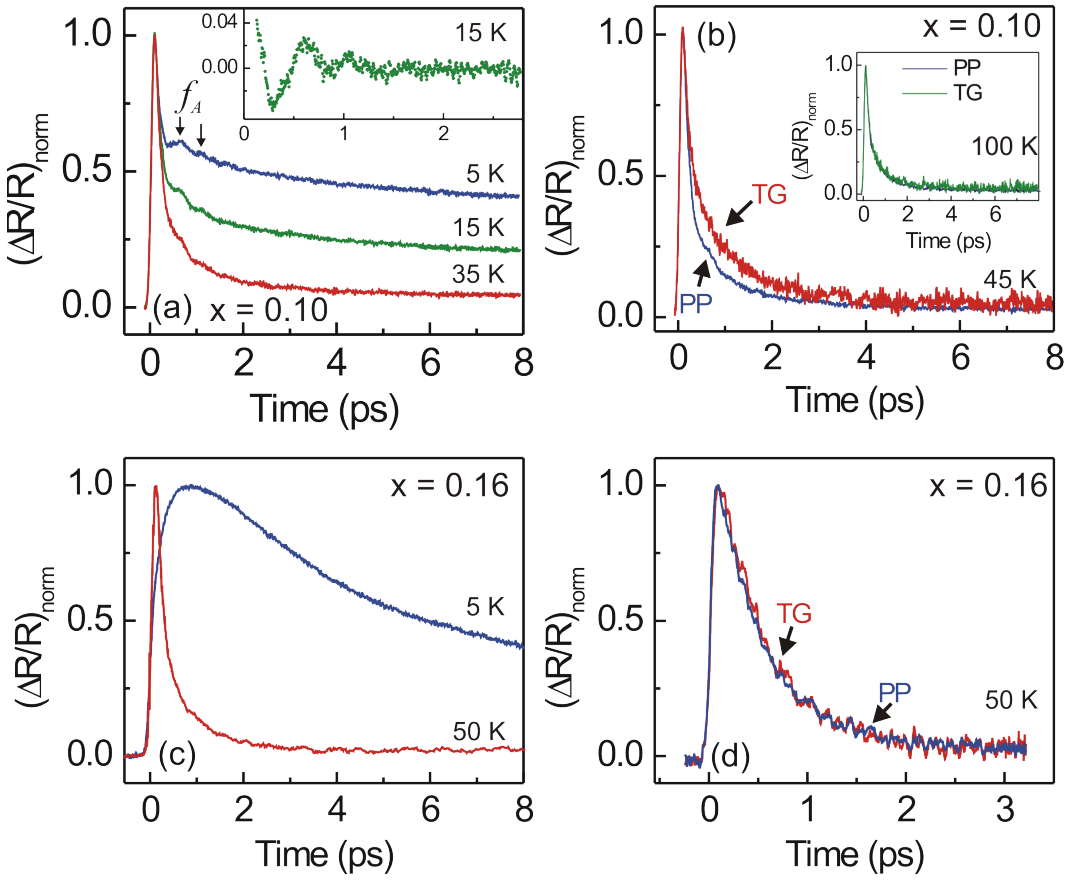


**Figure 3.7:** Raw data traces indicate the presence of coherent modes of the CDW in $La_{2-x}Sr_xCuO_4$ for $x = 0.10$ but not for $x = 0.16$. In **(a)**, the amplitudon response is evident via an oscillation of frequency $f_A$ in the reflectivity transients. This response is observed to persist above the superconducting transition temperature $T_c = 26\,\mathrm{K}$. Inset: the amplitudon response is isolated by subtracting the fitted background electronic response (see text). **(b)** Above $T_c$, there is a discrepancy between the PP and TG responses is attributed to the phason, as described in the text. This difference disappears at $\approx 100\,\mathrm{K}$ (inset). **(c)** Data from the $x = 0.16$ sample ($T_c = 38.5\,\mathrm{K}$) show only the quasiparticle recombination dynamics associated with non-equilibrium excitation of the superconducting state below $T_c$ and a fast electronic transient above $T_c$. There is no evidence of either the amplitudon or phason above or below the superconducting transition temperature. Similar behavior was observed in the $x = 0.33$ sample (not shown). **(d)** TG and PP transients at 50 K in the $x = 0.16$ sample. There is no discernible difference between the two traces.

is fitted to a model which comprises both the electronic and oscillatory components as $\Delta R(t)/R = Ae^{-t/\tau_A}\sin(2\pi f_A t)+Cs(t)$, where $A$ is the magnitude of the oscillating component, $\tau_A$ its lifetime and $f_A$ its frequency. $C$ represents the strength of the background electronic response s($t$) due to quasiparticle recombination below $T_c$ and due to charge relaxation above $T_c$ (see sec. 3.6 below for details on the exact fitting procedures). A representative fit is shown in fig. 3.8a, where excellent agreement is observed between the model function and the data, yielding the frequency $f_A = 2.0\,\mathrm{THz}$ ($67\,\mathrm{cm}^{-1}$) and the lifetime $\tau_A = 300\,\mathrm{fs}$. Neither $f_A$ nor $\tau_A$ were observed to vary with temperature within our experimental uncertainties, although the amplitude $A$ of the response diminishes with temperature until it is no longer detectable, as shown in fig. 3.8c. The obtained value for $f_A$ is lower in frequency than any optical phonon mode observed by frequency-domain Raman techniques [80], for which the full theoretical assignment of the lattice modes in the parent material has been made [81]. Rather, $f_A$ approximately matches the value assigned by Sugai et al. [68] to the amplitudon in their study of LSCO single crystals by Raman spectroscopy.

In the absence of optical phonon modes that match the observed oscillation, it is quite likely that this oscillatory response is due to an amplitudon driven by a mechanism akin to the displacive excitation of coherent phonons (DECP) [31, 65]. The general theory behind the DECP mechanism is discussed in sec. 2.1.1. In this scenario, depicted in fig. 3.8d, single-particle excitations and hot carriers arising from optical excitations of the CDW alter the local potential $V_0$ of the CDW. Their sudden photo-generation results in an impulsive change of the potential energy landscape of the modulated order $V'$ which shifts the equilibrium charge modulation away from the photoexcited state configuration. In response, the system oscillates about the new equilibrium charge configuration with frequency $f_A$, modulating the reflectivity.

Further evidence to support the identification of the oscillation as the amplitudon is provided in the plot of $A/\Delta R(0)/R$, i.e. the ratio of the amplitude ($A$) of the amplitudon to the total amount of signal ($\Delta R(0)/R$), as a function of the incident laser fluence in fig. 3.8b. Here, the oscillation strength decreases relative to the total amount of signal as the excitation fluence is increased, indicating a saturation of the oscillatory response. While

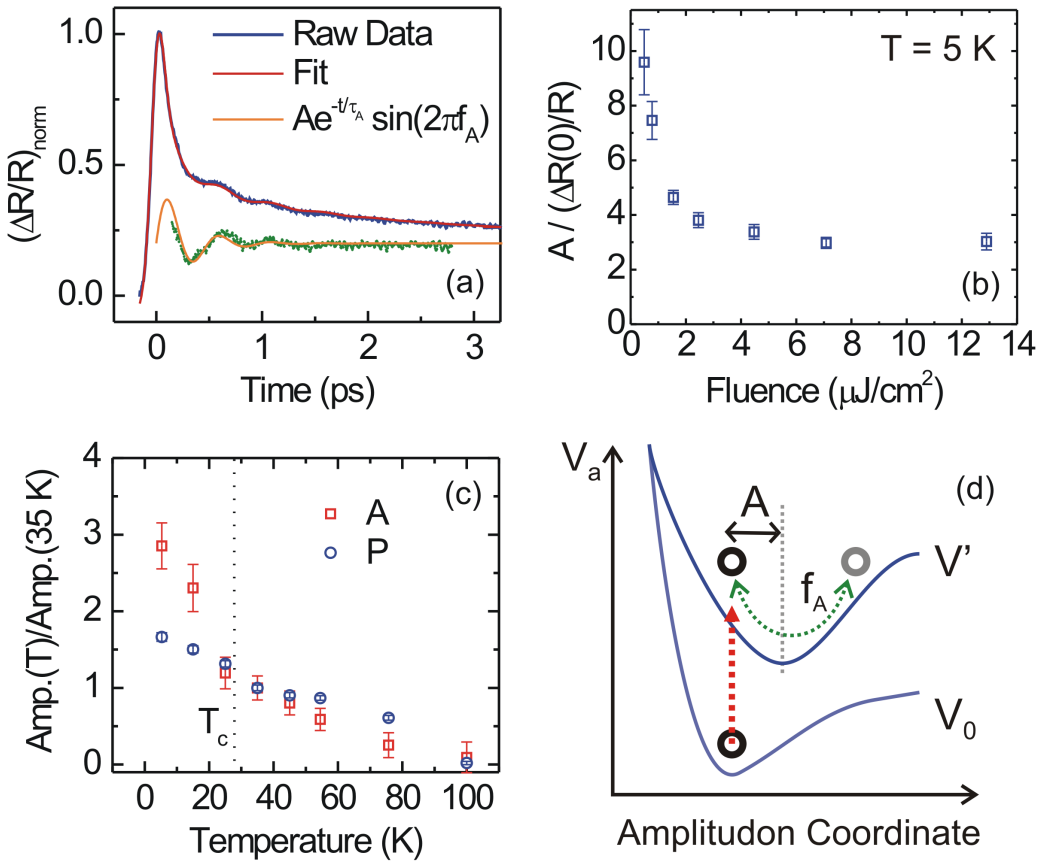


**Figure 3.8:** Analysis of the amplitudon response as a function of temperature. **(a)** Representative data at $T = 15\,\mathrm{K}$ are shown along with the fit to the model described in the text and the residual due to the amplitudon response. Excellent agreement between the model function and the data is found at all temperatures. **(b)** Ratio of the amplitude ($A$) of the amplitudon to the total amount of signal ($\Delta R(0)/R$) as a function of fluence. The saturation of the amplitude with fluence is consistent with other measurements of the amplitudon in conventional CDW systems. **(c)** The magnitude of the amplitudon and phason as a function of temperature, both normalized to the value at $T = 35\,\mathrm{K}$ for comparison. Their common disappearance indicates that $T_{CDW} \approx 100\,\mathrm{K}$. **(d)** Representation of the displacive excitation mechanism (DECP) which drives the amplitudon. The system is represented by an open circle. $V_0$ and $V'$ represent the potential energy surfaces before and after the absorption of laser light, respectively. Error bars in **b**,**c** represent the 95% confidence interval (2s.d.) in extracting the fitting parameters $A$ and $P$.

for a Raman-active phonon mode the strength of the phonon response is proportional to the electron dynamics that drive the phonon, in the CDW case the finite concentration of the participating carriers (estimated by [68] at $\sim 10\%$) is depleted by the pump pulse at a relatively modest fluence of $\sim 3\,\mu J/cm^2$. Therefore, the oscillation observed in fig. 3.7a is not due to an optical phonon, but specifically due to the amplitudon of the CDW. Thus, the temperature at which the amplitudon disappears indicates that $T_{CDW} \approx 100\,K$, consistent with observations from Raman spectroscopy [68]. Since the processes responsible for the amplitudon damping rate may possibly be faster than $\tau_F$, the 300 fs lifetime measured above thus sets a lower bound on the CDW fluctuation lifetime.

### 3.3.2 Identifying the phason

In this subsection we assign the additional decay component observed in the TG configuration in fig. 3.7b to the phason. The data were analyzed by first fitting the PP response at 100 K. This produced an excellent phenomenological fit which was subtracted from the raw TG data at all temperatures to account for the unchanging normal component observed by the PP transients. The resulting TG − PP data were fitted to a single exponential $Pe^{-t/\tau_P}$ to represent the overdamped decay. A representative fit is presented in fig. 3.9a, showing agreement between the raw data and the model predictions. As with the amplitudon, the magnitude of the overdamped response $P$ diminishes with temperature and recedes below a detectable level at 100 K (fig. 3.8c), indicating its common origin with the amplitudon signal. Besides the phason, other possible sources listed below can also give rise to a difference between the TG and the PP signals:

1. Propagating optical phonons [82],
2. Propagating acoustic phonons [83],
3. Thermal diffusion [83],
4. Carrier diffusion [21]

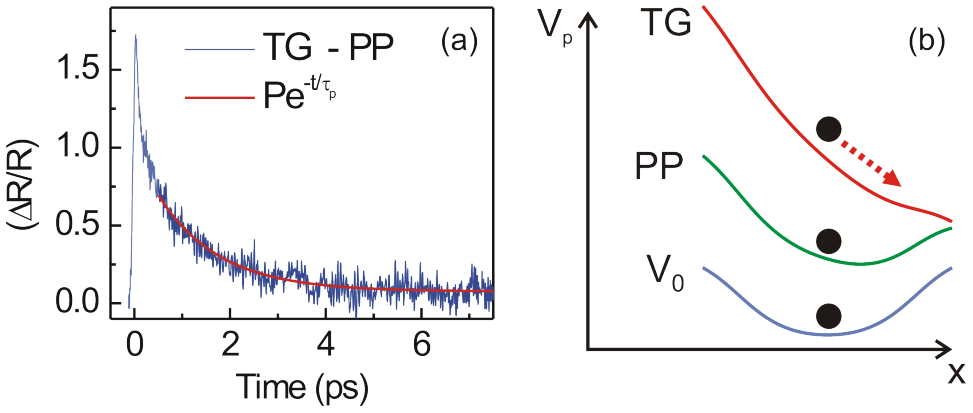


**Figure 3.9:** Phason response and depinning mechanism. **(a)** The difference between the TG and PP components yields the pure phason response, which is fitted to a decaying exponential yielding the phason magnitude $P$ and lifetime $\tau_P$. **(b)** Illustration of the depinning mechanism for phason generation. The gradient of the TG geometry is $\sim 100$ times larger than that of the PP geometry, allowing the CDW to slide.

None of the source listed above could cause the TG signal in fig. 3.7b: photo-generated coherent acoustic phonons in this system appear at too low frequencies [84] while the optical phonon modes frequencies are too high; both the optic and the acoustic phonon modes are underdamped [84], and the selection rules for optical phonons would imply that the response would be present both in the PP and TG geometries. Thermal diffusion is much slower than the $\sim 1$ ps timescales observed here, and both thermal and carrier diffusion would produce a TG response that is faster than in the PP geometry [21].

Given that the aforementioned sources of the TG signal can be ruled out and given that both the amplitudes $A$ and $P$ disappear together (fig.3.8c), we assign the observed TG signal in fig. 3.7b to the phason. Here the phason is generated via a mechanism, shown in fig. 3.9b, that is similar to that which drives the amplitudon. Since the CDW is known to be incommensurate in $La_{2-x}Ba_xCuO_4$ and $La_{2-x-y}Nd_ySr_xCuO_4$ even at the $x = 1/8$ doping of static charge order [85, 86], the phason is gapless. Impurities pin the phason and prohibit it from sliding [87] unless a depinning field is applied. However, due to the presence of the same single-particle excitations and hot carriers that drive the amplitudon, there is a change in the local electronic potential $V(x)$ experienced by the CDW as a function

of position $x$. This change $\delta V(x)$ shares the spatial profile of the driving laser field, i.e. it is Gaussian in the PP case with the FWHM of the laser, while in the TG geometry it is both Gaussian and spatially periodic with grating period $\Lambda$. In the PP configuration, the Gaussian of FWHM 60 µm produces a maximal gradient approximately two orders of magnitude smaller than that generated by the typical grating spacing in the TG geometry with grating period $\Lambda = 6\,\mu m$. The result is an in-plane, spatially periodic electric field $E = -\nabla\delta V(x)$ that serves as the depinning field and drives the phason.

## 3.4 CDW fluctuation lifetime in cuprates

In this section we discuss how the CDW fluctuation lifetime can be deduced from the phason lifetime. Figure 3.10a, shows the lifetime $\tau_P$ deduced from the fits as a function of temperature. It decreases monotonically from $\tau_P \sim 2\,ps$ at 5 K to $\tau_P < 500\,fs$ at 100 K. There are two mechanisms responsible for the lifetime of the phason: intrinsic damping and the lifetime of the CDW fluctuations. Intrinsic damping occurs owing to the emission of lower-energy phasons or phonons [88] and yields a damping rate $\Gamma_P = 1/\tau_P$ that has been shown to scale as $T^2$ at low temperatures and as $T^5$ closer to $T_{CDW}$ (refs. [88–90]). Plotting the value of $\Gamma_P$ obtained from the fits as a function of temperature in fig. 3.10b on a log-log scale, we observe a crossover from sublinear behavior ($\Gamma_P \propto T^{1/4}$) at low temperatures ($T < 40\,K$) to linear behavior ($\Gamma_P \propto T$) at higher temperatures ($T > 40\,K$), in contrast with theoretical predictions.

Moreover, if the lifetime of the phason were to depend on intrinsic damping only then it should also depend on the wave-vector of the phason since the damping rate of an overdamped mode is dependent on the wave-vector of that mode. To study this, we carried out the experiment in the transient grating geometry at $\Lambda = 2.5\,\mu m$ and found that the TG data matched with the TG data at $\Lambda = 6\,\mu m$ (fig. 3.10c). Thus, the lifetime of the detected phason does not depend on its wave vector for these particular grating spacings.

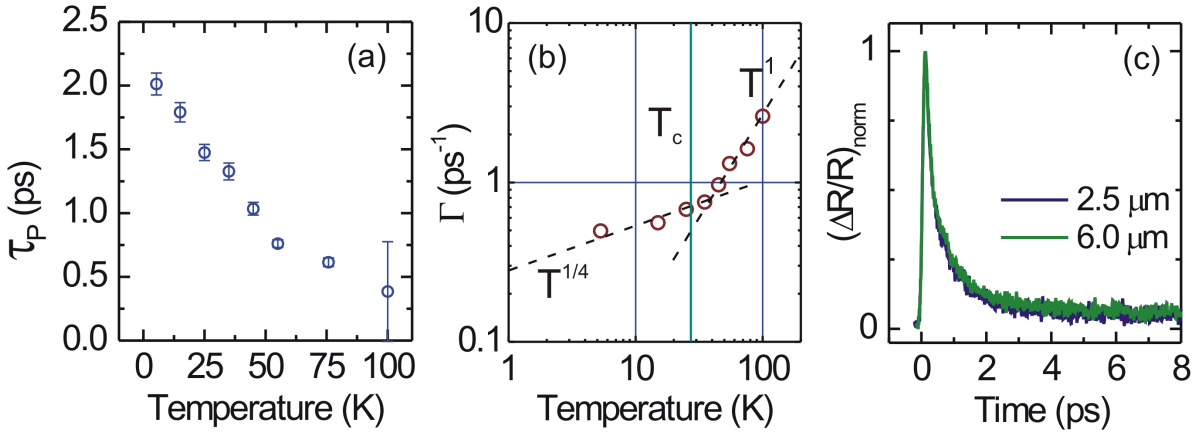


**Figure 3.10:** Analysis of the phason response as a function of temperature and grating spacing. **(a)** The CDW fluctuation lifetime decreases with temperature until it becomes immeasurably short at $T_{CDW}$. Error bars represent the 95% confidence interval (2 s.d.) in extracting the fitting parameters $\tau_P$. **(b)** A log-log plot of the phason decay rate as a function of temperature does not show the $\Gamma_P \propto T^2$ or $\Gamma_P \propto T^5$ behavior expected from intrinsic damping of the phason alone. **(c)** TG data at $\Lambda = 2.5\,\mu$m and at $\Lambda = 6\,\mu$m measured at 5 K

The above findings rule out intrinsic damping as the only source of the lifetime. We therefore posit that the short lifetime of the phason is due to the disappearance of the CDW within its lifetime $\tau_F$. As the charge modulation itself is fluctuating, the elementary excitations of the fluctuating order cannot persist longer than the order itself. Measurement of the phason's temporal evolution thus provides direct access to the temporal evolution of the fluctuating CDW.

## 3.5 Coupling between SC and CDW orders

As seen in fig. 3.8c, the magnitude of the amplitudon experiences an increase as the temperature is lowered into the superconducting region. This is surprising since it suggests that the CDW order gets stronger as the sample enters the superconducting (SC) phase which contradicts the competition scenario. This section describes how this curious behavior can naturally arise within the competition scenario due to the coupling between the SC and CDW order parameters.

It is important to note that similar observations were also made by Hinton et al. [91] on single crystals of the cuprate underdoped YBCO ($YBa_2Cu_3O_{6.67}$). Figure 3.11 compares the magnitude of the amplitudon with temperature in both this work and in [91] as measured using optical pump-probe. The temperature axis is renormalized with respect to the superconducting transition temperature ($T_c$). Despite the big differences in both the stoichiometry and the $T_c$ (26 K in $La_{1.9}Sr_{0.1}CuO_4$ and 67 K in $YBa_2Cu_3O_{6.67}$), in both cases there is a kink in the magnitude of the amplitudon right at $T_c$. Hinton et al. [91] were able to describe this odd but uniform behavior by using a Ginzburg-Landau treatment of coupled order parameters. Within Ginzburg-Landau, the free energy of coupled order parameters can be written as:

$$F(\Phi,\Psi) = -a|\Phi|^2 + \frac{b}{2}|\Phi|^4 - \alpha|\Psi|^2 + \frac{\beta}{2}|\Phi|^4 + \lambda|\Phi|^2|\Psi|^2 \tag{3.1}$$

where $\Phi$ and $\Psi$ are the CDW and SC order parameters, respectively, and $\lambda$ is a constant characterizing the coupling strength between the two orders. In the competition scenario (repulsive interaction), the parameters $a$, $\alpha$ and $\lambda$ are all positive. By minimizing the free energy with respect to the $|\Phi|$, we get the following expression for the equilibrium value of the CDW order parameter:

$$|\Phi_{eq}|^2 = \frac{a - \lambda|\Psi|^2}{b} \tag{3.2}$$

To see how this effects the magnitude of the amplitudon in the presence of SC order, we consider the initial change in $|\Phi|$ following photo-excitation which to first order can be derived as:

$$\delta|\Phi| = -|\Phi_0|\frac{\lambda}{2a}\delta|\Psi|^2 \tag{3.3}$$

where $\Phi_0$ is the equilibrium value of of the CDW order for $\lambda = 0$. Below Tc, due to the photo-excitation, the SC order is suppressed i.e. $\delta|\Psi|^2$ is negative and thus the change in $|\Phi|$ is positive. Due to the DECP mechanism sec. 3.3.1, the magnitude of the amplitudon is directly related to the initial change in $|\Phi|$ which increases across the SC transition due to photoexcitation which explains the observed kinks in fig. 3.11. Moreover, it is

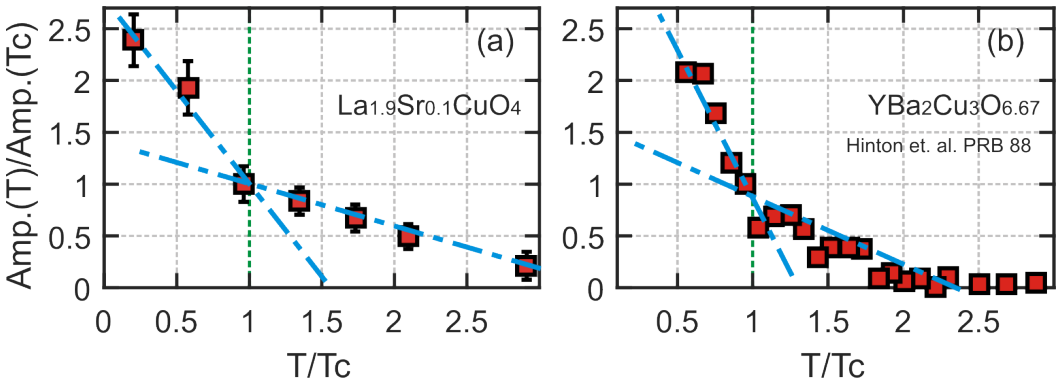


**Figure 3.11:** Normalized magnitude of the measured amplitudon response as a function of $T/T_c$ in **(a)** $La_{1.9}Sr_{0.1}CuO_4$ and **(b)** $YBa_2Cu_3O_{6.67}$. The data in (b) is extracted from [91]. For both cases, the magnitude at each temperature is normalized with respect to the magnitude at the superconducting transition temperature $T_c$. Blue lines are guides to the eye. In both cases, a kink is seen at $T_c$

known [92] that below $T_c$, the photoinduced decrease in the SC order is proportional to $|\Psi|^2$. Thus, the magnitude of the CDW amplitudon is directly proportional to the SC order parameter. This explains the continuous increase in the amplitudon strength for decreasing temperatures below $T_c$.

In summary, we have used ultrafast pump-probe and transient grating methods to observe the presence of fluctuating charge order in thin films of $La_{1.9}Sr_{0.1}CuO_4$ via the amplitudon and phason of the CDW. The amplitudon is observable through an oscillation in the PP reflectivity transients $\Delta R(t)/R$, while the phason is manifested through an additional relaxation component in the TG channel. Our data indicate that $T_{CDW} \sim 100\,\mathrm{K}$ and that the fluctuating CDW lifetime varies from $\tau_F \sim 2\,\mathrm{ps}$ at $5\,\mathrm{K}$ to $\tau_F < 500\,\mathrm{fs}$ at $100\,\mathrm{K}$. These experiments provide the first direct dynamical measurement of modulated charge in cuprates and establish ultrafast spectroscopies as a valuable probe of fluctuating CDW order. Absence of these modes in the optimally doped sample (with a higher Tc) strongly suggests that fluctuating CDW competes with HTS.

## 3.6 Supplementary: Fitting procedures

To extract information about the lifetime and frequency of the amplitudon, we fit the data in the pump-probe (PP) geometry to the DECP functional form:

$$Ae^{-t/\tau_A}\sin(2\pi f_A t) + B(1 - Ae^{-t/\tau_A}\cos(2\pi f_A t)) + \frac{C}{t^{\tau_{th}}} + D\delta(t) + E \tag{3.4}$$

This function was convolved with the Gaussian shape of the laser pulse: $y = e^{-((t-t_0)/\tau_{pu})}$, where $\tau_{pu}$ is the duration of the laser pulse. The first term in eq. (3.4) represents the response of the amplitudon with $A$ as its amplitude, $\tau_A$ as its lifetime and $f_A$. In our fits $B = 0$ and we only use the term in $A$ in the analysis above. The third term is used to model the electronic decay above and below $T_c$. The fourth term is used to isolate the initial fast spike we observe in our data at all temperatures. The last term is a constant used to model any long-lived change in reflectivity.

This fitting equation ensures that we can separate out the amplitudon response from the electronic decay. All of our analysis of the amplitudon is based on the first term in eq. (3.4); the term in $C$ is used only as a phenomenological function to eliminate the background so that we could isolate the oscillating component. We found that the term $\propto C$ provides a better fit to our data than an exponential function. The choice of this function does not affect the measured amplitudon life-time and frequency as their time scales are much different.

To extract information about the phason, we first fit the PP response for 100 K using the phenomenological fit in the second term in eq. (3.4). The resulting fit was then subtracted from the raw TG data (fig. 3.9a) so we could study the TG response independent of the unchanging normal component observed by the PP transients. The resulting TG − PP data is then the response from the overdamped phason and is fitted to a single exponential $Pe^{-t/\tau_P}$.

*"The difficulty really is psychological and exists in the perpetual torment that results from your saying to yourself, "But how can it be like that?" which is a reflection of uncontrolled but utterly vain desire to see it in terms of something familiar."*

— Richard Feynman

# 4

# Valley depolarization in monolayer $MoSe_2$

## Contents



The valley pseudospin in monolayer transition metal dichalcogenides (TMDs) has been proposed as a new way to manipulate information in various optoelectronic devices. This relies on a valley polarization that remains stable over long timescales (hundreds of ns). However, time resolved measurements report valley lifetimes of only a few ps. This has been attributed to mechanisms such as phonon-mediated inter-valley scattering and a precession of the valley psedospin through electron-hole exchange. In this chapter we use transient spin grating to directly measure the valley depolarization lifetime in monolayer $MoSe_2$. We find a fast valley decay rate that scales linearly with the excitation density at different

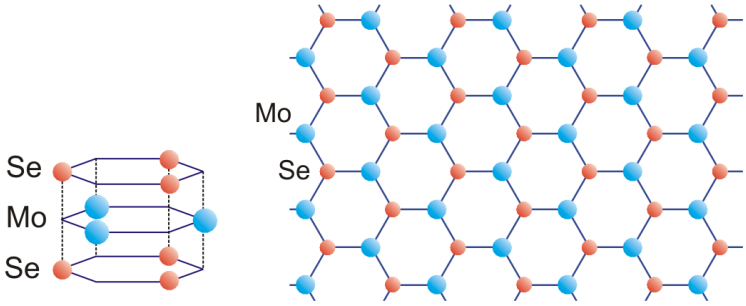


**Figure 4.1:** The honeycomb lattice structure of monolayer $MoSe_2$, the TMD used in this work. The two sublattice sites are occupied by one Mo and two Se atoms respectively which are arranged in a trigonal prismatic structure. Spatial inversion symmetry is explicitly broken.

temperatures. This establishes the presence of strong exciton-exciton Coulomb exchange interactions enhancing the valley depolarization. Our work highlights the microscopic processes inhibiting the efficient use of the exciton valley pseudospin in monolayer TMDs.

## 4.1 Monolayer transition metal dichalcogenides (TMDs)

Monolayer transition metal dichalcogenides (TMDs) are direct-gap semiconductors of the form $MX_2$ where M is a transition metal atom (typically Mo or W) and X is a chalcogen atom (S, Se or Te). Monolayer TMDs $MX_2$ consist of a single layer of M atoms sandwiched between two layers of X atoms to form a 2D hexagonal lattice structure as shown in fig. 4.1. Within this hexagonal lattice, inversion symmetry is broken because the two sublattices are occupied by different type of atoms: one M atom on one sublattice and two X atoms on the other sublattice. The two X atoms are slightly out of the plane of M atoms. In these monolayers, the conduction band (CB) minimum and the valence band maximum (VB) are located at the corners of the hexagonal Brillouin zone (i.e. the K and K' points) (fig. 4.2a). This leads to direct optical transitions in the visible range.

The CB and VB at the K point are mostly composed of $d$-orbitals ($l = 2$) of the transition metal (M) with $m_l = 0$ for the CB and $m_l = 2$ for the VB. The sign of $m_l$ for the VB at the K' point is reversed since K and K' are related to each other by time-reversal. Because of broken inversion symmetry, strong spin orbit coupling (SOC) can split the valence band

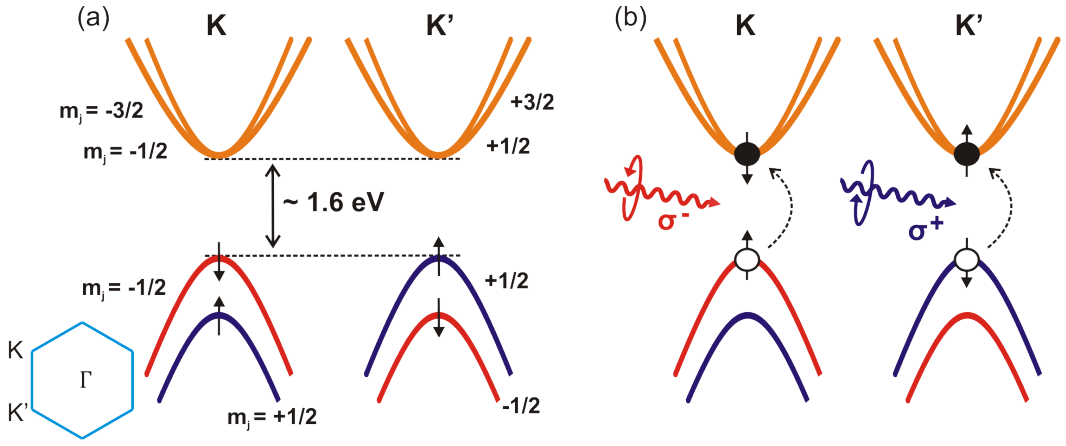


**Figure 4.2:** Schematic of the band structure of monolayer $MoSe_2$ at the K and K' points in the Brillouin zone (lower left). **(a)** The conduction and valence bands are labeled by the z-component of their total angular momentum ($m_j$). The valence band is split due to spin-orbit coupling. The valley and spin degrees of freedom become coupled. The band gap in monolayer $MoSe_2$ is about 1.6 eV. **(b)** Optical selection rules for the A optical transition at the K and K' valleys for circularly polarized light.

ranging from 160 meV in $MoS_2$ to 400 meV in $WSe_2$. Because of the opposite $m_l$ at opposite valleys, the $m_l S_z$ component of the SOC gives a valley dependent splitting of the VB as shown in fig. 4.2a. On the other hand, since the CB is made up of d-orbitals with $m_l = 0$, to first order it remains degenerate. A simple way to describe monolayer TMDs is to use a massive Dirac fermion Hamiltonian with SOC [93]:

$$H = at(\tau k_x \hat{\sigma_x} + k_y \hat{\sigma_y}) + \frac{\Delta}{2}\hat{\sigma_z} - \lambda\tau\frac{\hat{\sigma_z} - 1}{2}\hat{s_z} \tag{4.1}$$

where $a$ is the lattice constant, $t$ the effective hopping integral, and $\Delta$ the energy gap. $\tau = \pm 1$ is the valley index. The Pauli matrices $\hat{\sigma}$ are defined in a basis consisting of the two d-orbitals of the M atom, with $m = 0$ and $m = 2\tau$. $2\lambda$ is the spin-splitting at the valence band top cased by the SOC and $\hat{s_z}$ is the Pauli matrix for spin. The $\tau$ dependence in eq. (4.1) results in the carrier spin index becoming locked to its valley index or polarization. This leads to a valley-dependent selection rule for optical excitation with circularly polarized light: left circularly polarized ($\sigma^-$) and right circularly polarized ($\sigma^+$) excite carriers at opposite K or K' valleys respectively (fig. 4.2b). This valley selective optical transition is similar to the well-known spin optical selection rule in GaAs.

Due to the 2D nature of monolayer TMDs, strong electron-hole interactions give rise to the formation of A and B excitons [94] with very strong binding energies with the A exciton corresponding to the lowest energy transition. In addition, other electron-hole bound quasi-particles such as trions, biexcitons can also exist. It is important to note that the valley selective optical transitions also carry over for these bound particles since the selection rules are nearly exact over a large region around the K and K' valleys [95]. In this way, the valley polarization of excitonic quasi-particles (excitons, trions etc.) can be manipulated to process information in the emerging field of "valleytronics" [15].

The feasibility of these monolayer materials for this field is primarily determined by the valley polarization or inter-valley scattering lifetime i.e. how long it takes particles excited in the K valley to scatter to the K' valley and vice versa. Since this requires a simultaneous spin flip, the valley depolarization time was predicted to be quite long ($\sim$ a few ns) by various photoluminescence (PL) measurements [96–98]. However, a number of time-domain experiments such as transient Faraday [99] and Kerr rotation[100], time-resolved photoluminescence (TRPL) [101–103] and transient reflection and transmission spectroscopy [99, 104–106] have revealed valley polarization lifetimes orders of magnitude shorter ($\sim$ a few ps) than predicted. While there exist several theoretical proposals [107–109] to explain this discrepancy, a consensus has yet to emerge on the exact mechanisms for the fast valley depolarization. An understanding of these is crucial for engineering devices based on valleytronics.

### 4.1.1 Spin decay mechanisms in semiconductors

Two commonly discussed mechanisms to explain spin relaxation in metals and semiconductors are known as Elliot-Yafet (EY) and the D'yakonov-Perel (DP) [110]. In addition, the Maialle-Silve-Sham (MSS) mechanism has been invoked to describe exciton spin/valley relaxation in monolayer TMDs [109]. Below we describe each of these mechanisms.

**Elliot-Yafet (EY) mechanism:** In the EY mechanism [111, 112], carriers can relax their spin via momentum scattering from phonons and impurities. If the scatter induces

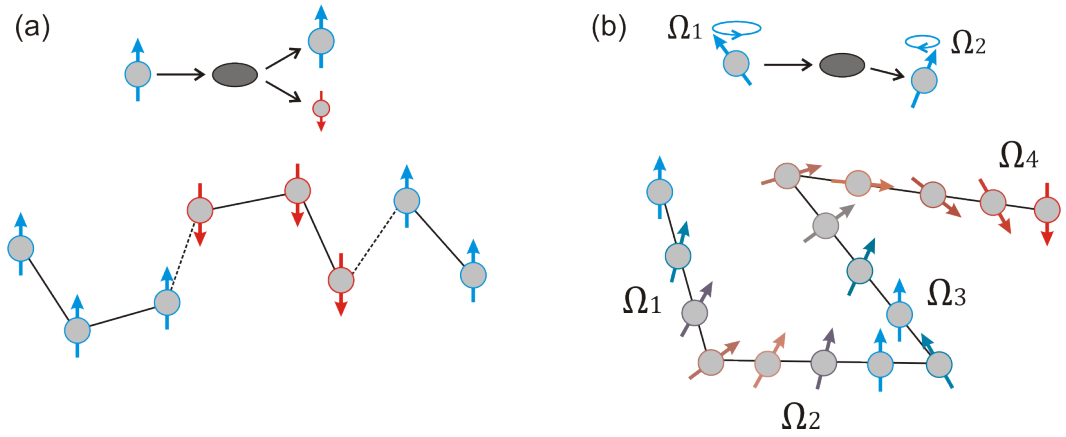


**Figure 4.3:** Schematic of the Elliot-Yafet and D'yakonov-Perel spin relaxation mechanisms. **(a)** The Elliot-Yafet mechanism. Top: the electron wavefunction becomes a mixture of opposite spin states upon momentum scattering. Bottom: the spin-relaxation rate is directly proportional to the momentum scattering rate. **(b)** The D'yakonov-Perel mechanism.Top: The electron spin precesses with frequency $\Omega_1$ which changes to a random frequency of $\Omega_2$ upon momentum scattering. Bottom: the spin-relaxation rate is inversely proportional to the momentum scattering rate.

spin-orbit coupling in the electron wavefunction then the wavefunction acquires a mixture of opposite spin states. This can be seen from the spin-orbit interaction due to the lattice ions:

$$V_{so} \propto \nabla V_{sc} \times \hat{\mathbf{p}} \cdot \hat{\sigma} \tag{4.2}$$

where $V_{sc}$ is the scalar periodic lattice potential, $\hat{\mathbf{p}}$ is the linear momentum operator and $\hat{\sigma}$ are the Pauli matrices. Thus, single-electron wavefunctions are now a mixture of spin-up and spin-down states rather than exact eigenstates of $\hat{\sigma_z}$. The spin can relax at every momentum scattering event and so the spin-relaxation rate ($\Gamma_s$) is directly proportional to the momentum scattering rate ($\Gamma_k$) i.e. $\Gamma_s \propto \Gamma_k$. The EY mechanism is illustrated in fig. 4.3a. In the context of monolayer TMDs, the EY mechanism has been considered by Ochoa et al. [113] to explain the spin/valley relaxation. However, this is predicted to lead to valley decay times in the order of ns [107, 113] rather than the ps time scale observed by time-resolved experiments.

**D'yakonov-Perel (DP) mechanism:** The DP mechanism [114, 115] is used to describe spin relaxation in semiconductors that lack inversion symmetry and have strong spin-orbit coupling. This splits the spin-up and down levels in the conduction band. The resulting splitting acts on the carriers as if an internal, $\vec{k}$-dependent magnetic field would be present

around which the electron spin can precess with a Larmor frequency of $\Omega(\vec{k})$. Spin relaxation then occurs based on momentum scattering of the electrons as described below.

Here we can consider two limiting cases. In case (i), the electron spin precesses many times before its momentum gets scattered i.e. $\Omega_{av}\tau_k \gg 1$ where $\tau_k$ is the momentum scattering time. In this case, spin information is lost at every random momentum scattering event and so like the EY mechanism, the spin-relaxation rate ($\Gamma_s$) is directly proportional to the momentum scattering rate ($\Gamma_k = 1/\tau_k$).

On the other hand, in case (ii) $\Omega_{av}\tau_k \ll 1$. In this case, the electron spin rotates by a small angle about the internal magnetic field before the electron changes its momentum and experiences another field and starts to rotate with another frequency and/or direction. Here, the electron can be thought of as precessing about fluctuating magnetic fields that change randomly within an average time of $\tau_k$, the momentum scattering time. The electron spin thus follows a random walk and the spin relaxation rate can be written as $\Gamma_s = \frac{|\Omega_{av}^2|}{\Gamma_k}$ [110]. This case is what is usually referred to as the DP mechanism and is illustrated in fig. 4.3b. Note that unlike EY, $\Gamma_s \propto 1/\Gamma_k$. This is extremely useful in distinguishing the two mechanisms in experiments.

Since monolayer TMDs lack inversion symmetry and have strong spin-orbit coupling, the DP mechanism was theorized to play a dominant role in the spin/valley relaxation [113]. However, this is again predicted to lead to decay times in the ns [113], orders of magnitude greater than what is observed.

**Maialle-Silve-Sham (MSS) mechanism:** Both the EY and DP mechanisms considered above describe the spin of an individual carrier (electron or hole) and do not take into account strong excitonic effects that are present in monolayer TMDs. One mechanism to describe the overall spin relaxation of excitons is known as the Maialle-Silve-Sham (MSS) mechanism [116]. Here the exchange interaction between electrons and holes in an exciton provides a $\vec{K}$-dependent magnetic field $\Omega(\vec{K})$ around which the overall spin of the exciton can precess. Excitons with different center-of-mass momentums $\vec{K}$ precess with different frequencies and/or directions. Note that this is similar to the DP mechanism but we are

now considering the overall spin of the exciton and the precession frequency of this spin is determined by the Coulomb exchange interaction between the electron and the hole in an exciton. Like the DP mechanism, we can consider two cases. In case (i) or weak scattering $\Omega\tau_k \gg 1$ and so the exciton spin relaxation $\Gamma_s \propto \Gamma_k$. In case (ii) or strong scattering $\Omega\tau_k \ll 1$ and so $\Gamma_s \propto 1/\Gamma_k$. Yu et al. [109] considered the MSS mechanism to describe the fast spin/valley decay of valley polarized excitons in monolayer TMDs. We discuss this mechanism in the context of our results in sec. 4.4.1.

## 4.2 Experimental methods: transient spin grating

To measure the valley depolarization lifetime we perform transient spin grating (TSG) on monolayer $MoSe_2$. TSG has been applied to a number of spin-split electronic systems to reveal spin relaxation times in quantum dots [117, 118] and GaAs quantum wells [119], spin helical modes [120] and spin-diffusion [121] in semiconductor quantum wells. The TSG measurement of spin relaxation in randomly oriented colloidal suspensions of quantum dots [122] demonstrates its unique ability to measure valley relaxation times in CVD-grown monolayer TMDs which inherently have disoriented $\mu$m [123] size domains.

In the TSG technique, two linearly cross polarized pump laser beams with an angle $\theta$ between them interfere on the sample surface to generate a spatially modulated circularly polarized intensity across the excitation spot as detailed in sec. 2.2.3 and in fig. 2.7. Since opposite helicities of light excite particles with opposite valley indices, this generates a spatially modulated valley density of wavelength $\Lambda$ which is referred here as the "valley grating". The decay of this grating directly corresponds to a decrease in the local imbalance between the two opposite polarized valley excitations. This can happen either through valley depolarization (i.e. the K polarized excitations scatter to the K' valley), or through spatial diffusion of the initially spatially separated K and K' excitations. Thus, the valley grating decay rate can be written as [121]:

$$\Gamma = D_v q^2 + \Gamma_v \tag{4.3}$$

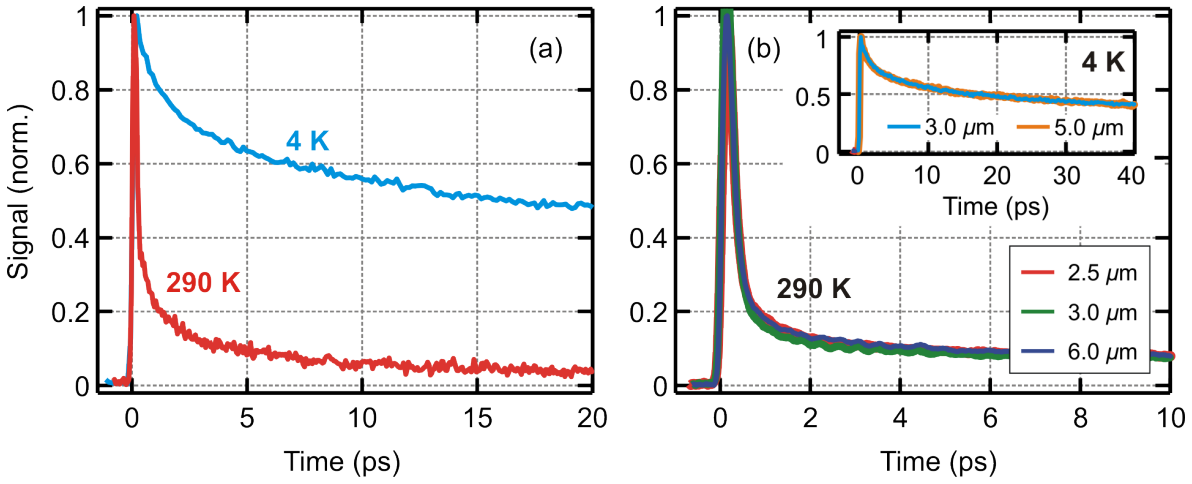


**Figure 4.4:** Transient spin grating (TSG) data on CVD-grown monolayer $MoSe_2$. **(a)** Intensity of the diffracted probe due to the valley grating as a function of the pump-probe delay time at both 290 K and 4 K. **(b)** TSG signal at 290 K for three different grating spacings $\Lambda$. Inset: signal at 4 K for two different $\Lambda$s.

where $D_v$ is the diffusion constant for valley polarized excitations, $q$ is the modulus of the grating wave vector ($q = 2\pi/\Lambda$) and $\Gamma_v$ is the intrinsic valley depolarization rate. To measure the grating decay, a time delayed probe beam with linear polarization impinges on the valley grating as shown in fig. 2.8. The probe beam diffracts of this grating and the intensity of this diffracted beam is detected with time $I_v(t)$ using heterodyne detection fig. 2.8b. In our measurements both the pump and probe beams are set to an energy resonant with the A-exciton transition ($\sim 1.6$ eV) in monolayer $MoSe_2$ [124]. The temporal width of each pulse is $\sim 60$ ps. Full details of the setup can be found in chap. 2.

## 4.3 Valley grating decay in monolayer $MoSe_2$

Figure 4.4a shows the valley grating signal $I_v(t)$ as a function of the time delay ($t$) between the pump and the probe at both 290 K and at 4 K. $t = 0$ refers to the time when the two pump pulses excite the valley grating. The diffracted signal is zero for $t < 0$ but acquires a finite positive value at $t = 0$. The signal then decays back to zero as the valley grating disappears. The overall decay time increases from a few ps at 290 K to tens of ps at 4 K. At both temperatures, the grating decay is much faster than the initially reported ns lifetime for

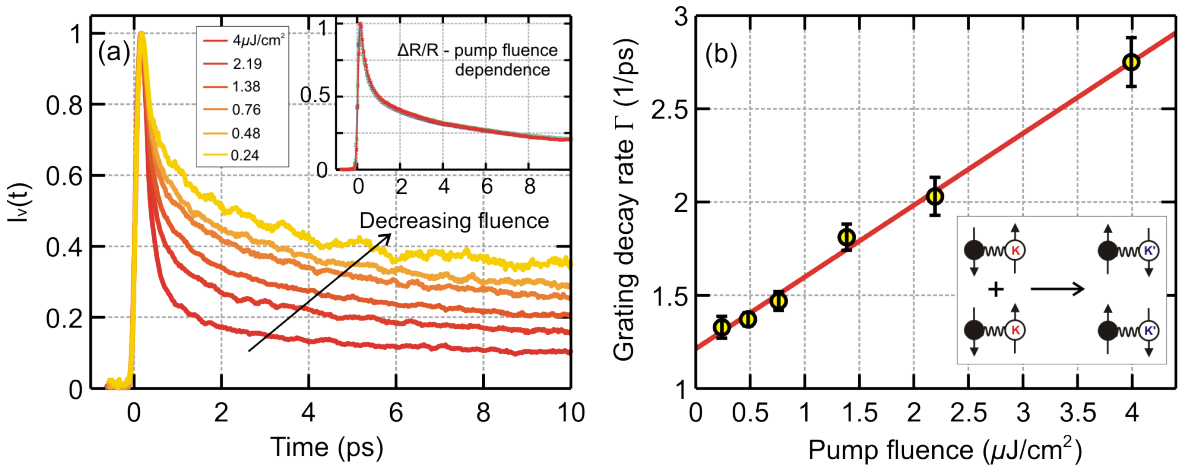


**Figure 4.5:** Effect of excitation density on the valley depolarization. **(a)** TSG signal at different pump fluences. Inset: Fractional change in reflectivity ($\Delta R/R$) of mono-layer $MoSe_2$ for various pump fluences. The data is obtained simultaneously as the TSG signal using a heterodyne detection scheme (chap. 2). **(b)** Grating decay rate as a function of the pump fluence. The rate at each fluence is obtained from fitting the initial slope of the TSG signal in (a). Error bars represent the 95% confidence interval (2 s.d.) in the fitting parameters. Red line is a linear best fit to the data points. Inset: Schematic illustrating the bimolecular process involved in the valley depolarization.

valley polarized excitons using steady-state photoluminescence (PL) measurements [96–98]. It does, however, match the few ps lifetime reported by various time-resolved techniques [99–106]

The larger valley grating lifetime at 4 K when compared with the lifetime at 290 K could either be due to decrease in the diffusion constant $D_v$ with decreasing temperature or a decrease in the valley depolarization rate. To separate out the effects of diffusion and valley relaxation we measured $I_v(t)$ for various values of the grating wavelength $\Lambda$ (fig. 4.4a). As can be seen, $I_v(t)$ is independent of $\Lambda$ at both 290 K and at 4 K indicating that the first term in eq. (4.3) can be neglected. This is not surprising; since the carrier mobility in CVD-grown films of TMDs is typically quite small due to the presence of traps [125, 126], the diffusion rate is expected to be negligible when compared to the valley relaxation rate. Therefore by eq. (4.3), the decay rate of the valley grating $\Gamma$ is a measure of the valley depolarization rate in monolayer $MoSe_2$ ($\Gamma_v$).

### 4.3.1 Effect of exciton density on valley depolarization

Having established that the TSG technique measures the relaxation of valley polarization in monolayer $MoSe_2$, we now proceed to study this relaxation as a function of the initial pump fluence i.e. on the initially excited particle density. While some studies on monolayer TMDs suggest an increase in the depolarization rate with increasing excitation density [99], others report a negligible dependence [100]. Figure 4.5a shows $I_v(t)$ for various pump fluences ($\mathcal{F}$) ranging from $\sim 0.24\,\mu J/cm^2$ to $\sim 4\,\mu J/cm^2$. This corresponds to an exciton density varying from $2.64 \times 10^{10}\,cm^{-2}$ to $4.1 \times 10^{11}\,cm^{-2}$ (sec. 4.5). With decreasing $\mathcal{F}$, i.e. decreasing initial exciton concentration, the transient signal slows down suggesting that the valley depolarization rate ($\Gamma_v$) decreases with initial exciton concentration. To determine whether the fluence dependence is intrinsic to the valley relaxation of the excitons instead of exciton recombination, we plot the optical pump-probe transient reflectivity $\Delta R/R$ (sec. 2.1) of the $MoSe_2$ monolayer for the same pump fluences and energy as the TSG experiment (inset of fig. 4.5a). Transient reflection/transmission of monolayer TMDs in an ultra-fast pump-probe experiments is known to encode the population dynamics of excitons [127–129]. As shown in the inset of fig. 4.5a, $\Delta R/R$ turns out to be independent of the pump fluence indicating that the overall excitation relaxation is independent of the initial density. This signifies that the fluence dependence seen in the TSG signal is intrinsic to the valley degree of freedom, suggesting a valley depolarization mechanism that depends on the initial exciton concentration.

In order to study this further, we extract the initial valley grating decay rate $\Gamma$ and plot it as a function of the pump fluence $\mathcal{F}$ (fig. 4.5b). Remarkably, $\Gamma$ scales linearly with $\mathcal{F}$. This type of linear dependence is typically seen in quasi-particle recombination in high-Tc superconductors ([19] and appendix A) as well as in exciton-exciton annihilation in various semiconductors including monolayer $MoS_2$ [128]. In such bimolecular processes, two exited particles interact with each other to induce a decay in their overall population. Thus, for valley polarized excitons in $MoSe_2$, $\Gamma$ being proportional to $\mathcal{F}$ suggests that two excitons with

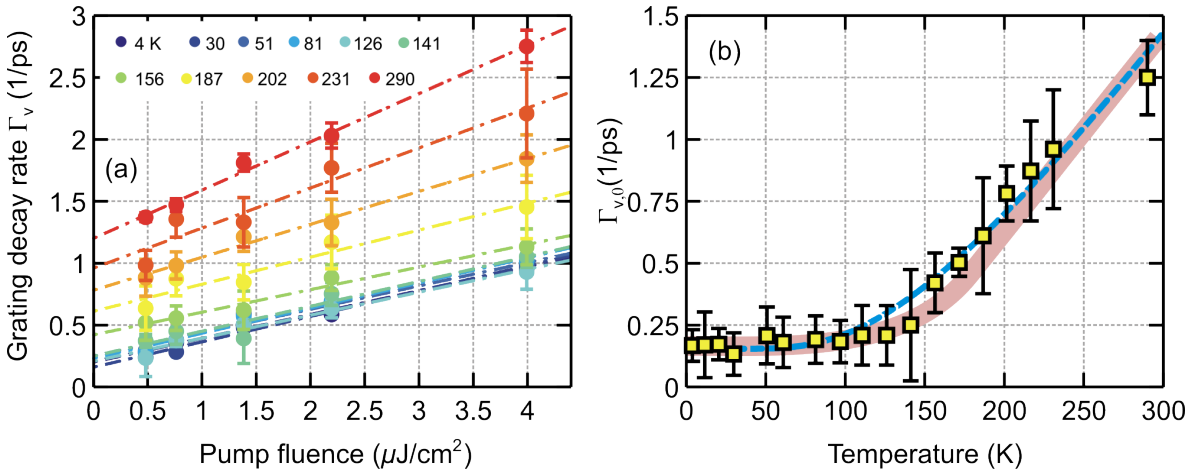


**Figure 4.6:** Effect of temperature on the valley depolarization. **(a)** Grating decay rate as a function of pump fluence for various temperatures. Straight colored lines are linear best fits to the data at each temperature. **(b)** Density independent rate $\Gamma_(v,0)$, obtained from the y-intercept of the linear best fits in (a) as a function of temperature. Error bars represent the 95% confidence interval (2 s.d.) in the fitting parameters. Pink line is a guide to the eye. Dashed blue line is a fit to $\Gamma_{v,0} = A + \frac{B}{\exp(E_p/k_BT)-1}$ with the fitting parameter $E_p = 37 \pm 9\,\text{meV} \sim 300\,\text{cm}^{-1}$.

the valley index (K) interact with each other to produces two excitons with the opposite valley index (K') (inset fig. 4.5b). This establishes the presence of a valley depolarization mechanism in monolayer $MoSe_2$ that depends linearly on the valley polarized exciton concentration.

### 4.3.2 Effect of temperature on valley depolarization

As seen in fig. 4.5b, the $\Gamma$ vs $\mathcal{F}$ plot has a positive non-zero intercept. This also points to a valley depolarization decay process that is independent of the excitation density. Based on this, the valley depolarization rate in fig. 4.5b can be written as:

$$\Gamma_v = \Gamma_{v,0} + \beta n \tag{4.4}$$

where $\Gamma_{v,0}$ is the density independent rate, $\beta$ is a phenomenological constant and $n$ is the valley polarized exciton concentration. $\Gamma_{v,0}$ is simply given by the y-intercept of the straight line in fig. 4.5. Previous studies e.g. [100] have reported this density-independent valley depolarization rate increasing linearly with temperature.

To compare our work with such studies, we took TSG data on monolayer $MoSe_2$ at various different temperatures between 4 K and 290 K. We extract the initial depolarization rate and plot it as a function of pump fluence in fig. 4.6a. The rate scales linearly with fluence for all temperatures with very little change in the slope $\beta$. $\Gamma_{v,0}$ is then extracted from the y-intercept for each trace and the resulting values are plotted as a function of temperature on fig. 4.6b. The density-independent rate is constant at low temperature and increases roughly linearly with temperature for $T > 130$ K. We discuss below (sec. 4.4) the possible origin for this particular temperature behavior in terms of the MSS mechanism.

Here we note that the observed temperature dependence for the valley depolarization can also be described in terms of a phonon-mediated process. For this, we fit the temperature dependence in fig. 4.6b to the following model for phonon occupation:

$$\Gamma_{v,0} = A + \frac{B}{\exp(E_p/k_B T) - 1} \tag{4.5}$$

where $E_p$ is the presumed phonon energy and $k_B$ is the Boltzmann constant. We obtain $E_p = 37 \pm 9$ meV which interestingly is quite close to the measured energies of the optical $A_{1g}$ (29.8 meV) and $E^1_{2g}$ (35.3 meV) phonons in monolayer $MoSe_2$ [130]. This suggests that zone edge phonons might be involved in our observed valley depolarization similar to the decay of pseudospin of resident holes in monolayer $WSe_2$ [131]. We compare this phonon mediated process with the MSS mechanism in the discussion below.

## 4.4 Discussion: mechanisms for fast valley decay

Our experimental results point to three key observations:

1. Fast valley decay in the order of a few tens of ps rather than ns.
2. Density-dependent valley depolarization rate that scales linearly with the excitation density.
3. Density-independent rate that is constant with temperature at low T but increases somewhat linearly with temperature at high T.

Below we discuss these observations in the context of the Maialle-Silve-Sham (MSS) mechanism.

### 4.4.1 Maialle-Silve-Sham (MSS) mechanism

The Maialle-Silve-Sham (MSS) mechanism is described in sec. 4.1.1 and has been proposed by Yu et al. [109] to explain the efficient valley depolarization in monolayer TMDs. In this mechanism excitons with opposite valley polarizations are assigned opposite valley pseudospins. The electron-hole exchange interaction within an exciton provides a momentum dependent magnetic field $\Omega(\vec{k})$ around which the valley pseudospin can precess. Excitons with different center-of-mass precess with different frequencies. Thus any random momentum scattering of the excitons will influence the overall valley depolarization rate. Based on the typically large impurity concentration in CVD grown TMD samples (sec. 4.5), we conclude that our system is in the strong scattering regime i.e. the momentum scattering rate $\tau_k^{-1}$ is much greater than the precession frequency i.e. $\tau_k^{-1} \gg \left\langle |\Omega(\vec{k})| \right\rangle$. In this regime, the momentum of an exciton changes continuously due to various scatterers (e.g. impurities, phonons, excitons) before the valley pseudospin can complete a full precession. Thus, similar to electron spin decay via the D'yakonov-Perel (DP) mechanism [114, 115], the valley depolarization rate scales inversely with the momentum scattering rate:

$$\tau_v^{-1} \propto \langle \Omega^2(\vec{k}) \rangle \tau_k \tag{4.6}$$

While this mechanism correctly predicts a fast valley polarization decay (ps instead of ns) [109], it does not fully explain our observed fluence-dependent valley depolarization. In fact, according to eq. (4.6), with an increase in exciton density i.e. an increase in momentum scattering due to exciton-exciton collisions, one would naively expect a decrease in the valley depolarization rate. However, we observe the exact opposite (fig. 4.5a). Moreover, given that the estimated impurity concentration ($\sim 10^{14}\,\mathrm{cm}^{-2}$) (sec. 4.5) is much greater than the exciton density ($\sim 10^{11}\,\mathrm{cm}^{-2}$), the momentum of an exciton is more likely to change due

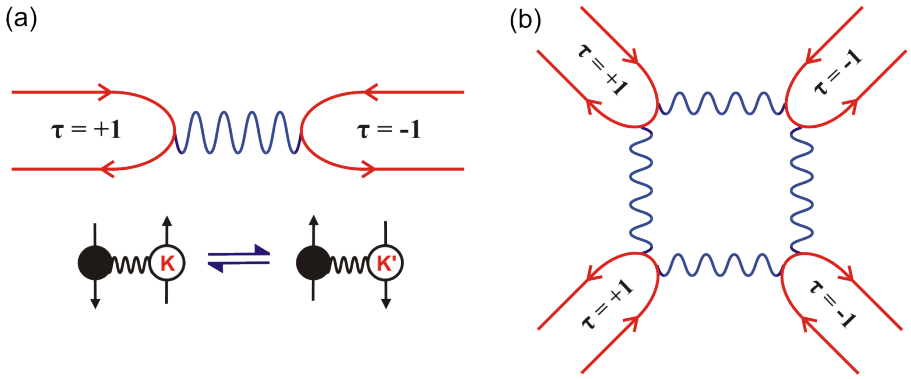


**Figure 4.7:** Electron-hole exchange processes due to Coulomb interactions **(a)** within an exciton and **(b)** between two excitons. $\tau$ denotes the valley index.

scattering with an impurity rather than through exciton-exciton scattering. Thus, eq. 4.6 cannot account for our observed fluence dependence.

To explain this discrepancy, we note that previous literature on the MSS mechanism has only considered e-h exchange interaction within an exciton. This leads to an annihilation of a K-exciton to yield a K'-exciton as illustrated in fig. 4.7a. However, we can also consider the interaction between two K-polarized excitons which will then lead to the annihilation of two K-excitons to generate two K'-excitons as shown in fig. 4.7b. This exciton-exciton interaction mediated valley depolarization scales linearly with the exciton density and thus is a probable explanation for our observed fluence dependence.

To explain the density-independent rate, we note that previous studies e.g. [100] have reported this density-independent valley depolarization as originating from e-h exchange interaction within an exciton as noted above. The observed temperature dependence of this rate can also be explained in terms of the MSS mechanism. If the homogenous or collisional broadening of excitons is greater than their average thermal energy ($\hbar/\tau_k > k_B T$), then the valley depolarization rate should be independent of temperature [100, 108]. Here $\tau_k$ is the average momentum scattering time. This, the low temperature behavior of the valley depolarization is determined by the collisional broadening of the A-exciton. As the temperature increases, the thermal energy becomes comparable to collisional broadening

($\hbar/\tau_k \sim k_B T$) and the resulting thermal variation in th effective magnetic field scales linearly with the temperature i.e. $\langle \Omega^2(\vec{k}) \rangle_T \propto T$. This causes thermal fluctuations in the precession frequency of the valley pseudospin and thus the valley depolarization rate $\Gamma_{v,0} \propto T$ at high temperatures which is consistent with the data.

As noted in fig. 4.6b, the observed temperature dependence can also be described by a phonon-activated process which would suggest that $A_{1g}$ and $E^1_{2g}$ phonons might mediate the observed valley depolarization. This conclusion was reached by Hsu et al. [131] in experiments on monolayer $WSe_2$. However, here we observe a very fast depolarization time on the order of a few tens of ps rather than the ns timescale measured by Hsu et al. [131]. Indeed, theory [107, 109] predicts that phonon-mediated intervalley scattering would yield valley lifetimes much longer than what we observe.

Based on the above we conclude that e-h Coulomb exchange interaction both within and between excitons is a likely explanation for our observed valley depolarization, with the latter significantly increasing the valley decay with increasing exciton density.

## 4.5 Supplementary information

**Extracting decay rates from the TSG data**

To extract the valley grating decay rates we use two different methods. The first method involves fitting the data to a sum of two exponentials:

$$y = A\mathrm{e}^{-t/\tau_{fast}} + B\mathrm{e}^{-t/\tau_{slow}} \tag{4.7}$$

This function is convolved with the Gaussian shape of the laser pulse: $y_{pu} = \mathrm{e}^{-((t-t_0)/\tau_{pu})}$, where $\tau_{pu}$ is the duration of the laser pulse. The first term is the fast component in the valley decay while the second term is the slow component. The results of this fit for the data at $T = 290\,\mathrm{K}$ are shown in fig. 4.8a. The fast ($\Gamma_{fast} = \tau^{-1}_{fast}$) and slow ($\Gamma_{slow} = \tau^{-1}_{slow}$) rates are extracted and plotted in fig. 4.8b. As can be seen, the fast rate scales linearly with pump fluence while the slow rate is fluence-independent (inset of fig. 4.8b).

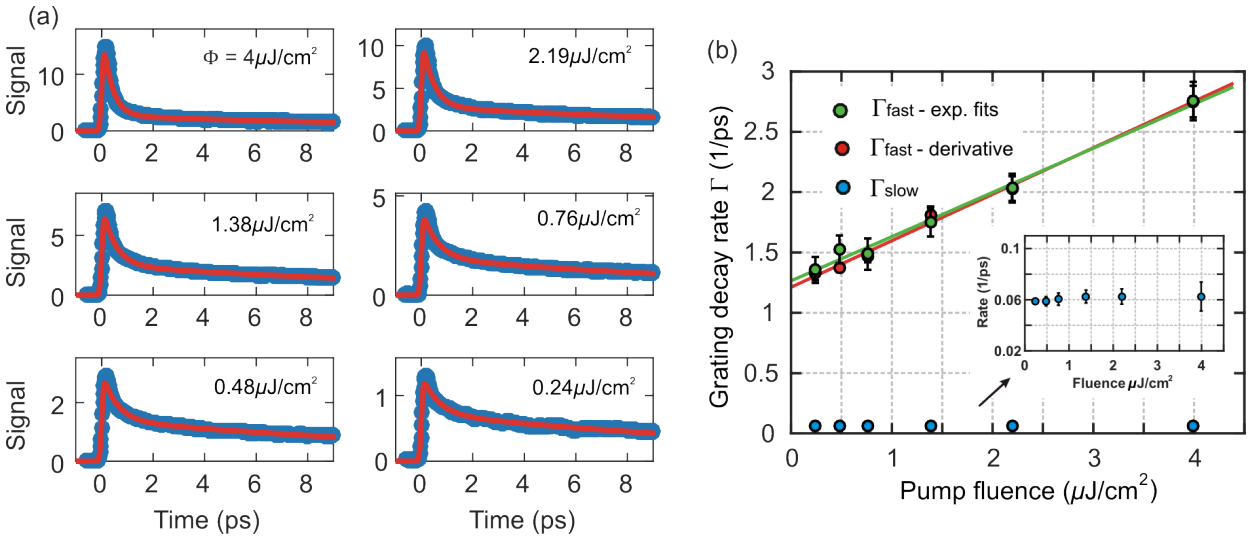


**Figure 4.8:** Double-exponential fits to the TSG data & extraction of fast & slow rates. **(a)** The raw data in fig. 4.5b is fitted to a sum of two exponentials convolved with the Gaussian shape of the pulse width. The raw data is in blue while the fit is in red. **(b)** The fast (green dots) and slow (blue dots) rates extracted from the fits in (a) are plotted as a function of pump fluence. The fast rate extracted from the derivative of the raw data in fig. 4.5b is also plotted (red dots). Inset: zoomed in axis showing that the slow rate is independent of the pump fluence.

The second method simply differentiates the observed normalized TSG signal with time to get the fast rate. Since the TSG signal at all temperatures and fluences consist of a fast, fluence-dependent decay and a slow, fluence-independent decay, differentiation is an easy way to extract the fast rate. We plot the fast rate extracted in this way on top of the rate extracted from exponential fits in fig. 4.8b. As can be seen, there is very good agreement between the two methods. The rates presented in fig. 4.5 and in fig. 4.6 above are extracted from the differentiation method.

**Estimation of exciton density**

To estimate the density of excitons generated by the pump pulse, we take into account the sample absorbance (A) which is estimated to be 5% [132] for free standing monolayer $MoSe_2$. In addition, interference from the sapphire substrate further reduces the effective pump intensity experienced by the monolayer sample by a factor of $4/(1+n_s)^2$ where $n_s = 1.7609$ is the refractive index of sapphire at the pump energy of 1.6 eV. As $n_s > 1$, at the sapphire substrate surface the reflected beam has a phase shit of 180° with respect

to the incident beam leading to destructive interference between the incident and reflected beams and thus, a decrease in the effective pump intensity.

Taking the above into account, the exciton density is estimated as:

$$n_{ex} = \frac{\mathcal{F}}{1.6\,\mathrm{eV}} \times \frac{4}{(1+n_s)^2} \times A \tag{4.8}$$

where $\mathcal{F}$ is the measured pump fluence in $\mu J/cm^2$. This gives an exciton density of $2.64 \times 10^{10}\,cm^{-2}$ to $4.1 \times 10^{11}\,cm^{-2}$ for pump fluences between $0.24\,\mu J/cm^2$ and $4\,\mu J/cm^2$.

**Estimation of impurity concentration** In this work, the term "impurity" refers to any static disorder that scatters the momentum of an exciton. Such defects include charged or neutral impurities and structural defects such as vacancies, dislocations and traps. The average impurity concentration $n_{imp}$ can be estimated from the typical mean free path $l$ of carriers and the scattering cross-section $\sigma$ as:

$$n_{imp} = \frac{1}{l\sigma} \tag{4.9}$$

In 2D, $\sigma = \pi d$ where $d$ is the typical diameter of the scattering center which we take to be on the order of the lattice constant i.e. $d \sim 0.5\,nm$. To determine $l$, we rely on the typical mobility $\mu$ for n-type CVD grown monolayer $MoSe_2$ samples. This has been measured to be up to $60\,cm^2\,s/V$ for films grown under similar conditions [126]. Other works also report similar values for the mobility of CVD grown TMD samples [123, 125, 133]. The mobility $\mu$ can be related to the mean free path by:

$$l = \mu v_{av} m^*/q \tag{4.10}$$

where $v_{av}$, $m^*$ and $q$ are the average velocity, effective mass and charge of the carriers respectively. For n-type $MoSe_2$, we take $m^*$ to be $0.38 \times 9.11 \times 10^{-31}\,kg$ [134] and $q = 1.602 \times 10^{-19}\,C$. $v_{av} \sim v_T$ where $v_T$ is the average thermal velocity of the carriers. Using kinetic theory in 2D, the average thermal velocity is simply given by: $v_T \sim \sqrt{2k_BT/m^*} \sim 10^7\,cm/s$ at $T = 300\,K$. Thus, $l \sim 1\,nm$.

Taking the above estimates into account in eq. (4.9), we conclude that the impurity concentration in our sample is $n_{imp} \sim 10^{14}\,cm^{-2} \gg n_{ex} \sim 10^{11}\,cm^{-2}$.

*"It turns out that an eerie type of chaos can lurk just behind a facade of order - and yet, deep inside the chaos lurks an even eerier type of order."*

— Douglas R. Hofstadter, *Metamagical Themas: Questing for the Essence of Mind and Pattern*

# 5

# Confinement-deconfinement of single-particle excitations in $Na_2IrO_3$

## Contents



In this chapter, we use optical pump-probe and transient grating spectroscopy to observe binding of charged single-particle excitations (SE) in the magnetically frustrated Mott insulator $Na_2IrO_3$. Above the antiferromagnetic ordering temperature ($T_N$) the system response is due to both Hubbard excitons (HE) and their constituent unpaired SE. The SE response becomes strongly suppressed immediately below $T_N$. We argue this increase in binding energy is due to a unique interplay between the frustrated Kitaev and the weak Heisenberg-type ordering term in the Hamiltonian, mediating an effective

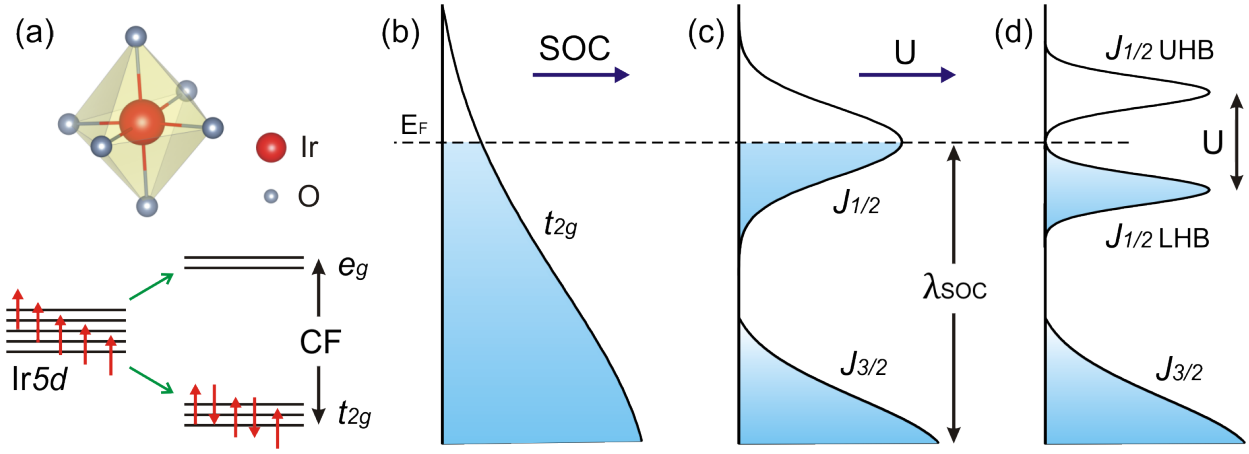


**Figure 5.1:** Electronic structure of iridate-oxides. **(a)** In the Ir-O octahedra, each iridium atoms is surrounded by 6 oxygen atoms such that the Ir $d$-orbitals hybridize with O $p$-orbitals. Crystal field (CF) splitting lifts the degeneracy of the Ir $5d$ states into an empty $e_g$ and **(b)** a wide partially filled $t_{2g}$ band. **(c)** Spin-orbit coupling (SOC) splits the wide $t_{2g}$ into a filled $J_{eff} = 3/2$ band and a narrow half-filled $J_{eff} = 1/2$ band. $\lambda_{SOC}$ indicates the strength of SOC. **(d)** Coulomb repulsion $U$ splits the $J_{eff} = 1/2$ band into a filled lower Hubbard band (LHB) and an empty upper Hubbard band (UHB). This splitting is $\sim 350\,\text{meV}$ in $Na_2IrO_3$.

interaction between the spin-singlet SE. This interaction grows with distance causing the SE to become trapped in the HE, similar to quark confinement inside hadrons. This binding of charged particles, induced by magnetic ordering, is a result of a confinement-deconfinement transition of spin excitations.

## 5.1 Iridate oxides: spin-orbit assisted Mott insulators

Spin-orbit coupling (SOC), the interaction between the orbital angular momentum (**L**) and spin angular momentum (**S**) of an electron, can give rise to a highly non-trivial electronic structure. Notable examples are topological insulators which have a topologically non-trivial band structure due to strong SOC ([135, 136]. In this case, the bulk band gap is determined by SOC and electron-electron Coulomb interactions are ignored. Topological insulators will be the main focus of chap. 8 and will be discussed in detail therein. Here we will focus on materials which have both strong SOC and strong electron-electron interactions.

Prime examples of such materials are the $5d$ iridate oxides that belong to a general class of

transition metal oxides (TMOs). In these oxides, the transition metal (TM) atom is usually surrounded by oxygen ions ($O^{2-}$) in an octahedral cage (fig. 5.1a). Hybridization between the TM $d$-orbitals and oxygen $p$-orbitals lifts the five-fold degeneracy of the $d$-orbitals. This is known as crystal field (CF) splitting and it results in higher energy, two-fold degenerate $e_g$ states and lower energy, three-fold degenerate $t_{2g}$ states (fig. 5.1a). In the case of iridate oxides, the Ir valence is $5d^5$ as the iridium atom transfers its two $6s$ electrons and two $5d$ electrons to oxygen $2p$ states. In this presence of CF splitting, the 5 valence electrons will partially fill the three-fold degenerate $t_{2g}$ states leaving one hole in the $t_{2g}$ band (fig. 5.1b).The large SOC of iridium then splits the $t_{2g}$ band into a fully filled $J_{eff} = 3/2$ band and a half-filled $J_{eff} = 1/2$ band (fig. 5.1c). As a result, this iridate-oxide should be metallic. However, a number of iridate oxides such as $Sr_2IrO_4$ ([137] and $Na_2IrO_3$ [138] have been found to be insulating.

To explain this we have to consider on-site electron-electron Coulomb repulsion $U$. In general a gap opens up if the bandwidth $W$ of the valence band is smaller than $U$ even if the valence band is partially filled. This is the case for Mott insulators [9] which are typically realized in $3d$ TMOs. Here $W$ for the $t_{2g}$ bands is smaller than $U$. This is not the case for $5d$ states as they are more delocalized which lowers $U$ and increases $W$. This should make $5d$ TMOs metallic. However, as discussed above SOC splits the $t_{2g}$ bands to produce a $J_{eff} = 1/2$ valence band which has a much narrower bandwidth that turns out to be smaller than $U$. Thus, a Mott gap opens up which splits the $J_{eff} = 1/2$ band into a fully filled lower Hubbard band (LHB) and an empty upper Hubbard band (UHB) (fig. 5.1d). Thus, the insulating state in $5d$ iridate oxides is Mott like but mediated by spin-orbit coupling. Such a state was first reported by [139] in $Sr_2IrO_4$ in which the Ir-O octahedra form a square lattice similar to the $CuO_2$ plane in cuprates (fig. 3.1). Here we note that in these iridate insulators the Ir-O octahedra have an effective magnetic moment of $J_{eff} = 1/2$ which can interact to produce non-trivial frustrated magnetic systems as is the case for $Na_2IrO_3$ discussed below.

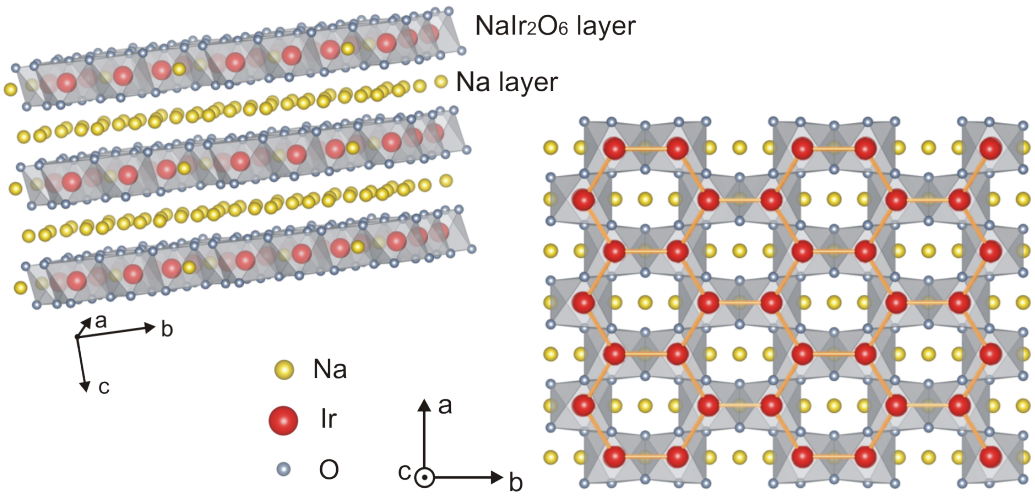


**Figure 5.2:** Crystal structure of $Na_2IrO_3$. (Left) The structure along the ab-plane. (Right) View of the $NaIr_2O_6$ along the c-axis. Drawn using Ref. [43] with crystal parameters from [140].

### 5.1.1 $Na_2IrO_3$: crystal, electronic & magnetic structure

**Crystal structure:** $Na_2IrO_3$ has a monoclinic structure with a C2/m space group ([140]) as shown in fig. 5.2. The quasi-2D structure consists of alternating stacking of a Na-layer and a $NaIr_2O_6$ layer. In the $NaIr_2O_6$ layer edge sharing $IrO_6$ octahedra are arranged in a honeycomb pattern with a Na atom at the center of the honeycomb. Each $IrO_6$ octahedra are connected with three other neighboring octahedra. We will primarily be concerned with this honeycomb arrangement of the $IrO_6$ octahedra.

**Electronic structure:** A number of studies (e.g. [138, 141]) have confirmed that $Na_2IrO_3$, like $Sr_2IrO_4$, is a spin-orbit assisted Mott insulator as described above. The gap between the LHB and UHB has been found to $\sim 350\,\text{meV}$ by ARPES measurements ([141]).

**Magnetic structure:** As discussed above, the interplay between spin-orbit interactions, crystal field splitting and Coulomb repulsion of $5d$ electrons in $Na_2IrO_3$ can lead to a formation of effective magnetic moments with $J_{eff} = 1/2$ on every $IrO_6$ octahedron. The nearest neighbor coupling of these moments is highly anisotropic. Because of this and, given its layered quasi-2D honeycomb lattice structure, $Na_2IrO_3$ was proposed [138, 142–144] to be a solid state realization of the Kitaev model [145] of a spin liquid.

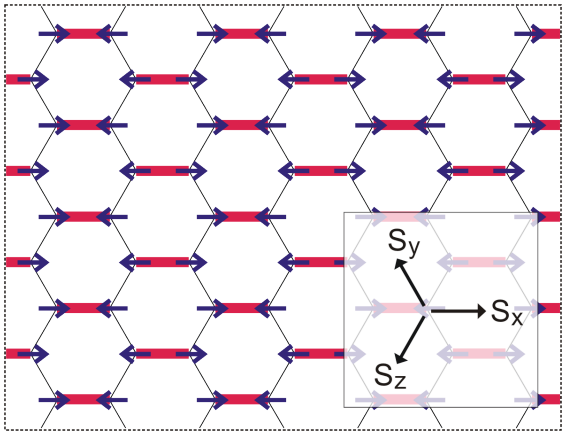


**Figure 5.3:** Sketch representing the zigzag ordered low temperature magnetic ground state in $Na_2IrO_3$. Each site represents the magnetic moment of a $IrO_6$ octahedron. Red bonds connect Kitaev partners while grey bonds have a spin configuration that minimizes the Heisenberg energy.

However, it was soon realized that $Na_2IrO_3$ is not a spin-liquid as neutron studies [140, 146, 147] have revealed an antiferromagnetic ground state of 'zigzag' type (fig. 5.3) with the Néel temperature of $T_N = 15.3\,\mathrm{K}$. A minimal Hamiltonian within the framework of a modified Kitaev model that can give such a ground state consists of an antiferromagnetic Kitaev term and a ferromagnetic Heisenberg term [143, 144, 148, 149]. The Kitaev-Heisenberg (KH) Hamiltonian can be written as [148]:

$$H_{KH} = J_K \sum_{\langle ij \rangle} S_i^l S_j^l + J_H \sum_{\langle ij \rangle} \vec{S}_i \cdot \vec{S}_j \tag{5.1}$$

where the first term in $J_K \approx 10\,\mathrm{meV}$ is the strongly frustrated Kitaev term ($T_\Theta = -125\,\mathrm{K}$), which by itself has a degenerate ground state. The system is unable to choose a particular configuration causing it to stay frustrated. However, after introducing a Heisenberg term (second term in eq. (5.1)) the degeneracy is lifted and the system 'freezes' into an ordered state below temperature $T_N$. In the zigzag order every spin finds its 'Kitaev partner' and anti-aligns itself with the spin of its partner in the direction determined by the orientation of the connecting bond. The much smaller Heisenberg term ($T_N = 15.3\,\mathrm{K}$) tries to minimize its energy under the condition that every spin has a Kitaev partner. As can be seen in fig. 5.3, zigzag order satisfies this condition for all bonds except those that connect Kitaev partners.

Although $Na_2IrO_3$ is not a quantum spin liquid, the fact that the ordering temperature $T_N = 15.3\,\mathrm{K}$ is considerably smaller than both Curie-Weiss temperature $T_\Theta = -125\,\mathrm{K}$) [144] and the spin wave energy $E_{sw} \sim 5\,\mathrm{meV}$ [140], implies that the degree of frustration is still quite strong and the Kitaev term should dominate the low energy physics.

## 5.2 Experimental methods: optical phase separation

We use standard optical pump-probe (OPP) as well as transient grating (TG) spectroscopy to study excitations in $Na_2IrO_3$. As will be discussed below, a 1.55 eV pump beam pulse generates a meta-stable state in $Na_2IrO_3$ with excited electrons in the UHB and equal number of holes in the LHB. This states causes a long-lived transient change in the sample reflectivity ($\delta\tilde{r}$) which can then be tracked using OPP. Given that $Na_2IrO_3$ is insulating, the sample response using TG spectroscopy ($\delta\eta$) is expected to be the same as $\delta\tilde{r}$. This indeed turns out to be the case from the measured data (fig. 5.7). We can thus use TG spectroscopy for optical phase separation as detailed in sec. 2.2.2.

This method, unlike OPP, can distinguish between components of $\delta\tilde{r}$ with different physical origins. We use the '2-point/shaker' scheme (sec. 2.3.4) to isolate the component in eq. (2.10) that depends on the optical phase $\psi$ between the probe and local-oscillator. $\psi$ is varied by controlling the angle $\varphi$ of a glass cover-slip place in the path of the local-oscillator. The time dependence, $\delta\tilde{r}(t)$, of a multi-component system response obtained this way, changes as a function of $\varphi$ eq. (2.12) whereas that of a single-component system just scales proportionally to $\cos(\varphi)$ i.e. $I \propto |\delta\tilde{r_1}|\cos(\phi_1 - \varphi)$.

## 5.3 Photo-induced reflectivity change of $Na_2IrO_3$

In this section we present measurements of the transient reflectivity of $Na_2IrO_3$ using standard OPP as well as optical phase separation. Given the band structure of $Na_2IrO_3$ (sec. 5.1) [141, 150, 151], the absorption of a pump photon with energy 1.55 eV causes an electron to transition from a $J_{eff} = 3/2$ band into the upper Hubbard band (UHB) (fig. 5.4a). This is

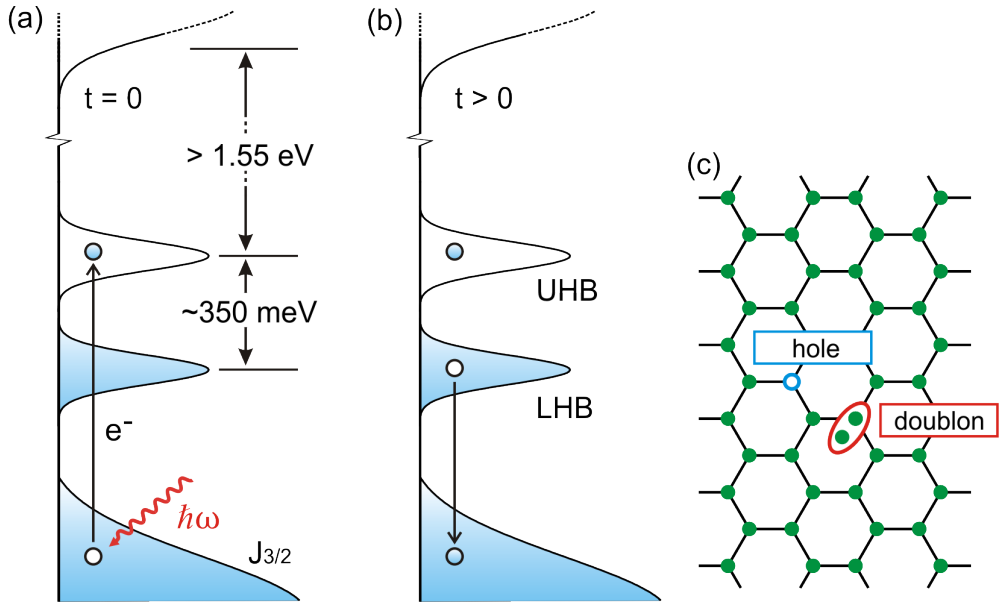


**Figure 5.4:** Photo-excitation of $Na_2IrO_3$ **(a)** Sketch of the band structure of $Na_2IrO_3$ at $t = 0$ illustrating the relevant processes during the photo-excitation with 1.55 eV light. **(b)** Excitation at $t > 0$. The holes in the $J_{eff} = 3/2$ band are filled with electrons from the LHB leaving a metastable excited state. **(c)** real space representation of the state in (b) with double occupancies (doublons) and holes.

possible since this is only accessible level for electrons to transition into at this phonon energy. The holes in the $J_{eff} = 3/2$ band are then quickly filled with electrons relaxing from the UHB and the lower Hubbard band (LHB). This results in some amount of excitations in the UHB and an equal number of holes in the LHB (fig. 5.4b). In real space, this corresponds to double occupancies or 'doublons' at some sites and an equal number of holes on other sites (fig. 5.4c). This excited state is metastable as the optical dipole transitions within the Hubbard band are prohibited by selection rules ($\Delta J = 0$ transition). One way this state can relax is by emission of magnons. However, the energy of the magnons ($\epsilon \approx 5 - 10\,\text{meV} \sim k_B T_\Theta$) [140] is much less than the Hubbard gap ($U \sim 350\,\text{meV}$) which is the energy needed to be dissipated during the doublon-hole recombination process. This makes the lifetime of this metastable stable exponentially large in $U/\epsilon$ [152]. Thus, we can consider holes and doublons as stable quasi-particles for the timescales relevant to our experiments ($\sim 100\,\text{ps}$).

Figures 5.5a and 5.5b show reflectivity transients ($\Delta R(t)/R$) taken using heterodyne

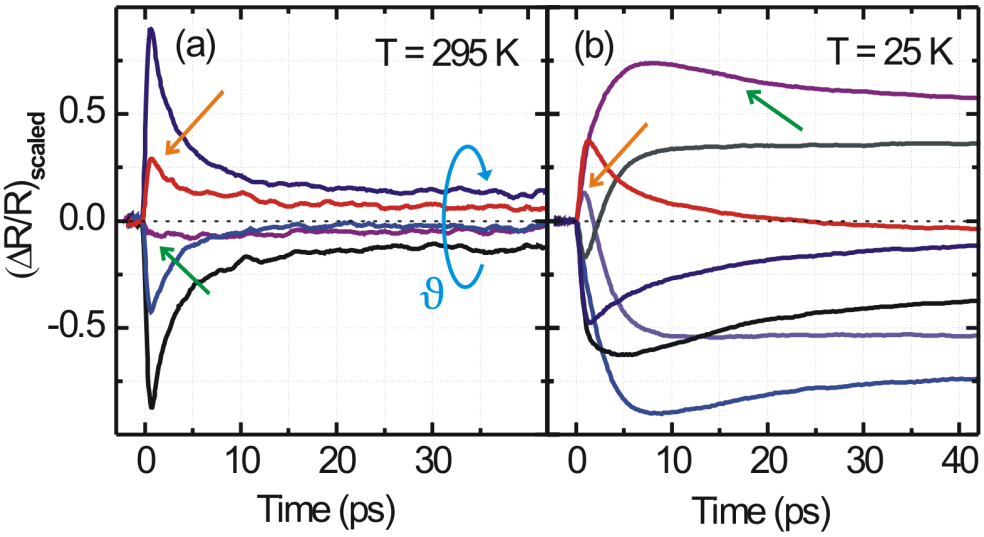


**Figure 5.5:** Reflectivity transients of $Na_2IrO_3$ taken using transient grating for selected values of the cover-slip angle $\varphi$ (see text) at a pump fluence of 9.5 µJ/cm$^2$ at **(a)** 295 K and **(b)** at 25 K. Note the multi-component behavior of the traces as a function of $\varphi$ and the relative weakening of the initial spike (orange arrow) associated with single-particle excitations (SE) at lower temperature and the relative strengthening of the slow component (green arrow) associated with Hubbard excitons (HE).

detection at a pump fluence of 9.5 µJ/cm$^2$ for various values of the cover slip angle $\varphi$ at 295 K and 25 K respectively. At each temperature the shape of $\Delta R(t)/R$ with time changes as $\varphi$ is varied indicating that there is more than one component in the system response. One component appears to be in the form of a sharp spike which decays quickly (orange arrow). The other component has a slow rise and a slow decay(green arrow). The possible presence of two different excitations is in agreement with earlier Resonant Inelastic X-ray Scattering (RIXS) studies [150, 153] which demonstrated that the low energy excitations of $Na_2IrO_3$ are single particle (doublons and holes) excitations (SE) and their bound state known as a Hubbard exciton (HE) [154]. Figure 5.5 demonstrates that the fast spike component near $t = 0$ is clearly stronger at room temperature than at 25 K, allowing us to identify it with SE as HE will thermally disassociate into SE with increasing temperature. This is similar with the results of studies of photo-excited Mott insulators in other systems [154] where the $\Delta R/R$ component with an initial fast spike was shown to be due to SE whereas the slow component

without the fast spike due to HE. It should also be noted that both components (SE and HE) are long lived and thus they both contribute to the long time composition of the total signal.

### 5.3.1 Extraction of Hubbard exciton binding energy

To further confirm the nature of the constituent components of the transient response, we analyze their relative strength as a function of temperature. In the long-time limit, a quasi-thermal equilibrium is established between SE and HE and thus their population ratio should be given by the Boltzmann factor $\exp(-\Delta/k_BT)$ where $\Delta$ is the HE binding energy. In this regime, the net optical phase $\phi$ of the signal response reaches an asymptotic value which is directly related to the quasi-equilibrium population ratio of SE and HE. By net optical phase, we mean the phase of the transient reflectivity ($\tilde{r}$) with respect to the static reflectivity ($\tilde{r_0}$) as detailed in sec. 2.2.1. By studying this value as function of temperature it is possible to deduce the dependence of the SE/HE population ratio on temperature and check if it is actually following the Boltzmann activation law above. This also allows us to extract the numerical value of the exciton binding energy.

The time dependence of the total phase of the signal $\phi$ at different temperatures is shown in fig. 5.6a. As can be seen, the initial ($t \to 0$) phase at different temperatures is roughly the same. This is consistent with the conclusion that immediately after the pump pulse the excitations are mostly overheated SE particles which later cool down and form Hubbard excitons. Another observation is that the $\phi$ approaches an asymptotic value at long times. The temperature dependence of this asymptotic phases relative to the initial value is shown in fig. 5.6b. In the zero-temperature limit, the signal should exclusively be due to excitons which allows us to determine the phase of the excitonic component at higher temperatures. In our case, this turns out be roughly $-\pi/2$ (fig. 5.6a). This is the value we adopted for further fitting to keep the expressions simpler. Following the phasor diagram for the total signal in the inset to fig. 5.6b we can express the phase $\phi$ of the signal in terms of strengths

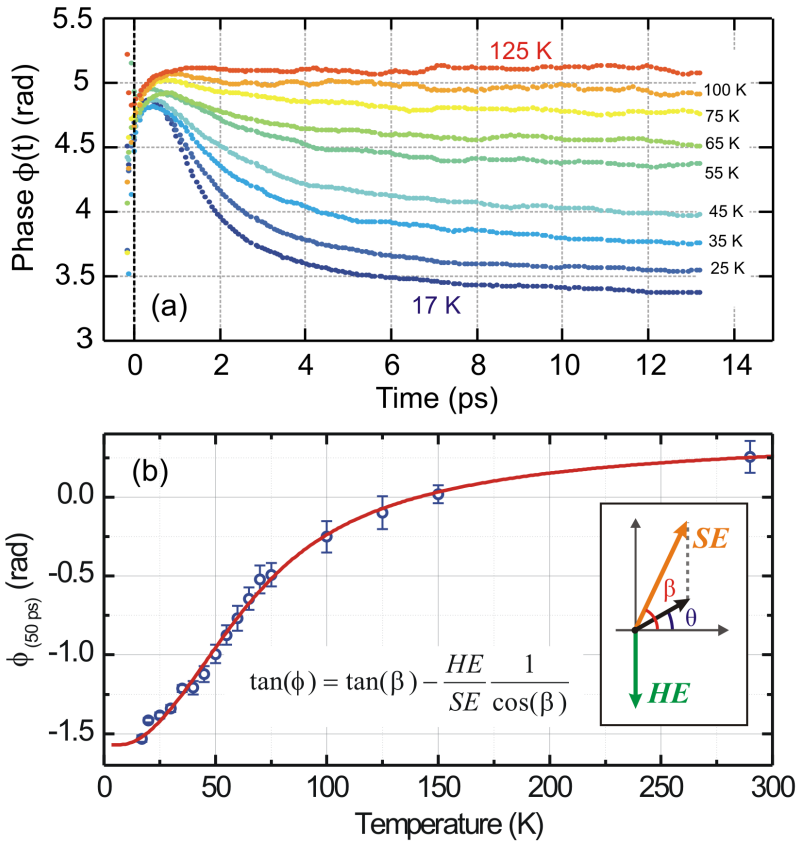


**Figure 5.6:** **(a)** Optical phase of the reflectivity transients $\phi(t)$ of $Na_2IrO_3$ at temperatures from 17 K to 125 K. **(b)** $\phi$ of the total signal at $t \approx 50$ ps in the quasi-equilibrium state as a function of temperature. Error bars represent the 95% confidence interval (2 s.d.) in extracting the phase. Solid red line is a fit to the data based on the Boltzmann distribution of SE and Hubbard exciton (HE) populations, $SE/HE \propto \exp(-\Delta/k_BT)$. The fit equation is given by eq. (5.2). Inset: phasor diagram representing quasi-equilibrium $\delta\tilde{r}$ (black phasor) due to SE and HE.

and phases of individual components assuming the phase of HE component is equal to $-\pi/2$:

$$\tan\phi = \tan\beta - \frac{\mathrm{HE}}{\mathrm{SE}}\frac{1}{\cos\beta} \tag{5.2}$$

where $\beta$ is a fitting parameter and is the phase of the SE component in thermal equilibrium. The ratio HE/SE denotes the population ratio between Hubbard excitons and single-particle excitations which is simply given by the Boltzmann factor $\exp(-\Delta/k_BT)$. By fitting the data in fig. 5.6b to this equation we can extract $\Delta$, the HE binding energy. The fits gives $\Delta \approx 4.6 \pm 0.8$ meV and $\beta \approx \pi/3$. Note that in the above analysis we assumed that the optical phase of the individual components (i.e. $\pi/2$ for HE and $\beta$ for SE) does not

change with temperature. The total phase of the signal changes with temperature due to a changes in the relative populations of HE and SE. The extracted value of $\Delta$ is within the bounds set by RIXS measurements [150] and confirms that the component featuring a fast spike at $t = 0$ is indeed due to SE.

### 5.3.2 Disappearance of single-particle excitations below $T_N$

Having confirmed that our response is sensitive to both SE anf HE, we now study how the response changes across the magnetic ordering temperature ($T_N = 15.3\,\mathrm{K}$) in $Na_2IrO_3$. Figure 5.7a and 5.7b show the reflectivity transients with different cover-slip angles $\varphi$ taken for a very low pump fluence of value of $9.5\,\mathrm{nJ/cm^2}$ at temperatures above and below $T_N$ respectively. Similar to the higher fluence data, the low fluence response above $T_N$ (fig. 5.7a) clearly features more than one component indicating the presence of both SE and HE. On the other hand, the low fluence response below $T_N$ (fig. 5.7b), strikingly, scales proportionally to $\cos(\varphi)$ implying a single component behavior which, as discussed above, is due to Hubbard excitons.

We now switch to standard OPP measurements to study this disappearance of SE as a function of temperature. We limit to low excitation densities to minimize heating effects. Figure 5.7d shows reflectivity transients for various temperatures below $T_N$ for two different pump fluences. As can be seen, the normalized system response in this regime is independent of temperature and also of pump fluence demonstrating that the single component behavior (HE) observed at $T = 5\,\mathrm{K}$ (fig. 5.7b) persists up to $T_N$. This indicates that SE are suppressed throughout the magnetically ordered phase. On the contrary, reflectivity transients right above $T_N$ (fig. 5.7c) strongly depend on temperature, which combined with the room temperature data (fig. 5.5a), indicate the formation and strengthening of the component due to SE. Moreover, above $T_N$, the normalized transients at each temperature are independent of pump fluence (fig. 5.7c) demonstrating that the relative composition of the signal (ratio between SE and HE populations) is constant as a function of pump fluence in this low

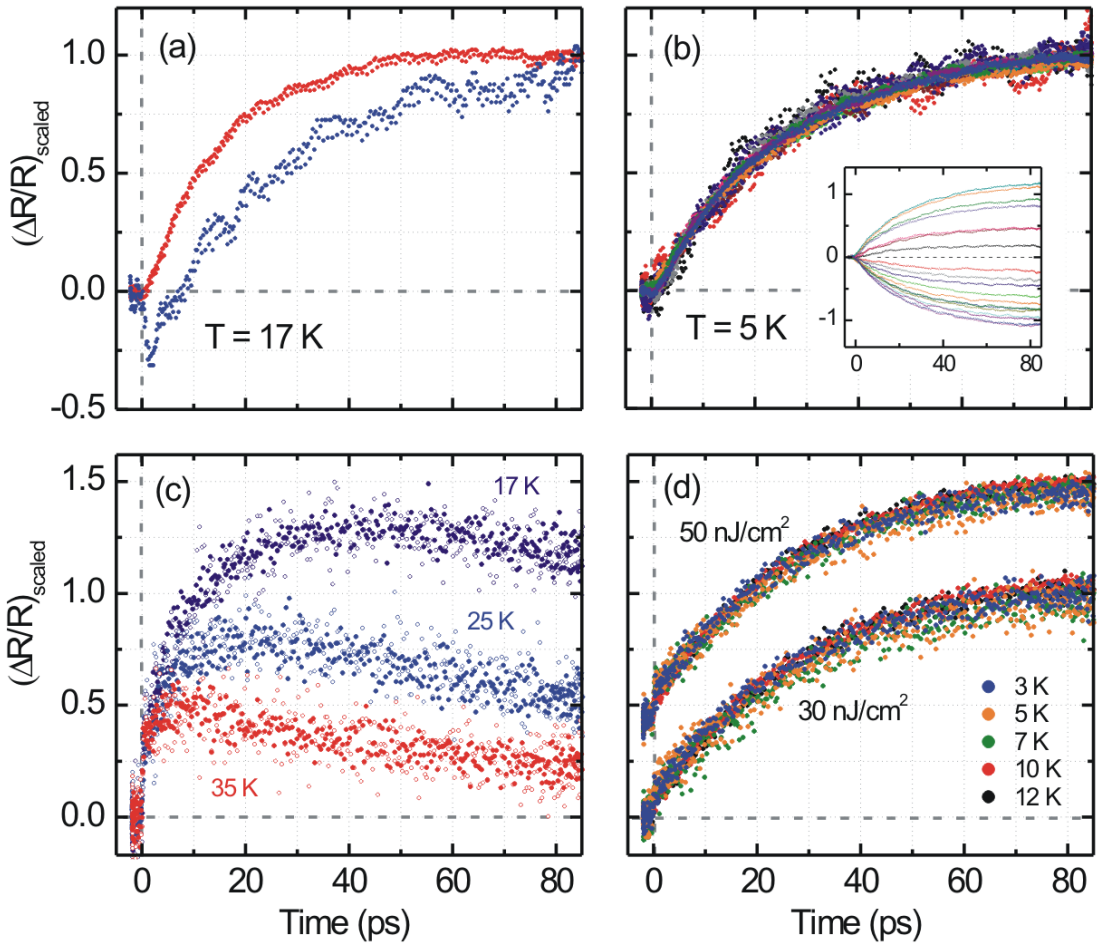


**Figure 5.7:** **(a)** Representative $\Delta R/R$ taken with transient grating (TG) at $T = 17\,\mathrm{K}$ for two different cover-slip angles $\varphi$ at a pump fluence of $30\,\mathrm{nJ/cm^2}$. The traces exhibit qualitatively different shapes indicating the presence of both SE and HE. Note the fast spike around $t = 0$ for the purple curve. This is a signature of SE (see fig. 5.5). **(b)** TG data at $T = 5\,\mathrm{K}$ for 19 different values of $\varphi$ at a pump fluence of $30\,\mathrm{nJ/cm^2}$, scaled to emphasize the single component (HE) nature of the response; inset: unscaled TG traces. **(c)** Scaled $\Delta R/R$ traces for temperatures above $T_N$ ($T = 17\,\mathrm{K}$, $25\,\mathrm{K}$ and $35\,\mathrm{K}$) at different fluences: $100\,\mathrm{nJ/cm^2}$ (filled markers) and $50\,\mathrm{nJ/cm^2}$ (open markers). This data is taken using standard optical pump-probe. Note the strong temperature dependence and the lack of fluence dependence in this limit. **(d)** $\Delta R/R$ traces for temperatures below $T_N$, scaled to emphasize the universal behavior of transient traces. Upper curve: $50\,\mathrm{nJ/cm^2}$, lower curve: $30\,\mathrm{nJ/cm^2}$. Curves at different fluence values are shifted for better clarity.

excitation density regime. This sudden disappearance of SE below $T_N$ suggests a sharp increase in the HE binding energy associated with the onset of a magnetic order.

### 5.3.3 Fluence dependence in the vicinity of $T_N$

The observed suppression of SE could also be due to a simple thermal suppression governed by the Boltzmann factor $\exp(-\Delta/k_BT)$ rather than a sudden increase in the HE binding energy. This Boltzmann temperature dependence exhibits a strong exponential rise in the excitation population which can be mistaken for a phase transition if not studied right in the vicinity of the transition temperature. To resolve this issue we compare the fluence dependence of the OPP signal in the vicinity of $T_N = 15.3\,\mathrm{K}$. We picked two temperatures: $T = 14.5\,\mathrm{K}$ (fig. 5.8a), which is slightly below the transition temperature, and $T = 17.3\,\mathrm{K}$ (fig. 5.8b), which is slightly above.

Immediately after $t = 0$, the system is at a higher temperature than equilibrium due to laser-induced heating. If the reported change in the pump-probe transients with rising temperature is solely due to the thermal dissociation of excitons then the effects of laser heating should be similar at temperatures slightly above and below $T_N$. In fact, the effects of laser heating should be more pronounced at $T = 17.3\,\mathrm{K}$ since the derivative of the expression $\mathrm{e}^{-\Delta/k_BT}$ with respect to temperature is a monotonically growing function of $T$. Moreover, the heat capacity at $T = 14.5\,\mathrm{K}$ is known to be larger than that at $T = 17.3\,\mathrm{K}$ (due to the closer vicinity of the former to $T_N$) [138].

However, the observed behavior of the pump-probe transients in the vicinity of $T_N$ is quite different. As shown in fig. 5.8b, at sufficiently low fluences, the $T = 17.3\,\mathrm{K}$ data does not show any dependence on pump fluence. While for the same pump fluence values, the $T = 14.5\,\mathrm{K}$ data (fig. 5.8a) exhibits a clear transition behavior: It changes from the high temperature non-monotonic regime at higher fluences towards a monotonic regime associated with the ordered phase in the limit of low fluences. Moreover, it should be noted that for low temperatures when the ordering is strong enough there is no fluence dependence (fig. 5.7d) indicating that the effects of laser heating are only noticeable around $T_N$ in the low fluence

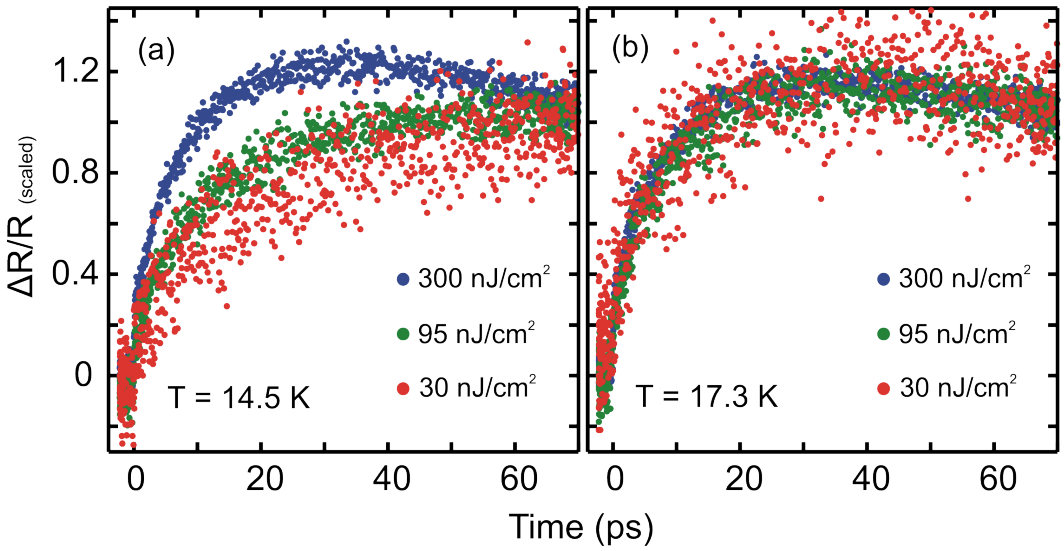


**Figure 5.8:** Comparison of the fluence dependences of the OPP traces for the temperatures slightly **(a)** below $T_N$ (at $T = 14.5\,\mathrm{K}$) and slightly **(b)** above $T_N$ (at $T = 17.3\,\mathrm{K}$). Strong fluence dependence at temperatures below and close to $T_N$ indicates the presence of a phase transition rather than a simple thermal suppression of single particle excitations.

regime. This further confirms that, instead of a simple thermal suppression of the SE, an abrupt increase in the HE binding energy is taking place at $T_N$.

## 5.4 Discussion: confinement-deconfinement transition

The key observation from our experiments is a complete disappearance of single-particle excitations (SE) in favor of Hubbard excitons (HE) right at the onset of magnetic order in $Na_2IrO_3$. This implies a sudden increase in the HE binding energy due to the order. This section discusses possible reasons for this increase.

In general an increase in binding energy of an exciton can be either due to an enhancement of the attracting potential of its constituents or due to a 'slowing down' of the overall dynamics. Slowing down can occur if the effective mass of the constituent doublon and/or holes is increased. Indeed, the effective mass of a single hole in a Mott insulator can be enhanced due to the emission of magnons, but this should happens in both the ordered and disordered phases [155] i.e. both above and below $T_N$. More importantly, it is known that the bandwidth of SE

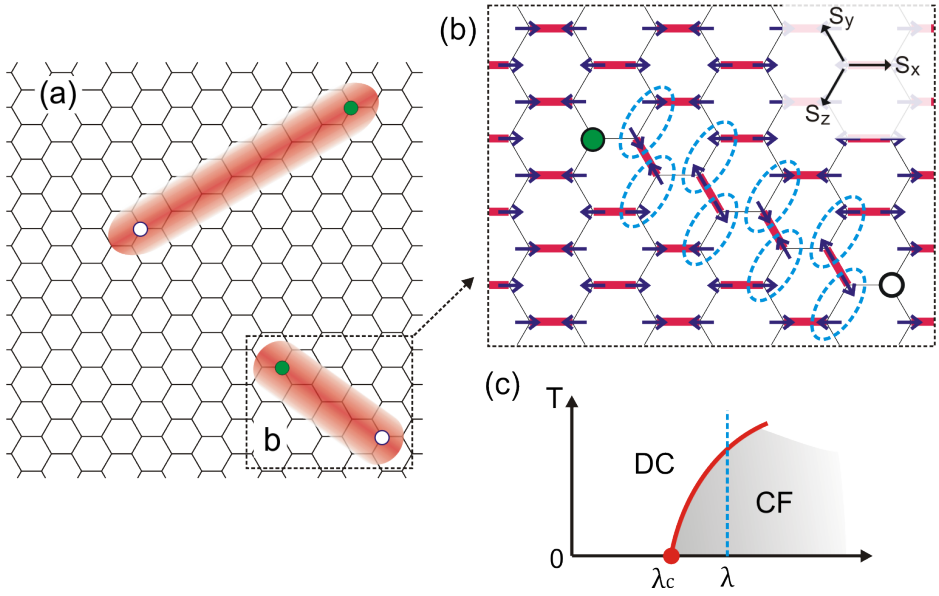


**Figure 5.9:** **(a)** Schematic view of an excited sample. Green dots correspond to doublons while the white dots represent holes. The shaded red area marks the region where the spins are affected by the reconstruction i.e. the 'string'. **(b)** Simplified representation of the restructured state with singlet defects (hole or doublon). The Heisenberg energy along the bonds highlighted by purple ovals is not minimal anymore. The string composed of such bonds must begin and end on a defect. **(c)** Cartoon of a phase diagram of modified Kitaev model with a first-order quantum critical point and a phase boundary between confined (CF) and deconfined (DC).

in $Na_2IrO_3$ is $\gtrsim 100\,\text{meV}$ ([150]) which is much greater the Heisenberg coupling responsible for magnetic ordering ($\sim k_B T_N \approx 1\,\text{meV}$). Thus, it is unlikely that the SE 'slows down' due to the onset of magnetic order. Based on this, we conclude that the binding energy of HE is a result of enhancement in attraction between single-particle excitations.

Here we present a simple intuitive picture based on the Kitaev-Heisenberg model (sec. 5.1.1) to describe the increase in the effective attraction between single-particle excitations. As discussed earlier (fig. 5.3), in zigzag order every spin finds its 'Kitaev partner' and anti-aligns itself with the spin of its partner in the direction determined by the orientation of the connecting bond. This situation changes drastically when spinless defects such as doublons or holes are introduced into the system. The spins that have lost their Kitaev partners reorganize the surrounding spin order at the expense of Heisenberg energy (fig. 5.9). Re-oriented spins form a string terminating on the other defect. The

energy cost of this configuration is proportional to the number of broken Heisenberg links which in turn is proportional to the length of the string connecting the two defects. This prohibits the long range separation of the defects which, in the case of low excitation density, will predominantly be of opposite charges (doublon-hole), leading to an enhanced binding between them in addition to Coulomb attraction. This is similar to the picture of the quark confinement in high energy physics [156]: separation of defects produces a string of perturbed vacuum between them with an energy proportional to its length. However, since breaking of this string in our case produces a pair of electrically neutral unpaired 'dangling' spins (which are confined), the binding energy between doublons and holes is limited by the cost of breaking a Kitaev pair, which is of the order of Kitaev coupling $J_K \approx 10\,\text{meV}$ in case of $Na_2IrO_3$. Based on the above discussion, we interpret our observations as an effective confinement-deconfinement transition of single-particle excitations.

This interpretation is consistent with previous theoretical works on Kitaev-Heisenberg model where it was observed that for sufficiently weak perturbations the Kitaev spin liquid state persists but as the extra term (Heisenberg) gets stronger the system enters an ordered state [142, 143, 157]. Formulated in terms of spinons this corresponds to the transition from a deconfined state (spin liquid) to a confined state (magnetically ordered) [157, 158]. Strictly speaking, a confinement-deconfinement is studied at $T = 0$ by tuning the strength ($\lambda$) of the Heisenberg perturbing term across a critical value $\lambda_c$ [157, 158]. However, we note that the transition from a deconfined state to a confined state is a first order phase transition [157, 158] and thus the two phases are separated by a simple boundary at finite $T$ and at $\lambda > \lambda_c$ [159] (fig. 5.9c). Therefore, the confinement-deconfinement transition can also be observed by going across the ordering temperature ($T_N$) for a fixed $\lambda > \lambda_c$. In the confined phase, all fractional excitations such as holons, doublons and spinons are bound to each other, and conversely, can move independently in the deconfined phase [160].

In conclusion, we performed an optical pump probe study of $Na_2IrO_3$, a material proposed to be a realization of the Kitaev model. We observed that photo-induced charged excitations display drastically different behavior below and above the Néel ordering temperature. Namely

the binding energy of the excitons that these particles form undergoes a sharp increase upon entering the ordered phase. Based on earlier theoretical studies on doped Mott insulators, we conjecture that this is due to an effective attraction brought about by the antiferromagnetic order rather than because of increase in effective mass of quasiparticles. We argue that this attraction is a manifestation of confinement of spin excitations anticipated in the ordered phase of the Kitaev-Heisenberg model.

*"Well, as it turns out, that's the world. All these incredibly complex, inscrutably intertwined Rube Goldberg machines that can only be seen in retrospect when something happens."*

— Adam Felber, *Schrödinger's Ball*

# 6

# Time & angle resolved photo-emission spectroscopy

## Contents



## 6.1 ARPES: overview & basic theory

This section gives a brief overview of angle-resolved photoemission spectroscopy (ARPES) which is a common technique to investigate the band structure of solids i.e. the relationship between energy $E$ and momentum $k$ of electrons inside the solid. In general, ARPES is based on the photoelectric effect and consists of photo-emitting electrons from a sample

with light of energy $\hbar\omega > \phi$ where $\phi$ is the work function of the sample. By energy conservation, the kinetic energy $E_k$ of a photo-emitted electron can be written in terms of the binding energy $E_B$ it had inside the solid:

$$E_k = \hbar\omega - \phi - E_B \tag{6.1}$$

here $E_B$ is typically defined with respect to the sample Fermi level $E_F$ i.e. $E_B = E_F - E$, which at $T = 0\,\mathrm{K}$ is equal to the chemical potential. In this work we use the two terms interchangeably for simplicity. Figure 6.1a illustrates a schematic of the kinetic energy spectrum that is typically measured in terms of the electron energy distribution inside the solid. Once $\phi$ is known, the energy spectrum of the solid can be worked out. For most metals, $\phi$ is between 4 eV and 5 eV, necessitating that UV light is used in ARPES experiments. The greater the energy of the light, the greater the binding energy that can be probed.

The electron momentum inside the solid is determined by measuring both the azimuthal $\varphi$ and polar $\theta$ angle at which the electron is photo-emitted as illustrated in fig. 6.1b. During the photo-emission process, the in-plane electron momentum ($k_\parallel$) is conserved since translational symmetry is not broken in the direction parallel to the surface. This implies that the measured in-plane electron momentum is the same as the in-plane electron momentum inside the sample. Thus, $k_\parallel$ is given by:

$$k_\parallel = \frac{\sqrt{2m}}{\hbar}\sqrt{E_k}\sin\theta \tag{6.2}$$

The coefficient $\frac{\sqrt{2m}}{\hbar} = 0.512\,\text{Å}^{-1}\text{eV}^{-1/2}$. From here, $k_x = k_\parallel\cos\varphi$ and $k_y = k_\parallel\sin\varphi$. On the other hand, the out-of-plane momentum $k_z$ is not conserved since translational symmetry is broken in a direction perpendicular to the sample. Relating $k_z$ to the measured out-of-plane momentum $k_{z,m} = \frac{\sqrt{2m}}{\hbar}\sqrt{E_k}\cos\theta$ is non-trivial and relies on varying the incident photon energy. Determining $k_z$ is beyond the scope of this thesis since we are mainly concerned with determining the dispersion of surface states which have $k_z \sim 0$.

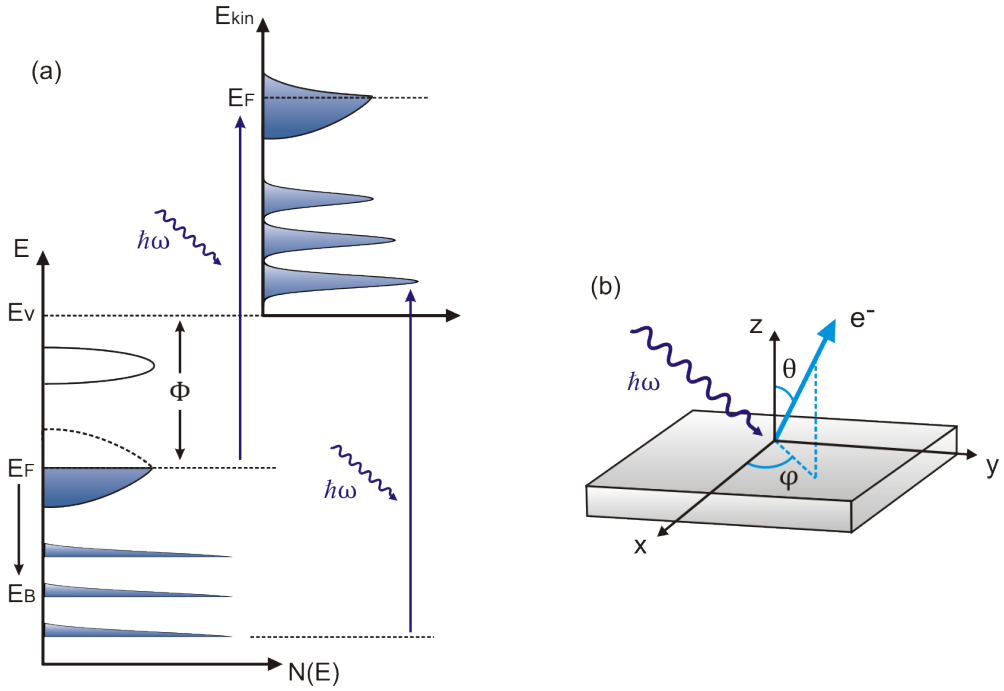


**Figure 6.1:** **(a)** Schematic of the density of states $N(E)$ of electrons inside the solid (left) and as measured by the detector (right). $E_v$, $E_F$ and $E_B$ denote the vacuum level, the Fermi level and the binding energy of electrons inside the solid respectively. $\phi = E_v - E_F$ is the sample work-function. Only occupied states are accessible. Figure adapted from [161]. **(b)** The electron in-plane momentum is determined by measuring the azimuthal $\varphi$ and polar $\theta$ angle at which the electron is photo-emitted.

An ARPES experiment measures the intensity distribution of electrons at various values of $\mathbf{k}_\parallel$ and energy $E$. In the absence of interactions, this distribution can be written as:

$$I(\mathbf{k}_\parallel, E) \propto I_0(\mathbf{k}_\parallel, E, \mathbf{A}) f(E) \otimes R(\Delta k, \Delta E) \tag{6.3}$$

where $I_0$ is known as the matrix-element term and describes the transitions between initial and final states of photoemission as discussed below. $f(E)$ is simply the Fermi-Dirac distribution i.e. $f(E) = 1/(e^{E/k_BT} + 1)$, where $E$ is with respect to the Fermi-level. $R(\Delta k, \Delta E)$ is the overall momentum and energy resolution as detailed in sec. 7.1.3. A good review paper for the ARPES intensity for interacting systems is [161].

As is obvious from the equation above, the Fermi-Dirac distribution cuts-off the ARPES spectrum such that only the occupied part of the band structure is visible. This is a key

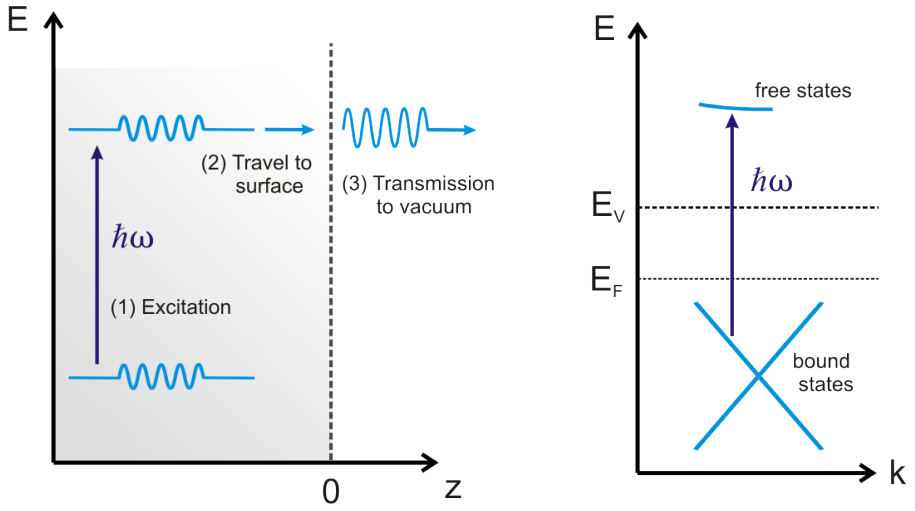


**Figure 6.2:** Illustration of the three-step model in photoemission. A photon with energy $\hbar\omega$ excites an electron from an initial bound state in the solid to a final free electron-like state (right). The electron travels to the surface and gets transmitted into vacuum (left).

limitation of traditional ARPES. One way to overcome this is to symmetrize the intensity distribution across the Fermi-level [45] although that assumes that particle-hole symmetry is obeyed. As will be seen below Tr-ARPES is a novel way to overcome this limitation to map out the unoccupied band structure of a sample.

### 6.1.1 Three-step model & matrix-element effects

The matrix-element term $I_0$ in the measured ARPES intensity describes transitions between initial and final states of photoemission. This can be interpreted in the so-called three-step model (fig. 6.2) which consists of the following three processes: (1) The incident photon excites an electron from bound states in the bulk to final states near the surface. (2) The excited electron travels to the surface and (3) gets emitted from the sample surface. Thus, the matrix-element term can be written as:

$$I_0 = |\left\langle \Psi_f | \vec{A} \cdot \vec{p} | \Psi_i \right\rangle|^2 \tag{6.4}$$

where $\Psi_i$ and $\Psi_f$ are the initial and final electron wavefunctions. $\vec{p}$ is the electron momentum and $\vec{A}$ is the vector potential of the photo-emitting beam. To explicitly calculate $I_0$ requires

knowledge of the electron wavefunction and crystal potential near the surface of the solid. In practice, the final states are taken to be time-reversed LEED (Low Energy Electron Diffraction) free electron-like states and occur in the continuum ([162]). Matrix elements also become important in samples with strong spin-orbit coupling. In this case the probe polarization couples to the spin of the initial state to effect of the overall spectra. Symmetry arguments can be used to quantify such matrix-elements without microscopic details as is done for ARPES spectra obtained on topological insulators (sec. 8.4.4).

### 6.1.2 Laser based ARPES

The light source for ARPES measurements is typically a large synchrotron facility which provides high photon energy and photon flux. Typically the photon energies are in the ultra-violet i.e. ($\hbar\omega < 100\,\text{eV}$). Another source is a He gas discharge lamp with a photon energy of 21.2 eV. Such sources are usually quasi-continuous and cannot be used for time-resolved measurements. Another key drawback at such energies is the limited probing depth of photoelectrons. As shown in fig. 6.3 the photonelectron mean free path in solids as a function of its kinetic energy exhibits a minimum at about 5 Å between 20 eV and 100 eV. Thus, the measured intensity will predominately reflect only the topmost surface layer. In contrast, the protected topological surface state (TSS) in topological insulators such as $Bi_2Se_3$ extends several layers deep into the bulk (about 2-3 nm) [163] and so an accurate measurement of the TSS requires a greater probing depth. This can be extended using photon energies beyond 100 eV (fig. 6.3). However, in addition to being costly, higher energy also degrades momentum resolution. This can easily be seen from eq. (6.2). Neglecting effects of energy resolution, $\Delta k_{\parallel} \propto \sqrt{E_k}(\cos\theta)\delta\theta$. Thus, the greater the $E_k$ of photoemitted electrons, the worse the momentum resolution. Similarly, using a higher photon energy will result in electrons from bulk like bands with high binding energies dominating the ARPES signal since the TSS is known to lie only within a few 100 meV from the Fermi level [164].

Instead of synchrotron facilities, we rely on laser-based ARPES to study topological insulators in this work. This is a tabletop setup (see chap. 7 for details) which provides us

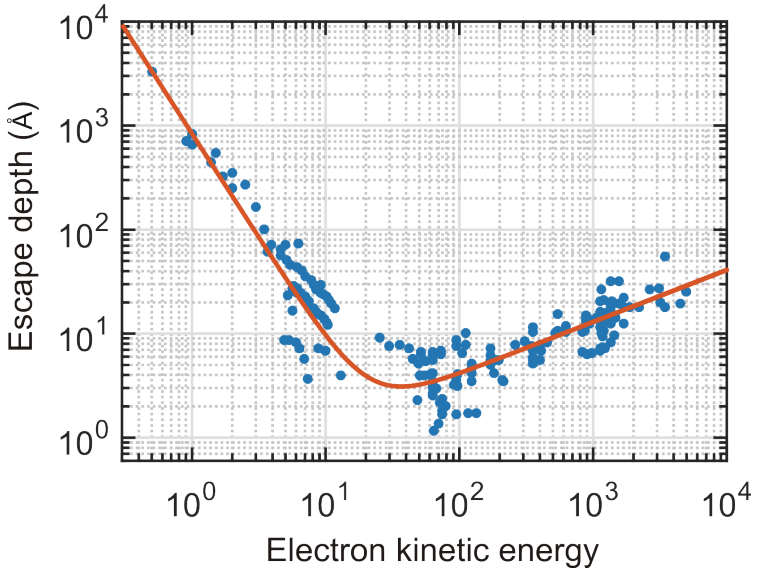


**Figure 6.3:** Universal curve of escape depth of a photoemitted electron as a function of its kinetic energy. Data extracted from [165].

with a photon energy of $\sim 6\,\text{eV}$. This not only enhances the sensitivity of the signal to the TSS but also enhances the momentum resolution so as to clearly identify the surface state Dirac cone. Moreover, the light source can be pulsed with temporal widths down to 100 fs to enable time resolved measurements as will be discussed below. However, a draw back of 6 eV ARPES is the limited momentum space available to study. From eq. (6.2), the maximum $k_{\parallel}$ that can be measured (for a $\theta$ of 22° and $E_k$ of 2 eV) is only $0.27\,\text{Å}^{-1}$. The value of 22° chosen here corresponds to the maximum polar angle that can accurately be measured by our detector (chap. 7). While this maximum $k_{\parallel}$ is nearly twice the typical $k_f$ for TSS, it is smaller then the typical position of the nodal points in cuprate superconductors and the K and K' points in graphene and hexagonal TMDs.This limits the materials that can be studied with 6 eV laser-based ARPES. Ways to extend the photon energy and thus the available momentum space while maintaining good time resolution for Tr-ARPES include high-harmonic generation (HHG) and a free electron laser (FEL).

### 6.1.3 Hemispherical analyzer vs Time-of-Flight detection

Conventional ARPES setups utilize a hemispherical analyzer to map out the energy and momentum distribution of the photoemitted electrons. As shown in fig. 6.4a, this type of analyzer consists of two concentric hemispheres with different radii and a potential difference across them. Electrons within a narrow kinetic energy pass between the two hemispheres which deflect the electrons based on their kinetic energies. The electrons are imaged on a positive-sensitive 2D detector with the position along one axis corresponding to the electron kinetic energy. The electron position along the other axis corresponds to its angle of emission and thus its in-plane momentum along a given direction. A narrow slit at the entrance of the analyzer selects electrons within a certain momentum range. In this way, a 2D image of the electron energy vs in-plane momentum is obtained. It is important to note that for a given sample orientation a hemispherical analyzer is able to resolve the band structure only along one momentum direction. To obtain a complete mapping with all directions of in-plane momentum, the samples have to be continuously rotated which is a time consuming process. Figure 6.4b shows a representative ARPES trace on the topological insulator $Bi_2Se_3$ taken with a hemispherical analyzer. The energy along only one momentum direction is obtained.

In contrast, we use an angle-resolved time-of-flight (ARTOF) analyzer which consist of a long tube that collects all electrons emitted within a 3D cone (fig. 6.5a). The electrons are focused onto a 2D grid-like detector. Each position on the grid corresponds to a unique polar ($\theta$) and azimuthal ($\varphi$) angle. In this way, both components of the in-plane momentum ($k_x$, $k_y$) are determined. The kinetic energy of photoemitted electrons is calculated from the time it takes the electrons to travel the meter long lens tube. Thus, the ARTOF detector determines the solid band-structure along both directions of the in-plane momentum without rotating the sample or the detector. Figure 6.5b shows a representative ARPES trace on the $Bi_2Se_3$ taken with our ARTOF detector. The full 3D Dirac cone is obtained without any sample rotation. Cuts along arbitrary directions can be taken to study a specific momentum dependence (fig. 6.5c,d). This capability of an ARTOF analyzer is

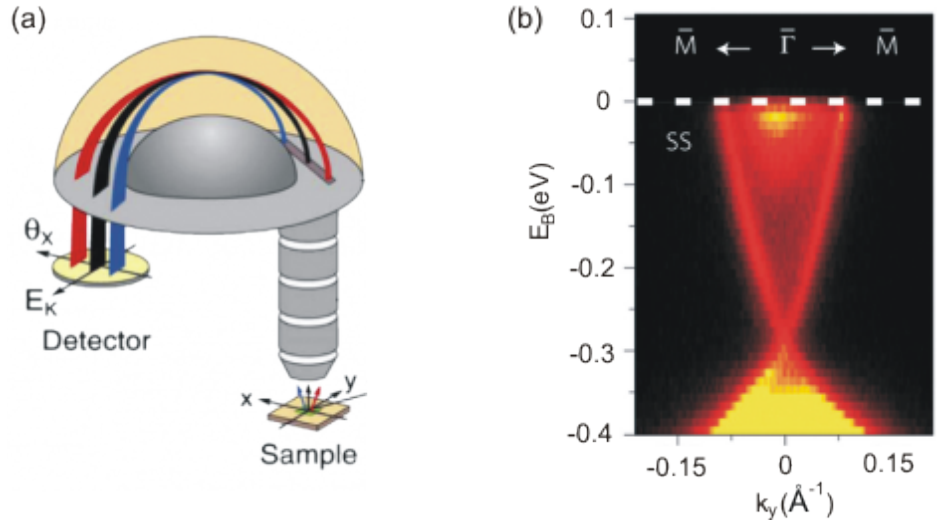


**Figure 6.4:** Hemispherical ARPES analyzer and representative spectra on $Bi_2Se_3$. **(a)** Schematic showing the workings of a hemispherical analyzer. Photoemitted electrons travel through a narrow slit in-between two concentric spheres with a voltage difference between them. The electron is imaged onto a detector with one axis corresponding to its energy and another to its in-plane momentum along a given direction. Figure reprinted from [161]. **(b)** ARPES spectra (binding energy vs. momentum) on the topological insulator $Bi_2Se_3$ taken using a hemispherical analyzer. Figure taken from [164]

invaluable for Tr-ARPES experiments as it allows study of pump-induced changes in the band structure along different momentum directions without changing the experimental geometry. This feature is utilized in studying the mixing between Floquet-Bloch and Volkov states in sec. 8.4. These are both photo-induced states and the mixing between them depends on the electron-momentum direction. ARTOF allows us to separate this mixing without rotating the sample as would be the case for a hemispherical analyzer.

Here we note that the energy resolution of the ARTOF analyzer is determined by how accurately it can measure the flight-time of the electron. Our particular analyzer has an uncertainty of $\Delta t_f = 100\,\text{ps}$ in the measurement of this flight-time. The energy resolution of the detector($\Delta E_d$) can be written in terms of this time-uncertainty as:

$$|\Delta E_d| = 2\sqrt{\frac{2}{m_e L^2}} E^{3/2} |\Delta t_f| \tag{6.5}$$

where $E$ is the kinetic energy of the electron, $m_e = 9.11 \times 10^{-31}\,\text{kg}$ and $L = 1\,\text{m}$ the length of the flight-tube. Thus, for a measured $E = 2\,\text{eV}$ the detector energy resolution is

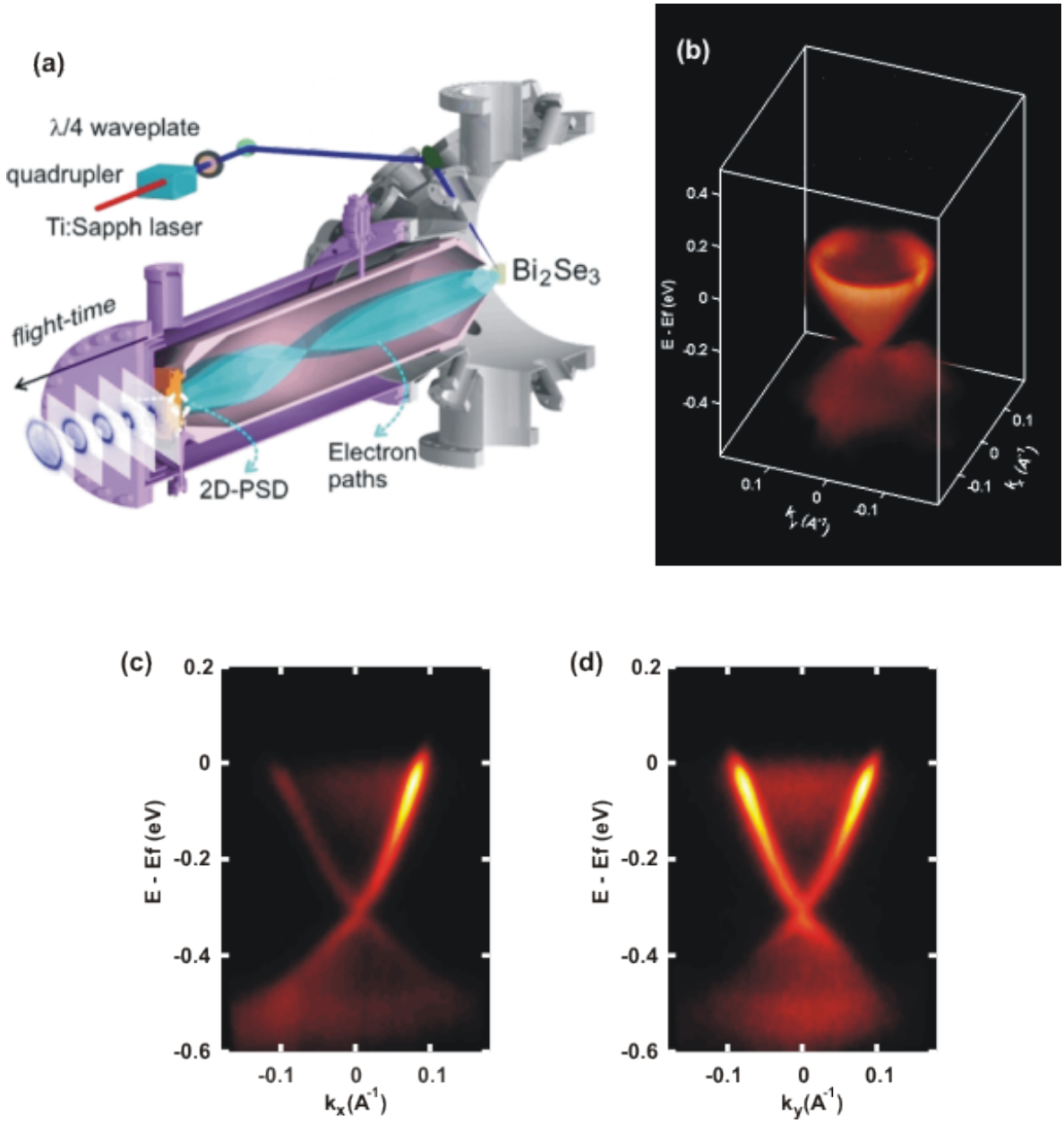


**Figure 6.5:** Angle-resolved time-of-flight (ARTOF) ARPES analyzer and representative spectra on $Bi_2Se_3$ **(a)** Schematic showing the workings of an ARTOF analyzer. Details of each component are discussed in chap. 7. Figure reprinted from [166]. **(b)** Intensity distribution of photoemitted electrons from $Bi_2Se_3$ as a function of energy relative to the Fermi-level ($E-E_f$) and both directions of in-plane electron momentum ($k_x$ and $k_y$). The full 3D Dirac cone is resolved. Cuts along $k_x$ and $k_y$ are shown in **(c)** and **(d)** respectively.

$|\Delta E_d| \sim 0.34\,\text{meV}$. As we will discuss in sec. 7.1.3, this is much less than the resolution set by the finite pulse width of the laser. Thus, for experiments discussed in this work, the finite energy resolution of the ARTOF detector does not play a significant role.

## 6.2 Tr-ARPES: overview

Time-resolved ARPES (Tr-ARPES) is a pump-probe based variation of conventional ARPES and allows access to the non-equilibrium band structure of a solid. It is similar to the optical pump-probe technique discussed in chap. 2 but resolves the photo-induced dynamics of a sample in terms of the energy and momentum of its photoemitted electrons. Like optical pump-probe, the laser beam is split into two parts: pump and the probe. The first part, the pump beam, is used to excite a non-equilibrium distribution of electrons inside the sample. The energy of the pump can be varied from the mid-IR ($\sim 100\,\text{meV}$) to the optical ($\sim 3\,\text{eV}$) spectrum. The probe part of the laser beam impinges on the sample a certain time delay $\Delta t$ after the pump pulse. The probe has energy in the UV range in order to photo-emit electrons from the sample which are then collected by an ARPES spectrometer to resolve their energy and momentum as detailed above. In this way, Tr-ARPES can map out the spectrum both above and below the Fermi-level. By acquiring the energy-momentum spectra at various values of $\Delta t$, Tr-ARPES can study the evolution of the photo-excited band structure.

Figure 6.6 illustrates the Tr-ARPES technique on a typical semi-conductor using a pump beam with energy greater than the bulk-band gap. At negative time delays ($\Delta t < 0$), the probe hits the sample before the pump pulse and measures the equilibrium band-structure. Only occupied states, i.e. states below the Fermi-level, are accessible (bottom panel in fig. 6.6). At $\Delta t = 0$, the pump and the probe pulse overlap in time and measured ARPES spectra has intensity both above and below the Fermi-level as the pump photo-excites electrons from the valence band to bands above the Fermi-level. Spectra taken at $\Delta t > 0$ then probe the resulting dynamics of these photo-excited electrons as they relax to the bottom of the conduction band and then back to the valence band (bottom panel in fig. 6.6).

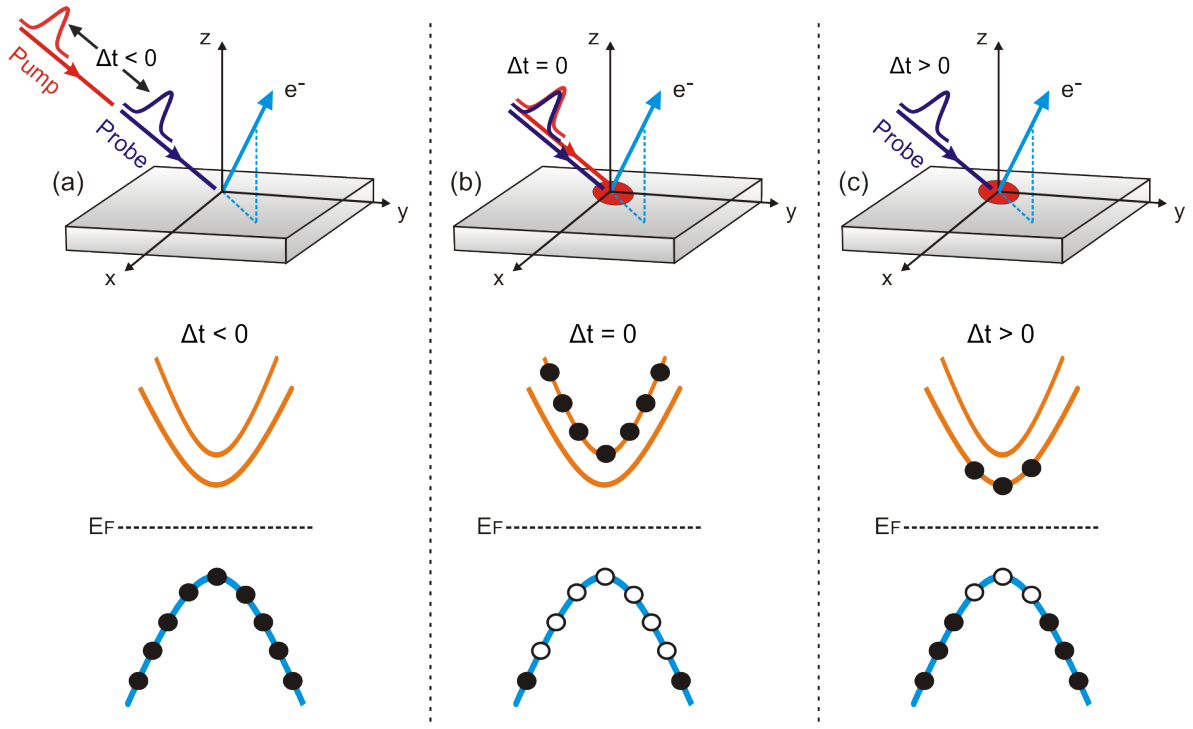


**Figure 6.6:** Stages in the time-resolved ARPES technique at different delay times $\Delta t$ between the pump and probe. **(a)** At negative $\Delta t$ the probe pulse arrives before the pump and the equilibrium band structure is measured i.e. only occupied states below the Fermi-level ($E_F$) (bottom panel) **(b)** At $\Delta t = 0$, the pump and probe pulses overlap in time and the spectra can resolve states above $E_F$. **(c)** Subsequent spectra taken at $\Delta t > 0$ measure the relaxation of electrons excited by the pump.

### 6.2.1 What can Tr-ARPES do?

Depending on the sample and the energy of the pump pulse, various types information about a material can be obtained from a Tr-ARPES experiment as detailed below:

1. **Energy and momentum-resolved electronic & lattice temperature relaxation pathways:** As discussed in sec. 2.1 and in fig. 2.1b, a pump pulse in the optical spectrum initially excites electrons into a non-Fermi distribution. The excited electrons inelastically scatter among themselves to return to a thermal distribution with a much greater electronic temperature ($T_{el}$) then that at equilibrium. Tr-ARPES can directly measure this non-Fermi distribution function and its subsequent evolution which gives clues into electron-electron interactions in the sample. This was initially achieved using

time-resolved photoemission (no momentum resolution) in metallic tungsten [167] and gold [168]. Subsequent advances allowed access to electron thermalization on the fs time scale in graphite [169–171].

The heated electronic system then transfers some of its energy to the lattice through electron-phonon coupling to raise the lattice temperature $T_{lat}$. The subsequent dynamics are then described by the two-temperature model (sec. 2.1). While Tr-ARPES does not have direct access to $T_{lat}$, the dynamic behavior of $T_{el}$ with both energy and momentum can give important insights into electron-phonon coupling. Here $T_{el}$ can be directly obtained as a function of time by fitting the energy distribution of the ARPES intensity $I(E,t)$ to a Fermi-Dirac function. This can also be used to separate out cooling mechanisms for electrons in bulk and surface states as was done for topological insulators excited with an optical $\sim 1.5\,\text{eV}$ pump pulse [172–174]. Recently Tr-ARPES was also used to study the dynamics of non-equilibrium photo-excited electron distribution in graphene [175].

2. **Momentum-resolved quasi-particle recombination and collective mode dynamics:** This refers to the generation of quasi-particles by an optical pulses in materials with a small gap at the Fermi-level such as in a superconductor. As seen in chap. 2, optical pump-probe spectroscopy (measuring change in the refelctivity) can resolve the subsequent recombination dynamics of these quasi-particles however it averages over all momentum. This obscures useful information especially for superconductors with an anisotropic gap such as the d-wave gap in cuprate superconductors. Tr-ARPES can resolve the momentum dependence of quasi-particle relaxation to give insights into the binding boson in high-temperature superconductors [20, 176].

   Tr-ARPES can also be used to observed recombination dynamics and collective modes of the order parameter in systems with anti-ferromagnetic (AFM) or charge-density wave (CDW) ordering. Similar to excitation across the SC gap, an optical pulse can

excite quasi-particles across the gap opened up by the reconstruction of the Fermi-surface due to AFM or CDW ordering. For high enough pump intensities, the order can be completely melted. Tr-ARPES then probes the subsequent recovery of the order parameter. Moreover, amplitude modes of the order parameter can also be excited. Tr-ARPES can directly access these as oscillations in the magnitude of the gap. Examples of such studies include [71, 72, 177–179].

3. **Map unoccupied band structure:** As discussed above, a major limitation of ARPES is its inability to probe states above the Fermi-level. Such states can be useful to understand macroscopic properties of various materials such as conductivity and optical absorption. There are predictions for the presence of electron and hole pockets in cuprate superconductors above the Fermi-level and so far these have been inferred only using thermally activated population of such states. Tr-ARPES naturally overcomes this limitation by re-distributing electrons into these unoccupied states and then measuring the resulting spectra. Examples include mapping a second un-occupied Dirac surface state in the topological insulator $Bi_2Se_3$ [180] and our work of mapping the unoccupied surface state and bulk conduction band in BSTS [181] (sec. 6.2.2).

4. **Band structure of periodically driven systems:** This is particularly important for this thesis. As will be discussed in sec. 8.1, there has been significant interest in realizing exotic phases using a strong periodic drive. One example is the possible enhancement of the superconducting Tc in cuprate superconductors [23, 24] and in $K_3C_{60}$ [182] in which THz photons first excite a coherent phonon mode in the system which then couples to the electronic system. Tr-ARPES is ideally suited to study this transient state as a THz pump can be used to excite the system and the resulting change in the spectrum (e.g. whether a SC gap opens up or not) can then be probed with the photoemitting beam.

   Another example involves directly coupling photons to the electronic system in a solid to generate Floquet-Bloch bands (chap. 8). In this way, a trivial insulator can be

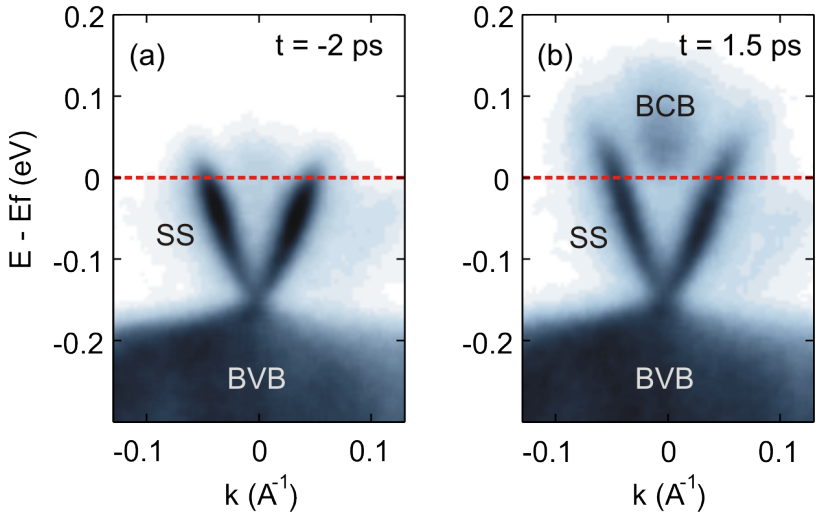


**Figure 6.7:** ARPES spectra on the topological insulator BSTS taken at **(a)** $t = -2\,\mathrm{ps}$ i.e. before the pump pulse hits the sample and at **(b)** $t = 1.5\,\mathrm{ps}$. SS, BVB and BCB denote the Dirac surface states, the bulk valence band and bulk conduction band respectively.

manipulated with light to realize exotic topological phases (sec. 8.1.1). Tr-ARPES provides an ideal opportunity both to generate such states using a high intensity pump-beam and to probe the transient band structure. This application of Tr-ARPES will be discussed in detail in chap. 8.

### 6.2.2 Example: Mapping unoccupied states in BSTS

This section demonstrates how Tr-ARPES can be used to map the unoccupied band structure of a solid. The sample under study is the topological insulator $Bi_{1.5}Sb_{0.5}Te_{1.7}Se_{1.3}$ (BSTS) which consists of protected Dirac-like surface states in between the bulk valence and conduction band. The physics of topological insulators is outlined in sec. 8.2. Here we focus on the Tr-ARPES spectra taken on BSTS using a 1.55 eV pump pulse. Figure 6.7a shows ARPES spectrum at negative time delay (i.e. before the pump pulse hits the sample). This spectra corresponds to the equilibrium band structure of BSTS. As seen, the chemical potential is located inside the bulk conduction band. The Dirac point and the valence band maximum are also observed.

Information about the band gap and conduction band can be obtained from Tr-ARPES which measures unoccupied states above the chemical potential. Figure 6.7b shows the Tr-ARPES spectra taken at 1.5 ps after the pump pulse hits the sample. The sample is still in its excited state and the conduction band along with the surface states above the chemical potential are clearly visible. This allows us to extract the bulk band gap, the surface state dispersion and the conduction band effective mass [181]. These parameters are used to understand electronic transport measurements on nanodevices made from BSTS. The results are published as part of collaboration with the Jarillo-Herrero group at MIT [181].

### 6.2.3 Example: Excitation & relaxation of Dirac fermions in $Bi_2Te_3$

This section demonstrates how Tr-ARPES can provide momentum-resolved information about mechanisms involved in the relaxation of heated electrons in a solid. This information is inaccessible to optical pump probe methods discussed in chap. 2. The sample under study here is the topological insulator $Bi_2Te_3$. We have already seen the transient reflectivity of the topological insulator $Bi_2Se_3$ when it is excited with an optical pump (fig. 2.2). There it was impossible to determine whether the signal originated from the bulk or the surface states.

Figure 6.8 shows the Tr-ARPES signal on $Bi_2Te_3$ when it is excited with a 1.55 eV pump pulse. Here the time-resolved population of the bulk conduction band (BCB) and the excited Dirac surface states (SS) are obtained separately by integrating over them in momentum space. As can be seen, the decay of SS excited population is much slower than that of the BCB. In fact, the decay time ($\sim 10$ ps) of the BCB is close to decay of the OPP signal in fig. 2.2 which confirms that OPP is primarily a bulk probe of the electron dynamics.

In contrast, Tr-ARPES is able to isolate the SS transient population which is characterized by an unusually long lifetime of $> 50$ ps. Similar results using this technique on $Bi_2Te_3$ were obtained by [183] and attributed to electron-hole asymmetry in the Dirac cone as a carrier recombination bottleneck. Here surface band bending spatially separates excess electrons and holes. For an initially p-type semi-conductor as the one used here, band bending induces a flow of photo-excited holes towards the bulk while the photo-excited electrons become trapped

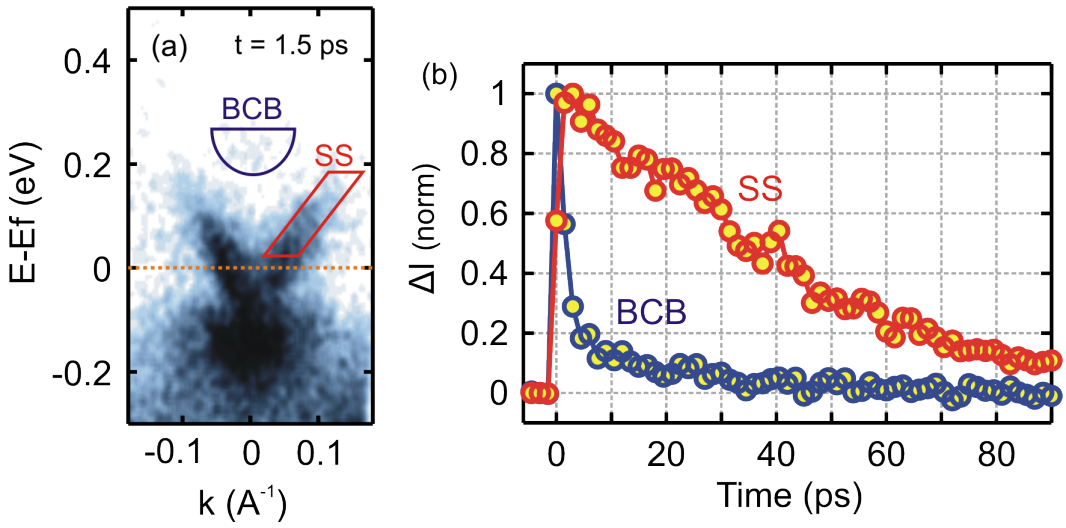


**Figure 6.8:** Relaxation of Dirac fermions in $Bi_2Te_3$. **(a)** ARPES spectra on the topological insulator $Bi_2Te_3$ taken at $t = 1.5\,ps$. SS and BCB denote the Dirac surface states and bulk conduction band respectively. Orange dotted line indicates the equilibrium Fermi level. Red and blue regions indicate the regions over which the intensity is integrated over for the time-resolved traces. **(b)** Normalized change in the Tr-ARPES intensity as a function of the delay time for the SS and BCB.

at the surface. This carrier asymmetry at the surface results in a extremely long lifetime for photoexcited Dirac electrons as there are not enough holes for them to recombine with.

### 6.2.4 Strong laser electric-field induced emission

This section discusses field-emission induced by the strong laser electric-fields used in Tr-ARPES. In general field-emission refers to the tunneling of surface electrons into vacuum by a strong electric-field altering their confining potential. Both photo-emission and field-emission are depicted in fig. 6.9. As illustrated, photoemission requires the absorption of a photon with energy greater than the sample work-function $\phi$. On the other hand, a strong static or quasi-static electric field changes the potential barrier experienced by surface electrons allowing them to tunnel out into vacuum without overcoming the work-function. The presence of low energy photons ($\hbar\omega \ll \phi$) further enhances the field emission as shown in fig. 6.9b. This effect is referred to as optical field emission and is used to generate electron pulses from nano-structures [184–186].

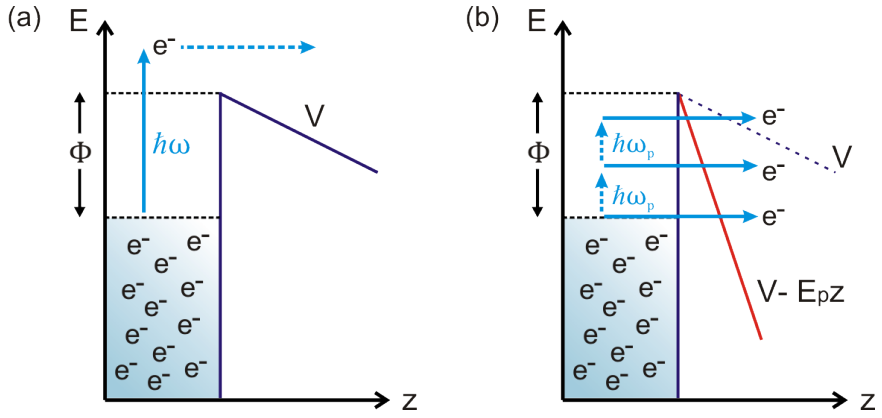


**Figure 6.9:** Photoemission vs field-emission of electrons **(a)** In photoemission, a photon with energy greater than the work-function $\phi$ of the solid causes an electron to overcome the confining potential $V$. **(b)** In field-emission a strong quasi-static electric-field ($E_p$) alters the confining potential of electrons causing them to tunnel out into vacuum.

Field emission becomes quite important for low frequency, high intensity and short pump pulses used in Tr-ARPES. The short duration of the pump pulse leads to very high peak electric fields in vacuum in the range of $10^7$ V/m to $10^8$ V/m (sec. 7.1.4). This field is further enhanced at the edges of the sample or around sharp defects or impurities on the sample surface where the curvature is higher. This 'lightning rod' effect can enhance the electric field by a factor of up to 50 around sharp protrusions in metallic samples [187]. In our case this can lead to surface potential gradients greater than 1 GV/m. For low-frequency pulses, electrons experience a quasi-static field and can thus tunnel into vacuum. This emission is further increased through multi-photon absorption of the pump pulses as well.

The electrons generated through the pump pulse field emission accelerate into the ARTOF detector and register as a background signal even in the absence of the photo-emitting probe beam. This background is highly susceptible to the sample surface quality necessitating the use of flat surfaces devoid of sharp edges or defects. Field emission can also worsen the energy and momentum resolution of the signal through space-charge effects as discussed in sec. 7.1.3.

*"Sometimes I'll start a sentence, and I don't even know where it's going. I just hope I find it along the way. Like an improv conversation. An improversation."*

— Michael Scott, *The Office, 2009*

# 7

# Tr-ARPES: Experimental setup

## Contents



Tr-ARPES is implemented in the Gedik lab by combining a Ti:Sapphire amplified laser system with a Angle-Resolved-Time-of-Flight (ARTOF) detector. The main components are the optical setup and the ARTOF system combined with Ultra-High-Vacuum (UHV) chambers and electronics for data acquisition.

The optical setup generates and characterizes both the pump and the photo-emitting probe beam. As detailed in the sections below, the energy of the pump beam can be varied between $\sim 100\,\text{meV}$ and $3\,\text{eV}$ while the photo-emitting probe beam's energy is set to $\sim 6.2\,\text{eV}$

via fourth harmonic generation (FHG) of the fundamental $\sim 1.55\,\text{eV}$ laser beam. A delay stage is used to control the time delay between the pump and probe beams. The beams are focused and spatially overlapped with each other at the sample in a UHV chamber. The sample is mounted on a 6-axis goniometer and is cleaved in-situ typically at a pressure $< 2 \times 10^{-10}\,\text{Torr}$. The energy and momentum of the photo-emitted electrons are measured using a commercial VG scienta TOF detector system (ARTOF).

Below we present details of each of these components in order to guide future researchers working with the Tr-ARPES setup in the Gedik lab. We also present a few limitations of the setup along with alignment and optimization tricks.

## 7.1 Optical components

Figure 7.1 shows the optical components and the complete beam path for the Tr-ARPES system. The laser is a KM Labs Wyvern 500 regenerative amplified system which gives ultra-short pulses centered at $\sim 1.55\,\text{eV}$ with duration $\sim 150\,\text{fs}$. The repetition rate can be varied between 10 kHz to 200 kHz though the experiments in this work are typically done at 30 kHz with pulse energies of $> 250\,\mu\text{J}$. A telescopic beam reducer is used to reduce the spot size at the output of the laser to match specifications for the Optical Parametric Amplifier (OPA), the 'Tripler' and the 'Quadrupler' (see below). The laser beam is then split into two using a half-wave plate and a thin-film polarizer combination. The thin-film polarizer reflects light polarized vertically with respect to plane of incidence while transmitting horizontal polarization. In this way the power can be continuously adjusted between the OPA and the rest of the setup.

The vertically polarized reflected beam from the thin-film polarizer is fed into the OPA which uses a combination of non-linear processes to generate the variable energy (100 meV to 3 eV) pump-beam for the Tr-ARPES system. This 'OPA pump' beam is filtered, collimated and elevated using a periscope to be focused into the UHV chamber with a silver or gold-

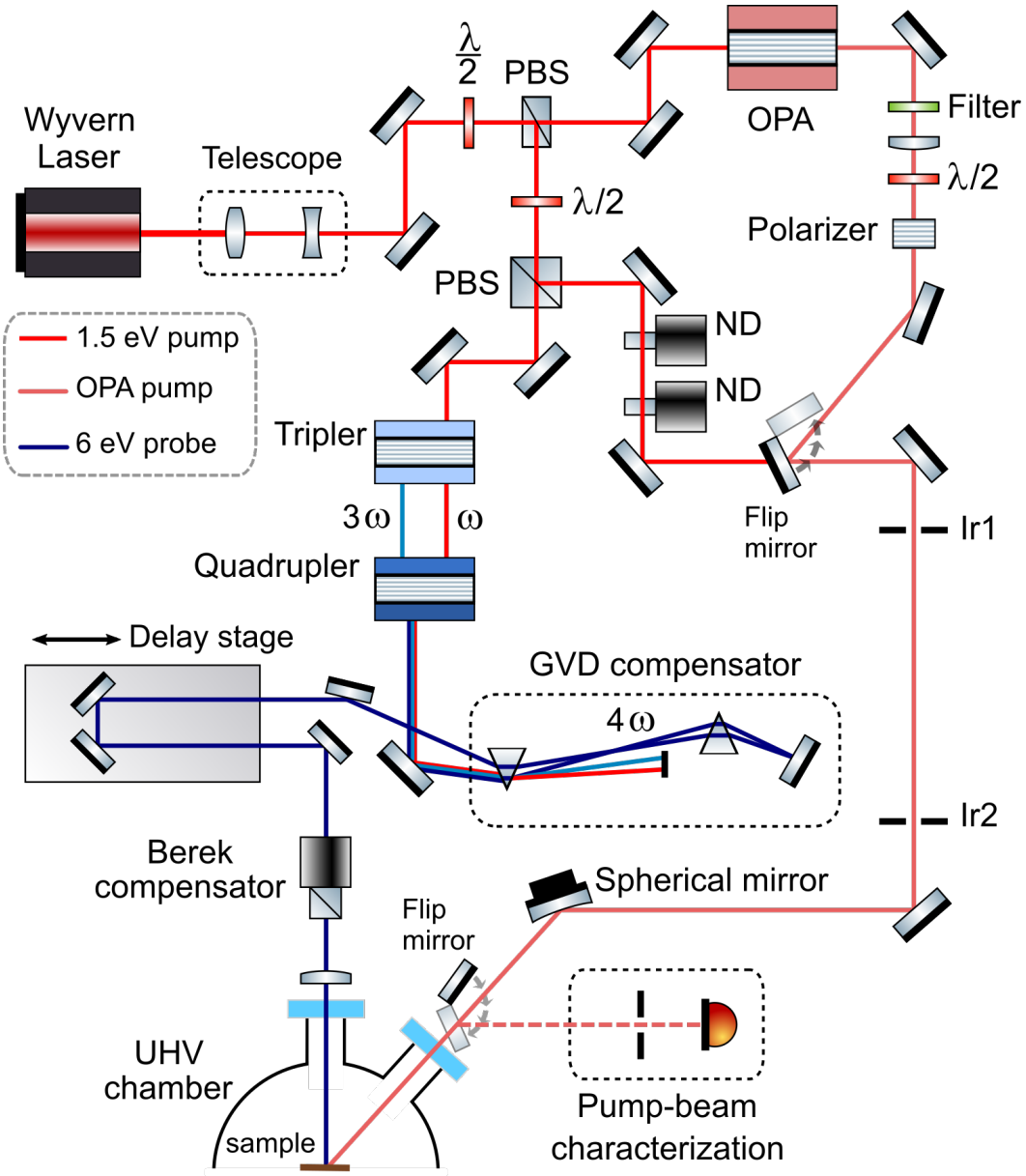


**Figure 7.1:** Optics setup for Tr-ARPES showing the complete beam path from the Wyvern laser to the sample inside the UHV detector. See text for a detailed description of the beam path and the indivindual components. A few abbreviations are as follows: $\lambda/2$: half-wave plate, PBS: polarizing beam splitter, ND: neutral-density Ir: Iris. Drawings of individual optical components are adapted from [42].

coated concave mirror. Various wave-plates (quarter and half) along with polarizers can be placed in the path of the OPA beam to adjust the polarization and fluence of the 'OPA pump'.

The horizontally polarized transmitted beam from the thin-film polarizer is further split into two using another half-wave plate and polarizing beam splitter. One part acts as the pump beam which is quite useful in Tr-ARPES experiments that need a pump energy of 1.55 eV since this path circumvents the complicated OPA stage. Neutral density (ND) filters can be used to alter the pump fluence. This 1.55 eV pump beam eventually follows the same path as the 'OPA pump' mentioned above.

The other part is fed into a 'Tripler' which generates the third harmonic ($3\omega$) of the fundamental frequency $\omega$ of the laser beam using non-linear optics. The third-harmonic and fundamental beams are summed together in a 'Quadrupler' to generate the fourth-harmonic $4\omega$. This has an energy of $\sim 6.2$ eV and is used as the photo-emitting probe pulse. The Quadrupler outputs beams at $\omega$, $3\omega$ and $4\omega$ which are separated using a prism pair which also compresses the $4\omega$ beam temporally. The probe beam then passes through a delay stage to adjust the time delay between the pump and probe pulses for time resolved experiments. The probe is then elevated with a persciope and focused into the chamber at the same spot as the pump beam. A 'Berek' compensator can be used to control the polarization of the probe. Below are the details of the physics of each component in the optical setup.

### 7.1.1 Laser system

The laser system consists of a KM labs Wyvern 500 regenerative amplifier. In general, for efficient Tr-ARPES experiments, a laser system needs to be pulsed and have the following specifications:

1. **Pulse duration:** This sets the time-resolution of the system so the shorter the pulse duration, the better the resolution. However, there is a trade-off between the time and energy resolution due to the uncertainty principle:

$$\sigma_t \sigma_E \geq \frac{\hbar}{2} \implies \Delta t \Delta E \geq 1.82\,\text{meV.ps} \tag{7.1}$$

where $\sigma_{t,E}$ are the RMS widths for Gaussian pulses and $\Delta t, \Delta E$ correspond to their FWHM which we use to define the resolution of our setup. Here we have used the relationship FWHM $= 2\sqrt{2\ln 2}\sigma$. This implies that a 150 fs pulse will have an energy resolution $> 12$ meV. The pulse duration of the Wyvern can be adjusted by modifying the stretcher (see below). We typically use pulses with duration 100 fs to 200 fs.

2. **Pulse energy:** This refers to the total amount of energy within a single pulse. In a Tr-ARPES experiment, sufficient pulse energy is needed to both drive the system out of equilibrium and generate the photo-emitting probe. In our case, high pulse energies are also needed for the OPA. In the Wyvern system, the pulse energy is typically $> 250$ µJ at a repetition rate of 30 kHz.

3. **Repetition rate:** This refers to the number of pulses per unit time at the output of the laser system. The repetition rate sets the electron count-rate ($N_e$) since our ARTOF detector uses a delay line that can at most count one electron per laser pulse. The greater the repetition rate, the faster the data acquisition since we get a better signal-to-noise ratio (SNR$\sim \sqrt{N_e}$). This is especially important for Tr-ARPES experiments as the change due to the pump pulse is typically quite small and the sample surface degrades over time (a few hours to a day) after cleaving which intrinsically broadens the ARPES spectra. However, there are two main limitations preventing a high laser repetition rate. Firstly, at higher repetition rates, the pulse energy of the Wyvern decreases which reduces the efficiency of the non-linear processes in the OPA. This reduces the available pump-energy needed to perturb the system. Secondly, a higher electron flux ($N_e$ per unit area) degrades the sensitivity of the multi-channel-plate (MCP) in the ARTOF detector necessitating frequent replacement of the MCP, an expensive and time-consuming process. We typically use a laser repetition rate of 30 kHz and adjust the photon flux to keep the electron count rate below 20,000 counts/sec (see below). This repetition rate also ensures optimum operation of the OPA.

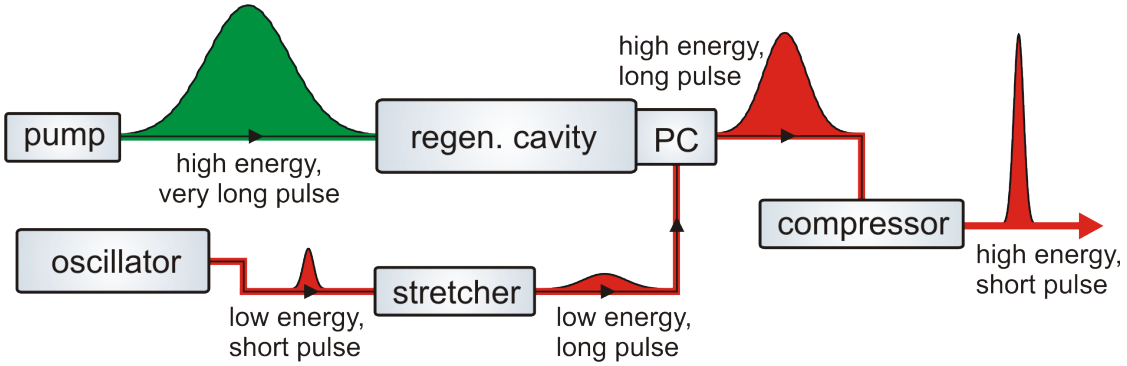


**Figure 7.2:** Stages of the Wyvern laser system. The oscillator outputs a $< 100$ fs short pulse 'seed' which gets elongated in time in the stretcher to reduce its peak intensity. The stretched seed pulse is trapped in the regenerative cavity using a pockels-cell (PC) to gain energy from the cavity which was stored in it using a high-energy 532 nm pump pulse. The high-energy pulse from the cavity is then compressed back to yield an ultra-short amplified output at 800 nm.

The various stages of the Wyvern laser system relevant for the day-to-day operation are illustrated in fig. 7.2 and outlined as follows:

**Oscillator:** The laser system starts with an oscillator which is simply an optical cavity that provides a 'seed' pulse that is amplified. The working principles behind an oscillator are detailed in sec. 2.3.1. The Wyvern oscillator outputs a short pulse with a duration $< 100$ fs.

**Stretcher:** The ultra-short seed pulse is then fed into a 'stretcher' which broadens the time duration of the pulse so as to reduce its peak intensity. This is to prevent damage to the gain medium in the amplification stage. The 'stretcher' is a pair of diffraction gratings that order the frequencies of the ultrashort pulse in time e.g. lower frequency components arrive earlier. The position of these gratings and hence the broadening of the pulse can be controlled by an external knob which is a convenient way to adjust the temporal pulse width of the amplifier output. The stretched seed pulses are then fed into the regenerative amplifier cavity to be amplified.

**Regenerative cavity:** Regenerative amplification consists of a resonator and a gain medium that is pumped externally to accumulate sufficient energy. A seed pulse is then trapped inside the gain medium to undergo many resonator round trips as it extracts all the energy stored in the gain medium. The resulting high energy pulse is then opto-electronically

released from the cavity. The amplifier cavity in the Wyvern consists of a Ti:sapphire crystal in a vacuum chamber that is cryogenically cooled to below 100 K to prevent heating and damaging the crystal. The external pump lasers (Photonics industries) excite that Ti:Sapphire crystal with a wavelength of $\sim 532$ nm and a repetition rate typically set to 30 kHz. The pump lasers excite the crystal to create population inversion which can then lead to stimulated emission at the wavelength of the seed pulses as they pass through the crystal. In this way the seed photons trapped in the regenerative cavity become amplified. For optimum amplification, the seed beam has to be spatially overlapped with the pump beams.

**Pockels cell:** The trapping and release of the pulses in the cavity is achieved using a Pockels cell (PC) which is a crystal whose birefringence (i.e. polarization dependent refractive index) can be controlled by applying a voltage pulse. The incoming seed pulse (horizontally polarized) passes through a thin-film polarizer and a $\frac{\lambda}{4}$ wave-plate and into the PC after which it is retro-reflected back. If the PC is off (i.e. no voltage is applied), the seed pulse will become vertically polarized and thus reflected into the cavity by the thin-film polarizer. At this point the PC is turned on making it act like an additional $\frac{\lambda}{4}$ wave-plate. This prevents any rotation of the pulse polarization from the PC-$\frac{\lambda}{4}$ wave-plate combination and thus traps the seed pulse inside the cavity in addition to preventing additional seed pulses from entering the cavity. After amplification is complete the PC is turned off and the high-energy pulse is released from the cavity. The timing of the PC can be adjusted such that the first pass of the seed pulse occurs at the falling edge of the pump pulse. This ensures that sufficient energy has been built into the amplifier cavity before the seed pulse passes through it. The amplified pulse is then directed to a compressor where a pair of gratings compress the stretched pulse to between 100 fs and 200 fs. The principles behind pulse compression are detailed in sec. 2.3.1.

The two most commonly encountered issues with the Wyvern laser system are loss of oscillator mode-locking and a decrease in the amplified power. These are typically encountered after the laser-system has been running continuously for a couple of weeks. The oscillator usually suffers due to dust accumulated in its optics that can prevent phase-locking of the longitudinal modes. Thorough cleaning of the optics usually fixes this issue. Similarly, the

decrease in the amplified power is a consequence of worsening pressure in the regenerative cavity which compromises the efficiency of the Ti:sapphire crystal. Initially, the Wyvern average power would drop from 10 W to about 7 W within a few days and the cavity had to be pumped out regularly. One improvement was the installation of an ion pump continuously pumping the cavity to keep it at a pressure of $\sim 1 \times 10^{-9}$ Torr. This allows the regenerative cavity to remain stable for a few weeks. A quick way to optimize the amplifier output is to adjust the $\sim 532$ nm pump beam steering mirrors for better spatial overlap between the pump beams and the seed pulse. It is recommended that the Wyvern laser system is optimized before a Tr-ARPES experiment to ensure continuous and stable operation.

### 7.1.2 Photo-emitting probe beam: generation & characterization

For photoemission, the photon energy must be greater than the work function ($\phi$) of the sample. For most metals, $\phi > 4$ eV necessitating a photon energy greater than the third harmonic of the fundamental light generated by the Wyvern. In addition by eq. 6.2 the greater the photon energy the larger the momentum space that can be measured. Here we use non-linear optics in a $\beta$-Barium Borate (BBO) crystal to generate the fourth harmonic of the 1.55 eV beam to get pulses at 6.2 eV for photoemission. Any harmonic greater than this cannot be generated in a BBO crystal as it cannot transmit wavelengths less than $\sim 190$ nm. Harmonic conversion in the BBO crystal is done using frequency mixing. To understand this we can write the optical response (induced polarization $P(t)$) of the crystal as a power series in the applied electric field $E(t)$ strength:

$$P(t) = \chi^{(1)}E(t) + \chi^{(2)}E^2(t) + \chi^{(3)}E^3(t) + ... \tag{7.2}$$

where $\chi^{(2)}$ and $\chi^{(3)}$ are the second-and third-order nonlinear optical susceptibilities. $\chi^{(2)}$ is the leading term that allows non-linear interactions and is non-zero only in materials that lack inversion symmetry such as BBO. As an example of harmonic conversion consider a laser beam with frequency $\omega$. For simplicity, the time-varying electric field can be written as $E(t) = E_0 \cos(\omega t)$. The second order polarization in eq. (7.2) becomes $P^{(2)} \propto$

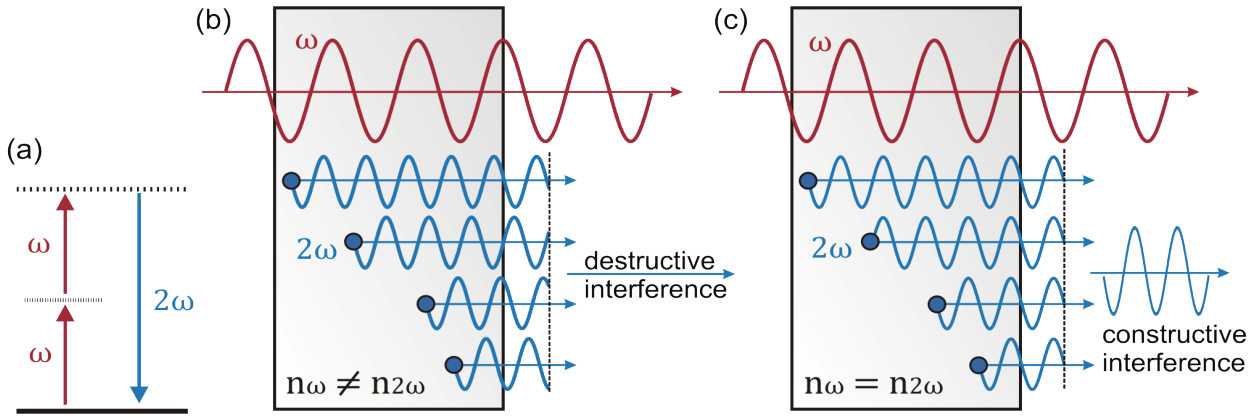


**Figure 7.3:** Harmonic generation & phase matching. **(a)** Energy conservation in second harmonic generation (SHG). Two photons with frequency $\omega$ are absorbed into a virtual state to emit one photon with frequency $2\omega$. **(b)** Tiny regions in a non-centrosymmetric crystal radiate SHG but with random phases with respect to each other due to the difference in dispersion for waves at $\omega$ and at $2\omega$ i.e. $n_\omega \neq n_{2\omega}$. As a result, the SHG waves destructively interfere. **(c)** If the phase-matching condition is met (i.e. $n_\omega = n_{2\omega}$), all the source radiate at the same phase and constructively interfere.

$\chi^{(2)}E_0^2 + \chi^{(2)}E_0^2\cos(2\omega t)$. The second term contains a contribution at $2\omega$ which can lead to the generation of radiation at the second-harmonic frequency. This process is referred to as second harmonic generation (SHG) and can be visualized as two photons of frequency $\omega$ being simultaneously destroyed to generate a photon at $2\omega$ (fig. 7.3a). Similarly, if the electric field contains two distinct frequency components i.e. $E(t) = E_1\cos(\omega_1 t) + E_1\cos(\omega_2 t)$, then the induced second-order polarization will contain frequency components at $2\omega_1$, $2\omega_2$, $\omega_1 + \omega_2$ and $\omega_1 - \omega_2$. The $\omega_1 + \omega_2$ process is appropriately called sum frequency generation (SFG) while the $\omega_1 - \omega_2$ is called difference frequency generation (DFG).

From the discussion above its clear that the intense electric field of an ultra-short pulse can induce second-order polarization in a non-centrosymmetric crystal. However, for the whole crystal to radiate nonlinearly, the waves emitted by the elementary sources need to constructively interfere. This process is called 'phase matching'. For example consider the microscopics of SHG in a BBO crystal (fig. 7.3b). Here different tiny regions of the crystal will emit wavelets at $2\omega$ in all directions. Since the refractive index for the source (fundamental beam at $\omega$) is in general different then for the SHG wavelets ($n_\omega \neq n_{2\omega}$), the wavelets emitted

from different regions of the crystal will have different phases and interfere destructively. This can be avoided in a birefringent crystal where the index of refraction is different along different crystallographic axes. The crystal is cut and oriented in such a way that perfect phase matching ($n_\omega = n_{2\omega}$) is achieved for different polarization of the $\omega$ and $2\omega$ beams.

In our lab harmonic conversion is achieved in a commercial Minioptic 'Tripler' and 'Quadrupler' system. The Tripler consists of two BBO crystals. The first generates SHG while the second uses SFG to combine $\omega$ and $2\omega$ into $3\omega$. External knobs allow fine tuning of the angle of orientation of the BBO crystals for efficient phase matching. The Quadrupler uses another BBO to combine $3\omega$ with $\omega$ to give $4\omega = 6.2\,\text{eV}$ at a few milliwatts of power. The output of the Quadrupler is then sent into a fused silica prism pair where different harmonics are separated and the 6.2 eV 'probe' pulses are compressed. The principles behind pulse compression using a prism pair are detailed in sec. 2.3.1.

After compression the probe pulses pass through a motorized translation stage (fig. 7.1) to adjust their timing with respect to the pump pulses. The delay stage (Newport) allows a scanning range of $> 1\,\text{ns}$. The probe beam is then directed and focused onto the sample in the UHV chamber using a focusing lens mounted on a translation stage. This allows us to adjust the spot size of the probe beam onto the sample which is important for optimizing the energy/momentum resolution of the ARPES spectra as discussed below.

### 7.1.3 Energy & momentum resolution

To take into account the finite energy and momentum resolution of the setup, the intensity measured in an ARPES experiment is convolved with a Gaussian ellipsoid with energy width $\Delta E$ and momentum width $\Delta k$ (eq. 6.3). $\Delta E$ is primarily affected by the finite bandwidth ($\Delta E_b$) of the probe pulse, the energy resolution ($\Delta E_d$) of the detector and space-charge ($\Delta E_{sc}$). Assuming each of these broaden the measured energy with a Gaussian distribution, $\Delta E$ can be written as:

$$(\Delta E)^2 = (\Delta E_b)^2 + (\Delta E_d)^2 + (\Delta E_{sc})^2 \tag{7.3}$$

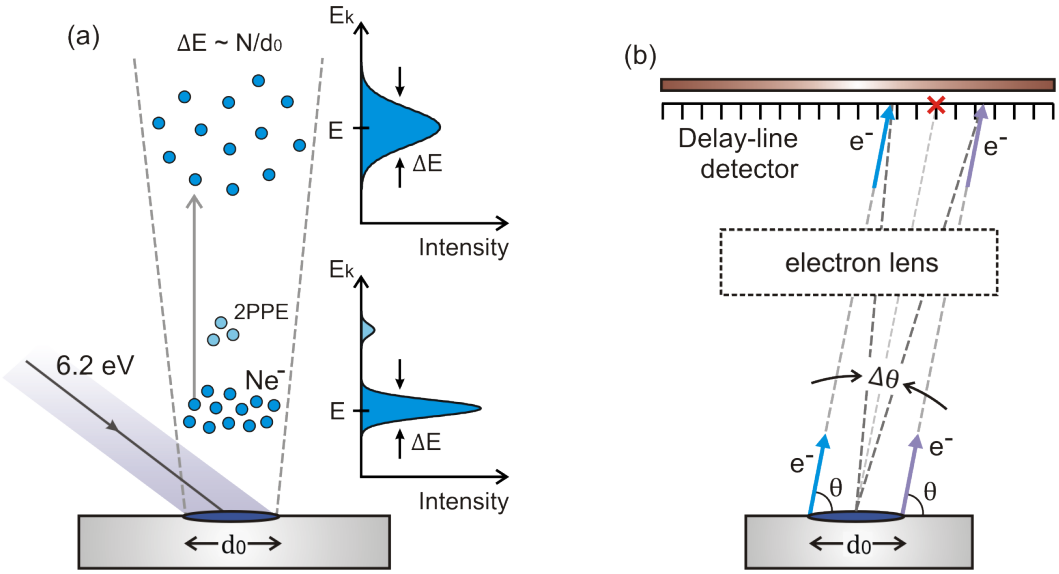


**Figure 7.4:** Schematic of the photoemission process illustrating space-charge & finite spot size effects on ARPES energy and momentum resolution. **(a)** Effect of space-charge. The probe beam impinges on the sample over an area with width $d_0$ resulting in a cloud of $N$ electrons being photo-emitted. 2PPE (two-photon photoemission) denotes electrons emitted through the simultaneous absorption of two probe photons. After propagation towards the detector, the electron cloud expands due to mutual Coulomb repulsion between electrons resulting in a broadened energy distribution as show on the right. **(b)** Effect of finite spot size. Two electrons with the same $k_{\|}$ are emitted at an angle $\theta$ from opposite edges of the finite spot-size probe (Fig. 7.4b). They are imaged at the detector at different points. The detector interprets these electrons as having different $k_{\|}$ and that difference sets the momentum resolution $\Delta k$.

As discussed above, the short time duration of the probe pulse sets a lower bound on the pulse bandwidth due to the uncertainty principle. A 150 fs pulse will have an energy bandwidth $\Delta E_b > 12$ meV. As specified by VG Scienta and in sec. 6.1.3 the detector has a resolution $\Delta E_d < 0.34$ meV and thus can be neglected in eq. (7.3). On the other hand space-charge can play a significant role in broadening the energy resolution.

**Space-charge effects:** Space-charge [188–190] refers to the repulsive Coulomb forces that photo-emitted electrons exert on each other as they travel between the sample and the detector. As shown in fig. 7.4a this lowers the kinetic energy for the lowest-energy photo-electrons while increasing the kinetic energy for the highest energy electrons i.e. effectively broadening the electron distribution and thus smearing the measured intensity. Space-charge can affect the energy resolution by as much as 10 meV [188] in ARPES experiments. Many

studies (e.g. [189–191]) have shown that the space-charge induced energy broadening $\Delta E_{sc}$ scales directly with the number of electrons ($N_e$) in the cloud and inversely with the pulse spot size on the sample ($d_0$). This is apparent since the repulsive Coulomb interaction will scale directly with the density of electrons in the electron cloud outside the sample. In our setup, the detector is capable of only measuring up to one electron per pulse. Thus, the probe photon flux (no. of photons per unit area) is adjusted so that we count less than one electron per pulse. Here it is important to note that detector count rate corresponds to the number of electrons measured within the energy window specified for the experiment (sec. 7.2). Even if the detector is measuring $< 1$ electron per pulse, significantly more than one electron can be photoemitted at the sample for every probe pulse. For example, there might be low energy photo-emitted electrons outside the energy window of the spectrometer. Another major source of electrons outside the detector energy window is 2 photon-photoemission (2-PPE) which refers to two photons being coherently absorbed by the sample to emit a single electron with kinetic energy $E_k = 2\hbar\omega - \phi$. 2-PPE can also broaden $\Delta E$ (fig. 7.4a) especially at high probe intensities as the number of 2-PPE electrons scales as the square of probe intensity. Thus, it is important to work with low probe beam intensities that do not smear out the ARPES distribution.

**Finite spot-size effects:** Similarly, $\Delta E_{sc}$ can be minimized by using a larger probe spot size ($d_0$) at the sample as that reduces the photon flux as well as the density of electrons in the photo-emitted cloud. However, increasing $d_0$ can adversely affect the angular/momentum resolution $\Delta k$ (fig. 7.4b). As explained in sec. 7.2.1, the ARTOF detector determines the momentum of an electron by recording the position at which the electron hits a 2D grid. Each point on the grid corresponds to a unique angle at which the electron is emitted from the sample and thus a unique in-plane momentum ($k_\parallel$). Now consider two electrons emitted from opposite edges of the finite spot-size probe (fig. 7.4b). Both electrons have the same $k_\parallel$ and are emitted at the same angle $\theta$ with respect to the sample but they are imaged at the detector at different points. The detector interprets these electrons as having different $k_\parallel$ and that difference sets $\Delta k$. For a probe spot size of 100 µm, $\Delta k \sim 0.001\,\text{Å}^{-1}$ for a measured

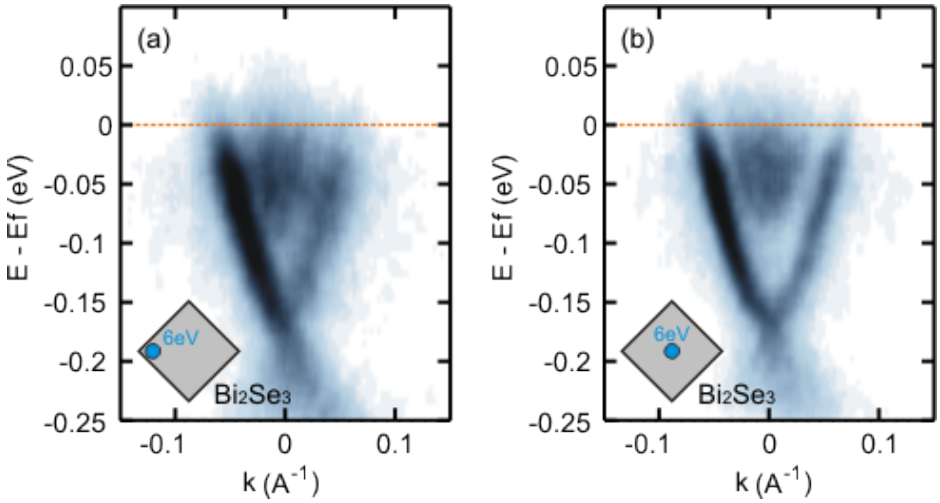


**Figure 7.5:** Sample edge effects on ARPES resolution. Data show the intensity distribution of photo-emitted electrons as a function of energy ($E - E_f$) and momentum ($k$) for a $Bi_2Se_3$ sample. In **(a)**, the probe beam is positioned near the edge of the sample while it is centered on the sample in **(b)**. Broadening of the surface states is more apparent in (a).

kinetic energy of $\sim 2\,\text{eV}$. Momentum resolution can also be affected by space-charge effects. Here two electrons emitted at the same angle repel each other to increase the uncertainty in their measured angle. Based on the above, it is clear that there is a trade-off in terms of the optimum probe size. A large probe beam reduces space-charge but broadens the measured momentum. We find that a probe size of $\sim 100\,\mu\text{m}$ at the sample optimizes both energy and momentum resolution. This was determined by adjusting the probe focusing lens right before the chamber and taking spectra at various positions.

**Sample edge effects:** As discussed in sec. 6.2.4, the strong electric field of an ultrashort pulse can lead to field emission from a metallic surface by altering the confining potential of surface electrons. The electric field of both the pump and probe beams can be significantly enhanced at the edges of the sample or around sharp defects or impurities on the sample surface. Electrons emitted through field emission will be accelerated into the lens tube and onto the detector as background noise. In addition they will also affect photo-emitted electrons through space-charge repulsion and thus worsen the energy and momentum resolution. The edge of the sample is also more likely to contain micro-sized domains possibly at different

angles with respect to the sample plane. Electrons with the same in-plane momentum but emitted from different domains will focus onto the detector at different points broadening the momentum resolution. To illustrate edge effects, we took ARPES spectra on $Bi_2Se_3$ at both the center of the sample and near the edge (fig. 7.5). As seen, the spectra at the center is much sharper than that on the edge. To minimize such edge-effects it is important to get a good cleave on the sample and work with relatively large samples ($> 1$ mm in diameter).

### 7.1.4 Pump beam: generation & characterization

There are two ways to pump the sample under study in our time resolved experiments. The simpler way is to split part of the laser beam before the harmonic conversion to excite the sample with 1.55 eV light. This pump beam can easily be guided to the chamber as it is visible with a standard white card. Similarly, it can be imaged on the sample holder making it easier to be spatially overlapped with the 6 eV probe (see sec. 7.4). Motorized ND filters can be used to adjust the fluence of the 1.55 eV pump. Finding spatial and temporal overlap between the 1.55 eV pump and the probe beams is typically the first step in time resolved experiments.

The second way is to use an Optical Parameteric Amplifier (OPA) which allows tuning the pump wavelength between 18 µm and 400 nm (corresponding to energies between 69 meV and 3 eV)) though the available energy in the pump pulse decreases significantly with increasing wavelength beyond $\sim 3$ µm. We use a Palitra OPA that is optimized at an input power of $\sim 7.2$ W at 30 kHz. The OPA uses a number of non-linear process and as such is highly sensitive to small changes in the laser pointing, bandwidth and peak power. It is recommended that the OPA be aligned and calibrated before any Tr-ARPES experiment for optimal performance.

In general, an OPA has three main stages as illustrated in fig. 7.6. In the first stage a single photon interacts with crystal with non-zero second-order susceptibility ($\chi^{(2)}$) to create two photons of lower and different energies. By conservation of energy: $\hbar\omega = \hbar\omega_s + \hbar\omega_i$, where $\omega$ is the frequency of the incoming photon while the subscripts $s$ and $i$ refer to the new photons that are created. They are typically known as the 'signal' and 'idler' with the

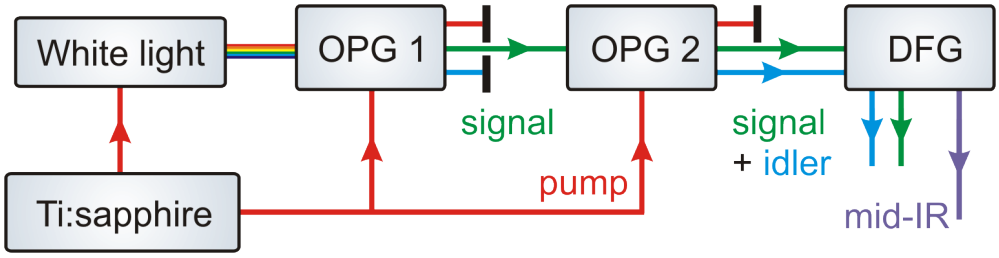


**Figure 7.6:** Stages of optical parametric amplification. OPG refers to optical parametric generation while DFG is difference frequency generation.

former referring to the photon with the higher(lower) energy(wavelength). Phase matching, as discussed above, determines which particular wavelengths are created. Phase matching is controlled by adjusting the angle of the non-linear crystal. In practice, a 'white-light' supercontinuum is used to 'seed' the first stage [192].

In the second stage (parametric amplification), the signal beam is amplified by an intense 'fundamental' beam with energy $\hbar\omega$. The fundamental photons are converted into the lower-energy signal photons and an equal number of idler photons by temporally and spatially overlapping the fundamental with the signal. In this way either the signal or the idler beam can be used to perturb (pump) the sample in Tr-ARPES experiments with a wavelength between $\sim 1\,\mu m$ and $\sim 3.4\,\mu m$. SHG and SFG of either the fundamental, signal and/or idler can extend this wavelength range down to $\sim 400\,nm$. In the third stage, also known as the IR stage, Difference Frequency Generation (DFG) is used to generate a photon with frequency at the difference between the signal and idler frequencies. Thus, the pump wavelength for Tr-ARPES can be extended all the way to $18\,\mu m$. For an IR-pump wavelength of $10\,\mu m$, the average power at the output of the OPA is $\sim 25\,mW$. Filters placed outside the OPA can be used to block the fundamental, signal and/or idler as needed.

Aligning the mid-IR pump beam is significantly harder than the $1.55\,eV$ pump beam because of its low power and high divergence. For a beam with a spatially Gaussian profile, the divergence scales linearly with the pump wavelength $\Theta \sim \lambda$. The diameter of a mid-IR beam with $\lambda = 10\,\mu m$ and beam waist $\sim 0.5\,mm$ at the OPA output expands to nearly an inch after $4\,m$ of propagation. The OPA beam needs to be guided through a distance

of nearly 7 m from the OPA to the sample in a UHV chamber without significant power loss. This is done with the use of 2" diameter gold mirrors to guide the beam. Similarly, the beam is collimated right out of the OPA and its path is then made collinear with the 1.55 eV pump using a flip mirror (see fig. 7.1). This makes it possible to spatially overlap the invisible mid-IR pump beam with the probe beam.

**Determining pump fluence & peak electric field:** Both the 1.55 eV pump beam and the mid-IR pump beam are focused onto the sample using a spherical mirror. Since the sample is in UHV, in order to determine the pump beam radius at the focus, a flip mirror is used to pick-off the pump beam right before the UHV chamber. The beam radius at the focus is determined using a horizontal slit and measuring the power after the slit as it is closed. By fitting the measured power with the open slit width to error functions, the Gaussian beam spatial parameters (FWHM, $1/e^2$ width) can be obtained. For the mid-IR OPA beam, there is typically a 50% drop in power in the beam between the OPA output and UHV chamber window. The loss is due to the mirrors, waveplates and the collimating lens. We also take into account 95% transmission through the ZeSe UHV window. For an average measured power of $P$, the pump fluence at the sample (energy per pulse per unit area) is determined as:

$$\mathcal{F} = 0.95 \times \frac{P \times 10^{-3}}{f_{rep} \times 10^6 \times (\pi/4) d^2 \times 10^{-8}} \times 10^6 \tag{7.4}$$

where $\mathcal{F}$ is the fluence in $\mu J/cm^2$, $P$ is the average power in mW, $f_{rep}$ is the repetition rate in MHz and $d$ is the beam diameter in $\mu$m. There are two common ways of defining the Gaussian beam diameter for fluence calculations. We can either take $d$ to be the FWHM or the $1/e^2$ width of the Gaussian where the latter is 1.699 times the FWHM value.

Since the intensity of a propagating Gaussian beam is related to the local electric field as $I = \frac{c\varepsilon_0}{2}|E|^2$, the peak electric field for the pump can be written as:

$$|E_0|^2 = \frac{4}{c\varepsilon_0}\sqrt{\frac{\ln 2}{\pi}}\frac{\mathcal{F} \times 10^{-2}}{\tau \times 10^{-15}} \tag{7.5}$$

where $E_0$ is in V/m, $\tau$ is the FWHM pulse duration of the pump pulse (see below) in fs, $\mathcal{F}$ is the fluence calculated from eq. (7.4), $c = 3 \times 10^8$ m/s and $\varepsilon_0 = 8.85 \times 10^{-12}$ F/m.

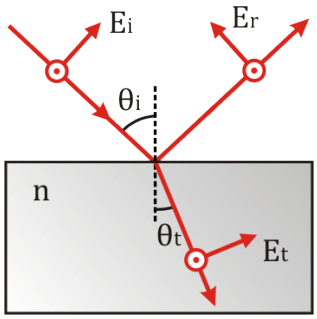


**Figure 7.7:** Geometry for computing the pump electric field inside & outside the sample for the case of P-polarized pump. $n$ is the sample refractive index. $E_i$, $E_r$ and $E_t$ are the electric fields for the incident, reflected and transmitted beams respectively. $\theta_i$ and $\theta_t$ are the angles of incidence and transmission respectively.

We note here that this is the peak electric field of the beam in free space. To determine the peak field experienced by the sample, we need to take into account the sample's refractive index $n$ to compute the reflected and transmitted fields using Fresnel equations. This is described as follows for the case when the pump electric field is parallel to the plane of incidence i.e. P-polarization.

Consider a P-polarized pump beam incident on the sample at an angle of $\theta_i$ as shown in fig. 7.6. By Fresnel equations, the reflection ($r_P$) and transmission ($t_P$) coefficients are given by:

$$r_P = \frac{n\cos\theta_i - \cos\theta_t}{n\cos\theta_i + \cos\theta_t} \tag{7.6}$$

$$t_P = \frac{2\cos\theta_i}{n\cos\theta_i + \cos\theta_t} \tag{7.7}$$

where $n = \frac{\sin\theta_i}{\sin\theta_t}$ is the sample refractive index, $\theta_i$ and $\theta_t$ are the angle of the incident and transmitted beams with respect to the surface normal. Using these, the transmitted electric field is simply $E_t = t_P E_i$, where $E_i$ is the incident electric field as computed using eq. (7.5). Thus, the in-plane ($E_{t,\parallel}$) and out-of-plane components ($E_{t,\perp}$) of the electric field experienced right inside the surface of the solid are given by: $E_{t,\parallel} = E_t\cos\theta_t$ and $E_{t,\perp} = E_t\sin\theta_t$. Similarly, the electric field right outside the sample along the surface normal is given by: $E_z = E_i\sin\theta_i + E_r\sin\theta_r$, where $E_r = r_P E_i$. In Tr-ARPES experiments,

these relationships are quite useful in determining the pump electric fields experienced by electrons both inside and outside the sample surface.

As an example consider a mid-IR $\sim 160\,\text{meV}$ pump beam incident a $Bi_2Se_3$ sample as discussed in chap. 8. From [193], the reflectance ($R = |r|^2$) of $Bi_2Se_3$ is 45% at this energy for normal incidence. This corresponds to a refractive index $n = 5.1$. Using eq. (7.6), for an incidence angle of $\theta_i = 45°$, $r_P = 0.57$ and $t_P = 0.31$. The average measured power of the pump beam is 11.5 mW at a repetition rate of 30 kHz, FWHM of 270 µm and pulse duration 250 fs. From eq. (7.4), eq. (7.5) and the corresponding relationships, we get $E_{t,\parallel} = 4.15 \times 10^7\,\text{V/m}$ taking $d$ as the FWHM, and $E_{t,\parallel} = 2.45 \times 10^7\,\text{V/m}$ taking $d$ as the $1/e^2$ width of the Gaussian. We therefore use the average value as the best estimate i.e. $E_{t,\parallel} = 3.3 \times 10^7\,\text{V/m}$. Similarly, the out-of-plane electric field right outside the surface can be computed using the above relations as $E_z = 11.6 \times 10^7\,\text{V/m}$.

**Duration of the pump pulse:** The pulse duration of the $\sim 1.55\,\text{eV}$ pump beam can be determined relatively easily using a commercially available autocorrelator. Here the pump beam is split into two parts and then recombined in a BBO crystal for SHG. Scanning the time-delay between the two parts gives the SHG intensity as a function of time from which the temporal profile of the input can be determined. On the other hand, it is not straightforward to determine the temporal profile of the mid-IR pump from the OPA. One approach is to use the rising edge of a Tr-ARPES trace. This edge can then be symmetrized around $t = 0$ to give the pump profile assuming that it is indeed symmetric.

Yet another way is to use the rising edge of the dynamics of image potential states (IPS) generated in some Tr-ARPES experiments. In general, an electron at a distance $z$ in front of a conducting surface can become trapped in the potential well formed by the Coulomb-like attractitive potential $V(z) = -e^2/4z$ of its positive image charge. Analogous to the Rydberg series of a hydrogen atom, the energies $E_n$ of the resulting states are quantized and given by $E_n = -0.85\text{eV}/n^2$ with $n = 1, 2, 3...$ [194]. The dispersion of these states is free electron-like with respect to the surface in-plane momentum. As shown in fig. 7.8a, these states can be resolved in a time resolved experiment. An initial photon, in this case

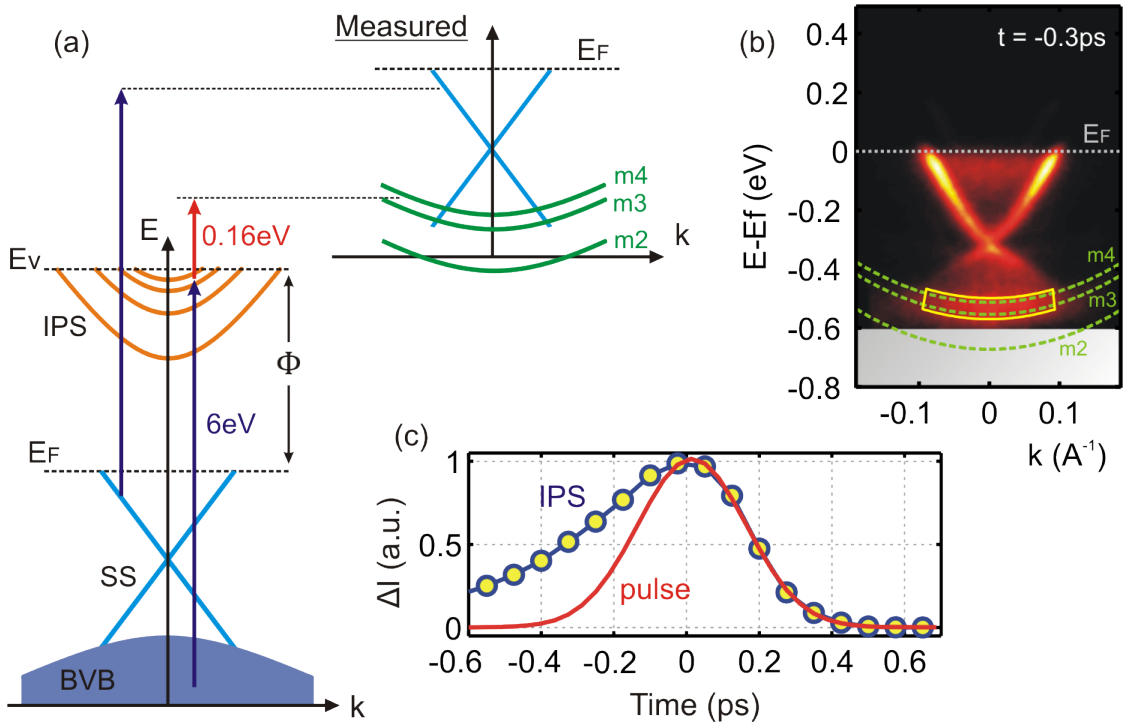


**Figure 7.8:** Image potential states (IPS) in a Tr-ARPES experiment. **(a)** Schematic of the IPS relative to the vacuum level $E_v$ and occupied states below the Fermi level $E_F$ in a topological insulator. Due to the particular pump and probe energies, the IPS are measured overlapping with the Dirac-like surface states (SS). **(b)** Tr-ARPES spectra on $Bi_2Se_3$ taken with mid-IR pump (160 meV) at $t = -0.3$ ps. Parabolic bands corresponding to $n = 3$ and $n = 4$ IPS are identified using guides to the eye. **(c)** Change in the Tr-ARPES intensity with time, integrated over the yellow boxed region in (b). Red trace indicates a Gaussian pulse obtained by fitting the right side of the IPS time profile (i.e. $t > 0$).

the photo-emitting 6 eV photon, first populates the IPS. A second pulse, in this case the mid-IR pulse, causes the electron to escape to vacuum. The resulting IPS is then resolved as parabolic bands that overlap with the equilibrium band-structure of the solid (fig. 7.8a & 7.8b). More importantly, in the generation of IPS, the role of the mid-IR pump and the photo-emitting probe are reversed. Thus, the profile of the IPS is time-reversed with respect to the time-profile of bound electronic states below $E_F$ i.e. $t \rightarrow -t$ (fig. 7.8c). The rising edge of the IPS state time-profile (for $t > 0$) can then be symmetrized about $t = 0$ to give the temporal profile of the pump pulse as shown in fig. 7.8c.

## 7.2 ARTOF system

We use an angle-resolved time-of-flight (ARTOF) spectrometer from VG Scienta to measure the kinetic energy ($E_k$) and momentum ($k$) of photoemitted electrons. As outlined in sec. 6.1.3, ARTOF works quite differently then a hemispherical spectrometer. Instead of passing electrons through a narrow slit, ARTOF collects all electrons photoemitted within a certain angle into an electron lens tube (fig. 7.9a). The tube uses a combination of 4 electrostatic lenses to focus the electrons onto a 2D detector. The detector measures the electron momentum by determining the position at which it his the 2D grid. Each point on the grid corresponds to a unique angle of emission and hence a unique $k_x$, $k_y$. The kinetic energy of electrons is measured from the time it takes the electrons to travel the meter long lens tube. In this way, both directions of the in-plane momentum and the kinetic energy are determined without rotating the sample or the detector. Below we detail each of the components of the ARTOF spectrometer:

**Electrostatic lens tube**: The lens tube has a maximum acceptance angle of $\pm 22°$ which corresponds to a maximum in-plane momentum $|k_\parallel| \approx 0.27\,\text{Å}^{-1}$ for maximum $E_k = 2\,\text{eV}$. The most common configuration of the lens tube typically accepts electrons with emission angles within $\pm 15°$ corresponding to $|k_\parallel| < 0.19\,\text{Å}^{-1}$. Each of the four electrostatic lenses in the tube has a preset high voltage applied to it as calibrated by VG Scienta. In a given voltage configuration (lens mode), the lens tube is able to focus electrons accurately within a particular energy range (window). The energy window is typically a certain percentage of the center kinetic energy of electrons being measured (fig. 7.9c). For example, the most commonly used lens mode has an energy window 50% of the center energy. If we measure an electron intensity distribution centered at 2 eV, then the detector is able to accurately measure electrons with kinetic energies between 1.5 eV and 2.5 eV. Measuring electrons outside this range would necessitate changing the center energy which results in different voltages applied to the lenses. It's important to match the lens mode being used with the corresponding electrical connections on the high-voltage supply.

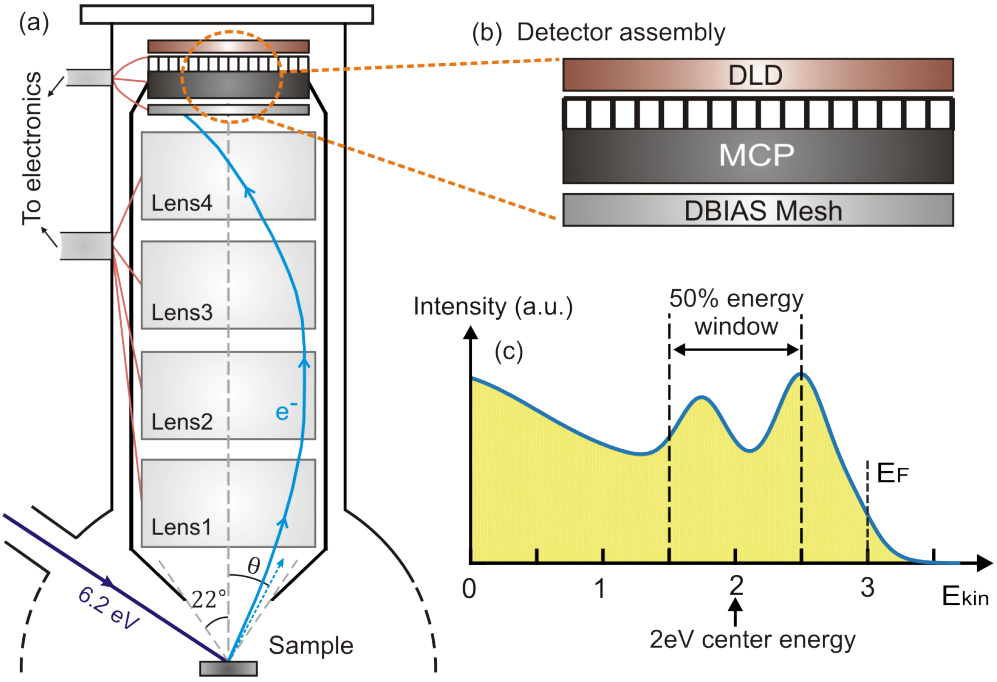


**Figure 7.9:** ARTOF lens tube, detector & energy window. **(a)** Schematic of the ARTOF lens tube and the path of a photo-emitted electron. Electrons emitted within a 22° cone can be collected into the tube which consists of four electro-static lenses. Pre-set voltages are applied to these to control the trajectory of the electron. **(b)** The detector stack consists of the DBIAS mesh to which a high bias voltage can be applied to filter out low-energy electrons. The multi-channel plate (MCP) amplifies the electron signal onto the delay line detector (DLD). **(c)** Energy-window for the most commonly used lens mode. Here the ARTOF lens tube is able to resolve the energy of and momentum of electrons emitted with energy within 50% of the desired center energy, in this case 2 eV

**DBIAS mesh plate**: The mesh plate is an extremely thin wire grid in front of the detector while DBIAS refers to detector bias. Applying a positive voltage to the mesh plate repels photoemitted electrons from the detector. In this way, the mesh plate acts as a high-pass filter and can be quite useful if only electrons beyond a certain kinetic energy need to be detected. This can speed up data acquisition. It is also useful in ensuring optimum spatial overlap of the pump and probe beams on the sample. We first set the DBIAS voltage to block all electrons below the Fermi-level and adjust the pump position on the sample to maximize the electron counts above the Fermi-level.

**Multi-channel plate (MCP)**: This amplifies the incoming electron signal and deter-

mines the flight time of the electrons. The MCP is a silicon wafer which consists of tiny micro-channels ($\sim 10\,\mu m$ in diameter). There is typically a high-voltage difference across the plate ($\sim 2000\,V$). As a result, an electron incident on the front of the MCP generates more electrons as it bombards the walls of a micro-channel. This 'avalanche' effect amplifies each incoming electron signal which is then used on the delay line detector to determine the electron position. In practice, two MCPs are stacked on top of each other and rotated 180° with respect to each other such that their micro-channels form a V-shape (chevron configuration). This optimizes the gain and prevents electron feedback in the MCP. It's crucial to preserve this configuration when replacing the MCPs. The MCPs can easily be damaged if the incoming electron flux is too high. Each MCP stack typically lasts for slightly more than a year if the count rate is kept less than 20,000 counts/second. Gradually 'dark' spots will be developed on the MCP stack with lower sensitivity (gain) and this can produce artifacts in the ARPES spectra. These artifacts are known as detector inhomogeneities and should be considered carefully in analyzing the data. The voltage on the MCP can be increased as well to temporarily increase the gain at the 'dark' spots though that will degrade the MCP faster. To determine flight-time of the electron, the ARTOF electronics compare each MCP event time ($t_e$) with the time at which the laser pulse hits the sample ($t_p$) as the MCP is triggered by the laser repetition rate. That time difference corresponds to the electron flight time. To calibrate $t_p$, the 'photon peak' is used (see below).

**Delay-line detector (DLD)**: The DLD is situated right after the MCP stack and measures the angle at which electrons are photoemitted from the sample. It does this by noting 2D position of the electron pulse amplified by the MCP. The DLD is basically a 2D grid and consists of two perpendicularly thin copper wires looping around a ceramic block (fig. 7.10). When the amplified electron pulse hits the DLD it generates two counter-propagating pulses along each wire. The times the two pulses take to travel to the ends of a wire are recorded and subtracted to determine the exact position at which the electron hit that particular wire. Each wire corresponds to each spatial dimension. The DLD outputs 4 signals ($x_1$, $x_2$, $y_1$, $y_2$) corresponding to the pulse travel time from the ends of each wire.

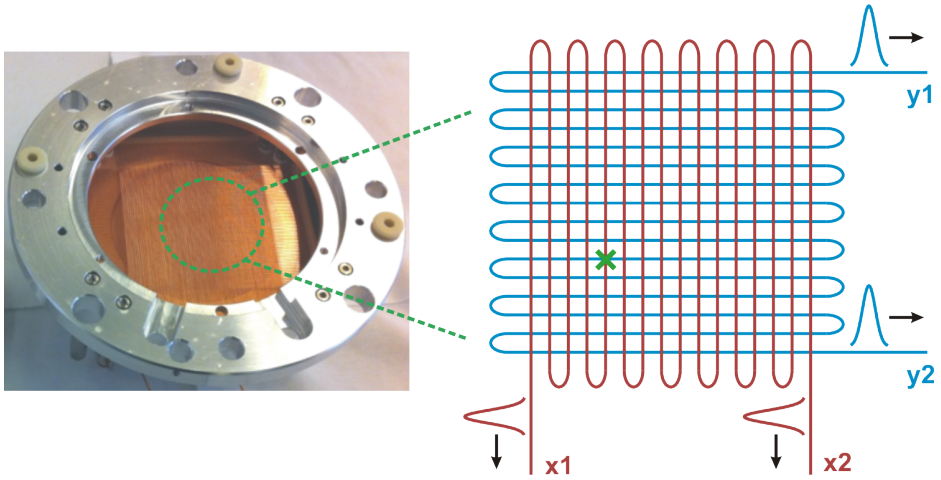


**Figure 7.10:** Picture and schematics of a the delay line detector (DLD) which consists of two perpendicularly thin copper wires looping around a ceramic block. When an electron pulse hits the DLD, two countr-propagating pulses are generated along each wire. The times the two pulses take to travel to the ends of a wire $x_1$, $x_2$ and $y_1$, $y_2$ are recorded to determine the exact position at which the electron hit the detector. This spatial position is then used to determine the in-plane electron momentum.

For a hit to be 'consistent', all 4 signals must have a value and the quantities $x_1 + x_2$ and $y_1 + y_2$ must be a constant since that corresponds to to the length of each wire. Combined with the MCP event timing, we thus get three values ($t$, $x = x_1 - x_2$, $y = y_1 - y_2$) for each electron hit. It's important to note that this way of measuring position prevents the DLD from distinguishing between different electron hits that occur at the same time. The DLD electronics trigger from the laser repetition rate. If two or more DLD hits occur within one trigger event, all the hits are discarded. This explains why the electron count rate is limited by the laser repetition rate i.e. the DLD can at most measure one electron per laser pulse.

### 7.2.1 ARTOF alignment & calibration

To determine the energy and momentum accurately from the ARTOF spectrometer proper beam/sample alignment and calibration of the timing and work function is necessary.

**ARTOF alignment:** As discussed above, the angle of emission of an electron is determined by the electron's position on a 2D grid. Here the detector assumes that the electron was photoemitted from a position on the sample that is in line with the detector

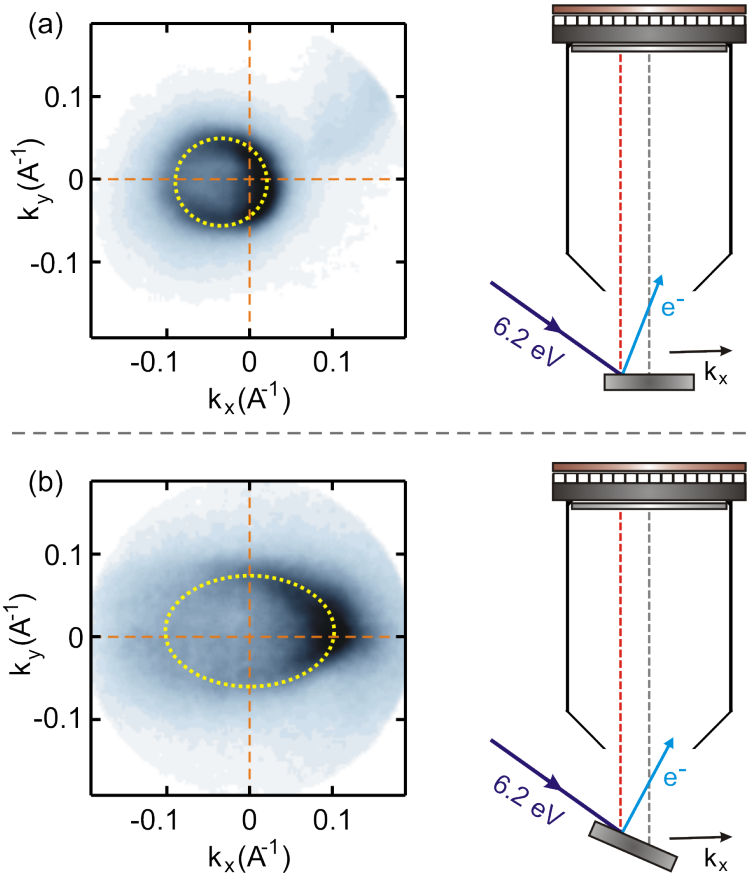


**Figure 7.11:** Examples of misaligned ARPES spectra taken on $Bi_2Se_3$ The spectra shown are constant energy cuts at the Fermi-level. Gray dashed line (right) indicates the detector center axis. For proper alignment, the probe beam should hit the sample where the gray line meets the sample-plane. In **(a)** the photo-emitting probe beam hits the sample away from the detector center and the sample is parallel to the detector. This results in the circular Fermi-surface being shifted away from the $(k_{x,y} = 0)$. If the sample is now tilted as shown in **(b)**, the Fermi-surface is centered but imaged as an ellipse instead of a circle.

center (fig. 7.11). Moreover, for the center of the detector $(x, y = 0)$ to correspond to zero in-plane momentum, the sample plane has to be parallel with the detector plane. These alignment issues can result in an inaccurate momentum determination as shown in fig. 7.11.

To ensure proper alignment, we use two guiding HeNe laser beams through opposite windows in the UHV chamber such that they intersect directly at the center of the chamber. The sample holder is then moved such that we can image the spatial overlap of the beams. The $\sim 6.2\,\text{eV}$ beam is then made to overlap with these two beams on the sample holder.

This sets the proper distance between the detector and the sample (1 m) and ensures that the $\sim 6.2$ eV beam meets the sample in-line with the detector center. The other variable is the tilt of the sample which has to be adjusted to ensure that it is parallel to the detector (to center spectra at $k_{\parallel} = 0$). This can be especially challenging for rough samples. Even if the sample holder is parallel to the detector, cleaving the sample in-situ can result in crystal faces at different angles with respect to the sample holder. One way to get the correct tilt is to reflect the HeNe guiding beam from one UHV window into its opposite window. In practice, we adjust the tilt to ensure that the measured spectra corresponds well with spectra already measured in literature.

**Determining photon timing:** The flight-time of the electron is the difference between time at which the the electron leaves the sample and and the time at which it reaches the detector (determined by the MCP). Since the former is hard to determine, we use the time at which the photoemitting pulse hits the sample relative to the trigger. This is known as 'photon timing'. Some of the scattered photons from the sample hit the MCP and cause photoionization to generate a single 'photon peak' in the spectra. This peak precedes all electron signals. A useful way to detect this peak is to use a high DBIAS voltage which blocks all photoemitted electrons from reaching the MCP. The ARTOF software determines the timing of each event with respect to the electronic trigger provided by the Wyvern system.

**Determining work function:** The ARTOF detector determines the kinetic energy $E_k$ of a photo-emitted electron by its flight-time. To convert $E_k$ into the binding energy of an electron $E_B$, we need to determine the sample work-function. From eq. (6.1), it is clear that the smallest $E_B$ that can be measured is simply $\hbar\omega - \phi$, where $\hbar\omega$ is the energy of the photo-emitting probe beam. This is known as the low energy cut-off and can be determined by lowering the center energy until the intensity-energy distribution has a sharp-cutoff within that particular energy window. Here we note that this cut-off is actually determined by the detector workfunction ($\phi_d$) rather than the sample workfunction ($\phi_s$). Since the sample and the detector share the same electrical ground (through the sample holder and the electronics), their chemical potentials equilibrate resulting in a potential of

$\phi_s$ - $\phi_d$ between them. Photoemitted electrons accelerate towards the detector and their kinetic energy increases by $\phi_s$ - $\phi_d$ i.e. $E_k = \hbar\omega - \phi_s - E_B + (\phi_s$ - $\phi_d) = \hbar\omega - E_B - \phi_d$. For our particular detector $\phi_d \approx 4.2 - 4.3\,\text{eV}$.

## 7.3 Vacuum system & sample preparation

As discussed in fig. 6.3, the electron escape depth in solids is typically only a few nm for the electron kinetic energies in ARPES experiments. The electrons measured by ARPES originate from only a few top-most layers at the surface of the solid. Any impurities or defects on the sample surface inelastically scatter the electrons as they are photoemitted and thus, obscure the measured energy-momentum band structure (fig. 7.5). Thus, it is important to use samples with homogeneous and clean surfaces.

The surface quality can deteriorate quickly as absorbates from the environment deposit on the surface. This is overcome by performing ARPES experiments in an ultra-high vacuum (UHV) environment with a pressure $< 1 \times 10^{-10}\,\text{Torr}$. The sample is cleaved in this UHV to obtain a fresh surface before measurement as discussed below. Nevertheless, any residual gas in the chamber can still deposit impurities on the surface and so its quality worsens over time. For example, the worsening surface of a freshly cleaved $Bi_2Se_3$ sample starts to broaden the measured Dirac cone surface states after about 1 day. Eventually by the 3rd day the surface states are no longer resolvable and only a broad continuum of occupied states is visible.

### 7.3.1 UHV components

The UHV chamber consists of two parts: the smaller preparation (prep) chamber in which samples are loaded and stored and the larger main chamber in which measurements are performed. A gate valve is used to isolate the two chambers. The prep chamber consists primarily of a sample holder storage unit ('the garage') that can hold upto 4 sample holders. This garage is loaded by opening up a flange in the prep chamber while the gate valve is closed to preserve the UHV the main chamber. The prep chamber is then baked (see below),

pumped out and cooled until the pressure reaches UHV. The sample holder is transferred from the prep chamber to the main chamber using a transfer arm.

The main chamber consists of 6-axis goniometer which holds the sample holder during measurements. This has three translation axes and three rotation axes and can be cooled down to 20 K. This chamber also houses the ARTOF lens tube and detector along with a wobble stick arm that can be used to cleave the samples in-situ. Conflate flanges with windows provide access for the pump and probe beams onto the sample. The main chamber is also shielded by two layers of $\mu$-metal sheets inside UHV that expel any stray magnetic fields. The two chambers are pumped down to a pressure $< 1 \times 10^{-10}$ Torr using a combination of roughing, turbo, ion and titanium sublimation pumps as outlined below.

The roughing/backing pump is a rotary vane pump attached to the prep chamber through the turbo pump. With both the main chamber and prep chmaber initially at room pressure, this pump is started to get the pressure down to $1 \times 10^{-2}$ Torr. It does this in about 30 minutes after which the turbo pump is turned on to reduce the pressure to $1 \times 10^{-7}$ Torr. At this point, the out-gassing rate of the absorbed molecules on the walls of the UHV chamber equals the pumping speed of the turbo pump and the pressure does not go down further. To overcome this limitation, the chambers are baked from the outside to a temperature $> 100$ K. This increases the out-gassing rate which at first increases the pressure. Eventually, over the course of a week, the pressure drops down to $1 \times 10^{-8}$ Torr as absorbed water molecules are removed. The chamber is then cooled to room temperature which brings the pressure down to high $10^{-10}$Torr.

The turbo pump is not able to reduce the pressure any further since its pumping efficiency is quite low for light molecules such as hydrogen. To remove such gases, an ion pump is used which ionizes molecules in the chamber and then accelerates them onto an electrode using a strong electric potential. In addition to this, a titanium sublimation pump (TSP) is also used to bring the final pressure to $< 1 \times 10^{-10}$ Torr. The TSP consists of a thin titanium filament through which a high current is passed. This sublimates the titanium which then gets deposited on the chamber walls to form a thin coating. This limits out-gassing of the chamber

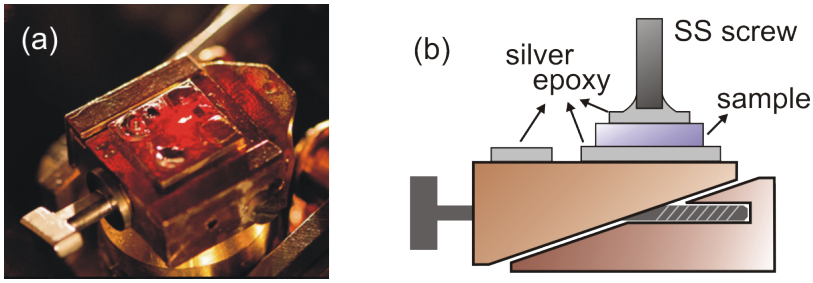


**Figure 7.12:** **(a)** Picture of the sample holder for ARPES inside the UHV chamber. **(b)** Schematic of the sample holder before cleaving mounted inside the chamber. The sample holder screws onto the mount on the goniometer. The is mounted between two layers of silver epoxy with a stainless-steel screw attached on top. This screw is hit with a wobble stick to cleave the sample. A small layer of silver epoxy is left exposed (left) to see the fluorescence of the 6.2 eV probe beam.

walls and any residual gases in the chamber can react with titanium to form a solid product on the walls. The TSP is typically turned on for only about 7 minutes after the initial bake-out.

To load samples, the gate valve is closed and the prep-chamber is vented while keeping the ion pump on in the main chamber. Once samples are loaded, the prep-chamber has to be baked for about 24 hours so that the pressure inside matches that in the main chamber. The ion pump is located directly below the ARTOF detector and so it can cause ions to directly impact the detector which results in background noise in the measured spectra. To prevent this, we turn off the ion pump during measurement while keeping the gate valve open so that the turbo pump can preserve the pressure in the main chamber.

### 7.3.2 Sample preparation & cryogenics

As discussed before, the samples for ARPES measurements need to have uniform surfaces free from defects. To achieve this, relatively large ($> 1\,\text{mm} \times 1\,\text{mm}$) are mounted on the sample holder. Generally, the larger the samples, the better the cleave. The sample holder (Fig. 7.12) is made from high thermal conductivity copper to ensure that the sample is in good thermal contact with the helium cryostat. This holder has a screw like knob that threads into mounts inside the UHV chamber.

The top of the sample holder is about $1\,\text{cm} \times 1\,\text{cm}$. Samples are cut into roughly square shapes and 'glued' onto the top using conductive silver epoxy to ensure good electrical and

thermal contact between the holder and the sample. A thin stainless steel screw is then mounted on top the sample using silver-epoxy (EPO-Tek H20E) to cleave the sample once it is inside UHV. Torr-seal or ceramic posts can also be used for this purpose however they can get electro-statically charged and thus affect the energy and momentum of the photoemitted electrons. One way to prevent this charging is to coat exposed insulating surfaces on the sample holder with conductive graphite paint. Typically 4 to 5 samples are mounted on one holder. We also leave some silver paint exposed on a small part of the sample holder to help achieve spatial overlap between the pump and probe beams (sec. 7.4).

Once inside the main chamber, the sample is cleaved by hitting the stainless steel screw with the wobble stick. For layered single crystals, the bonding force between the silver epoxy and the top-most layer is stronger than the van der Waals force between layers. This results in the top-most layer being removed if the screw is hit. Nevertheless, a good cleave is not guaranteed even for high-quality crystals like $Bi_2Se_3$. A bad cleave results in laser induced field-emission from the high intensity mid-IR pump beam which obscures the real signal as discussed in sec. 6.2.4.

The sample holder can be cooled down to $\sim 20\,\mathrm{K}$ using a copper braid connected to a cold finger of an open-cycle liquid helium cryostat. To cool the cryostat, a helium transfer line is inserted through the goniometer. A hermetically sealed diaphragm pump is used to pump liquid helium into the cryostat. Previously, the cryostat would get to base temperature in about 6 hours. This was due to a bad vacuum in the walls of the helium transfer line. This evaporates the liquid helium in the inner capillary of the transfer line before it reaches cold finger. To overcome this, the region between the inner capillary and the outer walls is pumped out using a turbo pump. In this way the cryostat can get to base temperature in about 2 hours. The helium consumption rate is 2 L/hour at $\sim 20\,\mathrm{K}$ and 1 L/hour at $\sim 30\,\mathrm{K}$.

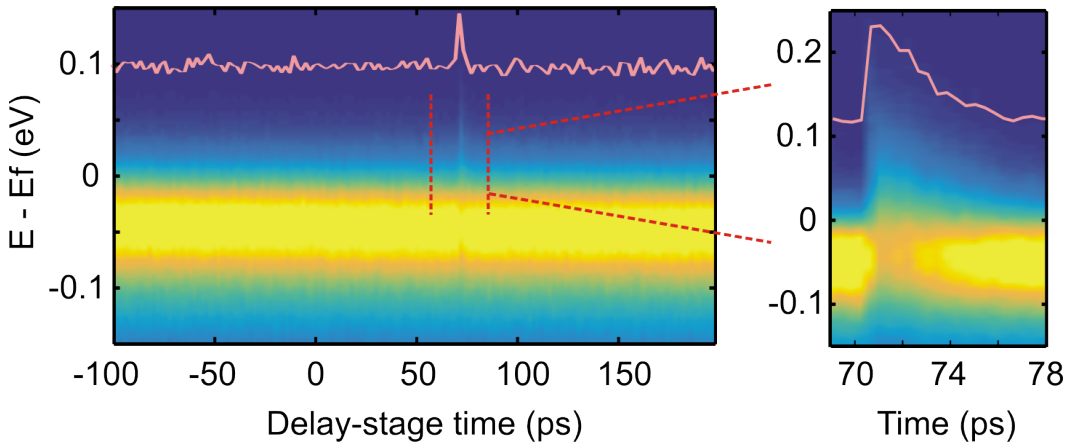


**Figure 7.13:** Finding time-zero in Tr-ARPES. The plots show the momentum-integrated intensity distribution of photo-emitted electrons as a function of $E - E_f$ and delay between the pump and probe as determined by the position of the stepper-motor stage (see text). This particular Tr-ARPES scan was taken on $Bi_2Se_3$ using a pump energy of $\sim 0.9\,\text{eV}$ from the OPA. The sharp spike corresponds to the stage position when the pump and probe pulses overlap in time at the sample. This position is known as time-zero. Pink traces in the figure correspond to the change in intensity at $E - E_f = 0.1\,\text{eV}$.

## 7.4 Tr-ARPES alignment

To get a pump-induced Tr-ARPES signal, the pump and probe beams must be spatially and temporally overlapped on the sample surface in an iterative process. Spatial overlap is relatively simpler to achieve for the 1.55 eV pump beam as this is directly visible on the sample holder. Similarly, the 6.2 eV probe beam causes the silver epoxy on the sample holder to fluorescence in the UV which also makes it visible. The position of these two beams can then be imaged onto the sample holder using a camera mounted right outside one of the windows in the UHV main chamber. The pump beam is then visibly overlapped with the probe beam on the silver epoxy using steering mirrors outside the chamber. Usually this is good enough to obtain a small pump-induced signal which can then be optimized. The sample holder is then moved such that these beams impinge on the sample.

The overlap of the mid-IR pump with the probe is significantly harder as it cannot be directly imaged. To achieve overlap, the mid-IR pump beam is made collinear with the 1.55 eV pump beam by using a pair of irises near the OPA (I1 and I2 in fig. 7.1). Ideally,

the mid-IR pump should then follow the same path as the 1.55 eV beam and should be overlapped with the probe. This is checked by using a flip-mirror right before the main chamber. Once spatial overlapped is optimized between the 1.55 eV pump and the probe beam, the flip-mirror picks-off the 1.55 eV pump beam before the chamber and passes it through a 100 µm pinhole placed at the focus of the last spherical mirror before the chamber. The position of the pinhole roughly corresponds to the position of the probe beam on the sample. The mid-IR pump beam is then made to pass through this pinhole. This procedure is usually sufficient to obtain a rough spatial overlap.

Temporal overlap between the pump and probe pulses is the key to all pump-probe type experiments. For our case, the time delay between the two is adjusted using a motorized stepper stage place in the probe beam path. For temporal overlap, initial alignment requires that the pump pulse hits the sample within the scan range of the delay stage which is about 1 ns $\sim$ 30 cm. Once a rough spatial overlap is achieved, a Tr-ARPES trace is taken over the full scan range of the stage to find $t = 0$. A reasonable step-size to use for this initial trace is 2 ps. An example of this initial Tr-ARPES trace, integrated over all momenta, is shown in fig. 7.13. The sharp spike seen in the intensity above $E_F$ corresponds to $t = 0$. Once this is found, scans with finer time steps are taken to narrow down the exact position of $t = 0$ to within $\pm$50 fs.

To optimize the spatial overlap, a trace is run at $t = 0$ and a high enough DBIAS is applied to block electrons below $E_F$. In this way, the total photoelectron intensity measured corresponds to the pump induced signal. This intensity is then maximized by using the pump steering mirror.

*"Lead will play its role until the world has no further need for lead; and then lead will have to turn itself to gold."*

— Paulo Coelho, *The Alchemist*

# 8

# Floquet-Bloch states on the surface of topological insulators

## Contents



The coherent optical manipulation of solids is emerging as a promising way to engineer novel quantum states of matter. The strong time periodic potential of intense laser light can be used to generate hybrid photon-electron states. Using time and angle resolved photoemission

spectroscopy (Tr-ARPES), we demonstrate that mid-infrared photons hybridize with the surface Dirac fermions of the topological insulator $Bi_2Se_3$ to form states that repeat in both momentum and energy. These Floquet-Bloch states exhibit band gaps at avoided crossings which are dependent on the incident light polarization and the electron momentum. Circularly polarized light induces an additional gap at the Dirac point by naturally breaking time reversal symmetry. We further characterize our findings in terms of the interference between Floquet-Bloch and Volkov states which are generated by photons interacting with free electrons near the surface. We find that the coupling between the two strongly depends on the electron momentum, providing a route to enhance or inhibit it. Moreover, by controlling the light polarization we can negate Volkov states in order to generate pure Floquet-Bloch states. The time dynamics of photon-dressed states in $Bi_2Se_3$ are also compared with those in $Bi_2Te_3$. Overall, these results establish a systematic path for the manipulation of electronic states in a solid.

## 8.1 Periodically driven quantum materials

Periodically driven systems are emerging as promising platforms to realize novel quantum states of matter. Temporal modulation of a quantum system can be used to generate new phases via Floquet theory, as has been recently realized in ultra-cold fermions [195] and in photonic crystals [196]. A prominent example of a driven solid-state system is the likely enhancement of superconducting-Tc in the certain cuprates in which (e.g. [23, 24]) mid-IR or THz photons first generate a coherent phonon mode in the system which then couples to the electronic system. While the mechanism of this enhancement is still under major debate, the intriguing results have invited comparison to the Kaptiza pendulum [197], implying the transient stabilization of a generically non-equilibrium phase by electrons coherently coupling to the generated phonons. Another approach, which will be the main subject of this chapter, is to directly couple photons to an electronic system to create hybrid electron-photon states.

In this case, the oscillating electric field of an intense laser pulse causes electrons in a crystal to experience a time-periodic potential, the effects of which are discussed below.

### 8.1.1 Electrons in a time-periodic potential

To understand how a time-periodic potential effects electrons, it is useful to review Bloch wavefunctions for electrons in a periodic solid. From basic solid-state theory, it is well known that an electron in a crystal experiences a spatially periodic potential i.e. its Hamiltonian is periodic, $H(\mathbf{r}+\mathbf{R}) = H(\mathbf{r})$. By Bloch theorem, the electron wave-function can be written as

$$\psi_{\mathbf{k}}(\mathbf{r}) = \mathrm{e}^{i\mathbf{k}\cdot\mathbf{r}} u_{\mathbf{k}}(\mathbf{r}) \tag{8.1}$$

where $u(\mathbf{r}) = u(\mathbf{r}+\mathbf{R})$ is a strictly periodic function and thus can be expressed as a Fourier series in the reciprocal lattice vector $\mathbf{G}$. In this way, the electron wavefunction repeats in momentum space with spacing equal to $\mathbf{G}$ (fig. 8.1a). This way of expressing the wavefunction highlights the conjugate relationship between $\mathbf{r}$ and $\mathbf{k}$. Moreover, at the Brillouin zone boundary Bloch wavefunctions mix to open up an energy gap whose magnitude is characterized by the energy scale of the spatially periodic potential.

The above described Bloch theorem is a solid-state analogue of the Floquet theorem which can also be used to solve a time-dependent Hamiltonian that is periodic in time i.e. $H(t+T) = H(t)$. In this case the Schrödinger equation is:

$$(H(t) - i\hbar\frac{\partial}{\partial t})\psi(t) = 0 \tag{8.2}$$

Analogous to eq. (8.1) and using the conjugate relationship between energy and time, the wavefunction can be written as:

$$\psi_\alpha(t) = \mathrm{e}^{-i\epsilon_\alpha t/\hbar}\phi_\alpha(t) \tag{8.3}$$

where $\phi_\alpha(t) = \phi_\alpha(t+T)$ are the periodic Floquet modes and $\epsilon_\alpha$ are the quasienergy levels being unique up to multiples of $\hbar\omega$, where $\omega = 2\pi/T$. From eq. (8.3), we can notice that the Floquet modes $\phi_{\alpha n}(t) = \phi_\alpha(t)e^{in\omega t}$ yield identical solutions to eq. (8.2) as eq. (8.3) but

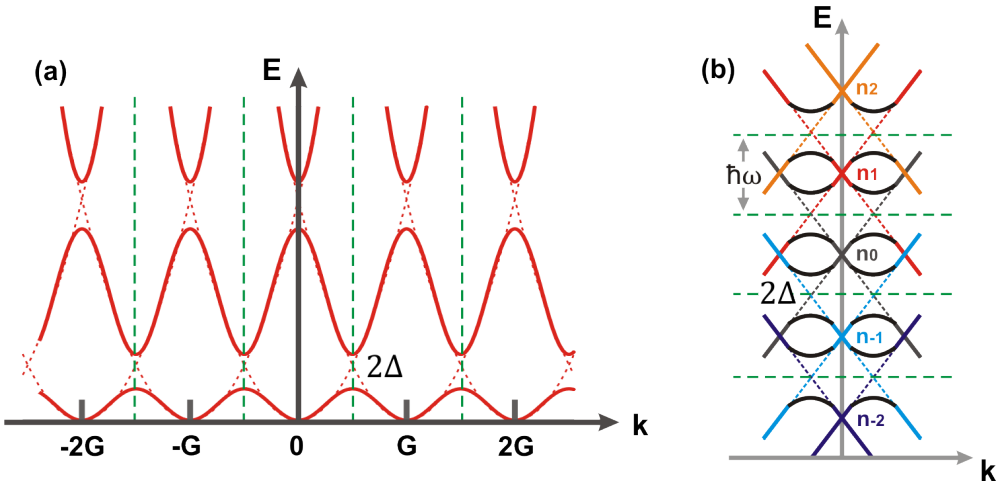


**Figure 8.1:** Representatative diagrams of Bloch & Floquet states. **(a)** Bloch wavefunctions repeat in momentum space with spacing given by the reciprocal lattice vector **G**. Green lines indicate the zone boundaries where gaps with magnitude $2\Delta$ open up. **(b)** Floquet modes repeat in energy space with spacing given by the frequency of the driving potential $\omega$. Dynamic gaps open up where modes with different $n$ intersect.

with shifted quasienergies i.e. $\epsilon_\alpha \rightarrow \epsilon_\alpha + n\hbar\omega$, with $n$ being an integer. Thus, similar to Bloch wavefunctions, Floquet states repeat in energy with spacing equal to $\hbar\omega$ (fig. 8.1b). In addition, Floquet modes with different $n$ interact to open up dynamic gaps at quasi-energy zone edge boundaries. The magnitude of these gaps is dictated by the energy scale of the time-periodic potential. Evidence for Floquet modes can be seen as hybridized states in atoms and molecules ([198]) and in photonic systems ([196]).

If electrons in a solid-state system experienced a time-periodic potential, their Hamiltonian can be separated into spatial and temporal parts i.e. $H(\mathbf{r}, t) = H(\mathbf{r}) + H(t)$ where $H(\mathbf{r}+\mathbf{R}) = H(\mathbf{r})$ and $H(t+T) = H(t)$. From the discussion above, it is clear the electron wavefunction can be written in terms of states that repeat in both energy and momentum. These states are what we call Floquet-Bloch states and they will be the main subject of this chapter.

In order to detect Floquet-Bloch states in an experiment it is important to drive the solid coherently with a strong time-periodic potential and simultaneously measure the resulting band structure. As seen in chap. 6, Tr-ARPES provides a unique way of measuring the electronic band-structure of a crystal as it is being pumped by a laser

pulse. Here the oscillating electric field of the pulse naturally provides a time-periodic perturbation which will result in Floquet-Bloch states separated in energy by $\hbar\omega$ where $\omega$ is the frequency of the pump pulse. This way of detecting Floquet-Bloch states in a solid was first realized by Wang et al. [27].

Recently, there has been significant theoretical interest in Floquet-Bloch states primarily in the context of engineering band structures in solid state systems. For example, it has been proposed that trivial equilibrium bands can be driven by a laser into topological non-equilibrium Floquet bands [199–210]. Such systems have been termed as Floquet-topological insulators [202]. There is also interest in using Floquet states to understand non-equilibrium periodic thermodynamics [211, 212]. Similarly, it is not clear how Floquet modes behave in interacting systems and how they couple to existing collective excitations in the system such as phonons [213–216]. In terms of materials systems, theory has primarily focused on graphene to understand Dirac electronic states driven by a periodic light pulse [199, 203, 204, 206–209, 217]. To understand Floquet-Bloch states, this work will rely on Tr-ARPES measurements on the surface of a topological insulator, which like graphene, has a Dirac electronic dispersion which is also protected by time-reversal symmetry.

## 8.2 Topological insulators

Topological insulators are a class of bulk insulators that are characterized by metallic edge/surface states protected by time-reversal symmetry (TRS). Recently, there has been considerable theoretical and experimental progress on these materials and excellent references to understand them include [135, 136, 218–220]. This section briefly overviews the development of key concepts and properties of topological insulators that are relevant to this work.

As outlined in chap. 1, phases of matter have historically been classified according to the symmetries they break (e.g. broken translation symmetry in charge density wave order or broken gauge symmetry in superconductors). This changed with the discovery of the integer quantum Hall (QH) insulator in 1980 [5]. Here electrons confined in two dimensions

undergo closed cyclotron orbits and form Landau levels under a strong magnetic field. As a result, the bulk of this two dimensional electron gas (2DEG) is insulating and has an energy gap. However, at the edges of the 2DEG electrons cannot complete full orbits but instead 'skip' along to form 1D longitudinal conduction channels. These metallic edge states arise because the wave-function of electrons executing a closed orbit in the 2DEG is topologically distinct [221] from the wave-function of free electrons in vacuum. Thus, as the wave-function transitions from the 2DEG bulk to vacuum, the gap has to close at the edge in order for the topology to change leading a linear dispersion for these edge states in momentum space.

Studying the above described QH insulator was challenging as it required low temperatures and high magnetic fields to observe the quantized phenomena. As discussed in sec. 5.1, spin-orbit coupling (SOC) can lift the spin degeneracy of electrons and open up an energy gap in the bulk of a material. It was shown by Kane et al. [12, 222], that strong SOC in certain insulators can play an analogous role to the external magnetic field in a QH insulator leading to similarly robust edge states but without a magnetic field. However, in this case the edge states are spin polarized and spin-up electrons propagate in one direction while spin-down electrons propagate in the opposite direction. These states are usually called helical edge states and the resulting class of materials in 2D is referred to as a quantum spin Hall (QSH) insulator. These were the predicted to exist in HgTe quantum wells by Bernevig et al. [13] and subsequently discovered by König et al. [14].

In a QSH, the spin-polarized edge states are protected by time-reversal symmetry (TRS). Since electron states in $\mathbf{k}$ and $-\mathbf{k}$ have opposite spins, an electron must necessarily flip its spin in order to back-scatter. This results in spin polarized edge states that are immune to non-magnetic disorder. In momentum space, these edge states are linearly dispersing similar to the case for a QH insulator but opposite spin states are mirror images of each other about $k = 0$.

A useful way to understand these edge states is through Kramers theorem which states that for any Bloch state $\psi_{k,\sigma}$ there is another state $\Theta\psi_{k,\sigma} = \psi'_{-k,-\sigma}$ which has the same energy, where $\Theta$ is the time-reversal operator. These states are known as the Kramers doublet and are located at opposite momenta ($k$ and $-k$). However at $k = 0$ or at the Brillouin

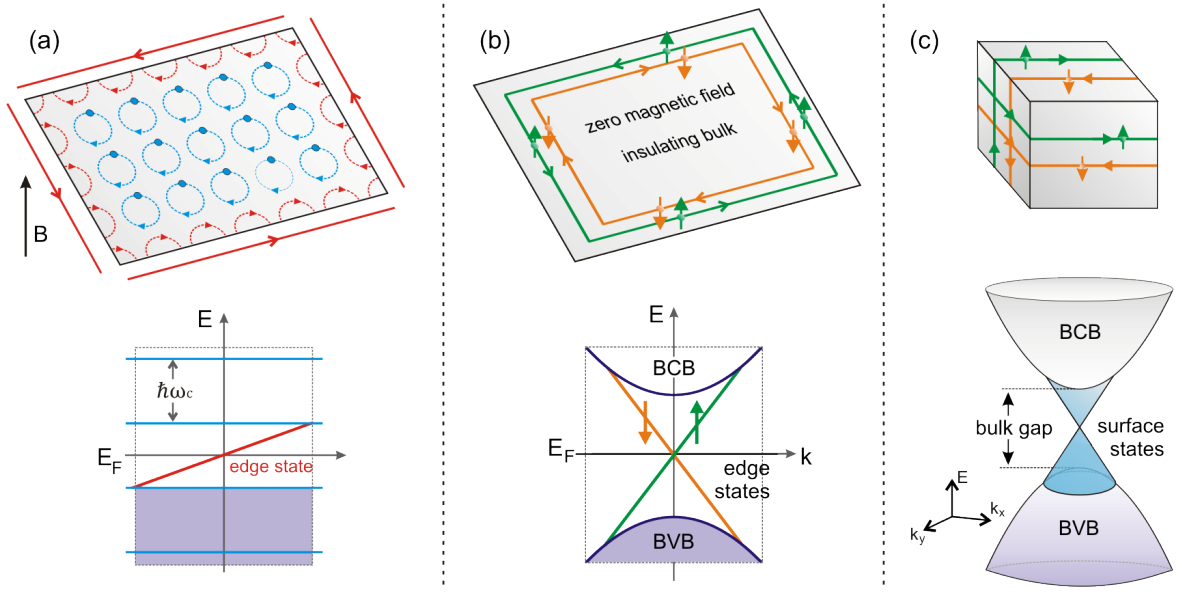


**Figure 8.2:** Real (top) & momentum (bottom) space representations of quantum Hall (QH), quantum spin Hall (QSH) & 3D topological insulator. **(a)** QH insulator: a 2D electron gas in a magnetic field (B) develops cyclotron orbits in the bulk (blue) and longitudinal conduction channels at the edges (red). A gap corresponding to the cyclotron frequency $\omega_c$ opens up in the bulk. **(b)** A QSH insulator has an insulating bulk in 2D without a magnetic field but spin polarized conducting 1D edge states. Spin-up electrons propagate in one direction while spin-down electrons propagate in the opposite direction. **(c)** A 3D TI has an insulating bulk in 3D but a conducting surface with the spin of the electron locked to its momentum.

zone edge i.e. at $k = \pi$, $k = -k$ and the states are double degenerate (one for each spin). Consider mid-gap states between the conduction and valence bands in an insulator. Away from $k = 0$ and $k = \pi$, SOC lifts this degeneracy and opposite spins have opposite momenta. Since energy is a smooth function of $k$, the mid-gap states at $k = 0$ and $k = \pi$ need to be connected which can be done in two possible ways. In one case or the trivial insulator case, the two degenerate states at $k = 0$ are connected to the same Kramers doublet at $k = \pi$. In this case the chemical potential will intersect the mid-gap bands an even number of times. In fact it is possible to have no edge states at all here (by adiabatically pushing all states out of the gap). On the other hand, it is also possible to connect the degenerate states at $k = 0$ to two different Kramers doublets. This is the case for a QSH. Here the number of crossings will be odd and these edge states are protected in the sense that there will always be edge

states no matter what the chemical potential. In fact, there is a left moving edge state with spin up and a right moving edge state with spin down. The crossing point between the two at $k = 0$ is known as the Dirac point and as discussed above Kramers degeneracy guarantees that it is impossible to gap out this point unless time-reversal symmetry (TRS) is broken.

This concept of the 2D QSH can be extended to 3D materials as was realized by Fu et al. [223], Moore et al. [224], and Roy [225] and subsequently confirmed in experiments on $Bi_{1-x}Sb_x$ [226], $Bi_2Se_3$ [164] and $Bi_2Te_3$ [227, 228]. The protected surface states now form a Dirac cone in momentum space and the spin of the electron becomes locked to its momentum.Such materials have been termed 3D topological insulators (TIs) and their discovery was a significant advance in condensed matter physics since (a) they are realized at room temperature without magentic field, (b) the protected states reside on the surface rather than in buried interfaces as is the case for the 2D QSH insulator and (c) their electronic structure can easily be studied with angle-resolved photoemission spectroscopy as shown in chap. 6.

In particular, $Bi_2Se_3$ has become the prototypical 3D TI as it contains a single Dirac cone at the $\Gamma$ point in momentum space ($Bi_{1-x}Sb_x$ has several Dirac cones) and it has a relatively large direct bulk band-gap of $\sim 300\,\mathrm{meV}$ with the Dirac point in between the valence and conduction bands. In contrast, $Bi_2Te_3$ has an indirect band gap with the Dirac point below the top of the valence band. This work will primarily focus on Tr-ARPES experiments on $Bi_2Se_3$ with a few results on $Bi_2Te_3$ as well.

Two crucial properties of the surface states of 3D TIs that are utilized in this work are their robustness to non-magnetic disorder and their Dirac-like electronic structure similar to that in graphene. The first property implies that even when disorder or impurities are added to the surface, the metallic surface states cannot be localized or gapped. Similar to the 2D QSH, the Dirac point remains gapless unless TRS is broken. The second property implies that surface states in a 3D TI have a linear energy-momentum relationship like that of a relativistic particle. Electrons on these surface states can be described by a 2D Dirac Hamiltonian:

$$H(\vec{k}) = \hbar v_f k_x \sigma_y - \hbar v_f k_y \sigma_x \tag{8.4}$$

where $v_f$ is the Fermi-velocity. The same equation describes electrons that are confined to a single graphene sheet. However, unlike graphene, a 3D topological insulator has only one Dirac cone instead of four degenerate ones (two for spin and two for valley). Moreover, the Dirac cones in graphene occur at the corners (K and K') of the Brillouin zone rather than at the zone center as in $Bi_2Se_3$. As discussed in chap. 6, it is not possible to access the zone corners in graphene with our current Tr-ARPES setup. Instead the similarity between the electronic structures allows us to experimentally study Floquet-Bloch systems, as theoretically studied in graphene, in surface states of 3D TIs.

### 8.2.1 Theory of Floquet-Bloch states in a Dirac system

A number of works such as [199, 217, 229–231] have considered the theory of a laser driven 2D Dirac Hamiltonian. This section summarizes some of the findings as they will be relevant to the discussion later on. Here we consider a mid-IR pump beam interacting with electrons on the surface of a TI. The unperturbed Hamiltonian $H_0(\vec{k})$ is given by eq. (8.4). The mid-IR pump of frequency $\omega$ and electric field amplitude $E_0$ is introduced through the Peierls' substitution i.e. $v_f\vec{k} \rightarrow v_f\vec{k} + ev_f\vec{A}(t)$, where $\vec{A}(t)$ is the vector potential of the pump light i.e. $\vec{A}(t) = A_0 g(t)\,(a_x \cos(\omega t), a_y \sin(\omega t))$. $A_0 = E_0/\omega$ is the peak vector potential, $g(t)$ describes the pump envelope and $0 \leq a_{x/y} \leq 1$ characterize its polarization. The time-periodic behavior of the vector potential $\vec{A}(t)$ is responsible for generating Floquet-Bloch states. In this section we set $\hbar = 1$ and $c = 1$ for simplicity.

With the Peierls' substitution, the time-dependent Hamiltonian can be separated as $H(\vec{k}, t) = H_0(\vec{k}) + H_p(t)$ where $H_0(\vec{k})$ is the unperturbed Dirac Hamiltonian and $H_p(t)$ is the perturbing Hamiltonian:

$$H_p(\vec{k}) = V g(t)[a_x \cos(\omega t)\sigma_y - a_y \sin(\omega t)\sigma_x] \tag{8.5}$$

where $V = evA_0 = evE_0/\omega$ is the energy scale of the perturbation. From here it is easy to see that the perturbation is periodic in time with strength $V$. This perturbation leads to the Dirac cone getting replicated in energy with spacing $\omega$. Moreover, bands

with different Floquet index $n$ cross each other at the quasi-energy zone boundaries where dynamic gaps can open up, as illustrated in fig. 8.1b. The magnitude of this gap ($2\Delta$) is simply the energy scale of the perturbation $V$:

$$2\Delta = V = evE_0/\omega \tag{8.6}$$

We also define $\beta = evE_0/\omega^2$ as a dimensionless 'Floquet' parameter and thus, $2\Delta = \beta\omega$.

Whether an avoided crossing gap opens up or not for any given direction of $\vec{k}$ depends strictly on the polarization of the pump. We first consider linearly polarized pump with an electric field along the $x$-direction i.e. $a_x = 1$ and $a_y = 0$ in eq. (8.5). In this case, the perturbing Hamiltonian $H_p(t)$ commutes with the first term of $H_0$ eq. (8.4) i.e. with the term in $k_x$ and thus, the crossings in the spectrum along $k_x$ remain gapless while the spectrum along $k_y$ is gapped at the crossing points with magnitude $V$. The opposite occurs when the polarization is along the $y$-direction i.e. when $a_x = 0$ and $a_y = 1$. Therefore, the crossings in the spectrum along the direction of the pump polarization are gapless. Evidence for this behavior with linearly polarized pump light in our Tr-ARPES experiments is presented in sec. 8.3.1.

When the light is circularly polarized i.e. $a_x, a_y = 1/\sqrt{2}$, avoided crossing gaps open up along both $k_x$ and $k_y$. In addition circularly polarized light naturally breaks time-reversal symmetry and this coupling to the surface states of a topological insulator can gap out the Dirac point as first pointed out by Oka et al. [199]. A full theoretical derivation of the size of this gap is beyond the scope of this thesis but a few excellent references are [199, 231]. The gap at the Dirac point due to circularly polarized light is given by [199] :

$$2\Delta_{\text{circ}} = \omega(\sqrt{4\beta^2 + 1} - 1) \tag{8.7}$$

where $\beta$ is the 'Floquet' parameter defined earlier. Evidence for circularly polarized light opening up a gap at the Dirac point is presented in sec. 8.3.2.

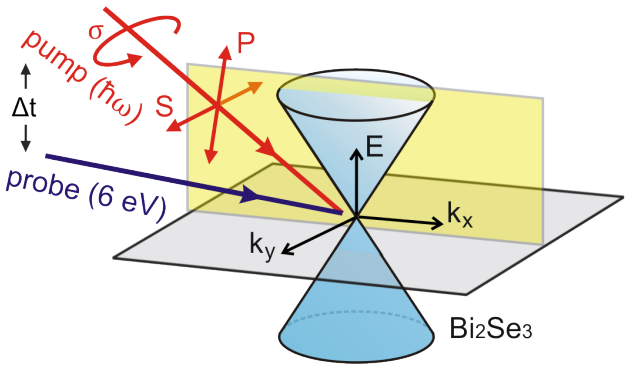


**Figure 8.3:** Geometry of Tr-ARPES setup on $Bi_2Se_3$. The pump light is incident onto the sample at an angle of $\sim 45°$. The pump can either be circularly polarized or linearly polarized with P-polarization having an E-field component out of the sample plane and an in-plane component along the $k_x$ direction whereas S-polarization is purely in the sample plane along the $k_y$ direction.

## 8.3 Observation of Floquet-Bloch states

As discussed in chap. 6, Tr-ARPES on topological insulators using $\sim 1.55$ eV pump pulses results in excitation of electrons from the bulk valence band to the bulk conduction band. Here any coherent effect of this high energy pump on Dirac electrons is negligible. Instead, for Dirac electrons to coherently interact with the electric field of the pump, it is important to minimize direct bulk excitations by pumping the sample with light below the bulk band gap which for most topological insulators is between 200 meV and 300 meV. As a result we carried out Tr-ARPES measurements on single crystals of $Bi_2Se_3$ using mid-IR 160 meV pulses as the pump. A time-of-flight analyzer (chap. 7) is used to simultaneously acquire the complete transient band structure of $Bi_2Se_3$ without rotating the sample or the detector ([232]).

Figure 8.3 shows the geometry of the setup. The mid-IR pump beam was incident on the sample at an angle of $\sim 45°$ and its polarization could be set to either linear (P or S) or circular. Here P and S are standard conventions to define the direction of the electric (E)-field of the light with respect to the plane of incidence. The E-field of the P-polarized pump is purely in the plane of incidence and thus has a component pointing out of the sample surface (fig. 8.3). On the other hand the E-field of the S-polarized pump is perpendicular to the plane of incidence and thus it is parallel to the sample surface.

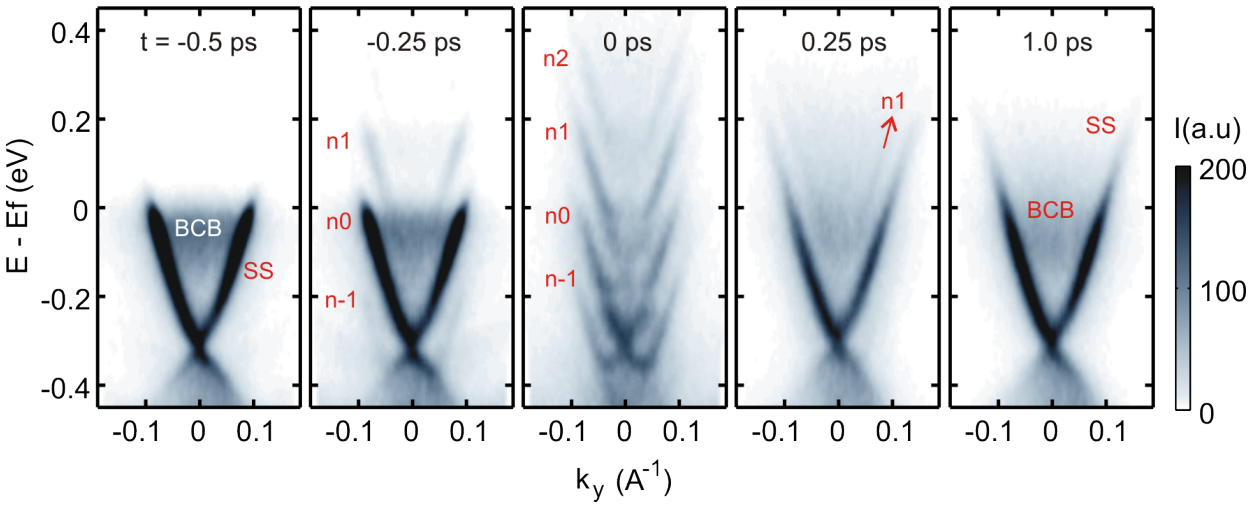


**Figure 8.4:** Tr-ARPES ($E - E_f$ vs $k_y$) spectra on $Bi_2Se_3$ using P-polarized mid-IR pump at various delay times between the pump and the probe. BCB refers to the bulk conduction band while SS refers to the topological surface state. The nth order sidebands are indicated in the spectra.

Figure 8.4 shows the Tr-ARPES spectra using P-polarized pump on $Bi_2Se_3$ at various delay times between the pump and probe. Replicas (sidebands) of the original Dirac cone appear when the pump and probe pulse overlap in time. These replicas are spaced exactly by the energy of the pump pulse ($\sim 160\,\text{meV}$). The index $n$ of a sideband refers to its spacing ($n\hbar\omega$) from the unperturbed Dirac cone. The intensity of these sidebands is maximized at $t = 0\,\text{ps}$ which refers to the maximum E-field of the pump beam coinciding with the maximum E-field of the probe. Once the dressing field of the pump pulse disappears ($t > 500\,\text{fs}$), the sidebands disappear leaving a heated Dirac cone i.e. an electronic temperature greater than that in equilibrium. The dynamics of this non-equilibrium heated distribution of electrons has been discussed in a number of Tr-ARPES experiments [172–174]. Here we will focus on the Tr-ARPES spectra taken at $t = 0\,\text{ps}$ to understand the nature of the sidebands.

### 8.3.1 Avoided crossing gap

If the sidebands observed above are indeed different orders of Floquet-Bloch states, then at their crossing points they should hybridize and open up dynamic gaps as discussed in sec. 8.2.1. Figure 8.5a and 8.5c show the Tr-ARPES spectra at $t = 0$ along the

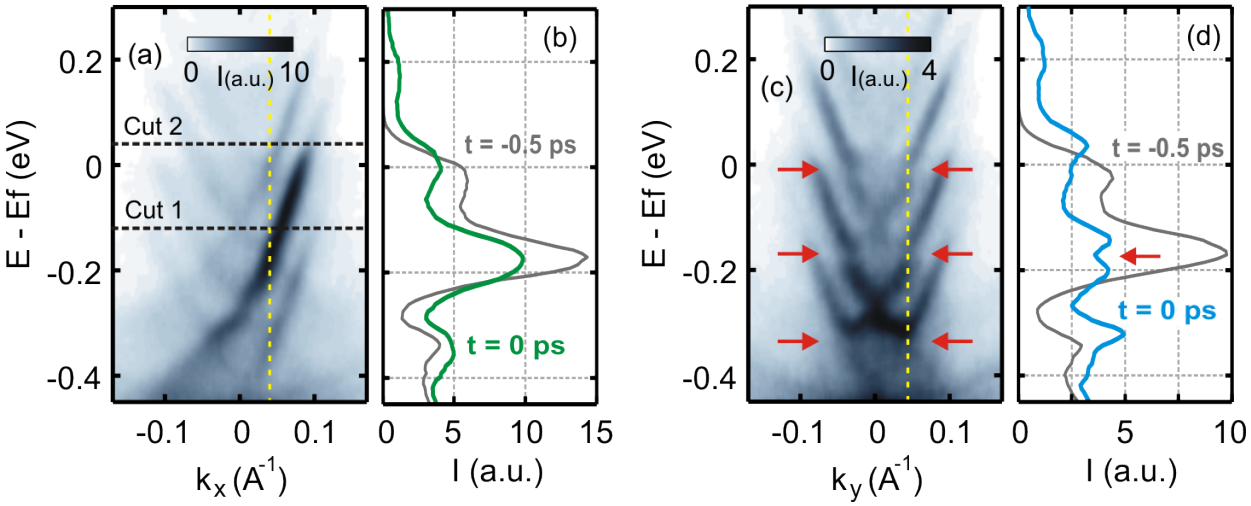


**Figure 8.5:** Tr-ARPES spectra & EDCs on $Bi_2Se_3$ at $t = 0$ for P-polarized mid-IR pump. **(a)** Energy (E) relative to the Fermi level ($E_f$) vs momentum along the $k_x$ direction and **(c)** along the $k_y$ direction. Red arrows indicate the avoided crossing gaps. Yellow lines indicate the momentum at which EDCs are taken. The corresponding EDCs (intensity vs E-$E_f$), are plotted in **(b)** (green plot) and **(d)** (blue plot). For comparison, EDCs are also taken for the pre-time zero spectra ($t = -0.5\,\text{ps}$)) and plotted in gray in (b) and (d). A gap opens up at the avoided crossing for momentum along $k_y$as indicated by the double peak structure in (d).

$k_x$ and $k_y$ directions respectively, taken with linear P-polarized pump with an in-plane electric field component along $k_x$ (fig. 8.3). A number of sidebands are observed along each momentum direction however avoided crossing gaps are observed only along $k_y$ (fig. 8.5c, red arrows) but not along $k_x$.

To corroborate this further, we take Energy Distribution Curves (EDCs) at $k_x, k_y = 0.035\,\text{Å}^{-1}$ which corresponds to the momentum where n0 and n1 sidebands cross (yellow lines in fig. 8.5a and fig. 8.5c). The EDCs are taken by integrating the spectra over a small momentum window $\sim 0.003\,\text{Å}^{-1}$. The resulting EDCs for both $t = 0$ and $t = -5\,\text{ps}$ (i.e. before the pump pulse hits the sample) are plotted in fig. 8.5b and fig. 8.5d. As seen, for momentum along $k_x$, the EDC retains its 'single peak' nature at the crossing point i.e. there is only a decrease of intensity at the crossing point due to the application of the pump pulse. On the other hand for momentum along $k_y$, the EDC develops a 'double peak' structure right at the crossing point (red arrow, fig. 8.5d). This observation is consistent with Floquet-Bloch

theory on Dirac systems (sec. 8.2.1). Since the pump E-field is along the x-direction (P-polarized), the perturbing Hamiltonian commutes with the Dirac Hamiltonian corresponding to electrons with momentum along $k_x$. This leads to a trivial crossing between sidebands along $k_x$ which thus remains gapless. However, along $k_y$, the direction perpendicular to the E-field, avoided crossing gaps open up as discussed in sec. 8.2.1.

We can extract the magnitude of the observed hybridization gap by fitting the EDC for momentum along $k_y$ with multi-peak Lorentz functions as shown in fig. 8.6a. The choice of the peak functions does not affect the obtained gap size in any significant way since we are only interested in the distance between the peaks. The avoided crossing gap is then given by the separation of the two peaks around energy, $E - E_f = -0.2$ eV (green peaks in fig. 8.6a). The resulting gap size for a pump power of 11.5 mW is then $2\Delta = 68\,\text{meV}$ which is in good agreement with theoretical predictions for the experimental parameters used here (sec. 8.6), as $2\Delta = \beta\omega$ eq. (8.6) with $\omega = 160$ meV and $\beta = 0.42$ i.e. $2\Delta_{calc.} = 67\,\text{meV}$. To test this further, we took Tr-ARPES spectra at $t = 0$ for a range of pump-powers. We extract the avoided crossing gap ($2\Delta$) between the n0 and n1 sidebands for each power and plot the results in fig. 8.6b on a log-log plot. $2\Delta$ is predicted (sec. 8.2.1) to scale linearly with the electric field amplitude ($E_0$) and thus $2\Delta \propto \sqrt{P}$ where $P$ is the applied average pump power. As shown in fig. 8.6b, $2\Delta$ indeed scales as the square root of the pump power.

Another way of confirming our conclusions regarding Floquet-Bloch states is to rotate the polarization of the mid-IR pump. Figure 8.7a and 8.7b show the Tr-ARPES spectra at $t = 0$ along the $k_x$ and $k_y$ directions respectively, taken with S-polarized pump oriented along the $k_y$ direction. We first notice a significant decrease in the intensity of the sidebands despite using a similar intensity for the pump pulse. This is due to the absence of Volkov states which will be discussed in detail in sec. 8.4. For now we focus on the avoided crossing gaps. Similar to the P-polarized pump, gaps are apparent (red arrows, fig. 8.7a) at points where the zeroth and first order sideband corss. However, the gaps are now observed along the $k_x$ direction but not along the $k_y$ direction. This is again consistent with Floquet-Bloch theory on Dirac electrons since the avoided crossing gaps are along the momentum direction ($k_x$)

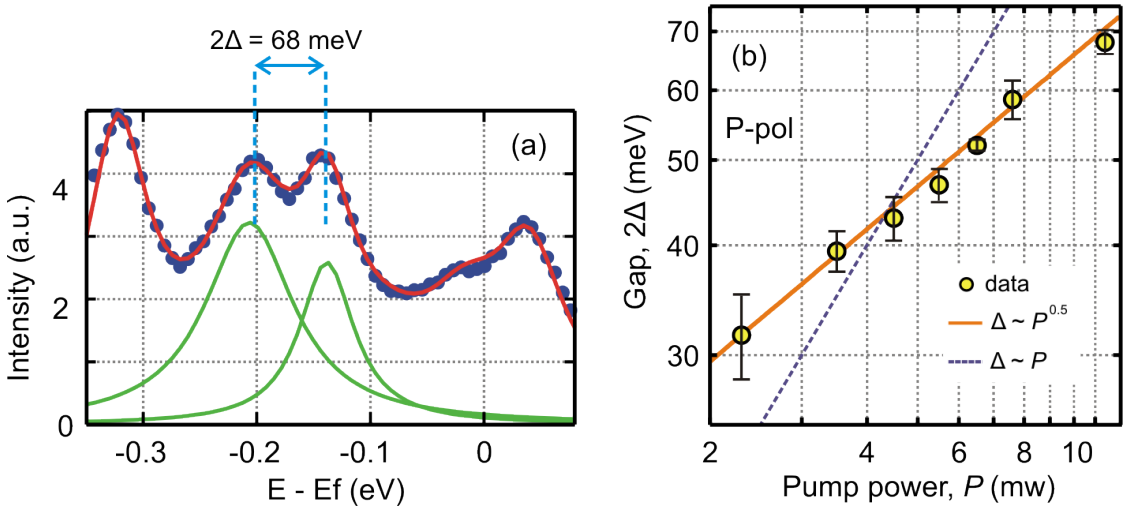


**Figure 8.6:** **(a)** EDC at $k_y = 0.035\,\text{Å}^{-1}$ through the Tr-ARPES spectra in fig. 8.5c. Blue dots indicate the raw data. The red line is a multi-peak Lorentzian function to best fit the data. Green peaks correspond to the peaks from which the avoided crossing gap is extracted. **(b)** Avoided crossing gap ($2\Delta$) as a function of incident pump power ($P$) for P-polarized pump on a log-log plot. The gap at each pump power is obtained by fitting the EDCs in the ARPES spectra with a pair of Lorentzians as shown in (a). Power laws ($\Delta \sim P^{\eta}$) with $\eta = 0.5$ (orange trace) and $\eta = 1$ (blue trace) are plotted as well to determine the analytical behavior of $2\Delta$ with $P$.

perpendicular to the direction of the E-field ($k_y$). The avoided crossing gap can explicitly be seen by taking an EDC along the crossing point as shown in fig. 8.7c. We further extract the magnitude of the gap ($2\Delta$) for S-polarized pump and plot it as function of pump power on a log-log plot (fig. 8.7d). Similar to the case of P-polarized pump, $2\Delta$ scales as the square root of the pump-power i.e. $2\Delta \propto \sqrt{P}$ in agreement with Floquet-Bloch theory on Dirac systems. These observations unequivocally establish the transient generation of Floquet-Bloch states.

### 8.3.2 Breaking time-reversal symmetry

As discussed in sec. 8.2, the Dirac point in topological insulators is protected by time-reversal symmetry (TRS) which can be spontaneously broken when circularly polarized light couples with the surface states [199, 201, 231]. This should in principle gap out the Dirac point. Having confirmed that the linearly polarized mid-IR pump photons coherently couple with the surface states of $Bi_2Se_3$, we will now study whether circularly polarized mid-IR pump couples with these states to break TRS.

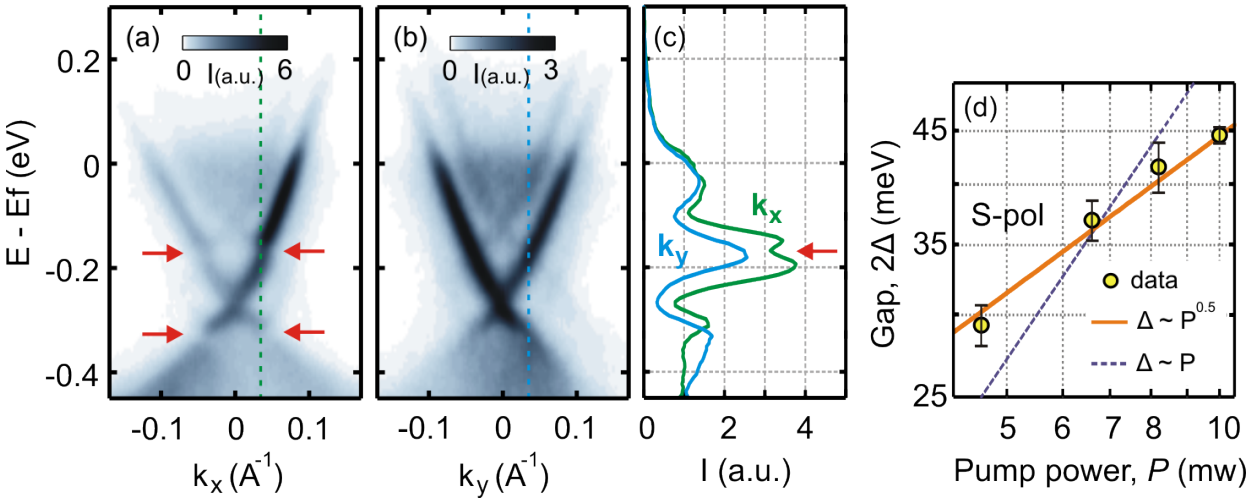


**Figure 8.7:** Tr-ARPES spectra & EDCs on $Bi_2Se_3$ at $t = 0$ for S-polarized mid-IR pump. **(a)** Energy (E) relative to the Fermi level ($E_f$) vs momentum along the $k_x$ direction and **(b)** along the $k_y$ direction. Red arrows indicate the avoided crossing gaps. Blue and green lines indicate the momentum at which EDCs are taken. The corresponding EDCs (intensity vs E-$E_f$), are plotted in **(c)**. A gap open ups at the avoided crossing for momentum along $k_x$ as indicated by the double peak structure. Avoided crossing gaps are absent for momentum along $k_y$. **(d)** Avoided crossing gap ($2\Delta$) as a function of incident pump power ($P$) for S-polarized pump on a log-log plot. Power laws ($\Delta \sim P^{\eta}$) with $\eta = 0.5$ (orange trace) and $\eta = 1$ (blue trace) are plotted as well.

Figure 8.8c shows the Tr-ARPES spectra at $t = 0$ along $k_y$ for circularly polarized pump. For comparison we also plot the pre-time zero (unperturbed) ARPES spectra in fig. 8.8a and the Tr-ARPES spectra at $t = 0$ for linear P-polarized pump fig. 8.8b. Sidebands and avoided crossing gaps (yellow arrows) appear for both linear and circularly polarized pump. More importantly, there seems to a depletion of intensity right at the Dirac point in the cirulary polarized pump spectra when compared with the P-polarized pump and the pre-time zero spectra. This strongly indicates the opening up of a gap at the Dirac point.

To confirm this we take EDCs at $k_y = 0$, i.e. through the $\Gamma$ point, along each of the spectra in fig. 8.8a-c. As seen in fig. 8.8d, only the EDC (blue) for cirularly polarized pump has a 'double peak' structure right at the Dirac point (i.e. at $E - E_f \approx 0.32\,\text{eV}$) whereas the EDC (red) for linearly polarized pump closely matches the unperturbed EDC (green) at the Dirac point. We note here that the asymmetric peak in the EDCs for linear pump and unperturbed spectra is due to the finite momentum resolution of our setup. By

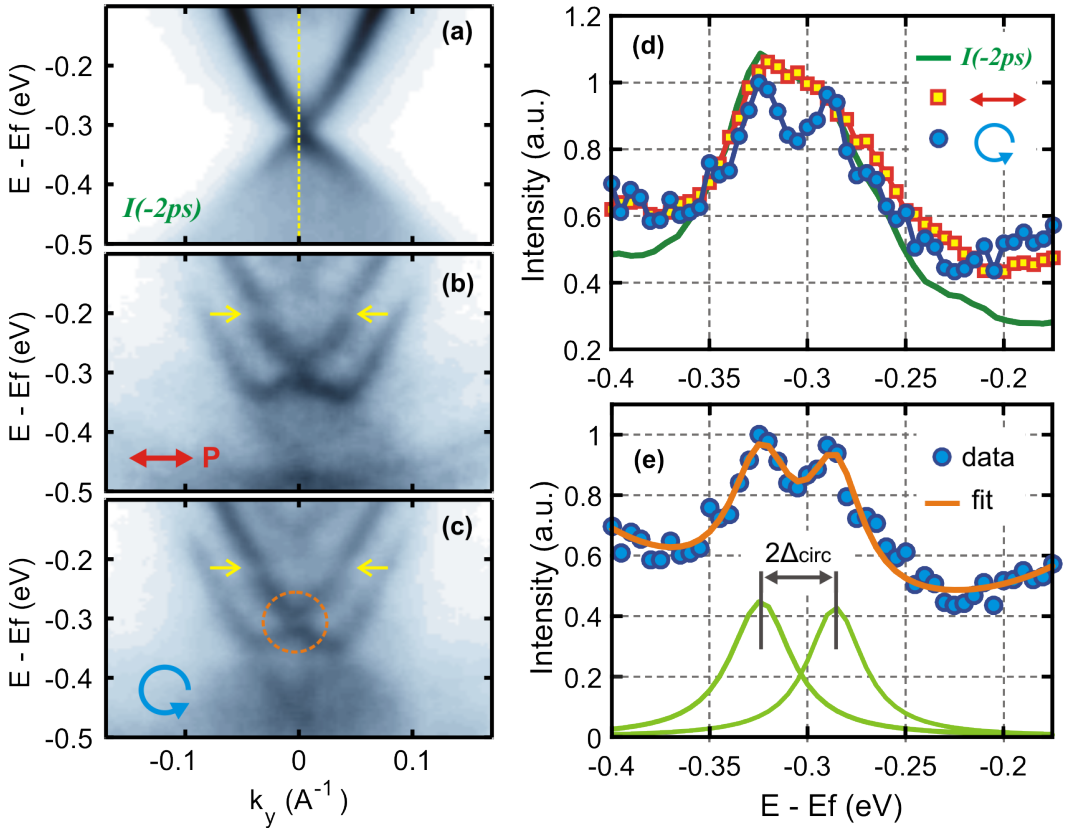


**Figure 8.8:** Photo-induced gap at the Dirac point using circularly polarized mid-IR pump. **(a)** Tr-ARPES spectra on $Bi_2Se_3$ a $t = -2ps$ i.e. before the pump pulse hits the sample. **(b)** spectra taken at $t = 0$ for linear P-polarized light and **(c)** circularly polarized light. Yellow arrows indicate the avoided crossing gaps. Orange circle in (c) is indicates the gapped Dirac point. **(d)** EDCs at the $\Gamma$ point $(k_x, k_y = 0)$ for the spectra in (a)-(c). A double peak feature is seen only for circularly polarized pump. **(e)** The photo-induced gap at the Dirac point is obtained by fitting the cirularly polarized pump EDC to a multi-peak Lorentzian fit as indicated by the orange line. The separation between the pair of Lorentzians (green) gives the photo-induced gap.

fitting the circularly polarized pump EDC to multi-peak Lorentz functions (fig. 8.8e) we can extract the gap at the Dirac point: $2\Delta_{\text{circ}} \approx 39\,\text{meV}$.

We can compare the measured value of $2\Delta_{\text{circ}}$ with the theoretically predicted gap as follows. The average circularly polarized pump power used in this experiment was $\sim 11\,\text{mW}$ which corresponds to a Floquet-parameter $\beta \approx 0.4$ (sec. 8.6). Floquet-Bloch theory as discussed earlier predicts $2\Delta_{\text{circ}} = \hbar\omega(\sqrt{4\beta^2 + 1} - 1) \approx 45\,\text{meV}$ eq. (8.7). This value is relatively close to the 39 meV gap obtained in fig. 8.8e. We attribute the small discrepancy

between the measured and calculated values of $2\Delta_{\text{circ}}$ to possible ellipticity in the mid-IR pump i.e. the pump beam is not purely circular but has an additional linear component as well resulting in an elliptically polarized beam. Since we measure the total power of the pump beam, it is possible that slightly less then the measured power couples to the Dirac point directly owing to the ellipticity in the beam.

From the above discussion, it is clear that circularly polarized pump photons hybridize with the surface Dirac Hamiltonian in a topological insulator to break TRS and photoinduce a gap at the Dirac point. As pointed out by [201], the above described problem of shining circularly polarized light onto a 2D Dirac system can be mapped onto the Haldane model [233]. The Haldane model considers a honeycomb lattice in which current loops within a unit cell break TRS locally while keeping the total magnetization zero. It turns out that the Haldane Hamiltonian at the valley points of the honeycomb lattice is the same as that of a circularly polarized photon coupled to a Dirac cone. As is well known, a realization of the Haldane model results in a quantum anomalous Hall effect (QAHE) without Landau levels. This suggests that our transient photo-generated state on $Bi_2Se_3$ with circularly polarized pump should display evidence of QAHE in conductivity measurements as has been shown for magnetically doped topological insulators [234].

## 8.4 Scattering between Floquet-Bloch & Volkov states

In the discussion so far we have established that the interaction of light with a solid can lead to hybrid photon-electron states known as Floquet-Bloch states inside the solid. These states are essential in realizing new photo-induced quantum phases [201, 202, 210]. Similar to Floquet-Bloch states, the dressing of free electron states near the surface of a solid generates Volkov states which are used to study non-linear optics in atoms and semiconductors [235]. The interaction of these two dynamic states with each other remains an open experimental problem. In this section we use Tr-ARPES to selectively study the transition between these two states on the surface of the topological insulator $Bi_2Se_3$. We find that the coupling

between the two strongly depends on the electron momentum, providing a route to enhance or inhibit it. Moreover, by controlling the light polarization we can negate Volkov states in order to generate pure Floquet-Bloch states.

### 8.4.1 Volkov states

As mentioned earlier, the sideband intensity observed for S-polarized pump (fig. 8.7) was significantly less than that for P-polarized pump (fig. 8.5) despite similar pump powers. This difference is attributed to the absence of Volkov states in S-polarizd pump. To understand this, it is important to consider the measured intensity in an ARPES experiment. As outlined in sec. 6.1, an ARPES experiment is typically modeled as an excitation of a bound electron in the bulk to a free electron-like state near the surface as illustrated in fig. 8.9a. The measured unperturbed intensity is thus given by:

$$I_0 = |\left\langle \Psi_f | \vec{A} \cdot \vec{p} | \Psi_i \right\rangle|^2 \tag{8.8}$$

where $\Psi_f$ and $\Psi_i$ are the final and initial electron wavefunctions. $\vec{p}$ is the electron momentum and $\vec{A}$ is the vector potential of the photo-emitting probe.

So far, we have only considered dressing of $\Psi_i$ due to pump photons (fig. 8.9b). However, pump light can also dress free electron states $\Psi_f$ near the surface of a solid (fig. 8.9c) since the surface can provide the momentum conservation necessary for a photon to interact with a free electron. This dressing was has been observed in time resolved photoemission experiments ([236, 237]) and is referred to as Laser Assisted Photoemission (LAPE). LAPE is typically understood [238–240] by invoking the Volkov solution which is an exact solution of the time dependent Schrodinger equation for a free electron interacting with a plane electromagnetic wave [241]. LAPE bands can thus be thought of as Volkov states in vacuum that electrons can transition into from initial Bloch states inside the solid (fig. 8.9c). In a Tr-ARPES experiment, the final state of photoemission is typically free electron-like and dressing of these final states generates Volkov states that, similar to Floquet-Bloch states, appear in the spectra as band

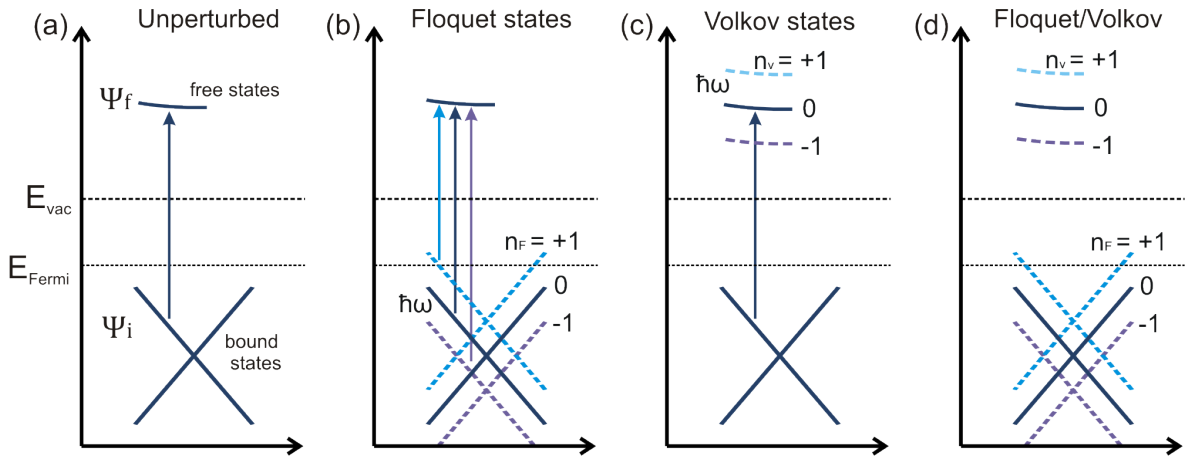


**Figure 8.9:** Schematic illustrating dressed initial and final electron states in a Tr-ARPES experiment **(a)** In the unperturbed case or before time zero, electrons transition from initial bound states $\Psi_i$ to final free electron-like states $\Psi_f$. **(b)** Dressing of the bound states results in Floquet states ($n_F$) separated by the drive photon energy $\hbar\omega$ whereas **(c)** dressing of the free electron-like states results in Volkov states ($n_V$).**(d)** If both the initial and final states are dressed, the ($n^{th}$) order sideband in the Tr-ARPES spectra is given by all transitions such that $n = n_F + n_V$.

replicas separated by the driving photon energy. In this work we will refer to the dressing of initial states as Floquet-Bloch states and the dressing of the final states as Volkov states.

Both these dressed states cause band replicas in the Tr-ARPES spectra which appear at the same energy and momentum regardless of whether they originate from Floquet-Bloch or Volkov states, making it difficult to distinguish them. Moreover, due to the coherent nature of both processes, electrons can scatter directly from Floquet-Bloch states into Volkov states [242] as shown in fig. 8.9d. In order to study the various exotic affects predicted by Floquet theory on solid-state systems, it is important to experimentally characterize and separate out Floquet-Bloch and Volkov states in a controlled way. Furthermore, the interaction between Volkov and Floquet-Bloch states can provide novel insights in using semi-conductors for non-linear optics [235].

### 8.4.2 Mixing between Floquet-Bloch & Volkov states

An interesting observation in the P-polarized pump Tr-ARPES spectra along $k_x$ (fig. 8.5a) is the asymmetry in the intensity of Floquet sidebands about $k_x = 0$. This asymmetry allows us

to establish scattering between Floquet-Bloch and Volkov states. As seen in fig. 8.5a, the first order sideband (n1) is not an exact replica of the original band (n0). Rather, the replication of the Dirac cone is asymmetric between the $+k_x$ and $-k_x$ directions. It is important to distinguish this from the asymmetry in the intensity of the Dirac cone that arises in the unperturbed ARPES spectra. Due to the coupling of the photo-emitting 6.2 eV probe beam to the spin texture of the Dirac cone, there is a natural asymmetry between the $+k_x$ and $-k_x$ direction since the incident plane of the photo-emitting probe is along the $k_x$ direction. This matrix element (spin-probe) effect has been well understood in other ARPES measurements on similar systems [232]. Here, we will study the additional asymmetry that is present in the replica of the original Dirac cone. This asymmetry is more evident in constant energy cuts separated by the driving photon energy (fig. 8.10a,b). These constant energy cuts are taken at $\mathrm{E} - \mathrm{E}_f = -0.12\,\mathrm{eV}$ and at $\mathrm{E} - \mathrm{E}_f = 0.04\,\mathrm{eV}$ (black dashed lines in fig. 8.5a). $I_0$ and $I_1$ correspond to the intensities of the n0 and n1 constant energy surfaces respectively. In order to minimize the effects of spin-texture as well as detector non-linearities, we divide these constant energy cuts ($I_1/I_0$) and plot the result in fig. 8.10c. If the n1 sideband were an exact replica of the n0 sideband, then $I_1/I_0$ would be constant as a function of the electron momentum. However, as can be seen in fig. 8.10c and in the angular distribution in fig. 8.10d, $I_1/I_0$ is stronger along the $-k_x$ direction than along the $+k_x$ direction indicating that the dressed bands strongly depend on the direction of the electron momentum.

To explain this, we model our Tr-ARPES spectra by including the effects of both Floquet-Bloch and Volkov states. We start with the Dirac Hamiltonian describing the surface states of a topological insulator (sec. 8.4.4). As discussed before, the mid-IR laser pump is introduced through the Peierls' substitution i.e. $v_f\vec{k} \rightarrow v_f\vec{k} + ev_f\vec{A}$, where $\vec{A}$ is the vector potential of the pump light and $v_f$ is the Fermi-velocity. The dimensionless parameter $\beta = ev_fA/\omega$ characterizes the strength of the Floquet interaction where $\omega$ is the frequency of the mid-IR laser pump. The resulting Tr-ARPES intensity can be obtained [243] by using the non-equilibrium two time correlation function of the driven electrons (sec. 8.4.4). Without including the effects of Volkov states (LAPE), this results in the

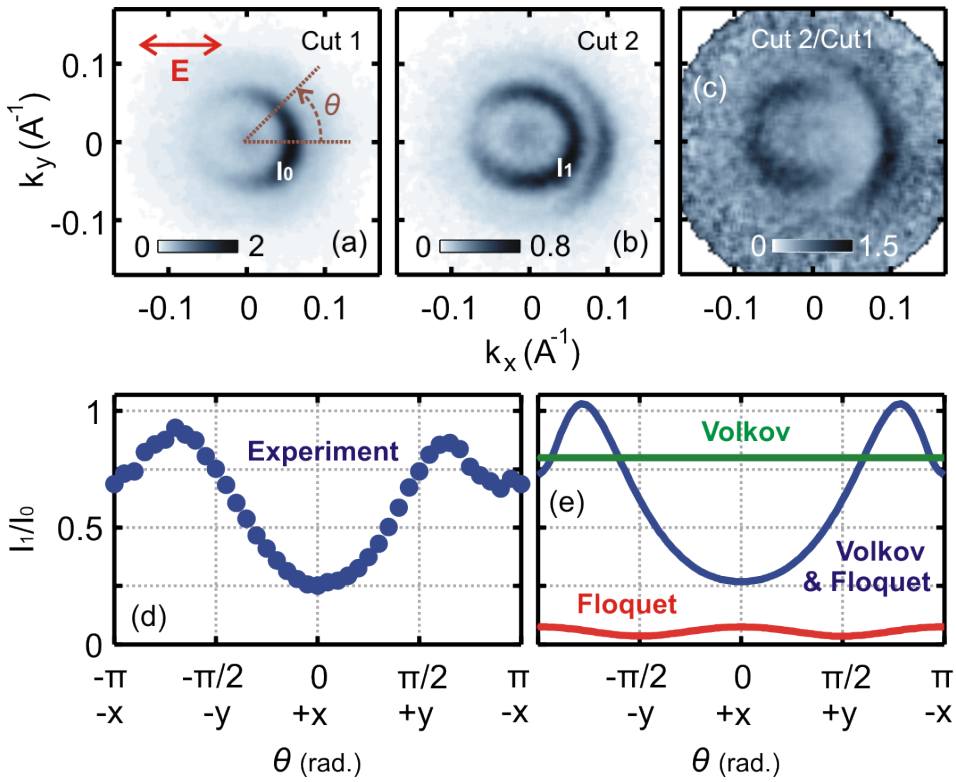


**Figure 8.10:** Asymmetry in the Tr-ARPES spectra for P-polarized mid-IR pump. **(a)** Constant energy cut at $\mathrm{E} - \mathrm{E}_f = -0.12\,\mathrm{eV}$, i.e. along dashed line 'Cut 1' in fig. 8.5a. The electric field ($\vec{E}$) is along the $k_x$ direction (red arrow). $I_0$ indicates the surface state contour for the zeroth order band i.e. the original Dirac cone. **(b)** Constant energy cut at $\mathrm{E} - \mathrm{E}_f = 0.04\,\mathrm{eV}$, i.e. along dashed line 'Cut 2' in fig. 8.5a. The two constant energy cuts are separated in energy by the driving pump energy of 160 meV. $I_1$ indicates the surface state contour for the first order side band. **(c)** The constant energy cut in (b) is divided by the cut in (a) and the result is displayed as a color plot. **(d)** Distribution of $I_1/I_0$ as a function of angle ($\theta$) measured from the $+k_x$ direction. The distribution is obtained by radially integrating the surface state contours in (a) and (b) over a 'k' space window of width $\sim 0.013\,\mathrm{\AA}^{-1}$. **(e)** Calculated angular distribution of $I_1/I_0$ for P-polarized pump at different values of the LAPE parameter ($\alpha$) and the Floquet parameter ($\beta$). Red trace: $\alpha = 0$ and $\beta = 0.5$. Green trace: $\alpha = 1.38$ and $\beta = 0$. Blue trace: $\alpha = 1.38$ and $\beta = 0.5$.

following expression for the photo-emitted intensity for the case of electron momentum along the linearly polarized pump direction (i.e. along $k_x$):

$$I(k_x, E) \propto \sum_n \left\{ \delta_{E,\hbar v_f k_x + n\hbar\omega} + \delta_{E,-\hbar v_f k_x + n\hbar\omega} \right\} J_n(\beta)^2 , \tag{8.9}$$

Therefore, the n-th Floquet-Bloch sideband has an intensity $\sim J_n(\beta)^2$ and is symmetric for $\pm k_x$. The situation becomes different when the effect of Volkov states is included. The corresponding Hamiltonian is $H_{LAPE} = \hbar e \vec{v_0} \cdot \vec{A}$, where $v_0$ is the free photoelectron velocity, obtained by conserving energy and in-plane momentum in the photoemission process. The dimensionless parameter $\alpha = e v_0 A/\omega$ characterizes the strength between light and the final states of photoemission. The photo-emitted intensity (along $k_x$) now becomes (sec. 8.4.4):

$$I(k_x, E) \propto \sum_n \left\{ \delta_{E,\hbar v_f k_x + n\hbar\omega} J_n(\beta - \alpha)^2 + \delta_{E,-\hbar v_f k_x + n\hbar\omega} J_n(\beta + \alpha)^2 \right\} \tag{8.10}$$

The dependence on both $\alpha$ and $\beta$ is due to the interference between Floquet-Bloch and Volkov states. The observed n-th order sideband is now a combination of different Fourier pairs of Floquet-Bloch ($n_F$) and Volkov ($n_V$) modes such that $n_F + n_V = n$ (fig. 8.9d). In order to explain the data fully, we have also included the spin-probe effect that describes the coupling of the photo-emitting probe to the spin texture of the Dirac cone (sec. 8.4.4).

Figure 8.10e shows the results of this calculation for three different cases: (i) $\alpha = 0$ and $\beta = 0.5$ (Floquet only), (ii) $\alpha = 1.38$ and $\beta = 0$ (Volkov only) and (iii) $\alpha = 1.38$ and $\beta = 0.5$ (Floquet & Volkov). The non-zero values used for $\alpha$ and $\beta$ agree quite well with the measured experimental parameters ($v_f$, $v_0$, $A$ and $\omega$) of the setup (sec. 8.6). In case i (red trace) electrons scatter from dressed states in the solid (Floquet-Bloch) into unperturbed free electron states. The two-fold rotational symmetry is understood by noting that the electrons scatter preferentially when their momentum is along the direction of the light polarization (in this case along $k_x$). Case ii (green trace) refers to the situation when only the final states are dressed (Volkov). Here it is important to note that in the photoemission process only the in-plane momentum is conserved whereas the electrons acquire a large out-of-plane momentum ($k_z$) due to the excess photon energy. Since the pump pulse is P-polarized, the electric field in

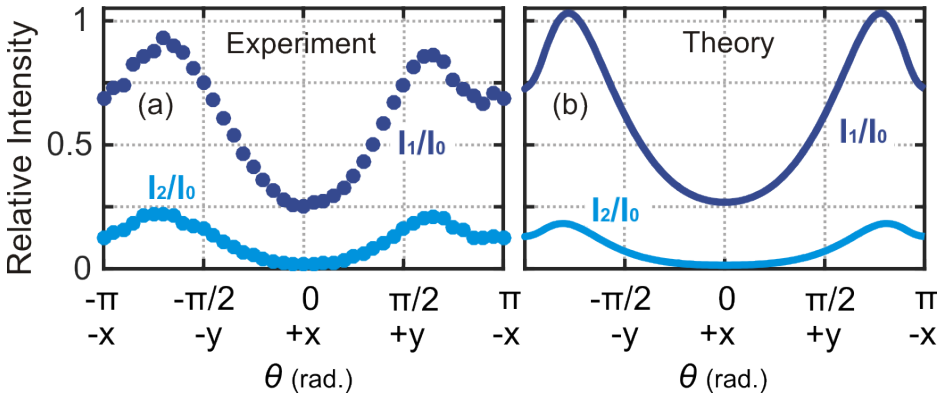


**Figure 8.11:** Angular distribution of the second-order sideband intensity. **(a)** Measured and **(b)** calculated angular distributions of $I_1/I_0$ and $I_2/I_0$ for P-polarized pump. $I_1/I_0$ is the same as in fig. 8.10d. $I_2/I_0$ is obtained by integrating over a constant energy cut across the second order sideband (i.e. $\Delta E = \hbar\omega_{pump} = +160meV$ from Cut 2 indicated in fig. 8.5a). The relative intensities in (b) are numerically calculated using $\alpha = 1.38$ and $\beta = 0.5$.

the $z$-direction strongly couples to free electron states with a large $v_z$ leading to a dressing of these final states that predominately depends on the out-of-plane momentum. The intensity of the sidebands is thus isotropic as a function of in-plane momentum (green trace).

Case iii (blue trace) includes the dressing of both the initial and final states and, as can be seen, this trace closely matches the observed angular dependence in the intensity of the first order sideband (fig. 8.10d). The calculation also captures the strong asymmetry in $I_1/I_0$ between $+k_x$ and $-k_x$, which would not be present for pure Floquet-Bloch (case i) or pure Volkov states (case ii). To test this further, we also extract $I_2/I_0$ for the P-polarized pump data and compare it with the numerically calculated $I_2/I_0$ using the same parameters as were used to calculate $I_1/I_0$ i.e. $\alpha = 1.38$ and $\beta = 0.5$. As shown in fig. 8.11 there is relatively good agreement between the measured and calculated $I_2/I_0$ which further confirms the validity of our analysis.

These results not only imply the presence of both Floquet-Bloch and Volkov states but also point to selective transitions between the two. For example, as the electron momentum is varied between $-k_x$ and $+k_x$, there is an increase and then decrease in the scattering intensity as recorded by Tr-ARPES. As discussed above, eq. (8.10) implies that for electron momentum along the light polarization direction (i.e. along $k_x$), the photo-emitted intensity

can be written as $\propto J_n(\beta \mp \alpha)^2$ for $\pm k_x$. Thus, by varying the electron momentum, we can control the scattering between Floquet-Bloch and Volkov states. We point out that these selective transitions are a direct consequence of Volkov states being generated primarily due to the out-of-plane E-field for P-polarized pump. This is because the out-of-plane velocity $v_z$ is much greater than the in-plane velocity $v_\parallel$ for free electron states i.e. ($v_z \gg v_\parallel$) as outlined in sec. 8.6. Moreover, the out-of-plane field $E_z$ is nearly 4 times greated than the in-plane-field $E_\parallel$. This significantly enhances the effect of Volkov states for an out-of-plane electric field as is present for P-polarized pump.

### 8.4.3 Generating pure Floquet-Bloch states

The aforementioned results suggest a way to reduce the effect of Volkov states: eliminating the out-of-plane electric field. This can be achieved by perturbing the system with S-polarized light instead which has an electric field purely along the sample plane (fig. 8.3). As pointed out in fig. 8.7, the measured intensity of sidebands generated from S-polarized mid-IR pump is significantly smaller then that for P-polarized pump (fig. 8.7). To understand this we take the ratio of the intensities of the first and zero order sidebands ($I_1/I_0$) for the S-polarized pump spectra in fig. 8.7 and plot it as a function of the electron momentum direction (fig. 8.12a). This ratio is almost 10 times less than what is observed for P-polarized pump. Since S-polarization has negligible out-of-plane E-field, this small sideband intensity could likely be due to an absence of Volkov states. We test this by numerically calculating the sideband intensities for the presence of Floquet-Bloch states only ($\alpha = 0$ and $\beta = 0.5$) using S-polarized pump. As can be seen fig. 8.12b, the calculation for Floquet states only (red trace) agrees quite well with the observed angular dependence of $I_1/I_0$.

It is possible that an in-plane electric field can also generate Volkov states by coupling to the in-plane free electron velocity $v_\parallel$. However, as pointed out before, this effect is negligible when compared with the out-of-plane component. In fact the Volkov parameter $\alpha = 0.05$ if we only consider the in-plane components. To rule out any noticeable effect of Volkov states in the observed angular distribution for S-polarized pump, we also calculate $I_1/I_0$

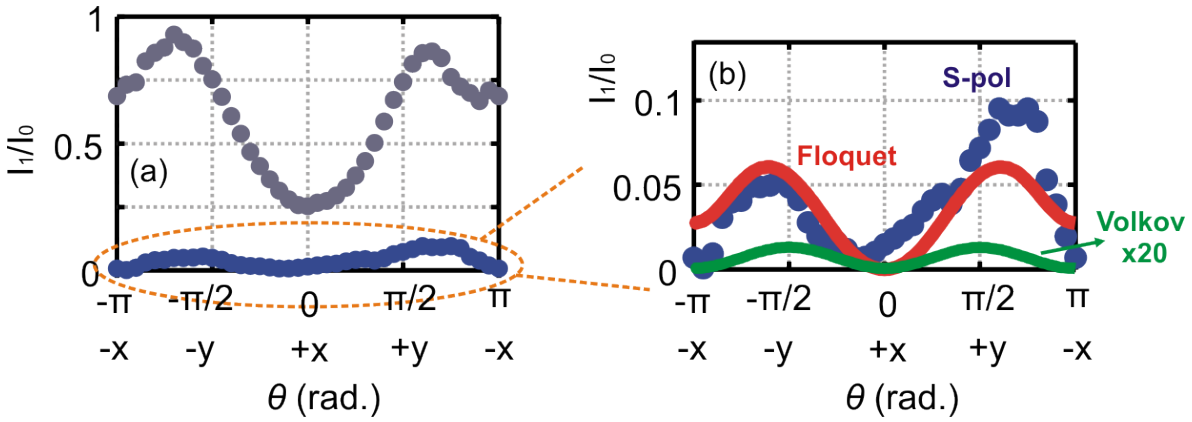


**Figure 8.12:** Angular distribution of sideband relative intensities for S-polarized pump. **(a)** Ratio of the first order side band intensity $I_1$ to the zeroth order intensity $I_1$ as a function of angle ($\theta$) measured from the $+k_x$ direction, for both P and S-polarized pump. $I_1/I_0$ for S-polarized pump is obtained from fig. 8.7 in the same way as that for P-polarized pump. **(b)** $I_1/I_0$ for S-polarized pump (blue trace) along with the calculated angular distribution of $I_1/I_0$ for S-polarized pump using: $\alpha = 0$ and $\beta = 0.5$ (red trace). The discrepancy between the calculated (red trace) and measured (blue dots) values is likely due to instrument limitations in measuring the extremely small intensity of the n1 sideband for S-polarized pump. Green trace represents the calculated $I_1/I_0$ for the case of $\alpha = 0.05$ and $\beta = 0$. These values correspond to Volkov states being generated by the in-plane electric field only. Note: $I_1/I_0$ for the green trace has been multiplied by 20 for better visual representation on this axis scale.

using $\alpha = 0.05$ and $\beta = 0$ (green trace fig. 8.12b). This 'Volkov only' $I_1/I_0$ is significantly smaller than what is actually measured (blue trace). Thus, perturbing the system with S-polarized mid-IR pump results in the generation and observation of pure Floquet-Bloch states. Moreover, by controlling the light polarization, we can enhance or completely inhibit the transition between Floquet-Bloch and Volkov states.

We note here that the angular dependence of the measured $I_1/I_0$ in fig. 8.12b shows an asymmetry between $+k_y$ and $-k_y$ that is not captured by the numerically calculated $I_1/I_0$. This asymmetry is primarily due to limitations in our Tr-ARPES experimental setup in accurately determining small pump induced changes. As seen in fig. 8.7b, the intensities of the sidebands for the S-polarized pump are extremely small. As such, any error in accurately measuring photo-emitted electrons is more noticeable. We suggest two common Tr-ARPES measurement errors that can likely cause an asymmetry between $-y$ and $+y$ in our data.

(1) Pump electric field induced emission: As discussed in sec. 6.2.4, in a Tr-ARPES experiment, the electric field of the pump can be enhanced around sharp defects or impurities on the sample surface. For sufficiently high pump intensities (such as the ones used in our experiment), this enhancement can cause field emission from the sample surface by altering the confining potential of surface electrons. This can lead to electrons being photo-generated by the pump pulse even in the absence of the photo-emitting probe beam. These electrons then appear as a background error in the Tr-ARPES spectra. The energy and momentum distribution $I_b(E, \vec{k})$ of these background electrons strongly depends on the details of surface defects and imperfections and as such is non-uniform over $E$ and $\vec{k}$ and is also highly uncontrollable. Moreover, it can also depend on the pump polarization and thus can be different for P and S polarized pump. Therefore, it is likely that an asymmetry in $I_b(E, \vec{k})$ between $-k_y$ and $-k_y$ gives us the asymmetry in the data in fig. 8.12b.

(2) Small misalignment between the electron detector and the sample plane: As discussed in sec. 7.2.1, in our ARPES setup, photo-emitted electrons travel through an electrostatic lens tube and are then imaged onto a 2D detector to determine their in-plane momentum ($k_x$ and $k_y$). In order to accurately determine ARPES spectra centered at the $\Gamma$ point, it is important that the sample surface and the 2D detector are parallel to each other. A small tilt in the sample surface plane can skew the measured ARPES spectra along a particular direction leading to an asymmetry across the $\Gamma$ point. Thus, this can also be a probable cause for the small asymmetry between $-k_y$ and $-k_y$ in fig. 8.12b.

### 8.4.4 Full theoretical details

In this section, we provide details of theoretical calculations that lead to the Tr-ARPES intensities discussed above. We consider the Floquet-Bloch states generated by the mid-IR pump, the spin-probe effect on the photoemission matrix elements, and the influence of Volkov states (LAPE).

The effective Hamiltonian describing the unperturbed surface states of a 3D topological insulator is given by:

$$H = \sum_{k=k_x,k_y} \begin{pmatrix} c^\dagger_{k,\uparrow} & c^\dagger_{k,\downarrow} \end{pmatrix} \begin{pmatrix} 0 & \hbar v_f(-ik_x - k_y) \\ \hbar v_f(ik_x - k_y) & 0 \end{pmatrix} \begin{pmatrix} c_{k,\uparrow} \\ c_{k,\downarrow} \end{pmatrix}, \tag{8.11}$$

where $c^\dagger_{k,\sigma}$ creates a bare electron with momentum $k$ and pseudospin $\sigma$. Diagonalizing the Hamiltonian would give the canonical linear dispersion of surface states, i.e. $\epsilon_\pm(\vec{k}) = \pm\hbar v_f|\vec{k}|$. The mid-IR pump is introduced through the Peierls' substitution: $v_f\vec{k} \to v_f\vec{k} + ev_f\vec{A}(t)$, with $\vec{A}(t) = A_0 g(t)\,(a_x\cos(\omega t), a_y\sin(\omega t))$. $A_0$ is the peak vector potential, $g(t)$ describes the Gaussian pump envelope and $0 \le a_{x/y} \le 1$ characterize its polarizations. We use $\beta = ev_f A_0/\omega$ as the dimensionless Floquet parameter.

**Tr-ARPES intensity:** As discussed by Freericks et al. [243], the intensity measured in Tr-ARPES experiments can be written in terms of photoelectron correlations:

$$I(\vec{k},E) = \int_{t_i}^{t_f} dt \int_0^{t_f - t} d\tau s(t)s(t+\tau) \sum_{\sigma_1,\sigma_2,\sigma_f} M^*_k(\sigma_f,\sigma_1)M_k(\sigma_f,\sigma_2) 2\,\mathrm{Re}\left[\langle c^\dagger_{k,\sigma_1}(t+\tau)c_{k,\sigma_2}(t)\rangle e^{-iE\tau/\hbar}\right], \tag{8.12}$$

caused by a probe field with a normalized Gaussian envelope $s(t)$, an initial time $t_i$ and a final time $t_f$. The expectation value is taken with respect to the wavefunction of the driven system. This expression describes a virtual process where an electron is photoexcited at time $t$ and then returns at time $t+\tau$. The matrix elements $M_k(\sigma',\sigma)$ correspond to transitions from spin $\sigma$ to $\sigma'$ and depend on the details of system-probe interactions. In the absence of spin-probe coupling, we have $M_k(\sigma',\sigma) \propto \delta_{\sigma,\sigma'}$ and the Tr-ARPES intensity becomes:

$$I_0(\vec{k},E) \propto \int_{t_i}^{t_f} dt \int_0^{t_f - t} d\tau s(t)s(t+\tau) \sum_\sigma 2\,\mathrm{Re}\left[\langle c^\dagger_{k,\sigma}(t+\tau)c_{k,\sigma}(t)\rangle e^{-iE\tau/\hbar}\right]. \tag{8.13}$$

To solve this we use the equations of motion for the two-time correlation functions as follows:

$$\begin{aligned} \frac{d}{d\tau}\langle c^\dagger_{k,\uparrow}(t+\tau)c_{k,\uparrow/\downarrow}(t)\rangle &= (-K_x(t+\tau) - iK_y(t+\tau))\langle c^\dagger_{k,\downarrow}(t+\tau)c_{k,\uparrow/\downarrow}(t)\rangle, \\ \frac{d}{d\tau}\langle c^\dagger_{k,\downarrow}(t+\tau)c_{k,\uparrow/\downarrow}(t)\rangle &= (K_x(t+\tau) - iK_y(t+\tau))\langle c^\dagger_{k,\uparrow}(t+\tau)c_{k,\uparrow/\downarrow}(t)\rangle. \end{aligned} \tag{8.14}$$

The initial condition at $\tau = 0$ is determined by the equal-time correlations $\langle c^\dagger_{k,\sigma}(t) c_{k,\sigma'}(t)\rangle$. Generally speaking, the initial condition $\langle c^\dagger_{k,\sigma}(t) c_{k,\sigma'}(t)\rangle$ depends on $t$ due to the non-equilibrium nature of the problem. However, here we are mostly interested in the cases of $|\vec{k}| \leq k_F$, where both the lower and upper band of the unperturbed Dirac cone are filled so that no vertical transition is allowed by the drive. In this regime, we have $\langle c^\dagger_{k,\sigma}(t) c_{k,\sigma'}(t)\rangle = \langle c^\dagger_{k,\sigma}(0) c_{k,\sigma'}(0)\rangle = \delta_{\sigma,\sigma'}$.

**Spin-probe effect:** When the photoemitting probe couples to the spin, one has to compute the matrix elements $M_k(f,i) = \langle f|\vec{P}_k \cdot \vec{A}_{\text{probe}}(t)|i\rangle$ [232]. In accordance with our experimental setup, we consider a p-polarized probe such that $\vec{A}_{\text{probe}} = (A_x, 0, A_z)$. In general, $\vec{P}_k$ is some generalized momentum and depends on the system details and spin-orbit couplings. However, by considering the mirror reflection symmetry and the three-fold rotational symmetry [232], one can simplify the matrix elements to (in the basis of spin up and down):

$$M_k = i \begin{pmatrix} b_k A_z & \frac{a_k A_x}{2} \\ -\frac{a_k A_x}{2} & b_k A_z \end{pmatrix}, \tag{8.15}$$

where $a_k$ and $b_k$ are real coefficients. Using these matrix elements, eq. (8.12) becomes:

$$I(\vec{k}, E) \propto I_0(\vec{k}, E) + c_{SP} \int_{t_i}^{t_f} dt \int_0^{t_f - t} d\tau s(t) s(t+\tau) 2 \,\text{Re}\left[e^{-iE\tau/\hbar} \langle -i c^\dagger_{k,\uparrow}(t+\tau) c_{k,\downarrow}(t) + i c^\dagger_{k,\downarrow}(t+\tau) c_{k,\uparrow}(t)\rangle\right], \tag{8.16}$$

where the parameter $c_{SP} = [i a_k b_k A_z^* A_x + \text{c.c.}]/[a_k^2 |A_x|^2/2 + 2 b_k^2 |A_z|^2]$ characterizes the spin-probe effect. Note that the spin-probe effect only couples to the $S_y$ component in this setting of a p-polarized probe. Because of the spin-momentum locking, we have $S_y \sim \cos\theta$ and thus the spin-probe effect is most prominent at $\theta = 0, \pi$, i.e. along the $k_x$ direction. For a probe with a general polarization, the $S_x$ and $S_z$ components can also be involved ($S_x$ couples to $A_{y,z}$ and $S_z$ couples to $A_{x,y}$).

**Volkov states (LAPE):** As discussed earlier, Volkov states (LAPE) is caused dressing of the final free electron-like states with the pump pulse. The corresponding Hamiltonian is $H_{\text{LAPE}} = \hbar e \vec{v}_0 \cdot \vec{A}(t)$, where $\vec{v}_0$ is the free electron velocity. Consequentially, the two-time

correlation function in the Tr-ARPES intensity (eq. (8.12)) picks up an additional phase:

$$\begin{aligned} e^{i\Theta(\alpha_k,t,\tau)} &= e^{-i\int_t^{t+\tau} dt' H_{\mathrm{LAPE}}(t')/\hbar} \\ &= e^{-i(\alpha_{k_x}+\alpha_{k_z})[\sin\omega(t+\tau)-\sin\omega t]+i\alpha_{k_y}[\cos\omega(t+\tau)-\cos\omega t]}, \end{aligned} \tag{8.17}$$

where $\alpha_{k_i} = ev_{0,i}A_{\mathrm{pump},i}/\omega$. Note that, unlike Floquet states, the pump field can give an out-of-plane ($z$) component contribution to Volkov states. In fact, for the p-polarized pump experiment, we have $\alpha_{k_z} \gg \alpha_{k_x/k_y}$, since the pump E-field has a larger $z$-component and $|v_{0,z}| \sim v_f \gg |v_{0,x/y}|$ (sec.8.6). Thus, we set $\alpha_{k_z} = \alpha$ and $\alpha_{k_x/k_y} = 0$ for calculations for p-polarized pump.

**Complete expression for Tr-ARPES intensity**: Based on the above, the net Tr-ARPES intensity, including the spin-probe ($c_{SP}$) and Volkov state ($\alpha_k$) effects, is given by:

$$I(\vec{k},E) \propto \int_{t_i}^{t_f} dt \int_0^{t_f-t} d\tau s(t)s(t+\tau) 2\,\mathrm{Re}\left\{e^{-iE\tau/\hbar}e^{i\Theta(\alpha_k,t,\tau)}\left[S_0(t,\tau)+c_{SP}S_y(t,\tau)\right]\right\}, \tag{8.18}$$

where $S_0(t,\tau) = \sum_\sigma \langle c^\dagger_{k,\sigma}(t+\tau)c_{k,\sigma}(t)\rangle$ and $S_y(t,\tau) = \langle -ic^\dagger_{k,\uparrow}(t+\tau)c_{k,\downarrow}(t) + ic^\dagger_{k,\downarrow}(t+\tau)c_{k,\uparrow}(t)\rangle$ can be obtained by solving eq. (8.14). The theory curves in fig. 8.10 and in fig. 8.12 are calculated using this expression.

**Analytical solutions without Volkov states**: Here we get analytical expressions for the Tr-ARPES intensity for the special cases where $\vec{k} \parallel \vec{A}(t)$ in order to get insights into the symmetry of the Tr-ARPES spectra with and without the Volkov states. This corresponds to the solution for $\pm k_x$ for a p-polarized pump, and for $\pm k_y$ for a s-polarized pump. We first consider the case without Volkov states (i.e. pure Floquet). For p-polarized pump, the driven Hamiltonian $H(t) = \hbar v_f\left(k_x + eA_0\cos\omega t\right)\sigma_y$. The two-time correlation functions can be solved from eq. (8.14):

$$\begin{aligned} S_0(t,\tau) &= 2\cos\left\{v_f k_x\tau + \beta\left[\sin\omega(t+\tau)-\sin\omega t\right]\right\} \\ &= \sum_{n_1,n_2} e^{i(v_f k_x+n_1\omega)\tau}e^{i(n_1+n_2)\omega t}J_{n_1}(\beta)\,J_{n_2}(-\beta) + c.c., \\ S_y(t,\tau) &= 2i\sin\left\{v_f k_x\tau + \beta\left[\sin\omega(t+\tau)-\sin\omega t\right]\right\} \\ &= \sum_{n_1,n_2} e^{i(v_f k_x+n_1\omega)\tau}e^{i(n_1+n_2)\omega t}J_{n_1}(\beta)\,J_{n_2}(-\beta) - c.c., \end{aligned} \tag{8.19}$$

Using these expressions, we can perform the double-time integral in eq. (8.18) for $|k_x| \leq k_F$. The $\tau$ integral leads to Tr-ARPES peaks, while the $t$ integral averages over different Fourier modes, leaving only the $n_1 = -n_2$ components. The Floquet only result for a p-polarized pump is:

$$I(k_x, E) \propto \sum_n \left\{(1 + c_{SP})\delta_{E,\hbar v_f k_x + n\hbar\omega} + (1 - c_{SP})\delta_{E,-\hbar v_f k_x + n\hbar\omega}\right\} J_n(\beta)^2 , \tag{8.20}$$

When $c_{SP} = 0$, the $n$-th intrinsic Floquet peak has an intensity of $J_n(\beta)^2$ and is symmetric about $\pm k_x$. Similarly, for the case of a s-polarized pump, the intensity for $\pm k_y$ for pure Floquet states is given by:

$$I(k_y, E) \propto T \sum_n \left\{\delta_{E,\hbar v_f k_y + n\hbar\omega} + \delta_{E,-\hbar v_f k_y + n\hbar\omega}\right\} J_n(\beta)^2 , \tag{8.21}$$

where the spin-probe effect does not enter due to the absence of the $S_y$ component along $k_y$.

**Analytical solutions with Volkov states**: The analytical expressions become very different in the presence of Volkov states. We first consider the case of $\pm k_x$ for p-polarization with a constant Volkov parameter $\alpha_{k_z} = \alpha$. From eq. (8.17), this gives rise to a phase:

$$\begin{aligned} e^{i\Theta(\alpha,t,\tau)} &= e^{-i\alpha[\sin\omega(t+\tau) - \sin\omega t]} \\ &= \sum_{m_1,m_2} e^{im_1\omega\tau} e^{i(m_1+m_2)\omega t} J_{m_1}(-\alpha) J_{m_2}(\alpha) . \end{aligned} \tag{8.22}$$

Inserting Eqs. (8.19) and (8.22) into eq. (8.18) and taking $c_{SP} = 0$ for simplicity, the Tr-ARPES intensity for p-polarization becomes:

$$\begin{aligned} I(k_x, E) &\propto \left[\sum_{n_1,m_1} \delta_{E,\hbar v_f k_x + (n_1+m_1)\hbar\omega}\ J_{n_1}(\beta) J_{m_1}(-\alpha)\right]^2 \\ &\quad + \left[\sum_{n_1,m_1} \delta_{E,-\hbar v_f k_x - (n_1-m_1)\hbar\omega}\ J_{n_1}(\beta) J_{m_1}(-\alpha)\right]^2 \\ &\propto \sum_n \left[\delta_{E,\hbar v_f k_x + n\hbar\omega}\ J_n(\beta-\alpha)^2 + \delta_{E,-\hbar v_f k_x + n\hbar\omega}\ J_n(\beta+\alpha)^2\right]. \end{aligned} \tag{8.23}$$

In comparison with eq. (8.20), these equations demonstrate how Volkov states interfere with the intrinsic Floquet-Bloch states. For example, for the zeroth order peak at $E = \hbar v_f k_x$, we can have contributions from different Fourier pairs of Floquet ($n_1$) and Volkov ($m_1$) modes

that satisfy $n_1 + m_1 = 0$ as shown in the first line of equations. This expression further illustrates that, in this case of a p-polarized pump, even in the absence of the spin-probe effect $c_{SP} = 0$, the measured intensity about $\pm k_x$ is asymmetric in each Floquet band. This is exactly what we observe in fig. 8.10 in the main text.

We can work out the analytical expression for $\pm k_y$ for s-polarized pump in the same way. The resultant Tr-ARPES intensity is:

$$I(k_y, E) \propto T \sum_n \left[ \delta_{E,\hbar v_f k_y + n\hbar\omega} \; J_n \left( \beta - \alpha_{k_y} \right)^2 + \delta_{E,-\hbar v_f k_y + n\hbar\omega} \; J_n \left( \beta + \alpha_{k_y} \right)^2 \right]. \tag{8.24}$$

Again, the spin-probe effect does not appear because of the vanishing of the $S_y$ component along $k_y$. We have included a small but finite Volkov parameter $\alpha_{k_y} \propto k_y$. Different from the p-polarization situation, $\alpha_{k_y}$ changes sign between $+k_y$ and $-k_y$ here. Thus, the Floquet sideband weights remain symmetric between $+k_y$ and $-k_y$. Based on this result, the slight asymmetry at $\pm k_y$ observed in fig. 8.12 is not caused by Volkov states but is likely due to experimental errors.

In summary, the systematic characterization of these electron-photon hybrid states presented in this section has important implications for the coherent manipulation of quantum states and various techniques used to investigate this phenomenon. Understanding the coupling of Floquet-Bloch states to other electronic states is crucial for engineering novel light-induced quantum phases of matter. Furthermore, the observed interference between initial and final dressed states extends beyond Tr-ARPES; it will also manifest in other experimental techniques such as tunneling spectroscopy of light-dressed electronic systems.

## 8.5 Dynamics of photon-dressed states

So far we have mainly focused on the mid-IR pump Tr-ARPES spectra at $t = 0$ i.e. where the intensity of the dressed sidebands is maximized. A key problem is understanding the interactions of these photon-dressed electronics states with other excitations in the system such as phonons. A number of theoretical works such as [214] and [213] have considered the effects of electron-photon and electron-electron interactions in stabilizing Floquet-Bloch modes.

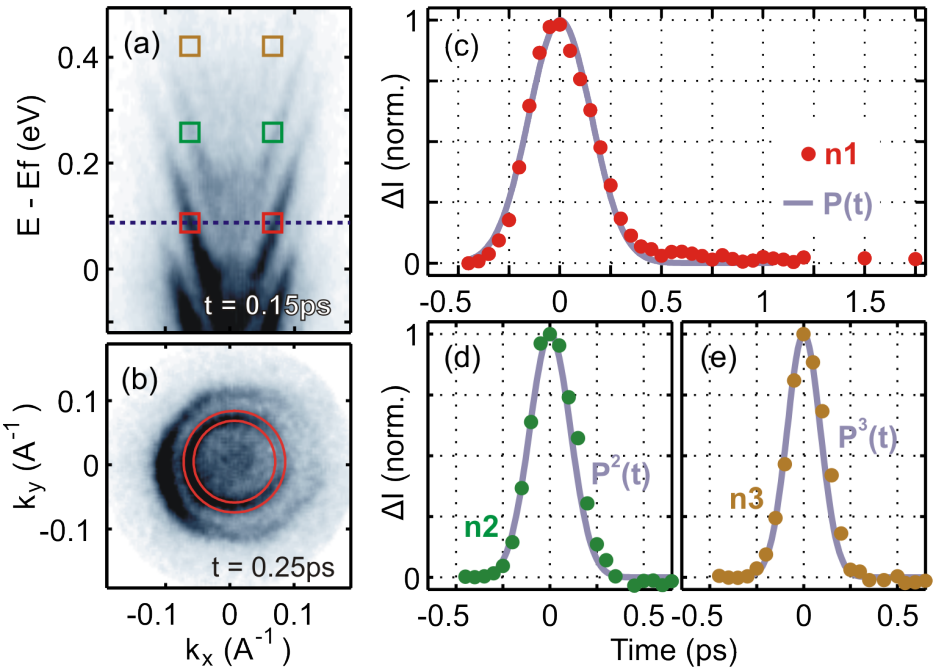


**Figure 8.13:** Dynamics of photon-dressed sidebands in $Bi_2Se_3$ **(a)** Tr-ARPES spectra on $Bi_2Se_3$ taken with $\sim 160$ meV mid-IR pump at $t = 0.15$ ps. Red, green and dark yellow squares indicate the regions corresponding to the 1st, 2nd and 3rd order sidebands over which the change in intensity $\Delta I$ is plotted as a function of time in **(c)**, **(d)** and **(e)**. Blue dotted line in (a) indicates the energy at which a constant energy cut is taken and shown in (**b**). Area between the red concentric circles indicates the region over which the intensity is integrated for the time-trace in (c). Similar integration is done in (d) and (e). The pump temporal profile $P(t)$, its square $P^2(t)$ and cube $P^3(t)$ are also plotted.

One way to understand these interactions is to study the relaxation dynamics of the excited dressed states in our Tr-ARPES experiments. We first study the case of $Bi_2Se_3$ as before. We take Tr-ARPES spectra using mid-IR ($\sim 160$ meV) P-polarized pump pulses at every 50 fs delay time between the pump and probe. In this way we can obtain the change in intensity $\Delta I_n(t)$ of the n-th order sideband to get a measure of the intinsic lifetime of a particular dressed state. Moreover, the dynamic behavior of $\Delta I_n(t)$ can also provide important clues into scattering between dressed states and other excitations in the system.

Figure 8.13c, d and e show the background-subtracted $\Delta I(t)$ for the first, second and third order photon dressed sidebands in $Bi_2Se_3$ respectively. For each sideband $\Delta I(t)$ is obtained by from the measured intensity in the square regions shown in fig. 8.13a. This intensity is then

integrated over the whole sideband in momentum space for the constant energy cut as shown in fig. 8.13b. The obtained results do not dependent on the energy at which the constant energy cut is taken, within experimental resolution. Our choice here gives approximately a circular surface state contour without any noticeable hexagonal warping effects [244].

As seen in fig. 8.13c, $\Delta I_1(t)$ roughly follows the Gaussian intensity profile $P(t)$ of the mid-IR pump pulse. Here $P(t)$ is obtained using image-potential states as discussed in sec. 7.1.4. This result is expected since, as outlined earlier, the n-th order sideband intensity is given by the square of a n-th order Bessel function in the electric field of the pump: $I_n \propto J_n(\beta \pm \alpha)^2$. Both $\beta$ and $\alpha$ depend linearly on the electric field ($E(t)$) and thus:

$$I_n(t) \propto (|E(t)|^2)^n \propto P^n(t). \tag{8.25}$$

Similar to $\Delta I_1(t)$ following $P(t)$, $\Delta I_2(t)$ and $\Delta I_3(t)$ match the temporal profile of $P^2(t)$ and $P^3(t)$ as plotted in fig. 8.13d and fig. 8.13e respectively. This behavior is expected from eq. (8.25) i.e. the second-order and third-order sidebands follow the square and cube of the intensity profile of the pump pulse. Taken together these results suggest that the intrinsic lifetime of dressed states in $Bi_2Se_3$ is less than or similar to the temporal width of the driving field.

### 8.5.1 Persistent photoinduced sidebands in $Bi_2Te_3$

The situation changes for the case of dressed bands in another topological insulator, $Bi_2Te3$. Here we perform the same Tr-ARPES experiment with the same p-polarized mid-IR ($\sim$ 160 meV) pump pulse as that used for $Bi_2Te3$. Figure 8.14 shows Tr-ARPES spectra using P-polarized pump on $Bi_2Se_3$ at various delay times between the pump and probe. Both $E - E_f$ vs $k_y$ (bottom panel) and constant energy surface contours at $E - E_f = 0.11$ eV (top panel) are shown. Similar to the case for $Bi_2Se_3$ (fig. 8.4), replicas (sidebands) of the original cone, spaced exactly by the energy of the pump pulse, appear when the pump and probe pulse overlap in time. However, unlike the spectra for $Bi_2Se_3$, the spectra here shows a sideband even after the pump pulse disappears. This is apparent in the spectra taken

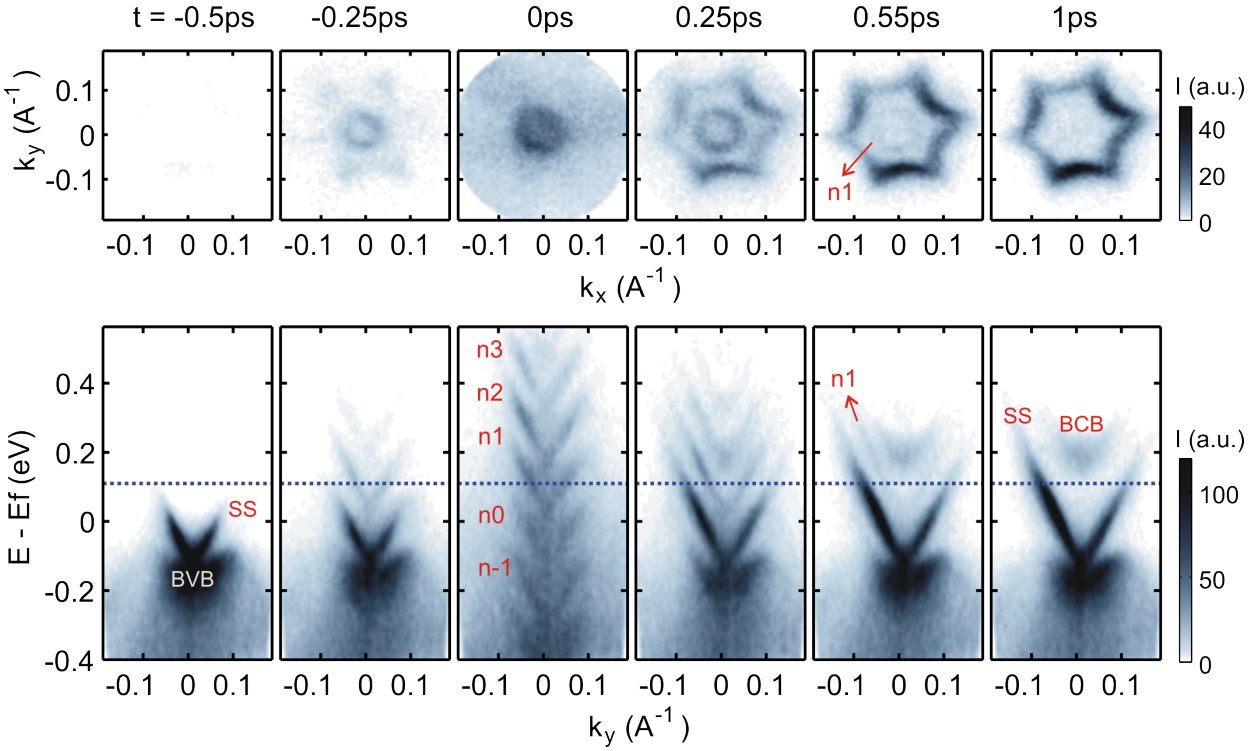


**Figure 8.14:** Bottom panel: Tr-ARPES ($E - E_f$ vs $k_y$) spectra on $Bi_2Te_3$ using P-polarized mid-IR ($\sim 160\,\text{meV}$) pump at various delay times between the pump and the probe. BCB refers to the bulk conduction band while SS refers to the topological surface state. The nth order sidebands are indicated in the spectra. Top panel: Constant energy cuts ($k_x$ vs $k_y$) at different delay times along the blue dotted line shown in the lower planel.

at $t = 0.55\,\text{ps}$ which shows a significant intensity of the first order (n1) sideband (labeled). This intensity eventually disappears for the spectra taken at $t = 1\,\text{ps}$.

To study this further, we extract the background-subtracted $\Delta I(t)$ for the first, second and third order sidebands in $Bi_2Te_3$ and plot the results in fig. 8.15c-e. For each sideband $\Delta I(t)$ is obtained by from the measured intensity in the square regions shown in fig. 8.13a. This intensity is then integrated over the whole sideband in momentum space for the constant energy cut as shown in fig. 8.13b. As expected from eq. (8.25), $\Delta I_2(t)$ and $\Delta I_3(t)$ follow the square and cube of the intensity profile of the pump respectively (fig. 8.15d,e). However, unexpectedly, $\Delta I_1(t)$ (fig. 8.15c) has a 'hump' like feature around $t = 0.4\,\text{ps}$ and remains non-zero even when the pump intensity profile $P(t)$ is zero.

Here we discuss a few possible reasons for this surprising behavior in $Bi_2Te_3$. The

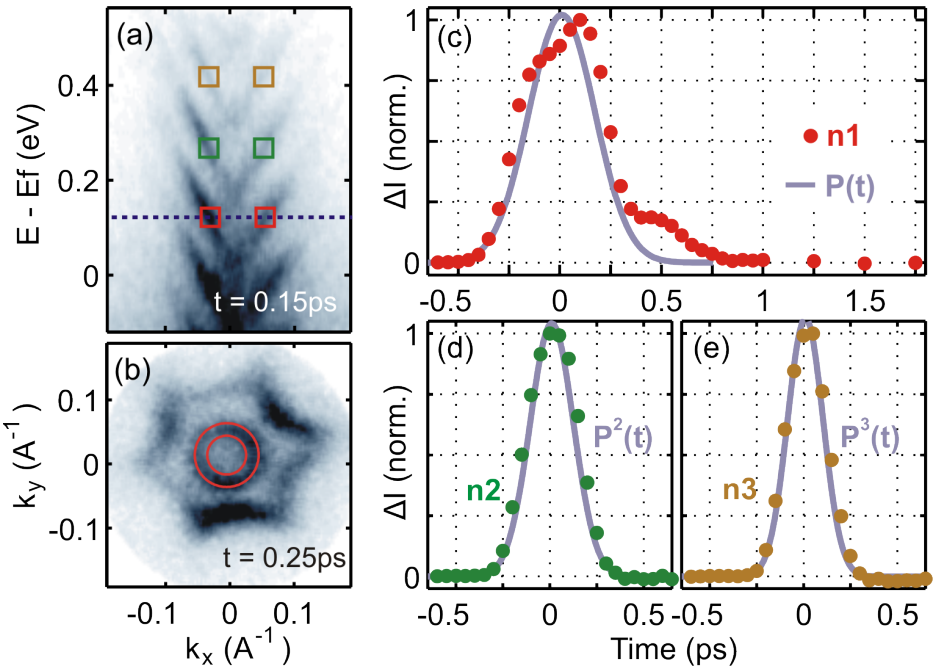


**Figure 8.15:** Dynamics of photon-dressed sidebands in $Bi_2Te_3$ **(a)** Tr-ARPES spectra on $Bi_2Te_3$ taken with $\sim 160$ meV mid-IR pump at $t = 0.15$ ps. Red, green and dark yellow squares indicate the regions corresponding to the 1st, 2nd and 3rd order sidebands over which the change in intensity $\Delta I$ is plotted as a function of time in **(c)**, **(d)** and **(e)**. Blue dotted line in (a) indicates the energy at which a constant energy cut is taken and shown in (**b**). Area between the red concentric circles indicates the region over which the intensity is integrated for the time-trace in (c). Similar integration is done in (d) and (e). The pump temporal profile $P(t)$, its square $P^2(t)$ and cube $P^3(t)$ are also plotted.

simplest explanation could be that the pump temporal profile is non-Gaussian and actually matches $\Delta I_1(t)$. However, in that case both $\Delta I_2(t)$ and $\Delta I_3(t)$ should be non-Gaussian as well which is clearly not the case in either $Bi_2Te_3$ or in $Bi_2Se_3$. Another, and more likely, explanation is based on the interaction of these dressed surface sidebands with existing bulk states in the sample. This is illustrated in fig. 8.16. If we consider the band structure of $Bi_2Se_3$, we first order sideband overlaps with the bulk conduction band (BCB) allowing scattering between the two. In contrast, in $Bi_2Te_3$, even though the bulk band gap is smaller, the distance between the Dirac point and the BCB is larger and so the first order sideband lies mostly in between the BCB and the original surface state (SS) (fig. 8.16b). This limits the interaction of the dressed surface state with the bulk and could lead to a

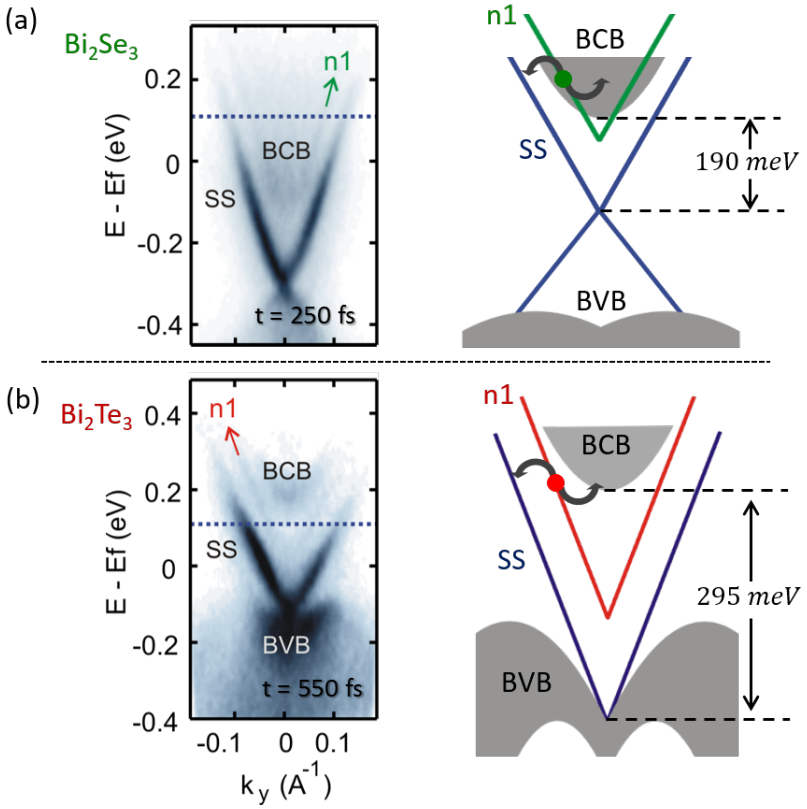


**Figure 8.16:** Comparison of the 1st order photon-dressed sideband in $Bi_2Se_3$ & $Bi_2Te_3$. **(a)** Left: Tr-ARPES spectra at $t = 250$ fs on $Bi_2Se_3$ with mid-IR pump. The first order sideband n1 is labeled. Right: Schematic of the original SS in $Bi_2Se_3$ and the n1 sideband due to a 160 meV pump. **(b)** Left: Tr-ARPES spectra at $t = 550$ fs on $Bi_2Te_3$ with the same mid-IR pump. The first order sideband n1 is labeled. Right: Schematic of the original SS in $Bi_2Te_3$ and the n1 sideband due to a 160 meV pump. BCB and BVB in (a) and (b) denote the bulk conduction and bulk valence bands respectively.

slightly longer lived n1 sideband in $Bi_2Te_3$ than in $Bi_2Se_3$.

The discussion above assumes that once generated a particular sideband is able to persist even without a periodic drive. This is counter to the theory for both Floquet-Bloch and Volkov states as presented in sec. 8.4.4. A particular Floquet or Volkov mode generated by the pump photon should only exist during the pulse width of the pump. Based on this the persistent sideband cannot be generated by the time-periodic potential of the pump pulse. Another option is that the persistent n1 sideband in $Bi_2Te_3$ is rather generated by the time-periodic potential of an internal collective excitation of the system such as

plasmons or a high-energy phonons. It is possible that the mid-IR pump resonantly excites an IR-active plasmon or phonon at the energy $\hbar\omega$ of the pump photon. In this case, the time periodic potential from the collective excitation is able to persist longer than the duration of the pump pulse. While there is little evidence for phonon modes in $Bi_2Te_3$ with such high energies, IR spectroscopy [245] does point to plasma frequencies in $Bi_2Te_3$ in the range of the frequency of the pump pulse. Thus, based on preliminary analysis, we posit that the persistent n1 sideband is generated by a plasma oscillation of charge carriers in $Bi_2Te_3$. Research into verifying this is ongoing.

## 8.6 Supplementary: experimental parameters

In this section we provide estimates of various experimental parameters. As discussed earlier the two dimensionless parameters relevant to this work are $\alpha$ and $\beta$. The Volkov parameters $\alpha = ev_0A_0/\omega$ characterizes the interaction strength between light and the final states of photoemission while the Floquet parameter $\beta = ev_fA_i/\omega$ characterizes the strength of the Floquet interaction. Here $A_{0,i} = E_{0,i}/\omega$ where $E_{0,i}$ is the electric field amplitude along a particular electron velocity direction. For Floquet states, the relevant velocity is the Fermi velocity for the surface state electrons. Since this velocity is purely in-plane, the relevant electric field ($E_i$) is the one parallel to the sample surface. This E-field can be calculated using the measured pump power, diameter and pulse width along with the refractive index of $Bi_2Se_3$ as detailed in sec. 7.1.4. Taking $E_i = 3.3 \times 10^7\,\mathrm{V/m}$ corresponding to a measured pump power of 11.5 mW and $v_f = 5 \times 10^5\,\mathrm{m/s}$, we obtain $\beta = 0.42$.

For Volkov states we need to determine the electron velocity in the final state of photoemission. As the in-plane momentum is conserved in the photoemission process and given that the final state is free electron-like, we determine the in-plane velocity, $v_\parallel = 5.79 \times 10^4\,\mathrm{m/s}$ for momentum, $k = 0.05\,\mathrm{\AA}^{-1}$. By conserving energy, this gives the out-of-plane electron velocity, $v_z = 4.55 \times 10^5\,\mathrm{m/s}$. Note that $v_z \gg v_\parallel$. Thus, the relevant velocity for the effect of Volkov states is $v_0 = v_z$ and the relevant electric field ($E_0$) is

the out-of-plane component of the electric field outside the sample surface. Using Fresnel equations (sec. 7.1.4), we obtain $E_0 = 11.6 \times 10^7$ V/m and thus $\alpha \sim 1.36 - 1.4$.

We note that the values of $\alpha = 1.38$ and $\beta = 0.5$ used in fig. 8.10 in fig. 8.12 are determined by fitting the observed angular dependence of the sideband intensities in the Tr-ARPES spectrum to the theoretically calculated intensities in sec. 8.4.4. We also used $c_{SP} = 0.96$ and 0.7 for the p- and s-polarized pumps, respectively, to account for the spin-probe effect. Given the large uncertainty in determining the exact electric field at the sample surface, these values are consistent with the values calculated in this section.

# Appendices

# A

# Quasi-particle recombination dynamics in underdoped $La_{2-x}Sr_xCuO_4$

In this appendix we review the Rothwarf-Taylor (RT) equations as they are used to understand time-resolved experiments on superconducting cuprates (e.g. [18]) and pnictides (e.g. [246]). We then apply these equations to quasi-particle (QP) recombination dynamics in the underdoped $La_{2-x}Sr_xCuO_4$ films studied in chap. 3 to gain insights into the symmetry of the superconducting order parameter.

In OPP experiments on superconductors, the 1.55 eV pump pulse breaks apart Cooper pairs to create an energetic QP population density $n$. The RT equations are a set of coupled differential equations that describe the resulting coupling between these QPs and the binding boson population density $N$:

$$\begin{aligned} \frac{dn}{dt} &= -\beta n^2 + 2\gamma_{pc} N \\ \frac{dN}{dt} &= \beta n^2/2 - \gamma_{pc} N - \gamma_{esc}(N - N_{eq}) \end{aligned} \tag{A.1}$$

The processes in these equations are illustrated in fig. A.1. The terms in $\beta$ represent the pair-wise recombination process of the QPs. These terms depend on the square of $n$ since two QPs must meet to form a Cooper pair. In that recombination process, a binding

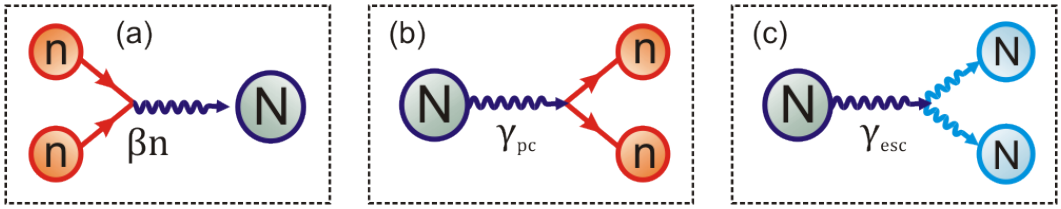


**Figure A.1:** Schematic representaton of the processes in the Rothwarf-Taylor equations. **(a)** Quasi-particle ($n$) pair-wise recombination to generate a binding boson (N) with rate $\beta n$. **(b)** Quasi-particle creation process by absorption of a binding boson with rate $\gamma_{pc}$. **(c)** Decay of binding boson into lower energy bosons with rate $\gamma_{esc}$.

boson is emitted (i.e. $n + n \rightarrow N$). The reverse process is also possible: a pair of QPs can be created by absorption of a boson (i.e. $N \rightarrow n + n$). The rate for this process is given by $\gamma_{pc}$. Additionally, $\gamma_{esc}$ is the rate at which the pair-creating bosons decay into lower energy bosons or leave the photo-excited region.

In conventional BCS superconductors, the binding boson is a phonon and the QP recombination rate is similar to $\gamma_{pc}$. As a resulting, the QP and pair-creating phonon populations quickly establish a quasi-equilibrium among each other and the eventual return to steady-state equilibrium is determined by the rate at which these populations escape the photo-excited region i.e. $\gamma_{esc}$. This is the 'phonon bottleneck regime'.

In contrast in cuprate superconductors, it is assumed that more relaxation pathways are available for the QPs to recombine than the emission of just one phonon. As a result $\gamma_{pc}$ is small compared to the recombination rate. Thus, the first equation in eq. (A.1) reduces to $dn/dt = -\beta n^2$ and so the recovery rate to steady-state equilibrium is $\gamma_r = (1/n)(dn/dt) = \beta n$. For an optical pump-probe experiment on cuprates, this implies that the decay of the signal $\gamma_r$, in the superconducting (SC) phase, should depend linearly on the initial photo-excited QP density which in turn should scale linearly with the pump fluence for low fluences (i.e. that don't melt the SC phase).

At finite temperatures, the RT equations get modified due to the presence of thermally excited QPs $n_{th}$. In this case, a photo-excited QP can recombine with a photo-excited one at a rate proportional to the population of thermally excited QPs. Thus, the first equation

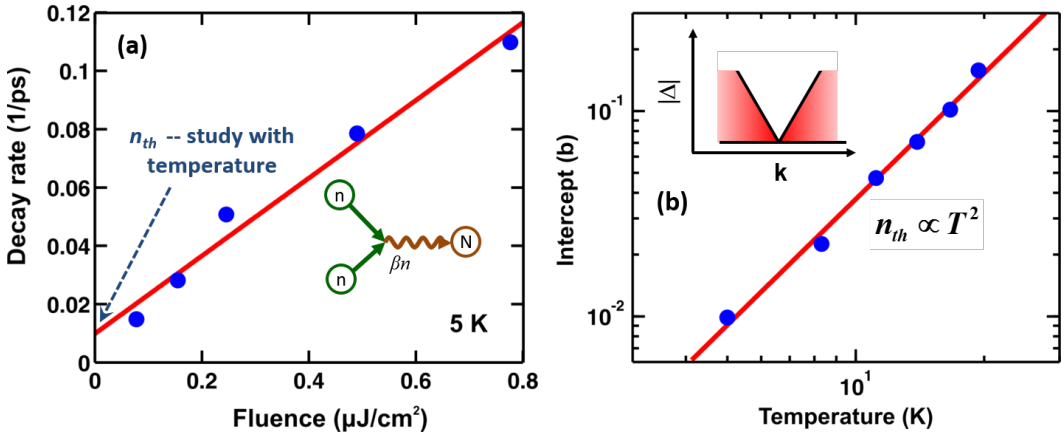


**Figure A.2:** **(a)** Initial decay rate of the OPP signal in $La_{1.9}Sr_{0.1}CuO_4$ at 5 K with pump fluence & temperature. Red line is a linear best fit to the data (blue dots). **(b)** The intercept in (a) is plotted as a function of temperature. Red line is a best-fit to a power-law.

in eq. (A.1) becomes $dn/dt = -\beta(n_{ph}^2 + 2n_{th}n_{ph})$ where $n_{ph}$ denotes the photo-excited QPs. Thus, the total decay rate of photo-excited QPs is given by:

$$\gamma_r = \beta(n_{ph} + 2n_{th}) \tag{A.2}$$

This observation is extremely helpful in understanding the OPP signal in cuprates below $T_c$ in chap. 3. Consider the PP signal in fig. 3.7a taken on an underdoped $La_{2-x}Sr_xCuO_4$ thin-film ($x = 0.10$) at 5 K. We extract the initial decay rate $\gamma$ for signals at various pump-fluences ($\mathcal{F}$) from 0 to 1 μJ/cm$^2$ and plot them as a function of $\mathcal{F}$ in fig. A.2a. As expected from eq. (A.2), $\gamma$ scales with the fluence i.e. with $n_ph$. Moreover, the line of best fit has a finite positive y-intercept. This signifies that in the $\mathcal{F} \to 0$ limit, the decay rate is governed by thermally excited QPs $n_{th}$. In fact, the intercept is proportional to $n_{th}$. By tracking this intercept rate ($\gamma_{th}$) as a function of temperature $T$, we can deduce how $n_{th}$ scales with $T$. This is plotted in fig. A.2b on a log-log plot for temperatures below $T_c$. As can be seen, the intercept in (a) follows a power-law dependence with temperature i.e. $\gamma_{th} \sim n_{th} \sim T^\eta$ with $\eta = 2$.

This power-law behavior can be understood using the d-wave gap symmetry of the a cuprate superconductor. Thermally excited QPs originate from near the node and so the QP dispersion is Dirac-like similar to the surface states of topological insulators and

graphene. In this case the density of states of QPs scales linearly with the energy i.e. $g(E) \propto E$ and so thermal excitations $n(T) = \int_0^{kT} g(E)dE \propto T^2$. Similar power laws have been observed in time-resolved THz experiments in optimally doped $La_{2-x}Sr_xCuO_4$ [247] and in OPP experiments in a pnictide superconductor [246]. Here we note that this power-law is unique to the presence of a node in the gap symmetry of cuprate superconductors. Had the Fermi-surface been fully gapped in momentum space, the expected thermal QP density would have scaled with an Arrhenius behavior i.e. $n_{th} \propto \exp(-\Delta/kT)$ where $\Delta$ is the SC gap. However, that is clearly not observed in fig. A.2b.

# References


[1] Joseph Orenstein. "Ultrafast spectroscopy of quantum materials". In: *PHYSICS TODAY* 65.9 (2012), pp. 44–50. URL: http://dx.doi.org/10.1063/PT.3.1717.

[2] Donghui Lu et al. "Angle-Resolved Photoemission Studies of Quantum Materials". In: *Annual Review of Condensed Matter Physics* 3.1 (2012), pp. 129–167. eprint: http://dx.doi.org/10.1146/annurev-conmatphys-020911-125027. URL: http://dx.doi.org/10.1146/annurev-conmatphys-020911-125027.

[3] Joel Moore. "Introduction to topology and new states in quantum materials". Conference: Big ideas in quantum materials. 2015.

[4] L. D. Landau. "The theory of a Fermi liquid". In: *Sov. Phys. JETP* 3.6 (1957), p. 920.

[5] K. v. Klitzing, G. Dorda, and M. Pepper. "New Method for High-Accuracy Determination of the Fine-Structure Constant Based on Quantized Hall Resistance". In: *Phys. Rev. Lett.* 45 (6 Aug. 1980), pp. 494–497. URL: http://link.aps.org/doi/10.1103/PhysRevLett.45.494.

[6] D. C. Tsui, H. L. Stormer, and A. C. Gossard. "Two-Dimensional Magnetotransport in the Extreme Quantum Limit". In: *Phys. Rev. Lett.* 48 (22 May 1982), pp. 1559–1562. URL: http://link.aps.org/doi/10.1103/PhysRevLett.48.1559.

[7] R. B. Laughlin. "Anomalous Quantum Hall Effect: An Incompressible Quantum Fluid with Fractionally Charged Excitations". In: *Phys. Rev. Lett.* 50 (18 May 1983), pp. 1395–1398. URL: http://link.aps.org/doi/10.1103/PhysRevLett.50.1395.

[8] J. G. Bednorz and K. A. Müller. "Possible high $T_c$ superconductivity in the Ba-La-Cu-O system". In: *Zeitschrift fur Physik B Condensed Matter* 64 (June 1986), pp. 189–193.

[9] N F Mott. "The Basis of the Electron Theory of Metals, with Special Reference to the Transition Metals". In: *Proceedings of the Physical Society. Section A* 62.7 (1949), p. 416. URL: http://stacks.iop.org/0370-1298/62/i=7/a=303.

[10] K. Andres, J. E. Graebner, and H. R. Ott. "$4f$-Virtual-Bound-State Formation in $CeAl_3$ at Low Temperatures". In: *Phys. Rev. Lett.* 35 (26 Dec. 1975), pp. 1779–1782. URL: http://link.aps.org/doi/10.1103/PhysRevLett.35.1779.

[11] K. S. Novoselov et al. "Electric Field Effect in Atomically Thin Carbon Films". In: *Science* 306.5696 (2004), pp. 666–669. eprint: http://science.sciencemag.org/content/306/5696/666.full.pdf. URL: http://science.sciencemag.org/content/306/5696/666.

[12] C. L. Kane and E. J. Mele. "$Z_2$ Topological Order and the Quantum Spin Hall Effect". In: *Phys. Rev. Lett.* 95 (14 Sept. 2005), p. 146802. URL: http://link.aps.org/doi/10.1103/PhysRevLett.95.146802.

[13] B. Andrei Bernevig, Taylor L. Hughes, and Shou-Cheng Zhang. "Quantum Spin Hall Effect and Topological Phase Transition in HgTe Quantum Wells". In: *Science* 314.5806 (2006), pp. 1757–1761. eprint: http://science.sciencemag.org/content/314/5806/1757.full.pdf. URL: http://science.sciencemag.org/content/314/5806/1757.

[14] Markus König et al. "Quantum Spin Hall Insulator State in HgTe Quantum Wells". In: *Science* 318.5851 (2007), pp. 766–770. eprint: http://science.sciencemag.org/content/318/5851/766.full.pdf. URL: http://science.sciencemag.org/content/318/5851/766.

[15] Xiaodong Xu, Wang Yao, Di Xiao, and Tony F. Heinz. "Spin and pseudospins in layered transition metal dichalcogenides". In: *Nat Phys* 10.5 (2014), pp. 343–350. URL: http://dx.doi.org/10.1038/nphys2942.

[16] B. Keimer, S. A. Kivelson, M. R. Norman, S. Uchida, and J. Zaanen. "From quantum matter to high-temperature superconductivity in copper oxides". In: *Nature* 518.7538 (2015), pp. 179–186. URL: http://dx.doi.org/10.1038/nature14165.

[17] B. J. Kim et al. "Phase-Sensitive Observation of a Spin-Orbital Mott State in Sr2IrO4". In: *Science* 323.5919 (2009), pp. 1329–1332. eprint: http://science.sciencemag.org/content/323/5919/1329.full.pdf. URL: http://science.sciencemag.org/content/323/5919/1329.

[18] G. P. Segre et al. "Photoinduced Changes of Reflectivity in Single Crystals of $YBa_2Cu_3O_{6.5}$ (Ortho II)". In: *Phys. Rev. Lett.* 88 (13 Mar. 2002), p. 137001. URL: http://link.aps.org/doi/10.1103/PhysRevLett.88.137001.

[19] N. Gedik et al. "Single-quasiparticle stability and quasiparticle-pair decay in $YBa_2Cu_3O_{6.5}$". In: *Physical Review B* 70.1 (2004). PRB, p. 014504. URL: http://link.aps.org/doi/10.1103/PhysRevB.70.014504.

[20] Christopher L. Smallwood et al. "Tracking Cooper Pairs in a Cuprate Superconductor by Ultrafast Angle-Resolved Photoemission". In: *Science* 336.6085 (2012), pp. 1137–1139. eprint: http://science.sciencemag.org/content/336/6085/1137.full.pdf. URL: http://science.sciencemag.org/content/336/6085/1137.

[21] N. Gedik, J. Orenstein, R. Liang, D. A. Bonn, and W. N. Hardy. "Diffusion of nonequilibrium quasi-particles in a cuprate superconductor". In: *Science* 300 (2003). 10.1126/science.1083038, pp. 1410–1412. URL: http://dx.doi.org/10.1126/science.1083038.

[22] Roman Yusupov et al. "Coherent dynamics of macroscopic electronic order through a symmetry breaking transition". In: *Nat Phys* 6.9 (2010). 10.1038/nphys1738, pp. 681–684. URL: http://dx.doi.org/10.1038/nphys1738.

[23] D. Fausti et al. “Light-Induced Superconductivity in a Stripe-Ordered Cuprate”. In: *Science* 331.6014 (2011), pp. 189–191. eprint: http://science.sciencemag.org/content/331/6014/189.full.pdf. URL: http://science.sciencemag.org/content/331/6014/189.

[24] W. Hu et al. “Optically enhanced coherent transport in YBa2Cu3O6.5 by ultrafast redistribution of interlayer coupling”. In: *Nat Mater* 13.7 (2014), pp. 705–711. URL: http://dx.doi.org/10.1038/nmat3963.

[25] Darius H. Torchinsky*, Fahad Mahmood*, Anthony T. Bollinger, Ivan Bozovic, and Nuh Gedik. “Fluctuating charge density waves in a cuprate superconductor”. In: *Nat Mater* 12.5 (2013), pp. 387–391. URL: http://dx.doi.org/10.1038/nmat3571.

[26] Zhanybek Alpichshev, Fahad Mahmood, Gang Cao, and Nuh Gedik. “Confinement-Deconfinement Transition as an Indication of Spin-Liquid-Type Behavior in $Na_2IrO_3$”. In: *Phys. Rev. Lett.* 114 (1 Jan. 2015), p. 017203. URL: http://link.aps.org/doi/10.1103/PhysRevLett.114.017203.

[27] Y. H. Wang, H. Steinberg, P. Jarillo-Herrero, and N. Gedik. “Observation of Floquet-Bloch States on the Surface of a Topological Insulator”. In: *Science* 342.6157 (2013), pp. 453–457. eprint: http://science.sciencemag.org/content/342/6157/453.full.pdf. URL: http://science.sciencemag.org/content/342/6157/453.

[28] Fahad Mahmood et al. “Selective scattering between Floquet-Bloch and Volkov states in a topological insulator”. In: *Nat Phys* 12.4 (2016), pp. 306–310. URL: http://dx.doi.org/10.1038/nphys3609.

[29] Philip B. Allen. “Theory of thermal relaxation of electrons in metals”. In: *Phys. Rev. Lett.* 59 (13 Sept. 1987), pp. 1460–1463. URL: http://link.aps.org/doi/10.1103/PhysRevLett.59.1460.

[30] Allen Rothwarf and B. N. Taylor. “Measurement of Recombination Lifetimes in Superconductors”. In: *Phys. Rev. Lett.* 19 (1 July 1967), pp. 27–30. URL: http://link.aps.org/doi/10.1103/PhysRevLett.19.27.

[31] H. Zeiger et al. “Theory for displacive excitation of coherent phonons”. In: *Phys. Rev. B* 45 (1992). 10.1103/PhysRevB.45.768, pp. 768–778. URL: http://dx.doi.org/10.1103/PhysRevB.45.768.

[32] W. Richter and C. R. Becker. “A Raman and far-infrared investigation of phonons in the rhombohedral V2–VI3 compounds Bi2Te3, Bi2Se3, Sb2Te3 and Bi2(Te1-xSex)3 ($0 < x < 1$), (Bi1-ySby)2Te3 ($0 < y < 1$)”. In: *physica status solidi (b)* 84.2 (1977), pp. 619–628. URL: http://dx.doi.org/10.1002/pssb.2220840226.

[33] J. Qi et al. “Ultrafast carrier and phonon dynamics in Bi2Se3 crystals”. In: *Applied Physics Letters* 97.18, 182102 (2010). URL: http://scitation.aip.org/content/aip/journal/apl/97/18/10.1063/1.3513826.

[34] Makoto Hashimoto, Inna M. Vishik, Rui-Hua He, Thomas P. Devereaux, and Zhi-Xun Shen. “Energy gaps in high-transition-temperature cuprate superconductors”. In: *Nat Phys* 10.7 (2014), pp. 483–495. URL: http://dx.doi.org/10.1038/nphys3009.

[35] Y. H. Liu et al. “Direct Observation of the Coexistence of the Pseudogap and Superconducting Quasiparticles in $Bi_2Sr_2CaCu_2O_{8+y}$ by Time-Resolved Optical Spectroscopy”. In: *Phys. Rev. Lett.* 101 (13 Sept. 2008), p. 137003. URL: http://link.aps.org/doi/10.1103/PhysRevLett.101.137003.

[36] S. Dal Conte et al. “Disentangling the Electronic and Phononic Glue in a High-Tc Superconductor”. In: *Science* 335.6076 (2012), pp. 1600–1603. eprint: http://science.sciencemag.org/content/335/6076/1600.full.pdf. URL: http://science.sciencemag.org/content/335/6076/1600.

[37] Hans Joachim Eichler, Peter Günter, and Dieter W. Pohl. *Laser-Induced Dynamic Gratings*. 1st ed. Vol. 50. Springer-Verlag Berlin Heidelberg, 1986.

[38] Alan Miller. “Chapter 5 - Transient Grating Studies of Carrier Diffusion and Mobility in Semiconductors”. In: *Nonlinear Optics in Semiconductors II*. Ed. by Elsa Garmire and Alan Kost. Vol. 59. Semiconductors and Semimetals. Elsevier, 1998, pp. 287–312. URL: http://www.sciencedirect.com/science/article/pii/S0080878408627349.

[39] JA Rogers, AA Maznev, MJ Banet, and KA Nelson. “Optical generation and characterization of acoustic waves in thin films: Fundamentals and applications”. In: *ANNUAL REVIEW OF MATERIALS SCIENCE* 30 (2000), 117–157.

[40] A. Honold, L. Schultheis, J. Kuhl, and C. W. Tu. “Reflected degenerate four-wave mixing on GaAs single quantum wells”. In: *Applied Physics Letters* 52.25 (1988), pp. 2105–2107. URL: http://scitation.aip.org/content/aip/journal/apl/52/25/10.1063/1.99549.

[41] N. Gedik and J. Orenstein. “Absolute phase measurement in heterodyne detection of transient gratings”. In: *Opt. Lett.* 29 (2004). 10.1364/OL.29.002109, pp. 2109–2111. URL: http://dx.doi.org/10.1364/OL.29.002109.

[42] Alexander Franzen. *ComponentLibrary*. Creative Commons Attribution-NonCommercial 3.0 Unported License. URL: http://www.gwoptics.org/ComponentLibrary/.

[43] Koichi Momma and Fujio Izumi. “*VESTA3* for three-dimensional visualization of crystal, volumetric and morphology data”. In: *Journal of Applied Crystallography* 44.6 (Dec. 2011), pp. 1272–1276. URL: http://dx.doi.org/10.1107/S0021889811038970.

[44] L. S. Bilbro et al. “Temporal correlations of superconductivity above the transition temperature in $La_{2-x}Sr_xCuO_4$ probed by terahertz spectroscopy”. In: *Nature Physics* 7 (2011), pp. 298–302. URL: http://dx.doi.org/10.1038/nphys1912.

[45] Inna Vishik. “Low energy excitations in cuprate high temperature superconductors angle-resolved photoemission spectroscopy studies”. PhD thesis. Stanford University, 2013.

[46] J.L. Tallon and J.W. Loram. “The doping dependence of T* – what is the real high-Tc phase diagram?” In: *Physica C: Superconductivity* 349.1–2 (2001), pp. 53–68. URL: http://www.sciencedirect.com/science/article/pii/S0921453400015240.

[47] J.W. Lorama, K.A. Mirza, J.R. Cooper, and J.L. Tallon. “{SPECIFIC} {HEAT} {EVIDENCE} {ON} {THE} {NORMAL} {STATE} {PSEUDOGAP}”. In: *Journal of Physics and Chemistry of Solids* 59.10–12 (1998), pp. 2091–2094. URL: http://www.sciencedirect.com/science/article/pii/S0022369798001802.

[48] C. V. Parker et al. “Fluctuating stripes at the onset of the pseudogap in the high-Tc superconductor Bi2Sr2CaCu2O8+x”. In: *Nature* 468 (2010). 10.1038/nature09597, pp. 677–680. URL: http://dx.doi.org/10.1038/nature09597.

[49] J. E. Hoffman et al. “A four unit cell periodic pattern of quasi-particle states surrounding vortex cores in Bi2Sr2CaCu2O8+y”. In: *Science* 295 (2002). 10.1126/science.1066974, pp. 466–469. URL: http://dx.doi.org/10.1126/science.1066974.

[50] W. D. Wise et al. “Charge-density-wave origin of cuprate checkerboard visualized by scanning tunnelling microscopy”. In: *Nature Phys.* 4 (2008). 10.1038/nphys1021, pp. 696–699. URL: http://dx.doi.org/10.1038/nphys1021.

[51] T. Wu et al. “Magnetic-field-induced charge-stripe order in the high-temperature superconductor YBa2Cu3Oy”. In: *Nature* 477 (2011). 10.1038/nature10345, pp. 191–194. URL: http://dx.doi.org/10.1038/nature10345.

[52] G. Ghiringhelli et al. “Long-range incommensurate charge fluctuations in (Y,Nd)Ba2Cu3O6+x”. In: *Science* 337 (2012). 10.1126/science.1223532, pp. 821–825. URL: http://dx.doi.org/10.1126/science.1223532.

[53] J. Chang et al. “Direct observation of competition between superconductivity and charge density wave order in YBa2Cu3Oy”. In: *Nature Phys.* 8 (2012). 10.1038/nphys2380, pp. 871–876. URL: http://dx.doi.org/10.1038/nphys2380.

[54] P Abbamonte et al. “Spatially modulated ‘Mottness’ in La2-xBaxCuO4”. In: *Nature Phys.* 1 (2005). 10.1038/nphys178, pp. 155–158. URL: http://dx.doi.org/10.1038/nphys178.

[55] J. Tranquada, B. Sternlieb, J. Axe, and Y. Nakamura. “Evidence for stripe correlations of spins and holes in copper oxide superconductors”. In: *Nature* 375 (1995). 10.1038/375561a0, pp. 561–563. URL: http://dx.doi.org/10.1038/375561a0.

[56] J. Zaanen and O. Gunnarsson. “Charged magnetic domain lines and the magnetism of high-Tc oxides”. In: *Phys. Rev. B* 40 (1989). 10.1103/PhysRevB.40.7391, pp. 7391–7394. URL: http://dx.doi.org/10.1103/PhysRevB.40.7391.

[57] J. D. Axe et al. “Structural phase transformations and superconductivity in La2-xBaxCuO4”. In: *Phys. Rev. Lett.* 62 (1989). 10.1103/PhysRevLett.62.2751, pp. 2751–2754. URL: http://dx.doi.org/10.1103/PhysRevLett.62.2751.

[58] S. Kivelson, I. Bindloss, and E. Fradkin. “How to detect fluctuating stripes in the high-temperature superconductors”. In: *Rev. Mod. Phys.* 75 (2003). 10.1103/RevModPhys.75.1201, pp. 1201–1241. URL: http://dx.doi.org/10.1103/RevModPhys.75.1201.

[59] B. Lake et al. “Antiferromagnetic order induced by an applied magnetic field in a high-temperature superconductor”. In: *Nature* 415 (2002). 10.1038/415299a, pp. 299–302. URL: http://dx.doi.org/10.1038/415299a.

[60] M. K. Crawford et al. “Lattice instabilities and the effect of copper-oxygen-sheet distortions on superconductivity in doped La2CuO4”. In: *Phys. Rev. B* 44 (1991). 10.1103/PhysRevB.44.7749, pp. 7749–7752. URL: http://dx.doi.org/10.1103/PhysRevB.44.7749.

[61] H. H. Klauss et al. “From antiferromagnetic order to static magnetic stripes: The phase diagram of (La,Eu)2-xSrxCuO4”. In: *Phys. Rev. Lett.* 85 (2000). 10.1103/PhysRevLett.85.4590, pp. 4590–4593. URL: http://dx.doi.org/10.1103/PhysRevLett.85.4590.

[62] R. Comin et al. “Charge Order Driven by Fermi-Arc Instability in Bi2Sr2-xLaxCuO6+y”. In: *Science* 343.6169 (2014), pp. 390–392. eprint: http://science.sciencemag.org/content/343/6169/390.full.pdf. URL: http://science.sciencemag.org/content/343/6169/390.

[63] Eduardo H. da Silva Neto et al. “Ubiquitous Interplay Between Charge Ordering and High-Temperature Superconductivity in Cuprates”. In: *Science* 343.6169 (2014), pp. 393–396. eprint: http://science.sciencemag.org/content/343/6169/393.full.pdf. URL: http://science.sciencemag.org/content/343/6169/393.

[64] R. D. Averitt and A. J. Taylor. “Ultrafast optical and far-infrared quasiparticle dynamics in correlated electron materials”. In: *J. Phys. Condens. Matter* 14 (2002). 10.1088/0953-8984/14/50/203, R1357. URL: http://dx.doi.org/10.1088/0953-8984/14/50/203.

[65] J. Demsar, K. Biljakovic, and D. Mihailovic. “Single particle and collective excitations in the one-dimensional charge density wave solid K0.3MoO3 probed in real time by femtosecond spectroscopy”. In: *Phys. Rev. Lett.* 83 (1999). 10.1103/PhysRevLett.83.800, pp. 800–803. URL: http://dx.doi.org/10.1103/PhysRevLett.83.800.

[66] G. Grüner. “The dynamics of charge-density waves”. In: *Rev. Mod. Phys.* 60 (4 Oct. 1988), pp. 1129–1181. URL: http://link.aps.org/doi/10.1103/RevModPhys.60.1129.

[67] L. Tassini et al. “Dynamical properties of charged stripes in La2-xSrxCuO4”. In: *Phys. Rev. Lett.* 95 (2005). 10.1103/PhysRevLett.95.117002, p. 117002. URL: http://dx.doi.org/10.1103/PhysRevLett.95.117002.

[68] S. Sugai, Y. Takayanagi, and N. Hayamizu. “Phason and amplitudon in the charge-density-wave phase of one-dimensional charge stripes in La2-xSrxCuO4”. In: *Phys. Rev. Lett.* 96 (2006). 10.1103/PhysRevLett.96.137003, p. 137003. URL: http://dx.doi.org/10.1103/PhysRevLett.96.137003.

[69] Y. Ren, Z. Xu, and G. Lüpke. “Ultrafast collective dynamics in the charge-density-wave conductor K0.3MoO3”. In: *J. Chem. Phys.* 120 (2004). 10.1063/1.1645785, pp. 4755–4758. URL: http://dx.doi.org/10.1063/1.1645785.

[70] D. M. Sagar, A. A. Tsvetkov, D. Fausti, S. V. Smaalen, and P. H. M. V. Loosdrecht. “Coherent amplitudon generation in blue bronze through ultrafast interband quasi-particle decay”. In: *J. Phys. Condens. Matter* 19 (2007). 10.1088/0953-8984/19/34/346208, p. 346208. URL: http://dx.doi.org/10.1088/0953-8984/19/34/346208.

[71] F. Schmitt et al. “Transient electronic structure and melting of a charge density wave in TbTe3”. In: *Science* 321 (2008). 10.1126/science.1160778, pp. 1649–1652. URL: http://dx.doi.org/10.1126/science.1160778.

[72] H. Y. Liu et al. "Possible observation of parametrically amplified coherent phasons in $K_{0.3}MoO_3$ using time-resolved extreme-ultraviolet angle-resolved photoemission spectroscopy". In: *Phys. Rev. B* 88 (4 July 2013), p. 045104. URL: http://link.aps.org/doi/10.1103/PhysRevB.88.045104.

[73] Ivan Bozovic, J.N. Eckstein, and G.F. Virshup. "Superconducting oxide multilayers and superlattices: Physics, chemistry, and nanoengineering". In: *Physica C: Superconductivity* 235 (1994), pp. 178–181. URL: http://www.sciencedirect.com/science/article/pii/0921453494913420.

[74] I. Bozovic, G. Logvenov, I. Belca, B. Narimbetov, and I. Sveklo. "Epitaxial Strain and Superconductivity in $La_{2-x}Sr_xCuO_4$ Thin Films". In: *Phys. Rev. Lett.* 89 (10 Aug. 2002), p. 107001. URL: http://link.aps.org/doi/10.1103/PhysRevLett.89.107001.

[75] G. Logvenov, A. Gozar, and I. Bozovic. "High-Temperature Superconductivity in a Single Copper-Oxygen Plane". In: *Science* 326.5953 (2009), pp. 699–702. eprint: http://science.sciencemag.org/content/326/5953/699.full.pdf. URL: http://science.sciencemag.org/content/326/5953/699.

[76] S. Smadici et al. "Superconducting Transition at 38 K in Insulating-Overdoped $La_2Cu\mathbf{O}_4$-$La_{1.64}Sr_{0.36}Cu\mathbf{O}_4$ Superlattices: Evidence for Interface Electronic Redistribution from Resonant Soft X-Ray Scattering". In: *Phys. Rev. Lett.* 102 (10 Mar. 2009), p. 107004. URL: http://link.aps.org/doi/10.1103/PhysRevLett.102.107004.

[77] A. T. Fiory, A. F. Hebard, P. M. Mankiewich, and R. E. Howard. "Penetration depths of high Tc films measured by two coil mutual inductances". In: *Applied Physics Letters* 52.25 (1988), pp. 2165–2167. URL: http://scitation.aip.org/content/aip/journal/apl/52/25/10.1063/1.99757.

[78] G. Bianchi, C. Chen, M. Nohara, H. Takagi, and J. F. Ryan. "Competing phases in the superconducting state of La2-xSrxCuO4: Temperature and magnetic field dependent quasiparticle relaxation measurements". In: *Phys. Rev. B* 72 (2005). 10.1103/PhysRevB.72.094516, p. 094516. URL: http://dx.doi.org/10.1103/PhysRevB.72.094516.

[79] M. Beyer et al. "Photoinduced melting of superconductivity in the high-Tc superconductor La2-xSrxCuO4 probed by time-resolved optical and terahertz techniques". In: *Phys. Rev. B* 83 (2011). 10.1103/PhysRevB.83.214515, p. 214515. URL: http://dx.doi.org/10.1103/PhysRevB.83.214515.

[80] S. Sugai et al. "Symmetry breaking on the phonon Raman spectra only at the superconductor compositions in La2-xSrxCuO4". In: *Solid State Commun.* 76 (1990). 10.1016/0038-1098(90)90857-8, pp. 371–376. URL: http://dx.doi.org/10.1016/0038-1098(90)90857-8.

[81] C. Z. Wang, R. Yu, and H. Krakauer. "First-principles calculations of phonon dispersion and lattice dynamics in La2CuO4". In: *Phys. Rev. B* 59 (1999). 10.1103/PhysRevB.59.9278, pp. 9278–9284. URL: http://dx.doi.org/10.1103/PhysRevB.59.9278.

[82] L. Dhar, J. A. Rogers, and K. A. Nelson. "Time-resolved vibrational spectroscopy in the impulsive limit". In: *Chem. Rev.* 94 (1994). 10.1021/cr00025a006, pp. 157–193. URL: http://dx.doi.org/10.1021/cr00025a006.

[83] Y. X. Yan and K. A. Nelson. "Impulsive stimulated light scattering. I. general theory". In: *J. Chem. Phys.* 87 (1987). 10.1063/1.453733, pp. 6240–6256. URL: http://dx.doi.org/10.1063/1.453733.

[84] I. Bozovic et al. "Long-lived coherent acoustic waves generated by femtosecond light pulses". In: *Phys. Rev. B* 69 (2004). 10.1103/PhysRevB.69.132503, p. 132503. URL: http://dx.doi.org/10.1103/PhysRevB.69.132503.

[85] Y. J. Kim, G. Gu, T. Gog, and D. Casa. "X-ray scattering study of charge density waves in La2-xBaxCuO4". In: *Phys. Rev. B* 77 (2008). 10.1103/PhysRevB.77.064520, p. 064520. URL: http://dx.doi.org/10.1103/PhysRevB.77.064520.

[86] S. Wilkins et al. "Comparison of stripe modulations in La1.875Ba0.125CuO4 and La1.48Nd0.4Sr0.12CuO4". In: *Phys. Rev. B* 84 (2011). 10.1103/PhysRevB.84.195101, p. 195101. URL: http://dx.doi.org/10.1103/PhysRevB.84.195101.

[87] P. A. Lee and T. M. Rice. "Electric field depinning of charge density waves". In: *Phys. Rev. B* 19 (1979). 10.1103/PhysRevB.19.3970, pp. 3970–3980. URL: http://dx.doi.org/10.1103/PhysRevB.19.3970.

[88] S. Takada, K. Wong, and T. Holstein. "Damping of charge-density-wave motion". In: *Phys. Rev. B* 32 (1985). 10.1103/PhysRevB.32.4639, pp. 4639–4652. URL: http://dx.doi.org/10.1103/PhysRevB.32.4639.

[89] A. P. Levanyuk, S. A. Minyukov, J. Etrillard, and B. Toudic. "Low-frequency phonon dynamics and spin-lattice relaxation time in the incommensurate phase at low temperatures". In: *Phys. Rev. B* 56 (1997). 10.1103/PhysRevB.56.8734, pp. 8734–8742. URL: http://dx.doi.org/10.1103/PhysRevB.56.8734.

[90] J. Richard and J. Chen. "Damping of charge density waves in NbSe3". In: *Solid State Commun.* 86 (1993). 10.1016/0038-1098(93)90093-3, pp. 485–488. URL: http://dx.doi.org/10.1016/0038-1098(93)90093-3.

[91] J. P. Hinton et al. "New collective mode in $YBa_2Cu_3O_{6+x}$ observed by time-domain reflectometry". In: *Phys. Rev. B* 88 (6 Aug. 2013), p. 060508. URL: http://link.aps.org/doi/10.1103/PhysRevB.88.060508.

[92] R. A. Kaindl et al. "Ultrafast Mid-Infrared Response of YBa2Cu3O7". In: *Science* 287.5452 (2000), pp. 470–473. eprint: http://science.sciencemag.org/content/287/5452/470.full.pdf. URL: http://science.sciencemag.org/content/287/5452/470.

[93] Di Xiao, Gui-Bin Liu, Wanxiang Feng, Xiaodong Xu, and Wang Yao. "Coupled Spin and Valley Physics in Monolayers of $MoS_2$ and Other Group-VI Dichalcogenides". In: *Physical Review Letters* 108.19 (2012). PRL, p. 196802. URL: http://link.aps.org/doi/10.1103/PhysRevLett.108.196802.

[94] Kin Fai Mak, Changgu Lee, James Hone, Jie Shan, and Tony F. Heinz. "Atomically Thin $MoS_2$: A New Direct-Gap Semiconductor". In: *Phys. Rev. Lett.* 105 (13 Sept. 2010), p. 136805. URL: http://link.aps.org/doi/10.1103/PhysRevLett.105.136805.

[95] Ting Cao et al. "Valley-selective circular dichroism of monolayer molybdenum disulphide". In: *Nat Commun* 3 (2012). 10.1038/ncomms1882, p. 887. URL: http://dx.doi.org/10.1038/ncomms1882.

[96] Kin Fai Mak, Keliang He, Jie Shan, and Tony F. Heinz. "Control of valley polarization in monolayer MoS2 by optical helicity". In: *Nat Nano* 7.8 (2012). 10.1038/nnano.2012.96, pp. 494–498. URL: http://dx.doi.org/10.1038/nnano.2012.96.

[97] Hualing Zeng, Junfeng Dai, Wang Yao, Di Xiao, and Xiaodong Cui. "Valley polarization in MoS2 monolayers by optical pumping". In: *Nat Nano* 7.8 (2012). 10.1038/nnano.2012.95, pp. 490–493. URL: http://dx.doi.org/10.1038/nnano.2012.95.

[98] G. Kioseoglou et al. "Valley polarization and intervalley scattering in monolayer MoS2". In: *Applied Physics Letters* 101.22 (2012), p. 221907. URL: http://scitation.aip.org/content/aip/journal/apl/101/22/10.1063/1.4768299.

[99] S. Dal Conte et al. "Ultrafast valley relaxation dynamics in monolayer $MoS_2$ probed by nonequilibrium optical techniques". In: *Physical Review B* 92.23 (2015). PRB, p. 235425. URL: http://link.aps.org/doi/10.1103/PhysRevB.92.235425.

[100] C. R. Zhu et al. "Exciton valley dynamics probed by Kerr rotation in $WSe_2$ monolayers". In: *Physical Review B* 90.16 (2014). PRB, p. 161302. URL: http://link.aps.org/doi/10.1103/PhysRevB.90.161302.

[101] D. Lagarde et al. "Carrier and Polarization Dynamics in Monolayer $MoS_2$". In: *Physical Review Letters* 112.4 (2014). PRL, p. 047401. URL: http://link.aps.org/doi/10.1103/PhysRevLett.112.047401.

[102] G. Wang et al. "Valley dynamics probed through charged and neutral exciton emission in monolayer $WSe_2$". In: *Physical Review B* 90.7 (2014). PRB, p. 075413. URL: http://link.aps.org/doi/10.1103/PhysRevB.90.075413.

[103] Tengfei Yan, Xiaofen Qiao, Pingheng Tan, and Xinhui Zhang. "Valley depolarization in monolayer WSe2". In: *Scientific Reports* 5 (2015), p. 15625. URL: http://dx.doi.org/10.1038/srep15625.

[104] Qinsheng Wang et al. "Valley Carrier Dynamics in Monolayer Molybdenum Disulfide from Helicity-Resolved Ultrafast Pump–Probe Spectroscopy". In: *ACS Nano* 7.12 (2013), pp. 11087–11093. URL: http://pubs.acs.org/doi/abs/10.1021/nn405419h.

[105] Cong Mai et al. "Many-Body Effects in Valleytronics: Direct Measurement of Valley Lifetimes in Single-Layer MoS2". In: *Nano Letters* 14.1 (2014), pp. 202–206. URL: http://dx.doi.org/10.1021/nl403742j.

[106] Nardeep Kumar, Jiaqi He, Dawei He, Yongsheng Wang, and Hui Zhao. "Valley and spin dynamics in MoSe2 two-dimensional crystals". In: *Nanoscale* 6.21 (2014), pp. 12690–12695. URL: http://dx.doi.org/10.1039/C4NR03607G.

[107] L. Wang and M. W. Wu. "Electron spin relaxation due to D'yakonov-Perel' and Elliot-Yafet mechanisms in monolayer $MoS_2$: Role of intravalley and intervalley processes". In: *Physical Review B* 89.11 (2014). PRB, p. 115302. URL: http://link.aps.org/doi/10.1103/PhysRevB.89.115302.

[108] M. M. Glazov et al. “Exciton fine structure and spin decoherence in monolayers of transition metal dichalcogenides”. In: *Physical Review B* 89.20 (2014). PRB, p. 201302. URL: http://link.aps.org/doi/10.1103/PhysRevB.89.201302.

[109] T. Yu and M. W. Wu. “Valley depolarization due to intervalley and intravalley electron-hole exchange interactions in monolayerMoS2”. In: *Physical Review B* 89.20 (2014).

[110] Igor Žuti ć, Jaroslav Fabian, and S. Das Sarma. “Spintronics: Fundamentals and applications”. In: *Rev. Mod. Phys.* 76 (2 Apr. 2004), pp. 323–410. URL: http://link.aps.org/doi/10.1103/RevModPhys.76.323.

[111] R. J. Elliott. “Theory of the Effect of Spin-Orbit Coupling on Magnetic Resonance in Some Semiconductors”. In: *Phys. Rev.* 96 (2 Oct. 1954), pp. 266–279. URL: http://link.aps.org/doi/10.1103/PhysRev.96.266.

[112] Y. Yafet. “Conduction electron spin relaxation in the superconducting state”. In: *Physics Letters A* 98.5–6 (1983), pp. 287–290. URL: http://www.sciencedirect.com/science/article/pii/0375960183908745.

[113] H. Ochoa and R. Roldán. “Spin-orbit-mediated spin relaxation in monolayer $MoS_2$”. In: *Phys. Rev. B* 87 (24 June 2013), p. 245421. URL: http://link.aps.org/doi/10.1103/PhysRevB.87.245421.

[114] M. I. Dyakonov and V. I. Perel. “Spin Relaxation of Conduction Electrons in Noncentrosymmetric Semiconductors”. In: *Sov. Phys. Solid State* 13 (1972), pp. 3023–3026.

[115] M. I. D’yakonov and V. I. Perel’. “Spin orientation of electrons associated with the interband absorption of light in semiconductors”. In: *Sov. Phys. JETP* 33 (1971), p. 1053.

[116] M. Z. Maialle, E. A. de Andrada e Silva, and L. J. Sham. “Exciton spin dynamics in quantum wells”. In: *Phys. Rev. B* 47 (23 June 1993), pp. 15776–15788. URL: http://link.aps.org/doi/10.1103/PhysRevB.47.15776.

[117] Gregory D. Scholes, Jeongho Kim, and Cathy Y. Wong. “Exciton spin relaxation in quantum dots measured using ultrafast transient polarization grating spectroscopy”. In: *Physical Review B* 73.19 (2006). PRB, p. 195325. URL: http://link.aps.org/doi/10.1103/PhysRevB.73.195325.

[118] Gregory D. Scholes et al. “Nanocrystal Shape and the Mechanism of Exciton Spin Relaxation”. In: *Nano Letters* 6.8 (2006), pp. 1765–1771. URL: http://dx.doi.org/10.1021/nl061414e.

[119] M. Q. Weng, M. W. Wu, and H. L. Cui. “Spin relaxation in n-type GaAs quantum wells with transient spin grating”. In: *Journal of Applied Physics* 103.6 (2008), p. 063714. URL: http://scitation.aip.org/content/aip/journal/jap/103/6/10.1063/1.2899962.

[120] J. D. Koralek et al. “Emergence of the persistent spin helix in semiconductor quantum wells”. In: *Nature* 458.7238 (2009). 10.1038/nature07871, pp. 610–613. URL: http://dx.doi.org/10.1038/nature07871.

[121] G. Wang et al. “Gate control of the electron spin-diffusion length in semiconductor quantum wells”. In: *Nat Commun* 4 (2013). URL: http://dx.doi.org/10.1038/ncomms3372.

[122] Jeongho Kim, Cathy Y. Wong, and Gregory D. Scholes. "Exciton Fine Structure and Spin Relaxation in Semiconductor Colloidal Quantum Dots". In: *Accounts of Chemical Research* 42.8 (2009), pp. 1037–1046. URL: http://dx.doi.org/10.1021/ar8002046.

[123] Yi-Hsien Lee et al. "Synthesis and Transfer of Single-Layer Transition Metal Disulfides on Diverse Surfaces". In: *Nano Letters* 13.4 (2013), pp. 1852–1857. URL: http://dx.doi.org/10.1021/nl400687n.

[124] Jason S. Ross et al. "Electrical control of neutral and charged excitons in a monolayer semiconductor". In: *Nat Commun* 4 (2013). 10.1038/ncomms2498, p. 1474. URL: http://dx.doi.org/10.1038/ncomms2498.

[125] Wenjuan Zhu et al. "Electronic transport and device prospects of monolayer molybdenum disulphide grown by chemical vapour deposition". In: *Nat Commun* 5 (2014). URL: http://dx.doi.org/10.1038/ncomms4087.

[126] Xingli
In: *ACS Nano* 8.5 (2014), pp. 5125–5131. URL: http://dx.doi.org/10.1021/nn501175k.

[127] Qiannan Cui, Frank Ceballos, Nardeep Kumar, and Hui Zhao. "Transient Absorption Microscopy of Monolayer and Bulk WSe2". In: *ACS Nano* 8.3 (2014), pp. 2970–2976. URL: http://dx.doi.org/10.1021/nn500277y.

[128] Dezheng Sun et al. "Observation of Rapid Exciton–Exciton Annihilation in Monolayer Molybdenum Disulfide". In: *Nano Letters* 14.10 (2014), pp. 5625–5629. URL: http://dx.doi.org/10.1021/nl5021975.

[129] Haining Wang, Changjian Zhang, and Farhan Rana. "Ultrafast Dynamics of Defect-Assisted Electron–Hole Recombination in Monolayer MoS2". In: *Nano Letters* 15.1 (2015), pp. 339–345. URL: http://dx.doi.org/10.1021/nl503636c.

[130] Philipp Tonndorf et al. "Photoluminescence emission and Raman response of monolayer MoS2, MoSe2, and WSe2". In: *Optics Express* 21.4 (2013), pp. 4908–4916. URL: http://www.opticsexpress.org/abstract.cfm?URI=oe-21-4-4908.

[131] Wei-Ting Hsu et al. "Optically initialized robust valley-polarized holes in monolayer WSe2". In: *Nat Commun* 6 (2015). URL: http://dx.doi.org/10.1038/ncomms9963.

[132] Yilei Li et al. "Measurement of the optical dielectric function of monolayer transition-metal dichalcogenides: $MoS_2$, $MoSe_2$, $WS_2$, and $WSe_2$". In: *Physical Review B* 90.20 (2014). PRB, p. 205422. URL: http://link.aps.org/doi/10.1103/PhysRevB.90.205422.

[133] Chulseung Jung et al. "Highly Crystalline CVD-grown Multilayer MoSe2 Thin Film Transistor for Fast Photodetector". In: *Scientific Reports* 5 (2015), p. 15313. URL: http://dx.doi.org/10.1038/srep15313.

[134] Hongliang Shi, Hui Pan, Yong-Wei Zhang, and Boris I. Yakobson. "Quasiparticle band structures and optical properties of strained monolayer $MoS_2$ and $WS_2$". In: *Phys. Rev. B* 87 (15 Apr. 2013), p. 155304. URL: http://link.aps.org/doi/10.1103/PhysRevB.87.155304.

[135] M. Z. Hasan and C. L. Kane. "*Colloquium* : Topological insulators". In: *Rev. Mod. Phys.* 82 (4 Nov. 2010), pp. 3045–3067. URL: http://link.aps.org/doi/10.1103/RevModPhys.82.3045.

[136] Xiao-Liang Qi and Shou-Cheng Zhang. "Topological insulators and superconductors". In: *Rev. Mod. Phys.* 83 (4 Oct. 2011), pp. 1057–1110. URL: http://link.aps.org/doi/10.1103/RevModPhys.83.1057.

[137] G. Cao, J. Bolivar, S. McCall, J. E. Crow, and R. P. Guertin. "Weak ferromagnetism, metal-to-nonmetal transition, and negative differential resistivity in single-crystal $Sr_2IrO_4$". In: *Phys. Rev. B* 57 (18 May 1998), R11039–R11042. URL: http://link.aps.org/doi/10.1103/PhysRevB.57.R11039.

[138] Yogesh Singh and P. Gegenwart. "Antiferromagnetic Mott insulating state in single crystals of the honeycomb lattice material $Na_2IrO_3$". In: *Phys. Rev. B* 82 (6 Aug. 2010), p. 064412. URL: http://link.aps.org/doi/10.1103/PhysRevB.82.064412.

[139] B. J. Kim et al. "Novel $J_{\text{eff}} = 1/2$ Mott State Induced by Relativistic Spin-Orbit Coupling in $Sr_2IrO_4$". In: *Phys. Rev. Lett.* 101 (7 Aug. 2008), p. 076402. URL: http://link.aps.org/doi/10.1103/PhysRevLett.101.076402.

[140] S. K. Choi et al. "Spin Waves and Revised Crystal Structure of Honeycomb Iridate $Na_2IrO_3$". In: *Phys. Rev. Lett.* 108 (12 Mar. 2012), p. 127204. URL: http://link.aps.org/doi/10.1103/PhysRevLett.108.127204.

[141] R. Comin et al. "$Na_2IrO_3$ as a Novel Relativistic Mott Insulator with a 340-meV Gap". In: *Phys. Rev. Lett.* 109 (26 Dec. 2012), p. 266406. URL: http://link.aps.org/doi/10.1103/PhysRevLett.109.266406.

[142] G. Jackeli and G. Khaliullin. "Mott Insulators in the Strong Spin-Orbit Coupling Limit: From Heisenberg to a Quantum Compass and Kitaev Models". In: *Phys. Rev. Lett.* 102 (1 Jan. 2009), p. 017205. URL: http://link.aps.org/doi/10.1103/PhysRevLett.102.017205.

[143] Jiri Chaloupka, George Jackeli, and Giniyat Khaliullin. "Kitaev-Heisenberg Model on a Honeycomb Lattice: Possible Exotic Phases in Iridium Oxides $A_2IrO_3$". In: *Phys. Rev. Lett.* 105 (2 July 2010), p. 027204. URL: http://link.aps.org/doi/10.1103/PhysRevLett.105.027204.

[144] Yogesh Singh et al. "Relevance of the Heisenberg-Kitaev Model for the Honeycomb Lattice Iridates $A_2IrO_3$". In: *Phys. Rev. Lett.* 108 (12 Mar. 2012), p. 127203. URL: http://link.aps.org/doi/10.1103/PhysRevLett.108.127203.

[145] Alexei Kitaev. "Anyons in an exactly solved model and beyond". In: *Annals of Physics* 321.1 (2006). January Special Issue, pp. 2–111. URL: http://www.sciencedirect.com/science/article/pii/S0003491605002381.

[146] X. Liu et al. "Long-range magnetic ordering in $Na_2IrO_3$". In: *Phys. Rev. B* 83 (22 June 2011), p. 220403. URL: http://link.aps.org/doi/10.1103/PhysRevB.83.220403.

[147] Feng Ye et al. "Direct evidence of a zigzag spin-chain structure in the honeycomb lattice: A neutron and x-ray diffraction investigation of single-crystal $Na_2IrO_3$". In: *Phys. Rev. B* 85 (18 May 2012), p. 180403. URL: http://link.aps.org/doi/10.1103/PhysRevB.85.180403.

[148] Jiri Chaloupka, George Jackeli, and Giniyat Khaliullin. "Zigzag Magnetic Order in the Iridium Oxide $Na_2IrO_3$". In: *Phys. Rev. Lett.* 110 (9 Feb. 2013), p. 097204. URL: http://link.aps.org/doi/10.1103/PhysRevLett.110.097204.

[149] Jeffrey G. Rau, Eric Kin-Ho Lee, and Hae-Young Kee. "Generic Spin Model for the Honeycomb Iridates beyond the Kitaev Limit". In: *Phys. Rev. Lett.* 112 (7 Feb. 2014), p. 077204. URL: http://link.aps.org/doi/10.1103/PhysRevLett.112.077204.

[150] H. Gretarsson et al. "Crystal-Field Splitting and Correlation Effect on the Electronic Structure of $A_2IrO_3$". In: *Phys. Rev. Lett.* 110 (7 Feb. 2013), p. 076402. URL: http://link.aps.org/doi/10.1103/PhysRevLett.110.076402.

[151] C. H. Sohn et al. "Mixing between $J_{\text{eff}} = \frac{1}{2}$ and $\frac{3}{2}$ orbitals in $Na_2IrO_3$: A spectroscopic and density functional calculation study". In: *Phys. Rev. B* 88 (8 Aug. 2013), p. 085125. URL: http://link.aps.org/doi/10.1103/PhysRevB.88.085125.

[152] Rajdeep Sensarma et al. "Lifetime of double occupancies in the Fermi-Hubbard model". In: *Phys. Rev. B* 82 (22 Dec. 2010), p. 224302. URL: http://link.aps.org/doi/10.1103/PhysRevB.82.224302.

[153] H. Gretarsson et al. "Magnetic excitation spectrum of $Na_2IrO_3$ probed with resonant inelastic x-ray scattering". In: *Phys. Rev. B* 87 (22 June 2013), p. 220407. URL: http://link.aps.org/doi/10.1103/PhysRevB.87.220407.

[154] Fabio Novelli et al. "Ultrafast optical spectroscopy of the lowest energy excitations in the Mott insulator compound $YVO_3$: Evidence for Hubbard-type excitons". In: *Phys. Rev. B* 86 (16 Oct. 2012), p. 165135. URL: http://link.aps.org/doi/10.1103/PhysRevB.86.165135.

[155] C. L. Kane, P. A. Lee, and N. Read. "Motion of a single hole in a quantum antiferromagnet". In: *Phys. Rev. B* 39 (10 Apr. 1989), pp. 6880–6897. URL: http://link.aps.org/doi/10.1103/PhysRevB.39.6880.

[156] A. M. Polyakov. *Gauge fields and strings.* Contemporary concepts in physics: v. 3. Chur, Switzerland ; New York : Harwood Academic Publishers, c1987., 1987. URL: http://libproxy.mit.edu/login?url=https://search.ebscohost.com/login.aspx?direct=true&AuthType=cookie,sso,ip,uid&db=cat00916a&AN=mit.000878781&site=eds-live.

[157] Robert Schaffer, Subhro Bhattacharjee, and Yong Baek Kim. "Quantum phase transition in Heisenberg-Kitaev model". In: *Phys. Rev. B* 86 (22 Dec. 2012), p. 224417. URL: http://link.aps.org/doi/10.1103/PhysRevB.86.224417.

[158] S. Mandal, Subhro Bhattacharjee, K. Sengupta, R. Shankar, and G. Baskaran. "Confinement-deconfinement transition and spin correlations in a generalized Kitaev model". In: *Phys. Rev. B* 84 (15 Oct. 2011), p. 155121. URL: http://link.aps.org/doi/10.1103/PhysRevB.84.155121.

[159] Subir Sachdev. "Quantum magnetism and criticality". In: *Nat Phys* 4.3 (2008). 10.1038/nphys894, pp. 173–185. URL: http://dx.doi.org/10.1038/nphys894.

[160] T Senthil and Matthew P A Fisher. "Fractionalization and confinement in the U(1) and Z2 gauge theories of strongly correlated systems". In: *Journal of Physics A: Mathematical and General* 34.10 (2001), p. L119. URL: http://stacks.iop.org/0305-4470/34/i=10/a=106.

[161] Andrea Damascelli, Zahid Hussain, and Zhi-Xun Shen. "Angle-resolved photoemission studies of the cuprate superconductors". In: *Rev. Mod. Phys.* 75 (2 Apr. 2003), pp. 473–541. URL: http://link.aps.org/doi/10.1103/RevModPhys.75.473.

[162] G. D. Mahan. "Theory of Photoemission in Simple Metals". In: *Phys. Rev. B* 2 (11 Dec. 1970), pp. 4334–4350. URL: http://link.aps.org/doi/10.1103/PhysRevB.2.4334.

[163] Wei Zhang, Rui Yu, Hai-Jun Zhang, Xi Dai, and Zhong Fang. "First-principles studies of the three-dimensional strong topological insulators Bi 2 Te 3 , Bi 2 Se 3 and Sb 2 Te 3". In: *New Journal of Physics* 12.6 (2010), p. 065013. URL: http://stacks.iop.org/1367-2630/12/i=6/a=065013.

[164] Y. Xia et al. "Observation of a large-gap topological-insulator class with a single Dirac cone on the surface". In: *Nat Phys* 5.6 (2009). 10.1038/nphys1274, pp. 398–402. URL: http://dx.doi.org/10.1038/nphys1274.

[165] M. P. Seah and W. A. Dench. "Quantitative electron spectroscopy of surfaces: A standard data base for electron inelastic mean free paths in solids". In: *Surface and Interface Analysis* 1.1 (1979), pp. 2–11. URL: http://dx.doi.org/10.1002/sia.740010103.

[166] Yihua Wang. "Laser-Based Angle-Resolved Photoemission Spectroscopy of Topological Insulators". PhD thesis. Harvard university, 2012.

[167] J. G. Fujimoto, J. M. Liu, E. P. Ippen, and N. Bloembergen. "Femtosecond Laser Interaction with Metallic Tungsten and Nonequilibrium Electron and Lattice Temperatures". In: *Phys. Rev. Lett.* 53 (19 Nov. 1984), pp. 1837–1840. URL: http://link.aps.org/doi/10.1103/PhysRevLett.53.1837.

[168] W. S. Fann, R. Storz, H. W. K. Tom, and J. Bokor. "Direct measurement of nonequilibrium electron-energy distributions in subpicosecond laser-heated gold films". In: *Phys. Rev. Lett.* 68 (18 May 1992), pp. 2834–2837. URL: http://link.aps.org/doi/10.1103/PhysRevLett.68.2834.

[169] S. Xu et al. "Energy Dependence of Electron Lifetime in Graphite Observed with Femtosecond Photoemission Spectroscopy". In: *Phys. Rev. Lett.* 76 (3 Jan. 1996), pp. 483–486. URL: http://link.aps.org/doi/10.1103/PhysRevLett.76.483.

[170] Gunnar Moos, Cornelius Gahl, Roman Fasel, Martin Wolf, and Tobias Hertel. "Anisotropy of Quasiparticle Lifetimes and the Role of Disorder in Graphite from Ultrafast Time-Resolved Photoemission Spectroscopy". In: *Phys. Rev. Lett.* 87 (26 Dec. 2001), p. 267402. URL: http://link.aps.org/doi/10.1103/PhysRevLett.87.267402.

[171] Y. Ishida et al. "Non-thermal hot electrons ultrafastly generating hot optical phonons in graphite". In: *Scientific Reports* 1 (2011), p. 64. URL: http://dx.doi.org/10.1038/srep00064.

[172] Y. H. Wang et al. "Measurement of Intrinsic Dirac Fermion Cooling on the Surface of the Topological Insulator $Bi_2Se_3$ Using Time-Resolved and Angle-Resolved Photoemission Spectroscopy". In: *Physical Review Letters* 109.12 (2012). PRL, p. 127401. URL: http://link.aps.org/doi/10.1103/PhysRevLett.109.127401.

[173] J. A. Sobota et al. "Ultrafast Optical Excitation of a Persistent Surface-State Population in the Topological Insulator $Bi_2Se_3$". In: *Physical Review Letters* 108.11 (2012). PRL, p. 117403. URL: http://link.aps.org/doi/10.1103/PhysRevLett.108.117403.

[174] M. Hajlaoui et al. "Ultrafast Surface Carrier Dynamics in the Topological Insulator Bi2Te3". In: *Nano Letters* 12.7 (2012), pp. 3532–3536. URL: http://dx.doi.org/10.1021/nl301035x.

[175] Isabella Gierz et al. "Snapshots of non-equilibrium Dirac carrier distributions in graphene". In: *Nat Mater* 12.12 (2013), pp. 1119–1124. URL: http://dx.doi.org/10.1038/nmat3757.

[176] R. Cortés et al. "Momentum-Resolved Ultrafast Electron Dynamics in Superconducting $Bi_2Sr_2CaCu_2\mathbf{O}_{8+\delta}$". In: *Phys. Rev. Lett.* 107 (9 Aug. 2011), p. 097002. URL: http://link.aps.org/doi/10.1103/PhysRevLett.107.097002.

[177] L. Rettig et al. "Ultrafast Momentum-Dependent Response of Electrons in Antiferromagnetic $EuFe_2As_2$ Driven by Optical Excitation". In: *Phys. Rev. Lett.* 108 (9 Feb. 2012), p. 097002. URL: http://link.aps.org/doi/10.1103/PhysRevLett.108.097002.

[178] Timm Rohwer et al. "Collapse of long-range charge order tracked by time-resolved photoemission at high momenta". In: *Nature* 471.7339 (2011). 10.1038/nature09829, pp. 490–493. URL: http://dx.doi.org/10.1038/nature09829.

[179] S. Hellmann et al. "Time-domain classification of charge-density-wave insulators". In: *Nat Commun* 3 (2012). 10.1038/ncomms2078, p. 1069. URL: http://dx.doi.org/10.1038/ncomms2078.

[180] J. A. Sobota et al. "Direct Optical Coupling to an Unoccupied Dirac Surface State in the Topological Insulator $Bi_2Se_3$". In: *Phys. Rev. Lett.* 111 (13 Sept. 2013), p. 136802. URL: http://link.aps.org/doi/10.1103/PhysRevLett.111.136802.

[181] Valla Fatemi et al. "Electrostatic Coupling between Two Surfaces of a Topological Insulator Nanodevice". In: *Phys. Rev. Lett.* 113 (20 Nov. 2014), p. 206801. URL: http://link.aps.org/doi/10.1103/PhysRevLett.113.206801.

[182] M. Mitrano et al. "Possible light-induced superconductivity in K3C60 at high temperature". In: *Nature* 530.7591 (2016), pp. 461–464. URL: http://dx.doi.org/10.1038/nature16522.

[183] M. Hajlaoui et al. "Tuning a Schottky barrier in a photoexcited topological insulator with transient Dirac cone electron-hole asymmetry". In: *Nat Commun* 5 (2014). URL: http://dx.doi.org/10.1038/ncomms4003.

[184] Peter Hommelhoff, Yvan Sortais, Anoush Aghajani-Talesh, and Mark A. Kasevich. "Field Emission Tip as a Nanometer Source of Free Electron Femtosecond Pulses". In: *Phys. Rev. Lett.* 96 (7 Feb. 2006), p. 077401. URL: http://link.aps.org/doi/10.1103/PhysRevLett.96.077401.

[185] Hirofumi Yanagisawa et al. "Optical Control of Field-Emission Sites by Femtosecond Laser Pulses". In: *Phys. Rev. Lett.* 103 (25 Dec. 2009), p. 257603. URL: http://link.aps.org/doi/10.1103/PhysRevLett.103.257603.

[186] R. Bormann, M. Gulde, A. Weismann, S. V. Yalunin, and C. Ropers. "Tip-Enhanced Strong-Field Photoemission". In: *Phys. Rev. Lett.* 105 (14 Sept. 2010), p. 147601. URL: http://link.aps.org/doi/10.1103/PhysRevLett.105.147601.

[187] Yves C. Martin, Hendrik F. Hamann, and H. Kumar Wickramasinghe. "Strength of the electric field in apertureless near-field optical microscopy". In: *Journal of Applied Physics* 89.10 (2001), pp. 5774–5778. URL: http://scitation.aip.org/content/aip/journal/jap/89/10/10.1063/1.1354655.

[188] X.J. Zhou et al. "Space charge effect and mirror charge effect in photoemission spectroscopy". In: *Journal of Electron Spectroscopy and Related Phenomena* 142.1 (2005), pp. 27–38.

[189] S. Passlack et al. "Space charge effects in photoemission with a low repetition, high intensity femtosecond laser source". In: *Journal of Applied Physics* 100.2, 024912 (2006). URL: http://scitation.aip.org/content/aip/journal/jap/100/2/10.1063/1.2217985.

[190] S. Hellmann, K. Rossnagel, M. Marczynski-Buhlow, and L. Kipp. "Vacuum space-charge effects in solid-state photoemission". In: *Phys. Rev. B* 79 (3 Jan. 2009), p. 035402. URL: http://link.aps.org/doi/10.1103/PhysRevB.79.035402.

[191] Bradley J. Siwick, Jason R. Dwyer, Robert E. Jordan, and R. J. Dwayne Miller. "Ultrafast electron optics: Propagation dynamics of femtosecond electron packets". In: *Journal of Applied Physics* 92.3 (2002), pp. 1643–1648. URL: http://scitation.aip.org/content/aip/journal/jap/92/3/10.1063/1.1487437.

[192] Kowalevicz Andrew. "Ultrashort Pulse Generation and Measurement". In: *Optical Techniques for Solid-State Materials Characterization*. doi:10.1201/b11040-11. CRC Press, 2011, pp. 237–289. URL: http://dx.doi.org/10.1201/b11040-11.

[193] A. D. LaForge et al. "Optical characterization of $Bi_2Se_3$ in a magnetic field: Infrared evidence for magnetoelectric coupling in a topological insulator material". In: *Phys. Rev. B* 81 (12 Mar. 2010), p. 125120. URL: http://link.aps.org/doi/10.1103/PhysRevB.81.125120.

[194] U. Höfer et al. "Time-Resolved Coherent Photoelectron Spectroscopy of Quantized Electronic States on Metal Surfaces". In: *Science* 277.5331 (1997), pp. 1480–1482. eprint: http://science.sciencemag.org/content/277/5331/1480.full.pdf. URL: http://science.sciencemag.org/content/277/5331/1480.

[195] Gregor Jotzu et al. "Experimental realization of the topological Haldane model with ultracold fermions". In: *Nature* 515.7526 (2014), pp. 237–240. URL: http://dx.doi.org/10.1038/nature13915.

[196] Mikael C. Rechtsman et al. "Photonic Floquet topological insulators". In: *Nature* 496.7444 (2013), pp. 196–200. URL: http://dx.doi.org/10.1038/nature12066.

[197] N. Peter Armitage. "Cuprate superconductors: Dynamic stabilization?" In: *Nat Mater* 13.7 (2014), pp. 665–666. URL: http://dx.doi.org/10.1038/nmat3995.

[198] Claude Cohen-Tannoudji, Jacques Dupont-Roc, and Gilbert Grynberg. *Atom-photon interactions : basic processes and applications.* Physics textbook. Weinheim : Wiley-VCH, c2004., 2004.

[199] T. Oka and H. Aoki. "Photovoltaic Hall effect in graphene". In: *Phys. Rev. B* 79 (2009). 10.1103/PhysRevB.79.081406, p. 081406. URL: http://dx.doi.org/10.1103/PhysRevB.79.081406.

[200] T. Kitagawa, E. Berg, M. Rudner, and E. Demler. "Topological characterization of periodically driven quantum systems". In: *Phys. Rev. B* 82 (2010). 10.1103/PhysRevB.82.235114, p. 235114. URL: http://dx.doi.org/10.1103/PhysRevB.82.235114.

[201] Takuya Kitagawa, Takashi Oka, Arne Brataas, Liang Fu, and Eugene Demler. "Transport properties of nonequilibrium systems under the application of light: Photoinduced quantum Hall insulators without Landau levels". In: *Physical Review B* 84.23 (2011). PRB, p. 235108. URL: http://link.aps.org/doi/10.1103/PhysRevB.84.235108.

[202] Netanel H. Lindner, Gil Refael, and Victor Galitski. "Floquet topological insulator in semiconductor quantum wells". In: *Nat Phys* 7.6 (2011). 10.1038/nphys1926, pp. 490–495. URL: http://dx.doi.org/10.1038/nphys1926.

[203] Z. Gu, H. A. Fertig, D. P. Arovas, and A. Auerbach. "Floquet spectrum and transport through an irradiated graphene ribbon". In: *Phys. Rev. Lett.* 107 (2011). 10.1103/PhysRevLett.107.216601, p. 216601. URL: http://dx.doi.org/10.1103/PhysRevLett.107.216601.

[204] H. L. Calvo, H. M. Pastawski, S. Roche, and L. E. F. Foa Torres. "Tuning laser-induced band gaps in graphene". In: *Appl. Phys. Lett.* 98 (2011). 10.1063/1.3597412, p. 232103. URL: http://dx.doi.org/10.1063/1.3597412.

[205] B. Dora, J. Cayssol, F. Simon, and R. Moessner. "Optically engineering the topological properties of a spin Hall insulator". In: *Phys. Rev. Lett.* 108 (2012). 10.1103/PhysRevLett.108.056602, p. 056602. URL: http://dx.doi.org/10.1103/PhysRevLett.108.056602.

[206] E. Suarez Morell and L. E. F. Foa Torres. "Radiation effects on the electronic properties of bilayer graphene". In: *Phys. Rev. B* 86 (2012). 10.1103/PhysRevB.86.125449, p. 125449. URL: http://dx.doi.org/10.1103/PhysRevB.86.125449.

[207] T. Iadecola. "Materials design from nonequilibrium steady states: driven graphene as a tunable semiconductor with topological properties". In: *Phys. Rev. Lett.* 110 (2013). 10.1103/PhysRevLett.110.176603, p. 176603. URL: http://dx.doi.org/10.1103/PhysRevLett.110.176603.

[208] M. S. Rudner, N. H. Lindner, E. Berg, and M. Levin. "Anomalous edge states and the bulk-edge correspondence for periodically driven two-dimensional systems". In: *Phys. Rev. X* 3 (2013), p. 031005.

[209] P. M. Perez-Piskunow, G. Usaj, C. A. Balseiro, and L. E. F. Foa Torres. "Floquet chiral edge states in graphene". In: *Phys. Rev. B* 89 (2014). 10.1103/PhysRevB.89.121401, p. 121401. URL: http://dx.doi.org/10.1103/PhysRevB.89.121401.

[210] Adolfo G. Grushin, Alvaro Gomez-Leon, and Titus Neupert. "Floquet Fractional Chern Insulators". In: *Physical Review Letters* 112.15 (2014). PRL, p. 156801. URL: http://link.aps.org/doi/10.1103/PhysRevLett.112.156801.

[211] Walter Kohn. "Periodic Thermodynamics". In: *Journal of Statistical Physics* 103.3-4 (2001), pp. 417–423. URL: http://dx.doi.org/10.1023/A%3A1010327828445.

[212] J. Eisert, M. Friesdorf, and C. Gogolin. "Quantum many-body systems out of equilibrium". In: *Nat Phys* 11.2 (2015), pp. 124–130. URL: http://dx.doi.org/10.1038/nphys3215.

[213] Karthik I. Seetharam, Charles-Edouard Bardyn, Netanel H. Lindner, Mark S. Rudner, and Gil Refael. "Controlled Population of Floquet-Bloch States via Coupling to Bose and Fermi Baths". In: *Phys. Rev. X* 5 (4 Dec. 2015), p. 041050. URL: http://link.aps.org/doi/10.1103/PhysRevX.5.041050.

[214] Thomas Bilitewski and Nigel R. Cooper. "Scattering theory for Floquet-Bloch states". In: *Phys. Rev. A* 91 (3 Mar. 2015), p. 033601. URL: http://link.aps.org/doi/10.1103/PhysRevA.91.033601.

[215] H. Dehghani, T. Oka, and A. Mitra. "Dissipative Floquet topological systems". In: *Phys. Rev. B* 90 (2014). 10.1103/PhysRevB.90.195429, p. 195429. URL: http://dx.doi.org/10.1103/PhysRevB.90.195429.

[216] A. Kundu, H. A. Fertig, and B. Seradjeh. "Effective theory of Floquet topological transitions". In: *Phys. Rev. Lett.* 113 (2014). 10.1103/PhysRevLett.113.236803, p. 236803. URL: http://dx.doi.org/10.1103/PhysRevLett.113.236803.

[217] M. A. Sentef et al. "Theory of Floquet band formation and local pseudospin textures in pump-probe photoemission of graphene". In: *Nat Commun* 6 (2015). URL: http://dx.doi.org/10.1038/ncomms8047.

[218] Joel E. Moore. "The birth of topological insulators". In: *Nature* 464.7286 (2010). 10.1038/nature08916, pp. 194–198. URL: http://dx.doi.org/10.1038/nature08916.

[219] Hari C. Manoharan. "Topological insulators: A romance with many dimensions". In: *Nat Nano* 5.7 (2010). 10.1038/nnano.2010.138, pp. 477–479. URL: http://dx.doi.org/10.1038/nnano.2010.138.

[220] XL Qi and SC Zhang. "The quantum spin Hall effect and topological insulators." In: *PHYSICS TODAY* 63.1 (), pp. 33–38.

[221] D. J. Thouless, M. Kohmoto, M. P. Nightingale, and M. den Nijs. "Quantized Hall Conductance in a Two-Dimensional Periodic Potential". In: *Phys. Rev. Lett.* 49 (6 Aug. 1982), pp. 405–408. URL: http://link.aps.org/doi/10.1103/PhysRevLett.49.405.

[222] C. L. Kane and E. J. Mele. "Quantum Spin Hall Effect in Graphene". In: *Phys. Rev. Lett.* 95 (22 Nov. 2005), p. 226801. URL: http://link.aps.org/doi/10.1103/PhysRevLett.95.226801.

[223] Liang Fu, C. L. Kane, and E. J. Mele. "Topological Insulators in Three Dimensions". In: *Phys. Rev. Lett.* 98 (10 Mar. 2007), p. 106803. URL: http://link.aps.org/doi/10.1103/PhysRevLett.98.106803.

[224] J. E. Moore and L. Balents. "Topological invariants of time-reversal-invariant band structures". In: *Phys. Rev. B* 75 (12 Mar. 2007), p. 121306. URL: http://link.aps.org/doi/10.1103/PhysRevB.75.121306.

[225] Rahul Roy. "$Z_2$ classification of quantum spin Hall systems: An approach using time-reversal invariance". In: *Phys. Rev. B* 79 (19 May 2009), p. 195321. URL: http://link.aps.org/doi/10.1103/PhysRevB.79.195321.

[226] D. Hsieh et al. "A topological Dirac insulator in a quantum spin Hall phase". In: *Nature* 452.7190 (2008). 10.1038/nature06843, pp. 970–974. URL: http://dx.doi.org/10.1038/nature06843.

[227] D. Hsieh et al. "Observation of Time-Reversal-Protected Single-Dirac-Cone Topological-Insulator States in $Bi_2Te_3$ and $Sb_2Te_3$". In: *Phys. Rev. Lett.* 103 (14 Sept. 2009), p. 146401. URL: http://link.aps.org/doi/10.1103/PhysRevLett.103.146401.

[228] Y. L. Chen et al. "Experimental Realization of a Three-Dimensional Topological Insulator, Bi2Te3". In: *Science* 325.5937 (2009), pp. 178–181. eprint: http://science.sciencemag.org/content/325/5937/178.full.pdf. URL: http://science.sciencemag.org/content/325/5937/178.

[229] Y. Zhou and M. W. Wu. "Optical response of graphene under intense terahertz fields". In: *Physical Review B* 83.24 (2011). PRB, p. 245436. URL: http://link.aps.org/doi/10.1103/PhysRevB.83.245436.

[230] S. V. Syzranov, M. V. Fistul, and K. B. Efetov. "Effect of radiation on transport in graphene". In: *Physical Review B* 78.4 (2008). PRB, p. 045407. URL: http://link.aps.org/doi/10.1103/PhysRevB.78.045407.

[231] Benjamin M. Fregoso, Y. H. Wang, N. Gedik, and Victor Galitski. "Driven electronic states at the surface of a topological insulator". In: *Physical Review B* 88.15 (2013). PRB, p. 155129. URL: http://link.aps.org/doi/10.1103/PhysRevB.88.155129.

[232] Y. H. Wang et al. "Observation of a Warped Helical Spin Texture in $Bi_2Se_3$ from Circular Dichroism Angle-Resolved Photoemission Spectroscopy". In: *Physical Review Letters* 107.20 (2011). PRL, p. 207602. URL: http://link.aps.org/doi/10.1103/PhysRevLett.107.207602.

[233] F. D. M. Haldane. "Model for a Quantum Hall Effect without Landau Levels: Condensed-Matter Realization of the "Parity Anomaly"". In: *Phys. Rev. Lett.* 61 (18 Oct. 1988), pp. 2015–2018. URL: http://link.aps.org/doi/10.1103/PhysRevLett.61.2015.

[234] Cui-Zu Chang et al. "Experimental Observation of the Quantum Anomalous Hall Effect in a Magnetic Topological Insulator". In: *Science* 340.6129 (2013), pp. 167–170. eprint: http://science.sciencemag.org/content/340/6129/167.full.pdf. URL: http://science.sciencemag.org/content/340/6129/167.

[235] Martin Wegener. *Extreme nonlinear optics : an introduction.* Advanced texts in physics. Berlin ; New York : Springer, c2005., 2005.

[236] G. Saathoff, L. Miaja-Avila, M. Aeschlimann, M. M. Murnane, and H. C. Kapteyn. "Laser-assisted photoemission from surfaces". In: *Physical Review A* 77.2 (2008). PRA, p. 022903. URL: http://link.aps.org/doi/10.1103/PhysRevA.77.022903.

[237] L. Miaja-Avila et al. "Ultrafast studies of electronic processes at surfaces using the laser-assisted photoelectric effect with long-wavelength dressing light". In: *Physical Review A* 79.3 (2009). PRA, p. 030901. URL: http://link.aps.org/doi/10.1103/PhysRevA.79.030901.

[238] T. E. Glover, R. W. Schoenlein, A. H. Chin, and C. V. Shank. "Observation of Laser Assisted Photoelectric Effect and Femtosecond High Order Harmonic Radiation". In: *Physical Review Letters* 76.14 (1996). PRL, pp. 2468–2471. URL: http://link.aps.org/doi/10.1103/PhysRevLett.76.2468.

[239] Lars Bojer Madsen. "Strong-field approximation in laser-assisted dynamics". In: *American Journal of Physics* 73.1 (2005), pp. 57–62. URL: http://scitation.aip.org/content/aapt/journal/ajp/73/1/10.1119/1.1796791.

[240] J. C. Baggesen and L. B. Madsen. "Theory for time-resolved measurements of laser-induced electron emission from metal surfaces". In: *Physical Review A* 78.3 (2008). PRA, p. 032903. URL: http://link.aps.org/doi/10.1103/PhysRevA.78.032903.

[241] R. M. Potvliege C. J. Joachain N. J. Kylstra. *Atoms in Intense Laser Fields*. Cambrige University Press, 2014.

[242] Sang Tae Park. "Interference in Floquet-Volkov transitions". In: *Physical Review A* 90.1 (2014). PRA, p. 013420. URL: http://link.aps.org/doi/10.1103/PhysRevA.90.013420.

[243] J. K. Freericks, H. R. Krishnamurthy, and Th Pruschke. "Theoretical Description of Time-Resolved Photoemission Spectroscopy: Application to Pump-Probe Experiments". In: *Physical Review Letters* 102.13 (2009). PRL, p. 136401. URL: http://link.aps.org/doi/10.1103/PhysRevLett.102.136401.

[244] Liang Fu. "Hexagonal Warping Effects in the Surface States of the Topological Insulator $Bi_2Te_3$". In: *Phys. Rev. Lett.* 103 (26 Dec. 2009), p. 266801. URL: http://link.aps.org/doi/10.1103/PhysRevLett.103.266801.

[245] S V Dordevic, M S Wolf, N Stojilovic, Hechang Lei, and C Petrovic. "Signatures of charge inhomogeneities in the infrared spectra of topological insulators Bi 2 Se 3 , Bi 2 Te 3 and Sb 2 Te 3". In: *Journal of Physics: Condensed Matter* 25.7 (2013), p. 075501. URL: http://stacks.iop.org/0953-8984/25/i=7/a=075501.

[246] Darius H. Torchinsky, G. F. Chen, J. L. Luo, N. L. Wang, and Nuh Gedik. "Band-dependent Quasiparticle Dynamics in Single Crystals of the $Ba_{0.6}\mathbf{K}_{0.4}Fe_2As_2$ Superconductor Revealed by Pump-Probe Spectroscopy". In: *Phys. Rev. Lett.* 105 (2 July 2010), p. 027005. URL: http://link.aps.org/doi/10.1103/PhysRevLett.105.027005.

[247] Alex Frenzel. "Terahertz Electrodynamics of Dirac Fermions in Graphene". PhD thesis. Harvard University, 2015.